

*A Unified Monte Carlo Approach for Quantitative Standardless X-Ray  
Fluorescence and Electron Probe Microanalysis inside the Scanning  
Electron Microscope*

\*\*\*

*Ein Vereinheitlichter Monte-Carlo-Ansatz zur Quantitativen  
Standardfreien Röntgenfluoreszenz - und Elektronenstrahl-  
mikroanalyse im Rasterelektronenmikroskop*

**Dissertation**

Zur Erlangung des Grades eines Doktors der Naturwissenschaften  
der Fakultät für Mathematik und Physik  
der Eberhard-Karls-Universität Tübingen

vorgelegt von  
Stefan Steinbrecher  
aus Ludwigshafen/Rhein

**2004**

Tag der mündlichen Prüfung : 6. Juli 2004

Dekan Prof. Dr. H. Müther

1. Berichterstatter : Prof. Dr. E. Plies

2. Berichterstatter : Prof. Dr. O. Eibl

3. Berichterstatter : Prof. Dr. J. Wernisch

Die vorliegende Arbeit wurde am  
Institut für Angewandte Physik,  
Eberhard-Karls-Universität Tübingen,  
in der Arbeitsgruppe von  
Herrn Prof. Dr. E. Plies  
angefertigt.

Herrn Prof. Dr. E. Plies möchte ich an dieser Stelle für die freundliche Aufnahme in seine  
Arbeitsgruppe,  
die Möglichkeit, das vorliegende Thema zu bearbeiten und die Ergebnisse auf Tagungen zu  
präsentieren,  
die hervorragenden Arbeitsbedingungen, sowie sein Interesse an dieser Arbeit und die  
gewährte Unterstützung

sehr herzlich danken !



*Wer immer tut, was er schon kann,  
bleibt immer das, was er schon ist.*

HENRY FORD



# TABLE OF CONTENTS

<b>Abstract</b>	<b>I</b>
-----------------	----------

---

<b>Kurzfassung</b>	<b>III</b>
--------------------	------------

---

<b>Definitions</b>	<b>VII</b>
--------------------	------------

---

Constants	VII
List of Abbreviations	VIII
List of Symbols and Definitions	IX
Subscripts	XIII
Superscripts	XIV
Prefixes	XIV
Units	XV

<b>Introduction</b>	<b>1</b>
---------------------	----------

---

## I. THEORETICAL ASPECTS OF X-RAY EMISSION SPECTROSCOPY

<b>1 X-Ray Emission Spectroscopy</b>	<b>3</b>
--------------------------------------	----------

---

1.1 X-Ray Emission Spectroscopic Techniques	3
1.2 Dispersive Detection of X-Rays	6

<b>2 Generation of Characteristic X-Ray Spectra</b>	<b>9</b>
---	----------

---

2.1 Interaction of X-Rays with Matter	12
2.1.1 Photoelectric Interaction	14
2.1.2 Photon Scattering	15
2.2 Interaction of Electrons with Matter	17
2.2.1 Elastic Electron Scattering	17

2.2.2	<i>Inelastic Electron Scattering</i>	21
2.2.3	<i>Inner Shell Ionisation by Electron Impact</i>	23
2.3	Description of Multiple Electron Energy Losses	25
2.3.1	<i>Continuous Electron Energy Loss Approximation</i>	25
2.3.2	<i>Phenomenology of Electron Scattering</i>	27
2.3.3	<i>Depth Distribution of Characteristic X-Ray Generation</i>	29

### **3 Quantification Methods in X-Ray Emission Spectroscopy** **33**

---

3.1	The Analytical Problem	33
3.1.1	<i>Empirical Coefficient Methods</i>	34
3.1.2	<i>Fundamental Parameter Methods</i>	35
3.2	Quantitative X-Ray Fluorescence Analysis	38
3.2.1	<i>Monochromatic Excitation</i>	38
3.2.2	<i>Polychromatic Excitation</i>	40
3.3	Quantitative Electron Probe Microanalysis	41
3.3.1	<i>Atomic Number (Z-) Correction</i>	42
3.3.2	<i>Absorption (A-) Correction</i>	43
3.3.3	<i>The <math>\phi(\rho z)</math> Technique</i>	44
3.3.4	<i>Fluorescence (F-) Correction</i>	46
3.4	Modelling the Detection Process	47
3.4.1	<i>Detector Resolution and Efficiency</i>	48
3.4.2	<i>Detector Artifacts</i>	50
3.5	Matrix Correction Procedures in Practice	51
3.6	Analytical Sensitivity and Detection Limits	53

## II. COMPUTATIONAL METHODS

<b>4 Monte Carlo Simulation of X-Ray Emission Spectra</b>	<b>57</b>
4.1 The Fundamental Computational Procedure	58
4.2 The Spectral Response of X-Ray Excited Samples	60
4.2.1 <i>X-Ray Source Emission</i>	62
4.2.2 <i>Photon-Matter Interactions</i>	66
4.2.3 <i>Modelling the Photoelectric Effect</i>	67
4.2.4 <i>Modelling Photon Scattering</i>	68
4.2.5 <i>Probabilistic Interpretation of X-Ray Emission</i>	72
4.3 The Spectral Response of Electron Excited Samples	74
4.3.1 <i>Electron Diffusion</i>	75
4.3.2 <i>Implementation of X-Ray Emission</i>	77
4.4 Processing of Simulation Data	80
4.4.1 <i>Conversion of Simulation Data into Spectra</i>	80
4.4.2 <i>Comparison of Experimental and Simulated Data</i>	82
4.5 Conclusions	83

## III. RESULTS AND DISCUSSION

<b>5 X-Ray Fluorescence Analysis in the Scanning Electron Microscope</b>	<b>85</b>
5.1 Lowering the Detection Limits in the Scanning Electron Microscope	85
5.2 Sample Holder Design	89
5.2.1 <i>Instrumental Parameters and Geometric Preconditions</i>	89
5.2.2 <i>Implementation</i>	90
5.3 Characterisation of X-Ray Sources	93
5.3.1 <i>Spectral Distribution of X-Ray Source Emission</i>	93
5.3.2 <i>Angular Distribution of X-Ray Source Emission</i>	103
5.4 Performance of X-Ray Fluorescence Analysis	106
5.4.1 <i>Adjustment and Efficiency of Excitation</i>	106

5.4.2	<i>X-Ray Scatter Peaks</i>	112
5.5	Conclusions	114
<b>6</b>	<b>Application of Monte Carlo Methods in X-Ray Emission Spectroscopy</b>	<b>117</b>
6.1	Assessment of Fundamental Parameters in Electron Microprobe Analysis	117
6.1.1	<i>Backscatter Coefficient and Energy Spectra of Backscattered Electrons</i>	117
6.1.2	<i>Intensity of Characteristic Radiation</i>	122
6.2	Simulation of X-Ray Emission Spectra	125
6.3	Quantitative X-Ray Emission Spectroscopy	129
6.4	Computation Speed	139
6.5	Detection Limits	143
6.6	Conclusions	145
<b>7</b>	<b>Further Applications</b>	<b>147</b>
7.1	Determination of k Ratios and Detection of Fluorescent Pathways	147
7.2	Thin Samples	151
7.3	Tilted Samples	159
7.4	Conclusions	160
<b>8</b>	<b>Summary</b>	<b>163</b>
<b>9</b>	<b>Appendix</b>	<b>171</b>
9.1	Flow Diagrams of Monte Carlo Algorithms	171
9.2	Construction Drawings of the X-Ray Fluorescence Specimen Stage	174
9.3	Resolution of the EDS Detection System	180
9.4	List of Materials Utilised to Construct the X-Ray Fluorescence Facilities	181
9.5	List of Samples and Experimental Conditions for Quantitative Analysis	182
<b>10</b>	<b>References</b>	<b>185</b>





## Abstract

The implementation of standardless quantitative X-ray fluorescence analysis to a conventional scanning electron microscope equipped with an X-ray spectrometer is subject of the present work. For this purpose, an optimised sample holder was designed, constructed, successfully characterised and tested, which transfers the operation principle of a transmission-type end-window X-ray tube into the specimen chamber of a scanning electron microscope. The device allows a fast and easy exchange of target, filter, and sample and therefore offers flexible excitation conditions and a high sample throughput. As modifications of the microscope hardware are not necessary, switching between electron microprobe analysis and X-ray fluorescence analysis is easily accomplished. X-ray fluorescence analysis inside the scanning electron microscope offers significantly improved detection limits compared to electron excitation of the X-ray emission spectrum. The analytical results show that in common alloys composed of first row transition metals a two to seven fold decrease of detection limits is achieved. Standardless quantitative trace analysis of heavy elements in a light element matrix is even shown to be possible down to mass concentrations of approximately 3 ppm lead in aluminium corresponding to an atom fraction of only 400 ppb.

A Monte Carlo procedure to predict the spectral response of X-ray excited samples is described. An expansion of this procedure to simulate subsequent electron-photon interactions is presented, which advantageously enables the simulation of electron excited X-ray emission spectra including the Bremsstrahlung background. Standardless unified Monte Carlo quantification of X-ray emission spectra acquired in a scanning electron microscope is thus possible with high accuracy and precision. As Monte Carlo simulations do not distinguish between characteristic X-rays and continuous background, numerical processing of spectra prior to analysis, such as background removal, peak fitting, and overlap correction, can be entirely abandoned.

Unlike fundamental parameter methods, Monte Carlo simulations are solely based on atomic properties. Therefore, valuable additional information such as size and shape of the electron diffusion volume, X-ray depth distribution functions, or many analytical signals such as the spectral distribution of backscattered or transmitted electrons are simulated at the same time. Monte Carlo techniques are easily adapted to suit special requirements, such as more complex

---

sample geometries. In this context, additional applications of the proposed Monte Carlo techniques to the metrology of thin samples by X-ray scattering and electron backscattering are reported exemplarily. These also show excellent agreement between experimental and simulated data in this field.

---

## **Kurzfassung**

Die vorliegende Arbeit befaßt sich mit der Implementierung der Röntgenfluoreszenzanalyse in ein konventionelles, mit einem Röntgenspektrometer ausgestattetes Rasterelektronenmikroskop. Zu diesem Zweck wurde ein optimierter Probenhalter entworfen und gebaut, welcher das Funktionsprinzip einer in Transmission arbeitenden Röntgenröhre in das Rasterelektronenmikroskop überträgt. Dieser wurde charakterisiert und erfolgreich getestet. Der Probenhalter ermöglicht einen schnellen und einfachen Austausch der als Target und Filter eingesetzten Metallfolien sowie der Probe, wodurch eine hohe Flexibilität der Anregungsbedingungen und ein hoher Probendurchsatz erzielt werden. Da Veränderungen an Bauteilen des Mikroskops selbst nicht nötig sind, kann durch die beschriebene Anordnung sehr leicht zwischen Röntgenfluoreszenzanalyse und Elektronenstrahlmikroanalyse gewechselt werden. Gegenüber der Elektronenstrahlmikroanalyse bietet die Röntgenfluoreszenzanalyse eine wesentliche Verbesserung der Nachweisgrenzen. Die Analyseergebnisse für kommerziell erhältliche Legierungen aus Elementen der ersten Übergangsmetallreihe zeigen eine Erniedrigung der Nachweisgrenzen um einen Faktor von zwei bis sieben, während Spuren mittelschwerer und schwerer Elemente in Leichtelementmatrices sogar bis in den Bereich weniger ppm standardfrei quantitativ nachgewiesen werden können. Für Blei in Aluminium wurde eine Nachweisgrenze von 3 ppm nach Masse erhalten, was einem Atomverhältnis von nur 400 ppb entspricht.

Ein Monte-Carlo-Verfahren zur Simulation der spektralen Antwort röntgenangeregter Proben im Bereich charakteristischer Röntgenstrahlung wird beschrieben. Dieses wird durch Kopplung an einen Algorithmus zur Simulation der Diffusion von Strahlelektronen erweitert, sodaß in vorteilhafter Weise die elektroneninduzierte Emission sowohl charakteristischer als auch kontinuierlicher Röntgenstrahlung zugänglich ist. Dieser vereinheitlichte Ansatz ermöglicht die standardfreie Quantifizierung von im Rasterelektronenmikroskop aufgenommenen Röntgenemissionsspektren mit sehr hoher Genauigkeit und Präzision. Da Monte-Carlo-Simulationen nicht zwischen charakteristischem und kontinuierlichem Röntgenspektrum unterscheiden, kann sogar auf eine numerische Vorbearbeitung der Spektren, das heißt Untergrund- und Überlappungskorrektur sowie analytische Anpassung der Linien an Gaußprofile, komplett verzichtet werden.

---

Im Gegensatz zu Fundamental-Parameter-Methoden nutzen Monte-Carlo-Verfahren lediglich atomare Größen. Daher sind wertvolle zusätzliche Informationen in der gleichen Simulation zusammen mit dem Röntgenspektrum sehr einfach erhältlich. Diese umfassen die Streubirne, die Röntgen-Tiefenverteilungsfunktionen oder viele analytisch verwertbare Signale, wie zum Beispiel Rückstreuелеktronenspektren oder Energieverlustspektren transmittierter Elektronen. Darüberhinaus sind Monte-Carlo-Verfahren sehr leicht an spezielle analytische Probleme, wie beispielsweise Proben komplexerer Geometrie, adaptierbar. Zusätzlich zu den berichteten Anwendungen wird in diesem Zusammenhang die Nutzbarkeit des vorgestellten Monte-Carlo-Verfahrens für die Metrologie dünner Proben durch Röntgenstreuung und Elektronenrückstreuung exemplarisch dargestellt. Auch auf diesem Gebiet ist die exzellente Übereinstimmung von Experiment und Simulation sichtbar.

---





---

**Definitions**
Constants

$\pi$	3.141592654...		
$c$	299792458	msec <sup>-1</sup>	Speed of light in vacuum
$e$	$1.60217733 \cdot 10^{-19}$	C	Electron charge
$h$	$6.6260755 \cdot 10^{-34}$	Jsec	PLANCK constant
$m_e$	$9.1093897 \cdot 10^{-31}$	kg	Electron rest mass
$N_A$	$6.0221367 \cdot 10^{23}$	mol <sup>-1</sup>	AVOGADRO constant
$\mu_0$	$4\pi \cdot 10^{-7}$	Nm <sup>-2</sup>	Permeability of vacuum
$a_K (= \frac{e^6}{6\sqrt{3}\pi\epsilon_0^3 hc^5 m_e^2})$	$5.6055353 \cdot 10^{-31}$	m <sup>2</sup>	KRAMERS cross- section
$a_0 (= \alpha / 4\pi R)$	$5.29177249 \cdot 10^{-11}$	m	BOHR radius
$m_e c^2$	$8.1871112 \cdot 10^{-14}$	J	Electron rest energy
	510.9990645	keV	
$R$	$1.0973731534 \cdot 10^7$	m <sup>-1</sup>	RYDBERG constant
$r_e (= \alpha^2 a_0)$	$2.81794092 \cdot 10^{-15}$	m	Classical electron radius
$Rhc$	$2.1798741 \cdot 10^{-18}$	J	
	13.6055296	eV	
$\alpha (= \mu_0 c e^2 / 2h)$	$7.29735308 \cdot 10^{-3}$	1	Fine structure constant
$\epsilon_0 (= 1/\mu_0 c^2)$	$8.854187817 \cdot 10^{-12}$	AsecV <sup>-1</sup> m <sup>-1</sup>	Permittivity of vacuum
$\sigma_0 (= e^4 / 16\pi\epsilon_0^2)$	$1.67214916 \cdot 10^{-55}$	J <sup>2</sup> m <sup>2</sup>	
	$6.51409142 \cdot 10^{-20}$	keV <sup>2</sup> cm <sup>2</sup>	

---

---

List of Abbreviations

bkg.	Background, referring to spectral background
char.	Characteristic, referring to characteristic radiation
EELS	<u>E</u> lectron <u>e</u> nergy <u>l</u> oss <u>s</u> pectroscopy
EDS	<u>E</u> nergy dispersive <u>X</u> -ray <u>s</u> pectroscopy
EFTEM	<u>E</u> nergy <u>f</u> iltering <u>t</u> ransmission <u>e</u> lectron <u>m</u> icroscopy, <u>E</u> nergy <u>f</u> iltering <u>t</u> ransmission <u>e</u> lectron <u>m</u> icroscope
EP(X)MA	<u>E</u> lectron probe ( <u>X</u> -ray) <u>m</u> icro <u>a</u> nalysis
FP	<u>F</u> undamental <u>p</u> arameters, a set of suitable physical constants and atomic properties used to perform matrix correction in X-ray emission spectroscopy
n.d.	<u>n</u> ot <u>d</u> etectable
NIST	<u>N</u> ational <u>I</u> nstitute of <u>S</u> tandards and <u>T</u> echnology
PIXE	<u>P</u> roton <u>i</u> nduced <u>X</u> -ray <u>e</u> mission spectroscopy, <u>P</u> article <u>i</u> nduced <u>X</u> -ray <u>e</u> mission spectroscopy
ROI	<u>R</u> egion of <u>i</u> nterest
SEM	<u>S</u> canning <u>e</u> lectron <u>m</u> icroscopy, <u>S</u> canning <u>e</u> lectron <u>m</u> icroscope
SIMS	<u>S</u> econdary <u>i</u> on <u>m</u> ass <u>s</u> pectrometry
SRM	<u>S</u> tandard <u>R</u> eference <u>M</u> aterial
SRXRFA	<u>S</u> ynchrotron <u>r</u> adiation <u>X</u> -ray <u>f</u> luorescence <u>a</u> nalysis
TEM	<u>T</u> ransmission <u>e</u> lectron <u>m</u> icroscopy, <u>T</u> ransmission <u>e</u> lectron <u>m</u> icroscope
TRXRFA	<u>T</u> otal <u>r</u> eflection <u>X</u> -ray <u>f</u> luorescence <u>a</u> nalysis
var	variance
WDS	<u>W</u> avelength <u>d</u> ispersive <u>X</u> -ray <u>s</u> pectroscopy
XRFA	<u>X</u> -ray <u>f</u> luorescence <u>a</u> nalysis
ZAF	Procedure correcting for atomic number ( <u>Z</u> ), absorption ( <u>A</u> ), and fluorescence effects ( <u>F</u> ) in electron microprobe analysis
$\mu$ -XRFA	<u>M</u> icro- <u>X</u> -ray <u>f</u> luorescence <u>a</u> nalysis

---

---

## List of Symbols and Definitions

A	Atomic mass
A	Absorption correction factor
a	AUGER yield
c	Mass fraction
d	Diametre
D	Illuminated sample surface (X-ray fluorescence analysis)
E	Energy
f	Absorption edge jump ratio
f	Probability distribution function
F	Atomic form factor
F	Cumulative probability distribution function
F	FANO factor
g	Ionisation function
G	GAUSSIAN spreading function
j	Spin quantum number
I	Current
I	Intensity
H	Fluorescence correction factor
J	Momentum distribution function of a bound electron (COMPTON profile)
J	Mean ionisation potential of an atom
k	Intensity ratio of X-rays measured from sample and standard (electron probe microanalysis)
k	Constant in MOSELEY'S law, connected to the RYDBERG constant
l	Orbital quantum number
m	mass
n	set consisting of n members
N	Number of X-ray quanta, number of counts
p	probability
p	Transition probability, emission rate
p	Momentum of an electron
P	Statistical weight

---

q	Momentum transfer during a scattering process ( $= \sin(\vartheta/2)/\lambda$ )
r	Ratio of differential MOTT cross-section and RUTHERFORD cross-section
$\underline{r}$	Vector, direction
s	Path length
R	Intensity ratio of X-rays (X-ray fluorescence analysis)
R	Backscatter correction factor
Q	Reduced electron momentum, projection of the momentum transfer k on the electron momentum p before a scattering process
S	Absorption edge jump
S	Inelastic scattering function
S	Spectral distribution as measured by a detector
T	Transmission
t	Thickness
u	Overvoltage ratio ( $=E/E_{\text{crit}}$ )
U	Reduced electron energy ( $=E/E_0$ ) („incidence overvoltage“)
v	Velocity of an electron
x	Cartesian coordinate
y	Cartesian coordinate
Y	X-ray yield
z	Cartesian coordinate directed normal to sample surface
z	Number of electrons in an atomic shell
Z	Atomic number
$\alpha$	Fine structure constant
$\alpha$	Screening constant (RUTHERFORD scattering)
$\alpha$	Angle of incidence measured towards sample surface
$\beta$	Velocity of an electron relative to the speed of light ( $v/c$ )
$\gamma$	Ratio of total MOTT cross-section and total RUTHERFORD cross-section
$\Delta$	Difference
$\varepsilon$	Detection efficiency
$\varepsilon$	Electron energy relative to the electron rest energy ( $=E/m_e c^2$ )
$\varepsilon$	Convergence limit

---

---

$\varepsilon$	Refractive index
$\eta$	Fraction of electrons relative to the number of incident electrons
$\vartheta$	BRAGG angle
$\vartheta$	Scattering angle, polar angle of deflection measured towards the previous direction of movement of an X-ray photon or an electron
$\Theta$	Polar angle in the laboratory system
$\lambda$	Mean free path length
$\lambda$	Wavelength, DE BROGLIE wavelength
$\mu$	Total mass attenuation coefficient for X-ray photons
$\rho$	Density
$\sigma$	Standard deviation
$\sigma$	Screening constant (MOSELEY'S law)
$\sigma$	Cross-section
$\tau$	Total photoelectric cross-section for X-ray photons
$\tau$	Counting time corrected for dead time
$\varphi$	Depth distribution of ionisation events
$\phi$	Azimuthal angle, scattering angle measured perpendicularly towards the previous direction of movement of an X-ray photon or electron
$\Phi$	Azimuthal angle in the laboratory system
$\chi$	Generalised absorption factor
$\psi$	Take-off angle measured towards sample surface
$\Omega$	Solid angle
$\omega$	Fluorescence yield
$c_T$	TERRILL'S constant
$E_0$	Primary energy of an incident electron or X-ray beam
$E_{\text{crit}}$	Absorption edge energy, ionisation threshold
$E_{\text{intr}}$	Intrinsic energy of a transition between valence band and conduction band of a semiconductor
$E_{\text{offset}}$	Energy offset of an X-ray detector
$E_{\text{mean}}$	Mean energy

---

---

$E_X$	X-Ray energy
$K/K_0$	Energy of a photon after COMPTON scattering with a bound electron relative to the incident energy irrespective of the DOPPLER effect
$r_{\text{det}}$	Radius of a planar detector with circular cross-section
$R_B$	BETHE range
$R_{\text{TW}}$	THOMSON-WHIDDINGTON range
$S_{\text{Bethe}}$	BETHE stopping power
$S/B$	Signal-to-background ratio
$\eta_{\text{abs}}$	Absorption coefficient
$\eta_B$	Backscattering coefficient
$\eta_T$	Transmission coefficient
$\vartheta_0$	Characteristic angle of elastic electron scattering
$\vartheta_E$	Characteristic angle of inelastic electron scattering
$\sigma_{\text{Brake}}$	Total scattering cross-section for generation of Bremsstrahlung
$\sigma_{\text{Com}}$	Total COMPTON scattering cross-section for X-ray photons
$\sigma_{\text{el}}$	Total elastic scattering cross-section for electrons
$\sigma_{\text{inel}}$	Total inelastic scattering cross-section for electrons
$\sigma_{\text{KN}}$	Total KLEIN-NISHINA cross-section
$\sigma_M$	Total MOTT scattering cross-section for electrons
$\sigma_R$	Total RUTHERFORD cross-section
$\sigma_{\text{Ray}}$	Total RAYLEIGH scattering cross-section for X-ray photons
$\sigma_{\text{Tot}}$	Sum of elastic and inelastic electron cross-section
$\Delta d_{\text{fwhm}}$	Lateral resolution given by the full width at half maximum of the intensity distribution
$\Delta E_{\text{gain}}$	Energy gain of an X-ray detector
$\Delta E_{\text{fwhm}}$	Energy resolution given by the full width at half maximum of an X-ray emission line
$\Delta E_{\text{noise}}$	Energy resolution due to electronic noise

---

---

$\Delta E_{st}$	Energy resolution due to statistic fluctuations
$\Delta E_w$	Energy window
$\Delta s$	Step length, free-flight path of an X-ray quantum or electron

### Subscripts

B	Backscattering
Bkg	Background
BSE	Backscattered electrons
calc	Calculated
ch	Channels
char	Referring to characteristic X-rays
det	Detection
dir	Directional
em	Emitted
esc	Escape
exc	Excitation
f	Filter
gen	Generated
i	Number of an element in a multicomponent system
ion	Ionisation
j	Number of an X-ray emission line or absorption edge of an atom
l	Number of an element in a multicomponent system
m	Number of an X-ray emission line or absorption edge of an atom
max	Maximum
md	Denoting the minimum detectable quantity
min	Minimum
meas	Measured
mono	Monochromatic radiation
P	Probe
pivot	Largest value within a given set of values
poly	Polychromatic radiation

---

sample	Referring to the sample
scale	Concerning the scaling of calculated to measured data
src	Source
st	Standard
t	Target
trans	Transmitted

### Superscripts

mono	Refers to effects caused by monochromatic radiation
n	Index of an iteration loop
photo	Denoting a photoelectric interaction
photon	Referring to an X-ray photon
scatter	Denoting a scatter interaction
1,2...	Primary, secondary...X-rays

### Prefixes

G	giga ( $10^9$ )
M	mega ( $10^6$ )
k	kilo ( $10^3$ )
c	centi ( $10^{-2}$ )
m	milli ( $10^{-3}$ )
$\mu$	micro ( $10^{-6}$ )
n	nano ( $10^{-9}$ )
p	pico ( $10^{-12}$ )

---

Units

A	Ampère
barn	$10^{-28} \text{ m}^2 = 10^{-24} \text{ cm}^2$
eV	Electron volt (1 eV = $1.60219 \cdot 10^{-19}$ J)
g	Gram
m	Metre
min	Minute
ppb	Parts per billion
ppm	Parts per million
sec	Second
V	Volt

Operators

*	Convolution
---	-------------

---



## Introduction

As tools for non-destructive multielement analysis, X-ray fluorescence and electron microprobe analysis have found widespread applications in very different disciplines. Material science, metallurgy, mineralogy, archaeology, art, and forensics are only a few fields in which X-ray emission spectroscopic techniques have proved valuable. In this context, the investigations on the Shroud of Turin<sup>1</sup> provide an outstanding example.

X-ray detectors are rather commonly found in connection with scanning or transmission electron microscopes. In X-ray fluorescence analysis, the instrumentation ranges from hand-held metallurgic inspection tools to elaborate microbeam instruments to be attached to synchrotron beamlines. The simplicity of X-ray emission spectra, however, is common to all techniques as they are almost independent of the chemical and physical state of the portion of matter under investigation. Therefore, *qualitative* information on the sample composition is straightforwardly obtained. The retrieval of the concentration of the sample constituents, resulting in a simultaneous *quantitative* elemental analysis, however, has remained a strongly nontrivial task since the first proposal of a matrix correction procedure by CASTAING.<sup>2</sup> Sophisticated physical models adapted to the particular analytical situation encountered and describing the usually complex probe-matter interactions are therefore necessary. In this context, Monte Carlo methods are very promising techniques. Due to their inherent flexibility they provide the potential to address a huge variety of standard and non-standard analytical problems in X-ray fluorescence and electron microprobe analysis alike.

The present work describes the development, test, application, and characterisation of an entirely Monte Carlo based matrix correction procedure to be applied in *both* X-ray fluorescence and electron microprobe analysis. Special attention is paid to X-ray fluorescence analysis, which was performed in the scanning electron microscope by means of an improved specimen stage. The design, construction, and test of this device are also within the scope of this work. In order to achieve these goals, a broad physical database describing the interaction of X-rays and electrons with matter is required. For this purpose, a compilation of relevant aspects of probe-atom interactions and an outline of conventional matrix correction procedures is provided in the introductory section.

---



## 1 X-Ray Emission Spectroscopy

A beam of charged particles or electromagnetic radiation of sufficient energy will excite, among other interaction products, the emission of X-rays when directed onto a sample.<sup>3</sup> The energy or wavelength distribution of the emitted intensity can be recorded as a spectrum with a suitable detector. As spectra are composed of lines that are characteristic of the atoms comprising the sample, they convey useful qualitative and quantitative information about the portion of matter under investigation. This basic principle is underlying all branches of X-ray emission spectroscopy. Depending on the nature of the primary projectile, X-ray fluorescence analysis (XRFA), electron probe X-ray microanalysis (EPXMA) and proton induced X-ray emission spectroscopy (PIXE) are the three basic analytical techniques. Excitation of spectra by ion bombardment is also possible but has gained no significance as an analytical technique as it is an intrinsically destructive method. In this case it is more desirable to detect secondary ions rather than secondary radiation (secondary ion mass spectrometry, SIMS).

### 1.1 X-Ray Emission Spectroscopic Techniques

In the laboratory, X-ray fluorescence analysis is carried out using annular radioisotope sources as well as water cooled transmission type or rotating anode X-ray tubes operated at energies between 40-60 keV and currents between 10-50 mA. Anode materials most commonly in use are chromium, iron, copper, molybdenum, rhodium, or tungsten. These yield primary X-ray energies ranging from 5.412 keV (Cr  $K_{\alpha 1,2}$ ) to 20.169 keV (Rh  $K_{\alpha 1,2}$ ) or produce a Bremsstrahlung continuum when characteristic lines are too energetic to be excited as in the case of tungsten. The X-ray spot size depends on the electron beam size on the anode and is typically in the range of several square millimetres. Due to the comparably weak interaction of X-rays with matter the information depth is in the order of typically 10 to 1000  $\mu\text{m}$ , depending on the primary beam energy and sample composition. Therefore, conventional laboratory X-ray fluorescence analysis is a bulk technique nearly without lateral resolution.

Below a critical angle, which is dependent on the beam energy and the material of the reflector, an X-ray beam can be totally reflected at plain surfaces. In this context, the use of glass capillaries for collimation in analogy to fibre optics in the visible region has been proposed in the 1970s.<sup>4,5</sup> Although numerous set-ups have been implemented<sup>6-13</sup> and also

---

described theoretically<sup>14</sup>, it was not until the recent years that X-ray capillary optics of this type have become available in commercial table-top fluorescence and diffraction instruments.<sup>15</sup> At incidence angles below 0.5°, silica has been shown to be an effective reflector for X-rays in the energy region of interest. Bundles of capillaries that are slightly curved towards the bundle axis at the exit side are used as 'lenses'. Brilliance and flux are increased significantly compared to instruments without capillary optics and homogeneous spots with diameters down to 10 to 30 µm are achieved, thus enabling microscopic X-ray fluorescence analysis (µ-XRFA) with laboratory instruments.

In X-ray fluorescence analysis, in-depth beam broadening can be neglected as the annihilation of an X-ray quantum in the photoelectric effect at its first interaction site in the sample is the dominating process. Therefore, the spot diameter defines lateral resolution. The information depth, however, remains unchanged. When working under conditions of grazing incidence, using fine focus X-ray tubes and incidence angles usually below 0.1°, the information depth can be lowered to 1 to 500 nm. Simultaneously, the spectral background is reduced, increasing the sensitivity of analysis significantly. Total reflection X-ray fluorescence analysis (TRXRFA) reaches absolute detection limits of 0.1 µg to 1 pg and is therefore suitable as trace and ultra-trace detection method. A detailed discussion of this technique has been given by KLOCKENKÄMPER.<sup>16</sup>

Due to their tunability in a large energy range and high brilliance, synchrotrons are the most versatile X-ray sources. Synchrotron radiation X-ray fluorescence analysis (SRXRFA) also takes advantage of X-ray polarisation to minimise the spectral background of scattered radiation. Absolute detection limits from 1-10 fg are reported in favourable cases. Due to the low refractive index ( $\epsilon-1 \approx 10^{-5}$ - $10^{-7}$ ) of matter in the X-ray regime diffractive optics like FRESNEL zone plates are applied to synchrotron sources. Lateral resolutions of 10 µm have been achieved and values of down to 1 µm are expected in the near future. An extensive discussion on microscopic X-ray fluorescence analysis and related techniques has been provided by JANSSENS et al.<sup>17</sup>

Electron excitation of X-ray emission from samples occurs as a by-product in the scanning electron microscope (SEM) as well as in the transmission electron microscope (TEM). Typical experimental conditions in the scanning electron microscope are primary beam energies of 5-30 keV at probe currents of 0.5-1 nA and spot sizes of 20 nm at normal beam incidence. Concerning their cross-sections, electrons interact more effectively with matter

---

than X-rays by several orders of magnitude. Scattering processes cause electrons to change their direction and to lose energy as they diffuse through the sample. Size and form of the interaction volume depend on the sample composition and the primary beam energy. Electron diffusion extends to about 1-10  $\mu\text{m}$  beneath the sample surface, which defines the information depth of electron probe X-ray microanalysis performed in the scanning electron microscope. The lateral resolution is limited by the maximum cross-section of the electron diffusion area, which is also in the order of 1-10  $\mu\text{m}$ . Absolute detected masses are very low. As an example, 1  $\mu\text{m}^3$  of copper corresponds to a mass of approximately 8.9 pg.

In conventional transmission electron microscopy, beam energies between 60-200 keV are encountered. X-ray microanalysis is usually performed in the scanning mode of the transmission electron microscope (STEM mode) with probe diameters down to 0.2-0.5 nm. As samples are only a few nanometres thick, in-depth beam broadening can be neglected and a spatial resolution of about 1 nm is typical. Inelastically scattered electrons are deflected only through very small angles and thus give rise to an undesired background in transmission electron microscopic imaging, which decreases contrast. For this reason, different types of electron energy filters have been implemented. In energy filtering transmission electron microscopes (EFTEM), electron energy loss spectra can be recorded as inelastically scattered electrons are lacking the energy that has been consumed to generate X-ray quanta. A survey on electron energy loss spectroscopy (EELS) has been presented by EGERTON.<sup>18</sup> Detailed information on X-ray emission spectroscopy in connection with scanning and transmission electron microscopy is provided by the monographs of REIMER<sup>19,20</sup> and GOLDSTEIN<sup>21</sup>, for example.

In proton induced X-ray emission (PIXE) spectroscopy, beam currents of 100 pA at energies of 1-2 MeV can be considered typical. It takes an intermediate position between X-ray fluorescence and electron probe X-ray microanalysis, as beam broadening is not as pronounced as for an electron probe, and spot diameters along with a lateral resolution of 1  $\mu\text{m}$  are currently achieved. The information depth, however, is larger than for an electron probe, but its dependency on the sample composition is weak and amounts to 40-60  $\mu\text{m}$ . As protons are not a well available probe in laboratories, proton induced X-ray emission will be omitted from further discussion. Information on the use of ion beam techniques in material analysis<sup>22,23</sup> and specific problems in processing<sup>24-26</sup> and quantification<sup>27,28</sup> of ion beam induced X-ray spectra is found in the literature.

---

## 1.2 Dispersive Detection of X-Rays

X-ray spectra can be recorded by detecting either the energy or wavelength of the emitted quanta. Consequently, energy dispersive spectroscopy (EDS) or wavelength dispersive spectroscopy (WDS) is performed.

Semiconductor devices, such as the most commonly used lithium-drifted silicon Si(Li) detector, are energy dispersive. Si(Li) detectors are p-i-n diodes, which absorb X-rays in their intrinsic zone by the photoelectric effect. The excess energy of the AUGER- and photoelectrons generated by these X-rays is transferred to the crystal and creates a number of electron-hole pairs, which is proportional to the energy of the incident quantum. The resulting charge is collected by applying a reverse bias in the order of 1 kV across the intrinsic zone. Charge-to-voltage conversion is achieved by a field-effect transistor as first amplifying stage. After electronic processing the signal is output to a multi-channel analyser. To ensure complete absorption of X-rays in the energy range between 0-30 keV within the detector, the intrinsic zone of the silicon diode has a thickness of 3-5 mm. Active detector areas are usually 1-30 mm<sup>2</sup>. The intrinsic zone is generated by diffusing lithium into a p-type silicon crystal. Acceptor states are compensated and a depletion layer of high electric resistivity is obtained. Generally, Si(Li) detectors are cooled with liquid nitrogen when operated to reduce the leakage current and to suppress the thermal noise of the preamplifier electronics. High energy backscattered electrons from the specimen can enter the detector and give rise to an undesired background. This is avoided by placing a permanent magnet in front of the entrance window. Systems operated at room temperature have become available in the recent years.<sup>29</sup>

As in any counting device, the number of charge carriers generated by X-ray quanta is a statistical process. The mean energy for generation of electron-hole pairs is about 3.8 eV as compared to 20-30 eV in a gas filled proportional counter. A resolution of typically 150 eV at Mn K<sub>α</sub> (5.984 keV), measured as full-width at half maximum of the X-ray peak, can be obtained. Electronic noise still contributes significantly to this value. Microcalorimetric energy dispersive X-ray detectors with a resolution of 1 eV have been described recently.<sup>30,31</sup> Up to now, the need of liquid helium cooling and small detector areas limit their applicability.

---

---

Gas-filled proportional counters are used as detectors in wavelength dispersive X-ray detection units. A crystal selects the X-ray wavelength entering the detector by BRAGG reflection at the lattice planes. Spectra are scanned by changing the glancing angle. Crystal spectrometers exhibit an excellent resolution of about 1 eV. This advantage is outweighed by the small solid angle of detection, which limits the detectable intensity and increases measuring times. However, this angle can be increased considerably by X-ray focussing through curved crystals.

The most commonly applied focussing wavelength dispersive set-up is the JOHANSSON spectrometer. In this arrangement, the point of incidence of the probe on the sample and the detector entrance slit are situated in either of the foci of the curved crystal. Thus, a divergent beam of X-rays emitted from the sample is focussed into the detector. The sample, the analyser crystal, and the proportional counter are located on the focal circle of the crystal, which is known as ROWLAND circle. The crystal lattice planes are bent to twice the radius and the crystal is ground to the radius of the circle. For acquiring spectra over a large range of wavelengths, crystals with different lattice distances have to be used. The resolution of a JOHANSSON spectrometer depends on the crystal and the wavelength and is between 1-100 eV. Different X-ray detectors are discussed in the literature in detail .<sup>19,32</sup>

Generally, X-ray fluorescence instruments are equipped with energy dispersive spectrometers, whereas both types are found with scanning or transmission electron microscopes. Dedicated electron probe microanalysers are usually equipped with one energy dispersive X-ray detector and several wavelength dispersive units.

---



## 2 Generation of Characteristic X-Ray Spectra

If its energy exceeds the binding energy  $E_{\text{crit}}$ , a particle or an X-ray quantum can interact with an atom by ejecting a core-level electron. In this case, the incident electron will be deflected from its original direction and its energy will be decreased by the binding energy  $E_{\text{crit}}$ . When an atom is excited by an X-ray quantum, this process is referred to as photoelectric interaction and leads to annihilation of the incident X-ray quantum.

Relaxation by electronic transitions from outer shells into the vacancy occurs within 1 psec. In this transition, the difference between the atomic levels involved is released. Only transitions obeying the dipole selection rules  $\Delta l = \pm 1$ ,  $\Delta j = 0, \pm 1$  are possible, where  $l$  and  $j$  are denoting the orbital and the total angular momentum quantum number, respectively. This energy can be dissipated either by ejection of another core-level electron in the AUGER process or emitted as an X-ray quantum :

$$\Delta E = E_2 - E_1 = h\nu = h \frac{c}{\lambda} \quad (2.1)$$

As the atomic levels are sharply defined for every element, AUGER electrons and fluorescent X-rays are characteristic of the atom by which they are emitted. The different principal X-ray line series are named K-, L- and M series and arise when a vacancy in the corresponding shell is filled. The lines within a series differ in the origin of the outer electron, which is indicated by subscripts given according to relative intensities in the SIEGBAHN notation. According to the IUPAC nomenclature, which is entirely based on shell designations, the  $K_{\alpha 1}$  and  $K_{\alpha 2}$  line doublet corresponds to the K-L<sub>3</sub> and the K-L<sub>2</sub> transitions, respectively. A comparison of both notation systems is rendered by BEARDEN.<sup>33</sup> Generally, characteristic X-rays are emitted isotropically.

MOSELEY's law states that the energy of a characteristic X-ray line as well as the ionisation threshold  $E_{\text{crit}}$  increase with the square of the atomic number :

$$\Delta E = k_j \cdot (Z - \sigma_j)^2 \approx Rhc \cdot (Z - \sigma_j)^2 \quad (2.2)$$

The values of  $k$  and  $\sigma$  are constants for a given line series  $j$ . The RYDBERG constant is connected to  $k$  and  $\sigma$  can be interpreted as a screening constant, which describes the shielding of the nuclear charge  $Z$  from an outer electron. MOSELEY's law is not stringent as a slight atomic number dependence is observed for  $k_j$  and  $\sigma_j$ . Therefore, tabulations or numerical fits of line energies are generally preferred in X-ray analysis. Depending on the valence structure, changes below 1 eV in the energy of an emission line are observed with elements of atomic numbers  $Z < 30$ . This effect is usually disregarded in X-ray spectroscopy as it is not resolved by most spectrometers. Nevertheless, electron energy loss spectroscopy (EELS) is capable of discriminating valence states of light elements.<sup>18</sup> In Figure 2-1, X-ray line energies and critical energies are visualised in dependence of the atomic number.

X-ray and AUGER electron emission are competing effects. The probability that a core-shell ionised atom emits an X-ray quantum rather than an AUGER electron after ionisation of shell  $j$  is given by the fluorescence yield  $\omega_j$ . It is connected with the AUGER yield  $a_j$  by :

$$\omega_j(Z) + a_j(Z) = 1 \quad (2.3)$$

Numerical values of  $\omega_j$  are provided by several databases.<sup>34-37</sup> Figure 2-2 illustrates the dependence of the fluorescence and AUGER yield on the atomic number. For light elements, the AUGER process is predominant for a given atomic shell. The relative intensity of an X-ray emission line within its series is governed by the probability of the intershell transition. The transition probability  $p_j$  (used synonymously with emission rate) of a certain transition  $j$  is accessible either by quantum mechanical calculations<sup>38-41</sup> or by intensity measurements<sup>42 43-45</sup>. The transition probability for  $K_\alpha$  lines can be expressed in terms of intensities  $I$  :

$$P_{K\alpha} = \frac{I(K_{\alpha 1,2})}{I(\text{total K spectrum})} \quad (2.4)$$

Analogous expressions exist for  $L_\alpha$  and  $M_\alpha$  lines. The variation of  $p_j$  with atomic number is summarised in Figure 2-3.

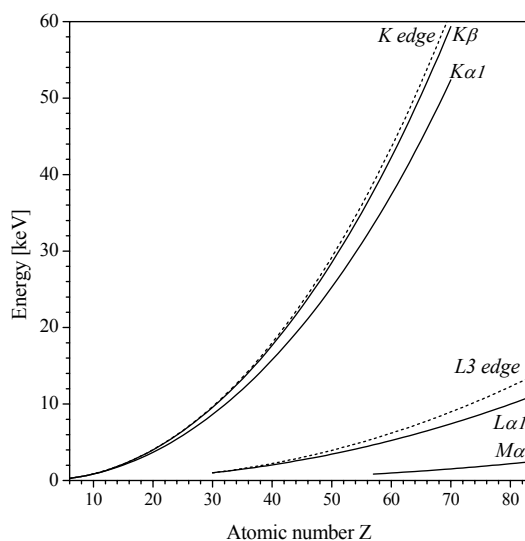


**Figure 2-1.** X-ray line energies (solid lines) and critical excitation energies (broken lines) of some principal emission lines across the periodic table.<sup>33</sup> The increase in energy is nearly parabolic with atomic number according to MOSELEY's law. Due to their high excitation energy, heavy elements are lacking their K peaks and L lines are used for analysis instead. From  $Z = 57$  (lanthanum) M peaks additionally appear in the spectrum.

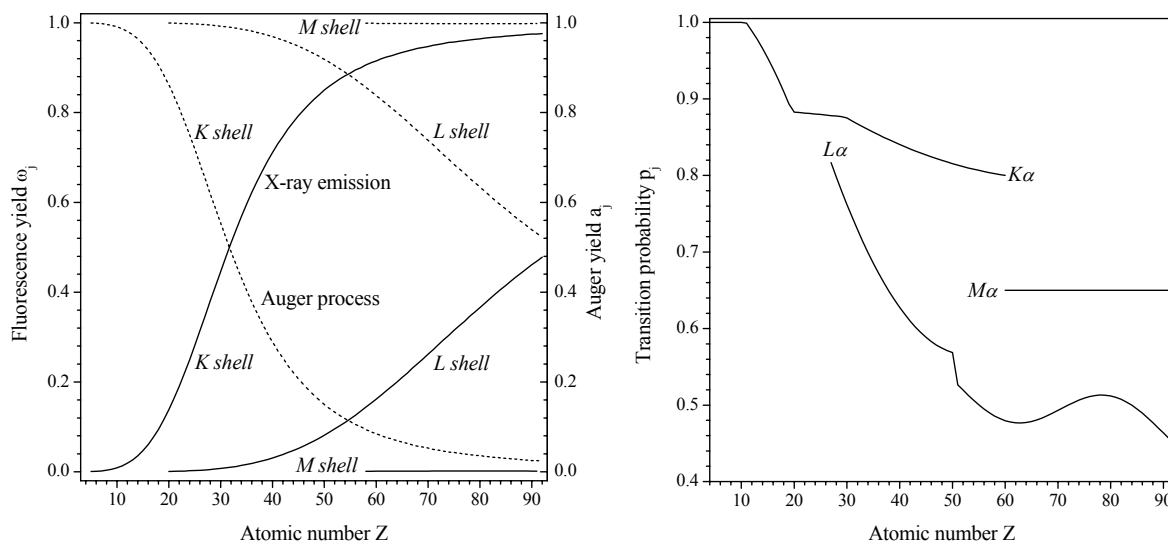


**Figure 2-2.** Fluorescence yield  $\omega_j$  (solid lines) and AUGER yield  $a_j$  (broken lines) as function of the atomic number for K-, L- and M shell ionisation.<sup>46</sup> Generation of AUGER electrons is the dominating process at low atomic number, which is one of the main problems in light element analysis.

**Figure 2-3.** Variation of the transition probability (or emission rate) for  $K_\alpha$ ,  $L_\alpha$  and  $M_\alpha$  lines with the atomic number.<sup>46</sup> It denotes the probability that a  $K_\alpha$ ,  $L_\alpha$  or  $M_\alpha$  transition occurs rather than another transition of the same line series. The  $\alpha_1$ - $\alpha_2$  doublet is not treated separately in this representation.

## 2.1 Interaction of X-Rays with Matter

An X-ray beam loses intensity as it penetrates matter. The attenuation is described by the LAMBERT-BEER law, which states that equal path lengths of the same material absorb the same fraction of intensity, given that the concentration of excited atoms is negligible. In an integral form the transmission  $T(z)$  is represented by an exponential decay :

$$T(z) = \frac{I(z)}{I(0)} = e^{-(\mu(Z,E)/\rho)\rho z} = e^{-\mu(Z,E)\rho z} = e^{-z/\lambda(Z,E)} \quad (2.5)$$

The transmission is expressed in terms of the residual intensity  $I(z)$  and the initial intensity  $I_0$  with the X-ray beam travelling along the  $z$  axis. The mass attenuation coefficient  $\mu(Z,E)$  is the total cross-section of the interaction of X-rays with matter. It quantifies the decay of intensity for a given element with atomic number  $Z$  for a monochromatic beam of energy  $E$  and is usually given in units of  $[\text{cm}^2/\text{g}]$  or  $[\text{barns}/\text{atom}]$ . For a given density,  $\mu(Z,E)$  is inversely proportional to the mean free path length  $\lambda(Z,E)$  of X-ray quanta. Normalisation to the density  $\rho$  renders the mass attenuation coefficient independent of the state of aggregation.

For multicomponent systems, the mass attenuation coefficient is readily obtained by summing up the single contributions of all constituents, weighed with their mass fraction  $c_i$  :

$$\mu(E) = \sum_{i=1}^n c_i \mu_i(Z, E) \quad (2.6)$$

Mass attenuation coefficients have been measured for all elements over a large range of energies. They are either tabulated<sup>47-50</sup> or given as numerical fits<sup>51-55</sup> in different compilations. The attenuation of X-rays mainly occurs due to interactions with the electron shell of an atom. Besides the photoelectric process, the mechanism of which has been discussed in the previous section, elastic and inelastic scattering effects have to be taken into account. Therefore, the mass attenuation coefficient is additively composed of the cross-sections for the photoelectric interaction  $\tau$  and the scattering contribution  $\sigma$  :

$$\mu = \tau + \sigma = \tau + \sigma_{\text{Ray}} + \sigma_{\text{Com}} \quad (2.7)$$

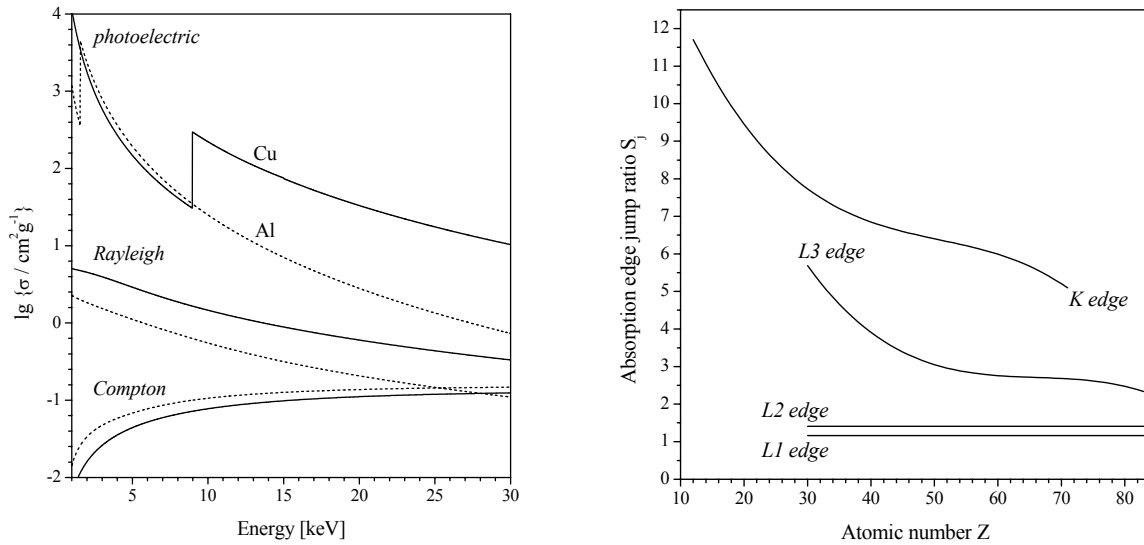


**Figure 2-4.** Photoelectric, RAYLEIGH and COMPTON cross-sections for aluminium (broken lines) and copper (solid lines) in the energy range between 1-30 keV on a semi-logarithmic scale.<sup>46</sup> Absorption edges are located at 1.560 keV (Al K) and 8.980 keV (Cu K), respectively. In contrast, the scattering cross-sections are not discontinuous.

**Figure 2-5.** Absorption edge jump ratios  $S_j$  for different atomic shells across the periodic table.<sup>46</sup> The absorption jump ratio is closely related to the contribution  $\tau_j$  of a specific shell to the total photoelectric cross-section  $\tau$ . Ionisation events by X-ray impact on the K shell are favoured over the L shell throughout the periodic table.

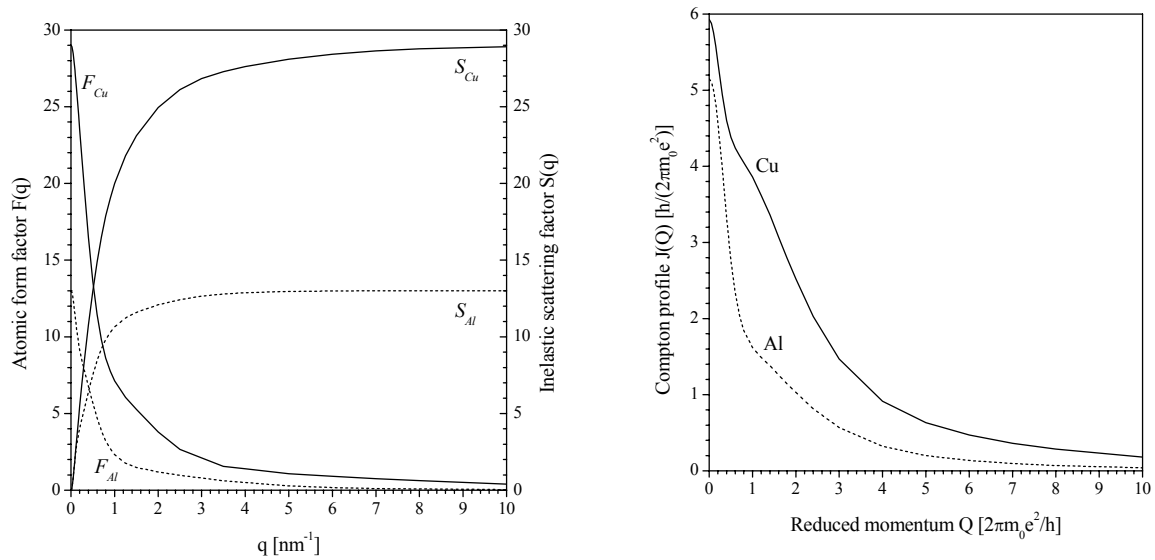


**Figure 2-6.** Total atomic form factor  $F(q)$  and inelastic scattering function  $S(q)$  for aluminium (broken lines) and copper (solid lines) as a function of momentum transfer  $q$ .<sup>56</sup> The atomic form factor approaches the total number of electrons of an atom for zero momentum transfer.

**Figure 2-7.** Momentum distribution of bound electrons ('COMPTON profiles')  $J(Q)$  in aluminium (broken line) and copper (solid line).<sup>57</sup>

The scattering cross-section is further subdivided into the cross-section for RAYLEIGH  $\sigma_{\text{Ray}}$  and COMPTON  $\sigma_{\text{Com}}$  scattering. As pair production does not occur at energies below  $2m_e c^2$  (1.044 MeV) it is omitted from further discussion.

### 2.1.1 Photoelectric Interaction

Various shells of an atom can be ionised and contribute to the photoelectric effect. The photoelectric cross-section  $\tau$  is therefore represented by the contributions of all shells of an atom :

$$\tau = \sum_{i=K,L,\dots}^{\text{all shells}} \tau_i \quad (2.8)$$

which in turn can still be split up in subshell contributions. However, a specific shell is only available to a photoelectric interaction when the X-ray quantum energy exceeds its ionisation threshold  $E_{\text{crit}}$ . At this energy, the cross-section jumps to higher values, giving rise to an absorption edge. Between the absorption edges the cross-section decreases in a monotonous way. This behaviour is illustrated for aluminium and copper in Figure 2-4. Numerical values for  $\tau$  can, for example, be approximated by the BRAGG-PIERCE law.<sup>58</sup>

The height of the absorption edge jump is quantified by the ratio of the photoelectric cross-section just above and below the edge  $E_{\text{crit}}$  :

$$S_j = \lim_{h \rightarrow 0} \frac{\tau(E_{\text{crit},j} + h)}{\tau(E_{\text{crit},j} - h)} \quad (2.9)$$

Absorption jump ratios  $S_j$  are plotted in Figure 2-5 for various elements and different absorption edges. They are correlated to the fraction  $\tau_j$  of its corresponding subshell to the total photoelectric cross-section :

$$f_j = \frac{\tau_j}{\tau} = 1 - \frac{1}{S_j} \quad (2.10)$$

$f_j$  is referred to as absorption jump factor. Ionisation events by X-ray impact in the K shell are favoured over the L shell (and M shell also) throughout the periodic table.

### 2.1.2 *Photon Scattering*

The collision of X-ray photons with bound electrons also gives rise to scattering processes. In contrast to the photoelectric absorption no ionisation event occurs, but the photon is deflected from its initial direction. The polar angle of deflection towards the initial direction of the incident quantum is referred to as scattering angle  $\vartheta$ . Momentum transfer results in a scattering vector  $\mathbf{q}$  the norm of which depends on the wavelength  $\lambda$  (or energy  $E$ ) of the photon :

$$q = \frac{\sin(\vartheta/2)}{\lambda} = \frac{E}{hc} \sin(\vartheta/2) \quad (2.11)$$

The coherent interaction of photons with bound electrons is referred to as RAYLEIGH scattering. The differential RAYLEIGH scattering cross-section  $\sigma_{\text{Ray}}$  can be given in the atomic form factor representation :

$$\frac{d\sigma_{\text{Ray}}}{d\Omega}(\vartheta, E) = \frac{d\sigma_{\text{Th}}}{d\Omega}(\vartheta) \cdot F^2(q, Z) = \frac{r_e^2}{2} \cdot (1 + \cos^2 \vartheta) \cdot F^2(q, Z) \quad (2.12)$$

where the term in brackets accounts for unpolarised radiation. The THOMSON cross-section  $\sigma_{\text{Th}}$  describes the coherent scattering of photons by free electrons. It is, by definition, transformed into the RAYLEIGH cross-section by the atomic form factor  $F(q, Z)$ , which is a measure of the number of electrons available for scattering. Atomic form factors are tabulated for all elements.<sup>56</sup> They are usually calculated by relativistic HARTREE-FOCK methods for every orbital of an atom and summed up to give the total atomic form factor. For zero momentum transfer, this is for low energies or low scattering angles, it approaches the number of electrons  $Z$  of an atom. At low energies the photon wavelength becomes larger than the size of the atom and all electrons are available for scattering.

X-ray photons are scattered incoherently by loosely bound atomic electrons in the COMPTON effect. The differential cross-section for COMPTON scattering  $\sigma_{Com}$  is given by :

$$\frac{d\sigma_{Com}}{d\Omega}(\vartheta, E) = \frac{d\sigma_{KN}}{d\Omega}(\vartheta) \cdot S(q, Z) = \frac{r_e^2}{2} \cdot \left(\frac{K_0}{K}\right)^2 \cdot \left(\frac{K_0}{K} + \frac{K}{K_0} - \sin^2 \vartheta\right) \cdot S(q, Z) \quad (2.13)$$

It is derived from the KLEIN-NISHINA cross-section  $\sigma_{KN}$ , which describes COMPTON scattering by a free electron by means of the inelastic scattering function  $S(q, Z)$ . Like the atomic form factor, numerical values of the inelastic scattering functions are tabulated for every element.<sup>56</sup> The factor  $K/K_0$  is related to the scattering angle and the rest energy of an electron according to :

$$\frac{K}{K_0} = 1 + \frac{E_i}{m_e c^2} (1 - \cos \vartheta) \quad (2.14)$$

Figure 2-6 visualises the atomic form factor  $F$  and the inelastic scattering function  $S$  for copper and aluminium as a function of the momentum transfer  $q$  in the scattering process. In contrast to RAYLEIGH scattering, the COMPTON effect is an inelastic interaction. In COMPTON scattering by electrons at rest, the X-ray photon loses a fixed amount of energy that only depends on the scattering angle. In this case, the energy of the scattered photon relative to that of the incident one is given by the factor  $K/K_0$  in eq. 2.14. Otherwise, the momentum  $p_z$  of the bound electron influences the energy transfer during the interaction. The final energy of the photon  $E_f$  depends on its initial energy  $E_i$  and the scattering angle :

$$E_f = \frac{E_i}{\frac{K_0}{K} - \frac{2p_z}{m_e c} \sin\left(\frac{\vartheta}{2}\right)} \quad (2.15)$$

The momentum  $p_z$  is usually expressed in units of the reduced momentum  $Q$  :

$$p_z = Q \frac{m_e e^2}{2\varepsilon_0 h} \quad (2.16)$$

which is given as the projection of the momentum transfer  $q$  on the original electron momentum  $p$  before the collision. The momentum  $p_z$  can be sampled from the momentum distribution function or COMPTON profile  $J_z(Q)$ . This has been reported on the basis of non-relativistic ( $Z \leq 36$ ) and relativistic ( $Z > 36$ ) HARTREE-FOCK calculations for all elements. The single contributions of every orbital of an atom are superimposed to yield total values for every element.<sup>57</sup> COMPTON profiles for copper and aluminium are shown in Figure 2-7. The momentum distribution of the scattering electron leads to an energy broadening of incoherently scattered X-ray photons compared to scattering by free electrons. This DOPPLER broadening also applies to the high energy side of a COMPTON peak. In contrast to incoherent free-electron scattering, energy can also be transferred from the scattering electron to the scattered photon according to *eq. 2.15*.

The total RAYLEIGH and COMPTON cross-sections are displayed along with the photoelectric cross-sections in Figure 2-4. Generally, scattering is only a minor contribution to the total attenuation of X-rays in the energy range of 1 to 100 keV. However, scattering effects cause the characteristic lines of an X-ray tube to appear in a fluorescence spectrum. The intensity of the scatter lines depends on the sample composition. According to Figure 2-4, RAYLEIGH scattering will increase with the atomic number of the sample and decrease with energy. In contrast, the COMPTON line will dominate the scattering contributions to the spectrum for low atomic number samples at high energies.

## 2.2 Interaction of Electrons with Matter

As it propagates through matter, an electron loses energy and experiences various scattering processes with nuclei and atomic shell electrons. Deflection of beam electrons in the COULOMB field of nuclei is responsible for elastic scattering and continuous energy losses. Ionisation of atomic shells is described in terms of electron-electron collisions.

### 2.2.1 Elastic Electron Scattering

The deflection of an electron in the electric field of a nucleus is known as RUTHERFORD scattering. The screening of the nuclear charge by the shell electrons has to be taken into account by a suitable radial distribution function of the COULOMB potential.<sup>59,60</sup>

---

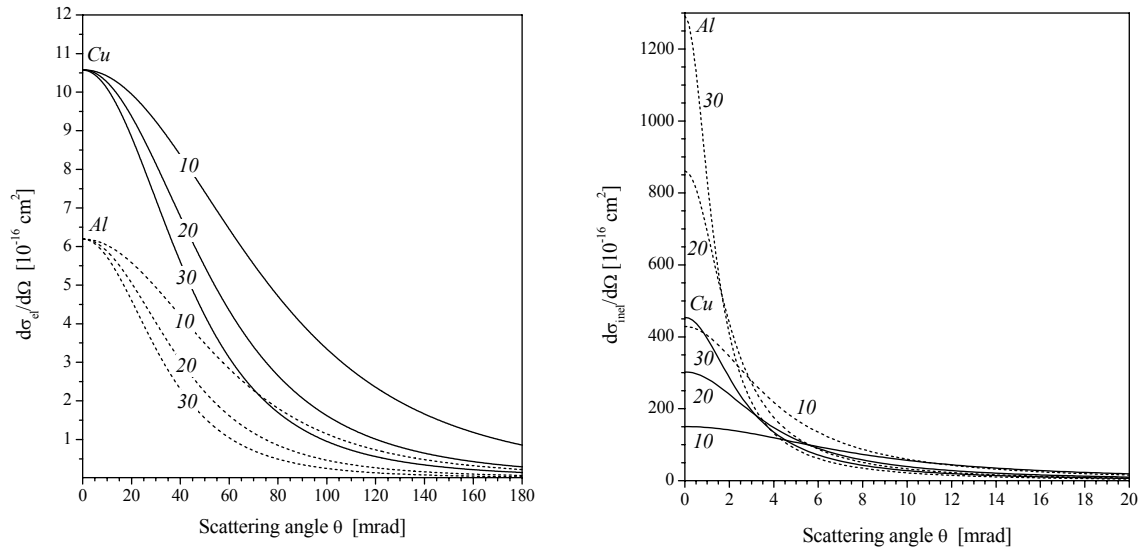


**Figure 2-8.** Differential RUTHERFORD scattering cross-sections for copper (solid lines) and aluminium (broken lines) at different electron energies (in keV) according the WENTZEL model. Other potential distributions are more accurate, especially at low scattering angles.

**Figure 2-9.** Differential inelastic electron scattering cross-sections for copper (solid lines) and aluminium (broken lines) at different electron energies (in keV). Inelastic scattering is concentrated within much smaller angles than RUTHERFORD scattering.

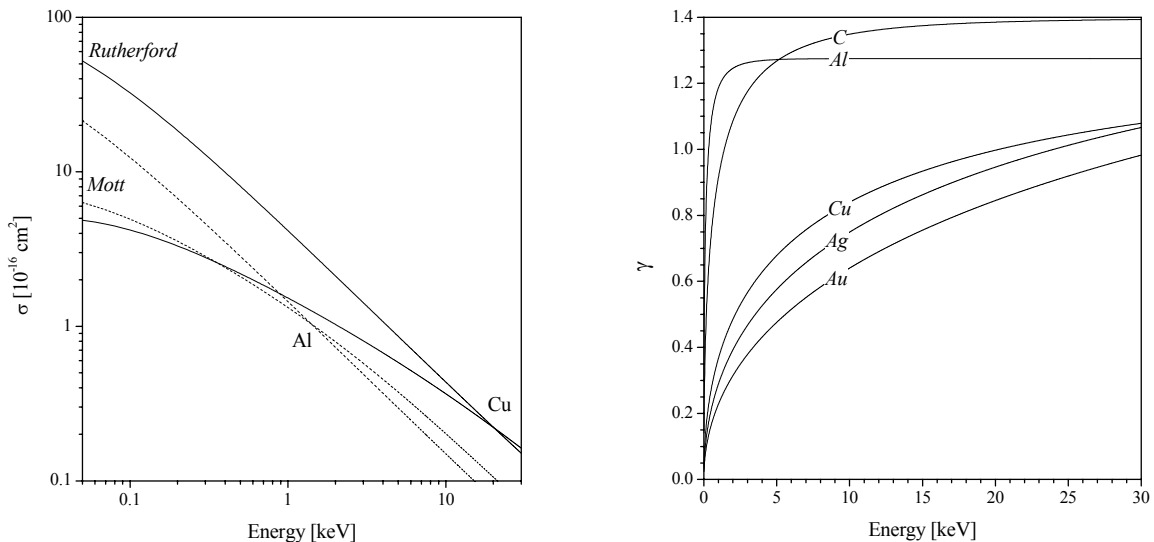


**Figure 2-10.** Double logarithmic representation of the total RUTHERFORD and MOTT scattering cross-sections as function of electron energy for aluminium (broken line) and copper (solid line).

**Figure 2-11.** The ratio  $\gamma$  of eq. 2.22 relating the total elastic MOTT cross-section to the total RUTHERFORD cross-sections displayed in the energy range 0-30 keV for various elements.<sup>61</sup> The point of balance between both values shifts to higher energies with increasing atomic number.

The commonly adopted WENTZEL model assumes an exponential radial decrease of the COULOMB potential. Solution of the SCHRÖDINGER equation for this model yields the differential elastic cross-section for a screened nucleus :

$$\begin{aligned} \frac{d\sigma_R}{d\Omega} &= |f(\vartheta)|^2 = \frac{\sigma_0 Z^2}{4\pi E^2} \frac{1}{[\sin^2(\vartheta/2) + \alpha]^2} = \frac{\sigma_0 Z^2}{4\pi E^2} \frac{1}{[\sin^2(\vartheta/2) + \sin^2(\vartheta_0/2)]^2} \\ &\approx \frac{\sigma_0 Z^2}{\pi E^2} \frac{1}{[\vartheta^2 + \vartheta_0^2]^2} \end{aligned} \quad (2.17)$$

with the low-angle approximation. The screening parameter  $\alpha$ , which is connected to the screening angle  $\theta_0$ , is given by :

$$\alpha = \sin^2\left(\frac{\vartheta_0}{2}\right) = \frac{\lambda Z^{1/3}}{4\pi a_0} \approx \frac{\vartheta_0^2}{4} \quad (2.18)$$

where  $\lambda$  denotes the DE BROGLIE wavelength of the electron and  $a_0$  the BOHR radius. The screening constant causes the elastic scattering function  $f(\theta)$  to take on finite values at zero scattering angle. The screening angle  $\theta_0$  is in the order of a few tens of milliradians. The differential RUTHERFORD scattering cross-section is plotted in Figure 2-8 for aluminium and copper at different electron energies. For the calculation of total RUTHERFORD cross-sections  $\sigma_R$  more elaborate potential distributions than the WENTZEL model have to be used, resulting in different atomic number dependencies of the screening constant. Unless tabulated values<sup>62</sup> or empirical equations<sup>63,64</sup> are employed, the use of the analytical expressions is rather advantageous. For practical purposes, the relationship :

$$\sigma_R = \sigma_0 \frac{Z^2}{E^2} \frac{1}{\alpha(1+\alpha)} \left( \frac{E + m_e c^2}{E + 2m_e c^2} \right)^2 [cm^2] \quad (2.19)$$

$$\text{where } \alpha = 3.4 \cdot 10^{-3} \cdot \frac{Z^{2/3}}{E} \quad (2.20)$$

with E in [keV] and the screening constant  $\alpha$  is in common use.<sup>65,66</sup>

MOTT cross-sections  $\sigma_M$ , which account for the effect of the electron spin on the scattering process, provide a more exact description for elastic deflections through large angles. They are obtained by solving the relativistic SCHRÖDINGER equation for the two possible spin directions of the electron separately. Elastic MOTT cross-sections have been computed and tabulated for a large number of elements.<sup>61,67,68</sup> In contrast to the RUTHERFORD cross-sections, they cannot be expressed analytically. For this reason, it is more convenient to describe the deviation  $r(\theta)$  and  $\gamma$  of the MOTT cross-sections from the differential and total RUTHERFORD cross-sections :

$$r(\vartheta) = \frac{\left( \frac{\partial \sigma_M}{\partial \Omega} \right)}{\left( \frac{\partial \sigma_R}{\partial \Omega} \right)} \quad (2.21)$$

$$\gamma = \frac{\sigma_M}{\sigma_R} \quad (2.22)$$

Numerical fits for these quantities have been reported<sup>61</sup> and are depicted in Figure 2-10 and Figure 2-11. In general, the discrepancies between MOTT and RUTHERFORD cross-sections increase with atomic number at low energies and very high scattering angles.

Due to the large mass of the nucleus, the energy transfer in the COULOMB interaction with an electron is negligible irrespective of the scattering angle. With a low probability, however, the deflection of the incident electron results in the emission of an X-ray quantum. This probability is defined by the KRAMERS cross-section  $a_K$  for the emission of a photon with energy  $E_X$  :

$$\frac{d\sigma_{Brake}}{dE_X} = \frac{a_K}{E_X} \frac{Z^2}{\beta^2} \cong \frac{a_K}{E_X} \frac{Z^2 m_e c^2}{2E} \quad (2.23)$$

with the non-relativistic approximation given on the right side. Unlike characteristic X-rays, the spectrum of energy losses  $E_X$  is continuous with an onset at the primary beam energy  $E_0$  (DUANE-HUNT-limit). This Bremsstrahlung ('braking radiation') is an undesired background of electron excited X-ray spectra. Bremsstrahlung is not emitted isotropically but exhibits a dipole emission characteristic.

Its exact shape depends on the energy  $E_x$  of emitted quanta as the COULOMB field of a moving relativistic charge is not radially symmetric. Nearly isotropic behaviour is only approached at low electron and Bremsstrahlung energies. Therefore, the KRAMERS cross-section is not a true constant. Deviations occur with decreasing Bremsstrahlung energy due to screening effects, which are not included in KRAMERS semi-classical treatment of continuous X-ray emission.<sup>69-76</sup>

### 2.2.2 Inelastic Electron Scattering

Incident electrons experience energy losses by transferring bound atomic electrons to excited states and thus are inelastically scattered. The participation of all electrons of an atom is taken into account by averaging the ionisation thresholds of the specific shells in introducing the mean ionisation potential  $J'$  of an atom:

$$J'[eV] = \begin{cases} 11.5 \cdot Z & \text{for } Z < 13 \\ 9.76 \cdot Z + 58.5 \cdot Z^{-0.19} & \text{for } Z \geq 13 \end{cases} \quad (2.24)$$

Only atomic electrons with binding energies smaller than the incident electron energy participate in ionisation processes. Eq. 2.24 has been chosen from the various available expressions<sup>77</sup> as it modifies the usually adopted linear relationship between the mean ionisation potential and the atomic number<sup>78</sup> and correctly models its decrease with electron energy  $E$ <sup>79,21</sup>:

$$J = \frac{J'}{1 + k \frac{J'}{E}} \quad \text{with } k = 0.734 \cdot Z^{0.037} \text{ or } k = 0.731 + 0.0688 \lg Z \quad (2.25)$$

The angular distribution of inelastic scattering is obtained by summing over the possible excitations of the  $Z$  atomic electrons. The quantum mechanical calculation yields the differential cross-section for inelastic electron scattering :

$$\frac{d\sigma_{inel}}{d\Omega} = \frac{\sigma_0}{\pi} \cdot \frac{Z}{E^2} \cdot \frac{1 - \left(1 + \frac{\vartheta^2 + \vartheta_E^2}{\vartheta_0^2}\right)^{-2}}{(\vartheta^2 + \vartheta_E^2)^2} \quad (2.26)$$

where the characteristic angle  $\theta_E$  is related to the mean ionisation energy<sup>59</sup> :

$$\vartheta_E = \frac{J}{4E} \quad (2.27)$$

For inelastic scattering,  $\theta_E$  plays the same role as  $\theta_0$  for elastic processes. As its value is only in the range of milliradians, electrons are scattered inelastically only through very small angles. The differential inelastic cross-sections are plotted exemplarily in Figure 2-9. Comparison of eqs. 2.17 and 2.26 for scattering angles  $\theta$ , which are large compared to both  $\theta_E$  and  $\theta_0$ , yields :

$$\frac{d\sigma_{inel}}{d\Omega} = \frac{1}{Z} \frac{d\sigma_{el}}{d\Omega} \quad (2.28)$$

In a similar manner, the total inelastic cross-section for electrons is expressed in terms of its elastic counterpart by<sup>59</sup> :

$$\frac{\sigma_{inel}}{\sigma_{el}} = \begin{cases} \frac{26}{Z} & \text{by theory} \\ \frac{20.2}{Z} & \text{by experiment} \end{cases} \quad (2.29)$$

in high accuracy for all elements when the experimentally determined relationship is employed.<sup>80,81</sup> Thus, the total cross-sections  $\sigma_{tot}$  for electrons can be expressed in a simple form by means of the elastic ones only by :

$$\frac{d\sigma_{tot}}{d\Omega} = \frac{d\sigma_{el}}{d\Omega} + \frac{d\sigma_{inel}}{d\Omega} \approx \frac{Z+1}{Z} \cdot \frac{d\sigma_{el}}{d\Omega} \quad (2.30)$$

$$\sigma_{tot} = \sigma_{el} + \sigma_{inel} = \frac{Z + 20.2}{Z} \cdot \sigma_{el} \quad (2.31)$$

where the approximation in eq. 2.30 holds for scattering angles larger than  $\theta_E$  of eq. 2.27. For multielement samples, the total scattering cross-section is given as weight average according to :

$$\sigma(E) = \sum_i c_i \sigma_i(E) \quad (2.32)$$

where  $\sigma_i(E)$  denotes the elastic, inelastic, or total cross-section of an atom of type  $i$  at energy  $E$ .

### 2.2.3 Inner Shell Ionisation by Electron Impact

The removal of an electron from an atomic shell is effected by collision with an incident electron when the energy transfer exceeds the binding energy. Quantum mechanically both particles cannot be distinguished and the more energetic one after the interaction is called the incident electron. The probability that an amount of energy is exchanged between an incident electron and an electron at rest has been given by MØLLER including spin interactions and relativistic effects.<sup>82</sup> In a semi-classical approach, GRYZINSKI has deduced the total cross-section  $\sigma_j$  for a bound electron with a mean kinetic energy in the order of the binding energy  $E_{crit,j}$  :

$$\sigma_j = \frac{\sigma_0 z_j}{E_{crit,j}^2} \cdot g_j(u) = \frac{\sigma_0 z_j}{E_{crit,j}^2} \cdot \frac{1}{u} \left( \frac{u-1}{u+1} \right)^{3/2} \left[ 1 + \frac{2}{3} \left( 1 - \frac{1}{2u} \right) \ln(2.7 + \sqrt{u-1}) \right] \quad (2.33)$$

where  $z_j$  denotes the number of electrons in the specific shell.<sup>83</sup> The ionisation function  $g(u)$  only depends on the overvoltage ratio  $u$ , which is defined as the incident electron energy  $E_0$  relative to the binding energy of an atomic electron :

$$u = \frac{E_0}{E_{crit,j}} \quad (2.34)$$

GRYZINSKI'S formula has been derived under the assumption that the atomic electron does not interact with the nucleus, which is justified when the energy transfer is larger than the binding energy. This results in a systematic error at low overvoltages. Ionisation functions have been approximated by several authors<sup>84,85</sup> and are plotted in Figure 2-12 in comparison with eq. 2.33, which provides the best fit to experiments. A survey of theoretical and experimental data on the cross-sections of inner shell ionisation by electron impact is provided by POWELL.<sup>86</sup>

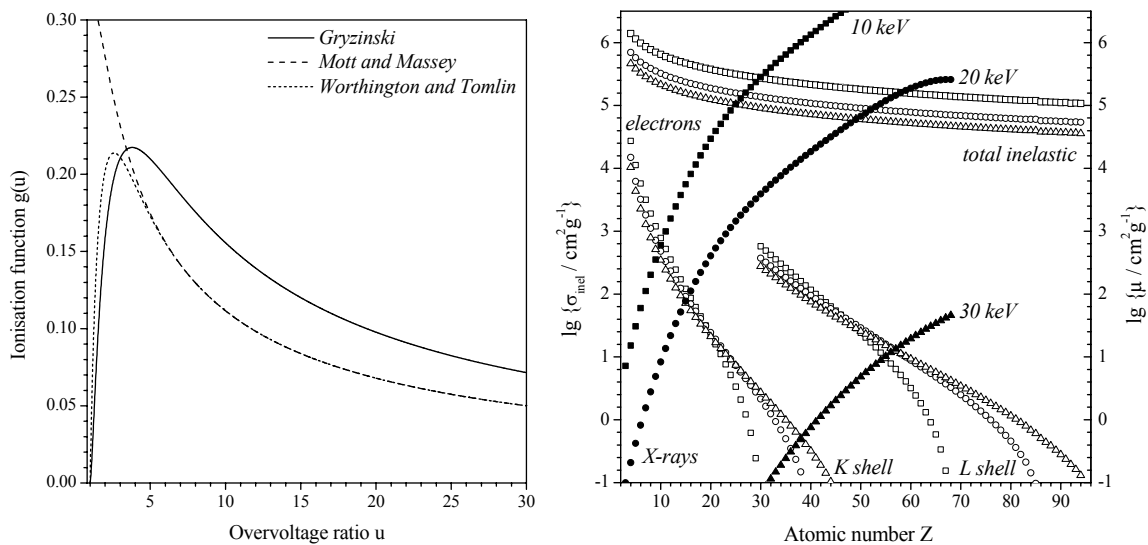


**Figure 2-12.** Ionisation function for electron impact as described by several authors. The function as derived by GRYZINSKI provides the best fit to experimental data.<sup>83-85</sup>

**Figure 2-13.** Variation of the total inelastic cross-sections for electrons  $\sigma_{inel}$  (open symbols) and X-ray mass attenuation coefficient  $\mu$  (solid symbols) across the periodic table at 10 ( $\square, \blacksquare$ ), 20 ( $\circ, \bullet$ ) and 30 keV ( $\blacktriangle, \triangle$ ) on a logarithmic scale. Total K- and L shell ionisation cross-sections are also plotted. With an electron probe, ionisation of L shells is favoured over K shells and decreases with atomic number, which is a marked contrast to X-ray excitation.

### 2.3 Description of Multiple Electron Energy Losses

The excitation of outer shell electrons does not give rise to emission of electromagnetic radiation in the X-ray region. Figure 2-13 displays the total inelastic, K-, and L shell ionisation cross-sections for electrons at different energies throughout the periodic table. Depending on the element, the total inelastic cross-section exceeds the core shell excitation by two to six orders of magnitude. Therefore, ionisation of an inner shell is a comparably rare event and a large amount of electron energy is consumed in the production of secondary electrons and electromagnetic radiation of lower energy. This is also elucidated by *eq. 2.33*, which states that cross-sections for the excitation of bound electrons increases as their binding energy decreases.

Detailed knowledge of the cross-sections for any inelastic process with any sample is not always available. Based on the solution of the transport equation for electrons, the simulation of energy loss spectra including the plasmon-loss region can be accomplished. This, however, necessitates considerable computational effort together with a huge database and was performed only for aluminium.<sup>87,88</sup> Monte Carlo models based on the calculation of only a few discrete loss mechanisms remain crude and fail to give exact results for large energy losses.<sup>89</sup> In most cases the calculation of the average effect of subsequent inelastic events is therefore the only practicable way to model the huge variety of energy loss mechanisms.

#### 2.3.1 Continuous Electron Energy Loss Approximation

As only a fraction of their actual energy is transferred in a single scattering process, electrons experience many inelastic processes until they have lost their kinetic energy entirely or leave the sample. This can be described as gradual deceleration. BETHE has established an expression, which has been shown to be in accordance with the treatment provided by MØLLER.<sup>82</sup> The relativistic BETHE formula for the stopping power  $S_{\text{Bethe}}$  yields the mean energy loss  $dE_{\text{mean}}$  of an electron along its trajectory segment  $ds$  :

$$S_{\text{Bethe}} = \frac{dE_{\text{mean}}}{ds} = \frac{2\sigma_0 N_A}{m_0 c^2} \cdot \frac{Z}{A\beta^2} \left\{ \ln \left[ \varepsilon^2 (\varepsilon + 2) \cdot \left( \frac{m_0 c^2}{2J} \right)^2 \right] + \frac{1 + \frac{\varepsilon^2}{8} - (2\varepsilon + 1) \ln 2}{(\varepsilon + 1)^2} \right\} \quad (2.35)$$

and can be approximated for non-relativistic energies according to :

$$S_{Bethe} = \frac{dE_{mean}}{ds} \approx 2\sigma_0 N_A \cdot \frac{Z}{AE} \ln\left(1.166 \frac{E}{J}\right) \quad (2.36)$$

Different values have been proposed for the constant in the logarithmic term in the non-relativistic case. The constant adopted here is based on quantum mechanical considerations.<sup>19</sup> With the energy dependence of the mean ionisation potential  $J$  as defined by eqs. 2.24 and 2.25, the above expression also remains physically meaningful at electron energies  $E < J$ .<sup>79</sup> In multicomponent samples, the stopping effects of the different constituents are additively superimposed (BRAGG's rule). The mean ionisation energy has to be replaced by its weight average according to :

$$\bar{J} = \frac{\sum_i c_i \frac{Z_i}{A_i} \ln J_i}{\sum_i c_i \frac{Z_i}{A_i}} \quad (2.37)$$

This procedure is equivalent to weight averaging the stopping power  $S_{Bethe}$  when derived from the BETHE expression eq. 2.36.<sup>58,90-92</sup> The BETHE range  $R_B$  is defined as the path along which electrons lose their entire kinetic energy. It is obtained by numerical integration of eq. 2.36 and can be approximated analytically.<sup>84,92</sup> Integration with neglect of the logarithmic term immediately leads to the THOMSON-WHIDDINGTON law :

$$E^2 - E_{mean}^2 = c_T \rho t \quad (2.38)$$

which was established empirically with TERRILL's constant  $c_T \approx 4 \cdot 10^{11} \text{ eV}^2 \text{ cm}^2 \text{ g}^{-1}$ .<sup>93,94</sup> It provides a suitable approximation for thin samples that cause small energy losses and is more accurately obeyed for the mean rather than for the most probable loss.<sup>94,95</sup> According to eq. 2.38 the mean electron energy approaches zero at :

$$R_{TW} = \frac{E^2}{c_T \rho} \quad (2.39)$$

which is the THOMSON-WHIDDINGTON range. TERRILL's 'constant' has been determined experimentally and shown to vary with sample composition and primary beam energy.<sup>95</sup>

### 2.3.2 *Phenomenology of Electron Scattering*

An electron undergoes many elastic and inelastic scattering events until it has lost its entire kinetic energy. For this reason, its deceleration takes place along irregularly shaped trajectories.

When the sample thickness amounts to a few nanometres like in the transmission electron microscope, only one or a few scattering events occur as the electron passes through the sample and result in an angular and energetic beam broadening. The fraction of impinging electrons that passes the sample defines the transmission coefficient  $\eta_T$  :

$$\eta_T(E_0, \alpha, t) = \frac{I_T}{I_p} = \int_0^{E_0} \int_{\Omega} \frac{\partial^2 \eta_T(E_0, Z, \alpha, t)}{\partial \Omega' \partial E} d\Omega' dE \quad (2.40)$$

where  $\Omega$  denotes the half space below the sample, and  $I_T$  and  $I_p$  are the transmitted and probe current, respectively. LENARD stated that the electron transmission through thin samples obeys an exponential law :

$$\eta_T = \frac{I_T}{I_p} = e^{-\sigma \rho t} \quad (2.41)$$

with an empirical cross-section  $\sigma$  ('LENARD coefficient'), which is analogous to the mass attenuation coefficient  $\mu$  for X-rays.<sup>95,96</sup> Eq. 2.41 is an approximative description of electron transmission as energy loss is entirely neglected and the cross-section  $\sigma$  is considered to remain constant along the electron path.

As the sample thickness increases, the directions of electron movement randomise due to multiple scattering. In bulk samples, the trajectories end within a pear- or half-sphere shaped

interaction volume unless the electron is backscattered. According to *eq. 2.36*, size and shape of the interaction volume depend on the primary beam energy as well as on the sample composition. Backscattering is the product of one or a few mostly elastic large angle scattering events causing electrons to change their direction through large angles and to exit the sample again. With the current  $I_B$  caused by backscattered electrons, this fraction of electrons is described by the backscatter coefficient  $\eta_B$  :

$$\eta_B(E_0, \alpha, t) = \frac{I_B}{I_p} = \int_{50\text{eV}}^{E_0} \int_{\Omega} \frac{\partial^2 \eta(E_0, Z, \alpha, t)}{\partial \Omega' \partial E} d\Omega' dE \quad (2.42)$$

where the spatial integration is now over the upper half space. By definition, electrons with an energy above 50 eV are called backscattered and below this value secondary electrons. The backscatter coefficient of multicomponent samples is obtained additively from the contribution of each element according to :

$$\eta_B = \sum_i c_i \eta_i \quad (2.43)$$

Due to the statistical nature of scattering, the energy of transmitted and backscattered electrons is distributed around a maximum defining the most probable energy loss. The corresponding mean energies  $E_{\text{mean}}$  are extracted from the backscatter and electron energy loss spectrum, respectively, by subtracting the mean energy loss  $\Delta E_{\text{mean}}$  from the primary beam energy  $E_0$ :

$$E_{\text{mean}} = E_0 - \Delta E_{\text{mean}} = \frac{\int_0^{E_0} \frac{d\eta}{dE} E dE}{\int_0^{E_0} \frac{d\eta}{dE} dE} = \frac{\int_0^1 \frac{d\eta}{dU} U dU}{\int_0^1 \frac{d\eta}{dU} dU} \quad \text{with } U = \frac{E}{E_0} \quad (2.44)$$

The shape of the transmission and backscatter electron energy distributions will be discussed later. Due to charge conservation, the fraction of primary electrons that comes to rest within the sample is given by :

$$\eta_{abs} = 1 - (\eta_T + \eta_B) \quad (2.45)$$

where  $\eta_{abs}$  denotes the „absorption“ coefficient of a sample. A detailed discussion of the physical background of electron backscattering is given by NIEDRIG.<sup>97</sup>

### 2.3.3 Depth Distribution of Characteristic X-Ray Generation

Electrons are able to produce characteristic X-rays of a specific emission line at any point on their way through matter as long as their energy still exceeds the corresponding ionisation threshold. Especially the depth distribution of characteristic X-ray generation is of considerable interest in electron probe microanalysis as it defines the information depth. The in-depth intensity profile of X-ray generation can be measured more easily than other energy loss mechanisms, for example by the tracer method.<sup>98-103</sup> Alternatively, depth distribution functions can be accessed theoretically by diffusion<sup>94,104</sup> and scattering<sup>105</sup> models or Monte Carlo simulations.<sup>103,104,106,107</sup>

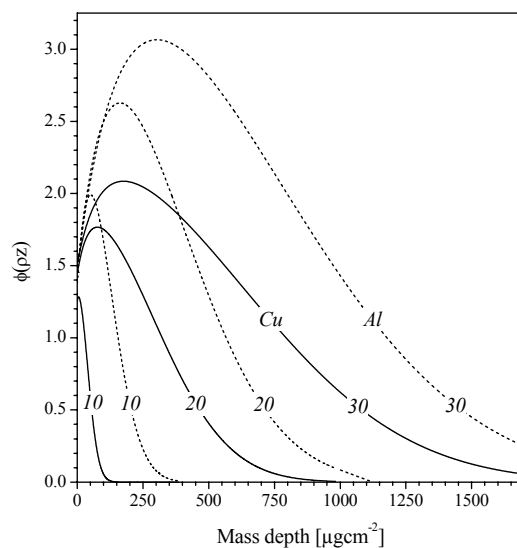


**Figure 2-14.** Depth distribution of  $K_{\alpha}$  radiation in copper ( $E_{crit} = 8.980$  keV,  $E_{K\alpha} = 8.041$  keV, solid lines) and aluminium ( $E_{crit} = 1.560$  keV,  $E_{K\alpha} = 1.487$  keV, broken lines) at different primary beam energies (in keV) and normal beam incidence as a function of the mass depth  $\rho z$ .<sup>77,108,109</sup> The primary beam energy corresponds to overvoltages above the maximum of the ionisation function (see also Figure 2-12) for aluminium.

The depth distribution function  $\varphi(\rho z)$  represents the X-ray intensity of a specific emission line generated in a segment  $d(\rho z)$  of mass thickness relative to the intensity generated in a self-supporting layer of equal mass thickness under the same irradiation conditions. In an early approach, CASTAING assumed the X-ray generation to be proportional to the electron cross-section  $\sigma$  and the number of electrons at a certain depth  $z$ . By applying LENARD's law *eq. 2.41* this model predicts an exponential decrease of  $\varphi(\rho z)$  with increasing depth :

$$\varphi(\rho z) \sim \sigma e^{-\sigma \rho z} \quad (2.46)$$

Despite of its shortcomings *eq. 2.46* is still in use for the calculation of absorption and fluorescence correction factors in quantitative electron microprobe analysis due to its numerical simplicity.<sup>19</sup> For this purpose, numerous empirical adjustments of the LENARD coefficient have been proposed.<sup>58</sup>

Figure 2-14 depicts the depth distribution functions  $\varphi(\rho z)$  of  $K_\alpha$  radiation of copper and aluminium at different electron energies.<sup>77,108,109</sup> In bulk samples, surface ionisation values  $\varphi(0)$  are always larger than unity as backscattered electrons generate X-rays on their way to exit the sample through the surface layer. Below the surface, electrons start to deviate from their original direction mainly due to elastic scattering. The way through deeper sample layers becomes larger than  $d(\rho z)$  as these are crossed at some oblique angle. This increases the probability of X-ray generation as long as the electron directions are not completely randomised and results in a maximum  $\varphi_{\max}$  occurring at some mass depth  $\rho z_{\max}$ . For low primary beam energies, this is less pronounced or even missing as in this case randomisation of electron movement already starts at low mass depths. Apart from this geometric consideration, for ionisation events connected with a low ionisation energy the primary beam energy can correspond to an overvoltage far above the maximum of the ionisation function (see Figure 2-12). In this case, electrons reach the energy for which the ionisation cross-section is largest at a certain depth within the sample, thus contributing to the maximum  $\varphi_{\max}$  of the X-ray depth distribution function.

The total cross-sections for elastic scattering, which is the main source of deflection (see Figure 2-8 and Figure 2-9), are large for heavy elements at low energies according to *eq. 2.17*. Consequently, the electron interaction volume and the X-ray depth distribution extend to larger depths for light elements. In very thin samples, as for example in the transmission

electron microscope, X-ray generation is uniform across the sample when multiple scattering can be neglected.

The ionisation cross-sections  $\sigma_j$  compared to the respective total inelastic cross-section  $\sigma_{inel}$  are higher for light elements as displayed in Figure 2-13. This is reflected in the total number of X-rays  $N_{ij}$  of line  $j$  ( $= K_\alpha, K_\beta, \dots$ ) generated from an element  $i$  :

$$N_{ij} \sim \int_0^\infty \varphi_{ij}(\rho z) d(\rho z) \quad (2.47)$$

and outweighs the effect of the lower fluorescence yield of light elements. As the X-ray depth distribution function is determined by the ionisation cross-section  $\sigma_{ij}$  along the electron path segment  $ds$  projected on the  $z$  axis, *eq. 2.47* can be rewritten

$$N_{ij} \sim \int_0^{s=R_B} \sigma_{ij}(s) \rho ds = \begin{cases} 0 & \text{for } 0 < E(s) < E_{crit,ij} \\ \int_{E_{crit,ij}}^{E_0} \frac{\sigma_{ij}(E)}{\left(\frac{dE_{mean}}{ds}\right)} dE = \int_{E_{crit,ij}}^{E_0} \frac{\sigma_{ij}(E)}{S(E)} dE & \text{for } E_{crit,ij} \leq E(s) \end{cases} \quad (2.48)$$

For practical evaluation, integration is carried out over the electron energy rather than over the unknown electron path by introducing a stopping power expression as given in *eq. 2.36*, for example. The higher X-ray yield of light elements in electron probe microanalysis is a marked difference to X-ray fluorescence analysis where the photoelectric cross-sections are increasing for heavy elements according to Figure 2-4 when assuming that  $\mu \approx \tau$ .



### 3 Quantification Methods in X-Ray Emission Spectroscopy

The aim of quantitative X-ray emission spectroscopy is to retrieve the composition of a multielement sample from the intensity of characteristic X-ray lines emitted from each present element. For exact determination of characteristic net intensities, spectra have to be acquired under well-defined conditions. In order to extract net peak intensities, spectra are usually subjected to numerical pre-processing to correct for line overlaps, background and detector artifacts. Numerical approaches towards peak recognition<sup>110-115</sup> and fitting<sup>116-119</sup> in the presence of statistical noise and background, removal of background from X-ray<sup>119-121</sup>, electron<sup>70,71,117</sup> and proton<sup>24-26</sup> induced X-ray emission spectra, elimination of detector artifacts<sup>122-124</sup> and line overlap<sup>117,125,126</sup>, and the retrieval of spectral net intensities<sup>112,116,118,127-130</sup> are discussed in the literature.

#### 3.1 The Analytical Problem

The intensity of primary fluorescent radiation generated by the incident beam and its further processes within the sample are subject to the sample composition. Therefore, the measured net intensity  $I_{ij}$  of line  $j$  emitted by an analyte  $i$  is affected by the concentrations of all remaining elements ('matrix') present in the sample. This is referred to as matrix effects and results in a functional relationship between concentrations and intensities :

$$I_{ij} = f(c_1, c_2, \dots, c_i, \dots, c_n) = f(\underline{c}) \quad (3.1)$$

$$\text{with } \sum_{i=1}^n c_i = 1 \quad (3.2)$$

which is not linear in the general case. As additional constraint, the normalisation condition *eq. 3.2* has to be satisfied. After its generation, the primary fluorescent radiation is attenuated by absorption as it emerges towards the detector from a certain depth beneath the surface. In turn, fluorescent radiation from another sample component with lower excitation energy can arise from this process. Apart from secondary fluorescence, tertiary and higher order effects are possible in complex samples. For exact determination of concentrations from measured X-ray intensities, matrix correction procedures have to be applied.

### 3.1.1 Empirical Coefficient Methods

When a sufficient number of standard samples is available, *eq. 3.1* can be established as empirical calibration curve. Standards in use are either the pure elements in the case of transition metals or compounds with well-defined and constant stoichiometry such as oxides or halogenides of rock-forming elements. To reduce the amount of data, analytical expressions are used to describe calibration curves. The most common relationship is given by a hyperbola :

$$\frac{I_{ij}}{I_{ij,st}} = \frac{c_i}{\sum_{i=1}^n \alpha_{ij} c_i} = \begin{cases} R_{ij} & (\text{XRF}) \\ k_{ij} & (\text{EPMA}) \end{cases} \quad (3.3)$$

where  $R_i$  and  $k_i$  denote the net intensities  $I_{ij}$  of a certain emission line relative to a standard sample  $I_{ij,st}$  and the empirical coefficients  $\alpha_{ij}$  account for interelement effects.

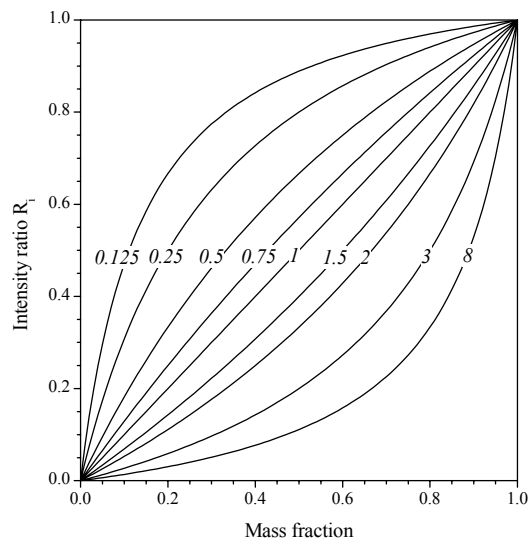


**Figure 3-1.** Calibration curve for a binary sample according to *eq. 3.4* with various coefficients  $a$ . The shape of the hyperbola is convex when fluorescence effects are predominant ( $a < 1$ ) whereas absorption effects are indicated by a concave shape ( $a > 1$ ). The absence of matrix effects corresponds to a straight calibration curve ( $a = 1$ ).

In the case of a binary sample, *eq. 3.3* simplifies to :

$$\frac{I_1}{I_{1,st}} = \frac{c_1}{(1-a) \cdot c_1 + a} \quad (3.4)$$

with a single empirical coefficient  $a$ . This equation is visualised in Figure 3-1.

In X-ray fluorescence<sup>131-139</sup> and electron-probe microanalysis<sup>140</sup>, several correction models similar to *eq. 3.3* have been devised for various matrices with different numbers of empirical coefficients. As a minimum, one standard sample less than the number of present elements is required. Reviews on different empirical coefficient methods in X-ray fluorescence analysis are found in the literature.<sup>135,141,142</sup>

Semi-empirical calibration methods rely on the theoretical assessment of empirical coefficients and thereby drastically reduce the number of required standard samples.

However, the use of calibration curves is effective only when a large number of samples with virtually the same matrix composition of only a few elements have to be routinely analysed under constant excitation conditions. As standards and unknown samples are measured under the same conditions, instrumental parameters are cancelled out. Nevertheless, calibration has to be repeated at certain intervals to ensure reproducibility of analysis. The uniformity of a set of standards concerning surface roughness and long-term stability is a crucial point in elemental analysis with standard samples.

### 3.1.2 Fundamental Parameter Methods

Based on the knowledge of the interaction processes of electrons and X-rays with matter, fundamental parameter methods calculate the characteristic X-ray net intensity emitted from a sample of given composition. Matrix effects are taken into account on the basis of the set of atomic constants ('fundamental parameters') introduced in the previous section.

Fundamental parameter approaches are applicable to a wide range of matrix compositions. Dedicated procedures are also able to deal with samples of intermediate thickness and are suitable where diverse materials have to be analysed. Some care has to be taken on the compilation of the fundamental parameters as uncertainties in the quantification results may arise from inaccuracies in the physical database. Standardless analysis can be performed with fundamental parameter methods when instrumental parameters are known. A comparison of

empirical coefficient methods versus fundamental parameter calculations is given by CRISS and BIRKS.<sup>131</sup>

The starting point for matrix correction is the calculation of the primary (superscript '1') fluorescent X-ray intensity detected from a homogeneous and flat sample, which is crossed by a quasi-parallel and monochromatic (superscript 'mono') X-ray or electron beam at a certain depth  $z$  :

$$dI_{ij}^{1,mono} = \left\{ \begin{array}{l} \frac{\Omega}{4\pi} \varepsilon(E_{ij}) \cdot c_i \rho dz \cdot \omega_{ij} p_{ij} \tau_{ij}(E_0) \cdot DI_0(E_0) \cdot e^{-\frac{\mu(E_0)}{\sin \alpha} \rho z} \cdot e^{-\frac{\mu(E_{ij})}{\sin \psi} \rho z} \quad (XRFA) \\ \frac{\Omega}{4\pi} \varepsilon(E_{ij}) \cdot c_i \rho dz \cdot \omega_{ij} p_{ij} \sigma_{ij}(E_0) \cdot \frac{I_p}{e} \cdot e^{-\frac{\mu(E_{ij})}{\sin \psi} \rho z} \quad (EPMA) \end{array} \right\} \quad (3.5)$$

$$= \frac{\Omega}{4\pi} \varepsilon(E_{ij}) \cdot dI_{gen,ij}^{1,mono} \cdot e^{-\frac{\mu(E_{ij})}{\sin \psi} \rho z}$$

In X-ray fluorescence analysis, the angle of incidence  $\alpha$  defines the footprint of area  $D$  of the primary X-ray beam with flux  $I_0$  [photons·cm<sup>-2</sup>·sec<sup>-1</sup>] on the sample surface. Instrumental parameters are represented by the solid angle of detection  $\Omega$ , the detector efficiency  $\varepsilon(E_{ij})$ , and the take-off angle  $\psi$ . The factor  $\Omega/4\pi$  is also referred to as geometric collection efficiency. The mass absorption coefficients  $\mu$  are determined by the composition of the sample according to eq. 2.6 and introduce matrix effects to the detected primary fluorescent intensity of line  $j$  from analyte  $i$ .

The primary fluorescent X-ray intensity still has to be corrected for secondary and higher order fluorescence effects. In its most general form, the fluorescence enhancement factor is given by the ratio of the fluorescent intensity of a specific line to the intensity generated (subscript 'gen') by the primary beam only :

$$H_{ij} = \frac{I_{gen,ij}}{I_{gen,ij}^1} = \frac{I_{gen,ij}^1 + \sum_{lm} I_{ijlm}}{I_{gen,ij}^1} = 1 + \frac{\sum_{lm} I_{ijlm}(E_{ij}, E_{lm}, E_0)}{I_{gen,ij}^1(E_{ij}, E_0)} \quad (3.6)$$

Here the summation is over all lines  $m$  of matrix elements  $l$  which are energetic enough to cause interelement fluorescence. It has to be noted that the enhancement factor accounts for

secondary and higher order effects as line  $l$  may itself be the product of fluorescence within the sample. The database necessary for a standardless fundamental parameter quantification of X-ray emission spectra is summarised in Table 3-1.

<i>atomic parameters</i>		<i>sample parameters</i>		<i>instrumental parameters</i>	
$E_{ij}$	characteristic line energies	$c_i$	mass fractions	$\alpha$	angle of incidence
$E_{crit,ij}$	absorption edge energies	$Z_i$	atomic numbers	$D$	illuminated sample area ( <i>XRFA</i> )
$\tau_{ij}(E)$	photoelectric cross-sections	$A_i$	atomic masses	$E_0$	primary beam energy
$\mu_{ij}(E)$	mass absorption coefficients	$\rho$	Density	$I_0(E)$	excitation spectrum ( <i>XRFA</i> )
$S_{ij}$	absorption edge jumps	$\eta_i(E)$	backscatter coefficients ( <i>EPMA</i> )	$\psi$	take-off angle
$\omega_{ij}$	fluorescence yields			$\Omega$	solid angle of detection
$p_{ij}$	Transition probabilities			$\varepsilon(E)$	detection efficiency
$\sigma_{ij}(E)$	inner shell ionisation cross-sections ( <i>EPMA</i> )				
$J_i(E)$	mean ionisation potentials ( <i>EPMA</i> )				

**Table 3-1.** Fundamental parameters required for standardless quantification of X-ray emission spectra. Abbreviations in brackets mark quantities that are necessary either for X-ray fluorescence (XRFA) or electron microprobe analysis (EPMA) only. A compilation of least square fits to fundamental parameters is found in the literature.<sup>46</sup>

### 3.2 Quantitative X-Ray Fluorescence Analysis

The calculation of intensities under conditions of monochromatic excitation is justified when X-ray fluorescence analysis is carried out using radioisotope sources or X-ray tubes equipped with filters. In the latter case, line couples are often selected from the spectral output. Even in this case the formulae for monochromatic excitation remain valid when evaluated for two energies separately or introducing an effective energy.

#### 3.2.1 Monochromatic Excitation

For quantitative evaluation of the X-ray intensity emitted from a thick sample, eq. 3.5 is rewritten in the form :

$$\begin{aligned} dI_{ij}^{1,mono} &= \frac{\Omega}{4\pi} \varepsilon(E_{ij}) \cdot c_i \rho dz \cdot \omega_{ij} p_{ij} \tau_{ij}(E_0) \cdot DI_0(E_0) \cdot e^{-\frac{\mu(E_0)}{\sin \alpha} \rho z} \cdot e^{-\frac{\mu(E_{ij})}{\sin \psi} \rho z} \\ &= Y_{ij}^{1,mono}(E_0) \cdot e^{-\chi(E_{ij}, E_0) \rho z} dm_i \end{aligned} \quad (3.7)$$

thereby collecting all terms that do not depend on the depth  $z$  and defining the elemental yield  $Y$  of primary fluorescent radiation under monochromatic excitation conditions :

$$Y_{ij}^{1,mono} = \frac{\Omega}{4\pi} \varepsilon(E_{ij}) \cdot \omega_{ij} p_{ij} \tau_{ij}(E_0) \cdot I_0(E_0) \quad (3.8)$$

The generalised absorption factor accounts for attenuation of the primary beam along its penetration path through the sample as well as for the absorption of the fluorescent radiation on its way towards the detector :

$$\chi(E_{ij}, E_0) = \frac{\mu(E_0)}{\sin \alpha} + \frac{\mu(E_{ij})}{\sin \psi} \quad (3.9)$$

The mass element probed by the X-ray beam is defined by the illuminated sample area  $D$ , the weight fraction  $c_i$ , and the sample density :

$$dm_i = D \rho c_i dz \quad (3.10)$$

When integrated over the sample thickness  $t$ , eq. 3.7 yields the total primary X-ray intensity of characteristic line  $j$  emitted by analyte  $i$  excited by monochromatic radiation :

$$\begin{aligned} I_{ij}^{1,mono} &= \int_0^t Y_{ij}^{1,mono} e^{-\chi(E_{ij}, E_0) \rho z} D \rho c_i dz = m_i Y_{ij}^{1,mono} \left[ \frac{1 - e^{-\chi(E_{ij}, E_0) \rho t}}{\chi(E_{ij}, E_0) \rho t} \right] \\ &= m_i Y_{ij}^{1,mono} A_{ij}^{mono}(E_{ij}, E_0) \end{aligned} \quad (3.11)$$

The absorption correction is included in the self-absorption coefficient  $A_{ij}$ . In thick samples, the secondary and higher order effects are of particular interest. Secondary fluorescence can contribute as much as 50 % to the line intensity in X-ray fluorescence spectroscopy. Therefore, the correct full count rate is only obtained when incorporating a fluorescence correction factor according to eq. 3.6 :

$$I_{ij}^{full,mono} = I_{ij}^{1,mono} \cdot H_{ij}^{mono} \quad (3.12)$$

Apart from the sample composition, fluorescent enhancement depends on the ratio of photoelectric absorption of characteristic and incident radiation by the analyte as well as on the amount of radiation causing secondary fluorescence, generated by the incident beam. In the case of second order effects and monochromatic excitation, the fluorescence correction factor takes the simple form<sup>17</sup> :

$$\begin{aligned} H_{ij}^{2,mono} &= 1 + \sum_{lm} c_l \omega_{lm} p_{lm} \tau_{lm}(E_0) \frac{\tau_{ij}(E_{lm})}{\tau_{ij}(E_0)} \\ &\quad \left\{ \frac{\sin \alpha}{\mu(E_0)} \ln \left[ 1 + \frac{\mu(E_0)}{\mu(E_{lm}) \sin \alpha} \right] + \frac{\sin \psi}{\mu(E_{ij})} \ln \left[ 1 + \frac{\mu(E_{ij})}{\mu(E_{lm}) \sin \alpha} \right] \right\} \end{aligned} \quad (3.13)$$

### 3.2.2 *Polychromatic Excitation*

In most cases an excitation spectrum consisting of characteristic lines superimposed on a Bremsstrahlung background is encountered. The spectral distribution of the incident X-rays then explicitly enters the theoretical evaluation of characteristic line intensities and has to be known. The spectral output of various types of X-ray tubes operated under different conditions has been determined<sup>143-145</sup> and was also calculated using either fundamental parameter methods<sup>146-149</sup>, transport equations<sup>150,151</sup> or Monte Carlo<sup>152</sup> methods.

In order to obtain the X-ray intensity generated by a polychromatic beam, integration of *eq. 3.5* has to be performed over the range of X-ray energies and the sample thickness  $t$ . The spectral output of an X-ray tube is limited at a maximum energy  $E_{\max}$  given by its operation voltage :

$$\begin{aligned}
 I_{ij}^{1,poly} &= \int_0^t \int_{E_{crit,ij}}^{E_{\max}} \frac{\Omega}{4\pi} \varepsilon(E_{ij}) \cdot c_i \rho \omega_{ij} p_{ij} \tau_{ij}(E) D I_0(E) \cdot e^{-\chi(E,E_0)\rho z} dE dz \\
 &= \int_{E_{crit,ij}}^{E_{\max}} Y_{ij}^{1,mono} \left( \int_0^t e^{-\chi(E,E_0)\rho z} D \rho c_i dz \right) dE
 \end{aligned} \tag{3.14}$$

Here the elemental yield as defined in *eq. 3.8* for the case of monochromatic excitation of the sample becomes a function of all energies in the excitation spectrum. In analogy, the polychromatic elemental yield is defined according to :

$$Y_{ij}^{1,poly} = \int_{E_{crit,ij}}^{E_{\max}} Y_{ij}^{1,mono}(E) dE \tag{3.15}$$

With this definition, *eq. 3.14* takes the same form as its monochromatic counterpart *eq. 3.11* after integration over the sample thickness :

$$\begin{aligned}
I_{ij}^{1,poly} &= \int_{E_{crit,ij}}^{E_{max}} Y_{ij}^{1,mono}(E) A_{ij}^{mono}(E, E_0) D \rho c_i dE \\
&= m_i \cdot Y_{ij}^{1,poly} \cdot \frac{\int_{E_{crit,ij}}^{E_{max}} Y_{ij}^{1,mono}(E) \cdot A_{ij}^{mono}(E) dE}{\int_{E_{crit,ij}}^{E_{max}} Y_{ij}^{1,mono}(E) dE} = m_i \cdot Y_{ij}^{1,poly} \cdot A_{ij}^{poly}
\end{aligned} \tag{3.16}$$

where the polychromatic self-absorption coefficient can be expressed in terms of monochromatic quantities only. The derivation of a polychromatic fluorescence correction factor to account for enhancement effects according to :

$$I_{ij}^{poly} = I_{ij}^{1,poly} \cdot H_{ij}^{poly} \tag{3.17}$$

in analogy to *eq. 3.12* is very lengthy and beyond the scope of the present discussion, though the second order correction term very much resembles *eq. 3.13*. Formulae for the intensity of primary, secondary and tertiary fluorescence radiation excited by a monochromatic X-ray source have been derived<sup>132,153,154</sup>, further simplified<sup>155</sup>, and finally corrected<sup>156</sup>. Extension of these expressions to polychromatic irradiation has been provided by SHIRAIWA and FUJINO who have also confirmed the practical applicability of the fundamental parameter approach.<sup>157-159</sup> A comprehensive formulation including secondary effects for polychromatic excitation and samples of intermediate thickness is to be found in the literature.<sup>17</sup> Beyond third order fluorescence, which can still amount to a few percent of the total intensity, no correction factors are available in the fundamental parameter model. An extension of this approach to calculate the intensity of scatter radiation has been reported by VAN ESPEN.<sup>160</sup>

### 3.3 Quantitative Electron Probe Microanalysis

In addition to self-absorption (A) and fluorescence (F) correction, an additional correction factor accounting for atomic number (Z) effects occurs in electron probe microanalysis. Fundamental parameter quantification techniques based on the knowledge of inner shell ionisation cross-sections treat these correction factors separately, giving rise to the most commonly applied ZAF algorithm. Atomic number and absorption correction are grouped when employing X-ray depth distribution functions in the  $\phi(\rho z)$  matrix correction procedure.

### 3.3.1 Atomic Number (Z-) Correction

The energy loss of electrons on their way through the sample is accompanied by a change of the cross-sections for inner shell ionisation. The coupling of ionisation cross-sections to the electron path length has been described in *eq. 2.48*. Applying this to *eq. 3.5*, the elemental yield of X-rays generated by a monochromatic electron beam of energy  $E_0$  and probe current  $I_p$  from a homogeneous sample with flat surface can be written :

$$Y_{ij}^1 = \frac{\Omega}{4\pi} \varepsilon(E_{ij}) \cdot c_i \omega_{ij} p_{ij} \cdot \frac{I_p}{e} \cdot \int_0^{s=R_B} \sigma_{ij}(s) \rho ds$$

$$= \begin{cases} 0 & \text{for } 0 < E \leq E_{\text{crit},ij} \\ \frac{\Omega}{4\pi} \varepsilon(E_{ij}) \cdot c_i \omega_{ij} p_{ij} \cdot \frac{I_p}{e} \cdot \int_{E_{\text{crit},ij}}^{E_0} \frac{\sigma_{ij}(E)}{S(E)} dE & \text{for } E_{\text{crit},ij} < E \end{cases} \quad (3.18)$$

The matrix composition influences the amount of X-ray generation as the stopping power  $S$  is governed by the mean ionisation potential of the sample. Matrices with a high stopping power will produce characteristic X-rays less efficiently as the electron energy is mainly consumed in outer shell ionisation events. In connection with *eq. 2.24*, this effect of the ionisation potentials is attributed to the atomic numbers of the elements present in the sample. The corresponding atomic number ( $Z$ ) correction factor (also referred to as 'stopping power correction') is provided by the integral in *eq. 3.18* describing the mean number of ionisations in a specific shell caused by a single electron. Typical values are in the order of  $10^{-5}$  to  $10^{-6}$ . Numerical evaluation of the atomic number correction factor yields analytical formulae that only depend on the overvoltage ratio, absorption edge energies, and the backscatter coefficient.<sup>91,92</sup> Backscattered electrons with energies  $E_B > E_{\text{crit},ij}$  do not produce further X-ray quanta. The intensity loss by backscattering is corrected by introducing a backscattering correction factor to *eq. 3.18*. This factor  $R_{B,ij}$  is defined as the number of characteristic X-rays actually generated relative to the hypothetical amount produced if backscattering was absent :

$$R_{B,ij} = 1 - \left\{ \frac{\int_{E_{crit,ij}}^{E_0} \frac{d\eta_B}{dE_B} \left[ \int_{E_{crit,ij}}^{E_B} \frac{\sigma_{ij}(E)}{S(E)} dE \right] dE_B}{\int_{E_{crit,ij}}^{E_0} \frac{\sigma_{ij}(E)}{S(E)} dE} \right\} = \sum_{i=1}^n c_i R_{B,ij} \quad (3.19)$$

In analogy to *eq. 2.43*, the factor  $R_{B,ij}$  of a multielement sample is given as weight average of all components. With this correction, the primary fluorescent X-ray intensity generated in the sample is given by :

$$I_{gen,ij}^1 = R_{B,ij} \cdot Y_{ij}^1 \quad (3.20)$$

The backscatter correction factor decreases with increasing primary beam energy. It becomes significantly smaller than unity for heavy elements for which high backscattering factors are observed. In principle, calculation of  $R_{B,ij}$  involves the integration of energy spectra of backscattered electrons, which, with respect to application in microanalysis, can be represented by a POISSONIAN distribution as pointed out by RIVEROS et al.<sup>161,162</sup> In order to maintain computational simplicity, a mean energy of backscattered electrons is introduced to avoid integration over the backscatter spectrum. The inner integral of *eq. 3.19* is usually replaced by the empirical relation between generated characteristic X-ray intensity and electron energy (*eq. 3.24*).<sup>163,164</sup> In this way, the backscattering correction factor is usually fitted by polynomials as a function of overvoltage ratio and backscatter coefficient.<sup>92</sup>

### 3.3.2 Absorption (A-) Correction

The absorption correction factor is defined by the ratio of X-ray intensity emerging from the sample to the total intensity generated in the electron diffusion volume. The non-uniformity of X-ray generation within this volume cannot be represented by a simple exponential term. Due to its rather complex shape, the depth distribution has to be considered explicitly in the absorption correction factor  $A_{ij}$  :

$$A_{ij}(E_{ij}, \chi) = \frac{\int_0^{\infty} \varphi(\rho z) \cdot e^{-\chi(E_{ij})\rho z} d(\rho z)}{\int_0^{\infty} \varphi(\rho z) d(\rho z)} \text{ with } \chi(E_{ij}) = \frac{\mu(E_{ij})}{\sin \psi} \quad (3.21)$$

where  $\chi(E_{ij})$  denotes the generalised absorption coefficient in analogy to *eq. 3.9*. The absorption correction in electron probe microanalysis takes the form of a normalised LAPLACE transform of the X-ray depth distribution function  $\varphi(\rho z)$ . For computational simplicity, it is advisable to represent these functions in an analytically integrable form.

The PHILIBERT model basically follows CASTAING's approach (*eq. 2.46*) but proposes a sum of two exponentials and is capable of modelling the maximum of the X-ray depth distributions, but entirely neglects surface ionisation. It is widely used and produces reasonable values for weak absorption. However, it fails for samples with strong self-absorption where the main amount of detected intensity emerges from near-surface regions.<sup>165</sup> BISHOP has devised a rectangular model by assuming  $\varphi(\rho z)$  to be constant from the surface down to twice the mean depth of X-ray generation and to switch to zero below.<sup>166</sup> The mean depth is deduced from the PHILIBERT model and has been corrected by comparison with Monte Carlo simulations<sup>90,166</sup> and experimental data<sup>103</sup> to compensate for the simplified shape of the model function. This model has the advantage of not falling to zero at the sample surface and is appropriate when moderate absorption effects are encountered. A closer approximation to reality with improved performance in cases of strong absorption is provided by the 'quadrilateral' model of LOVE and SCOTT.<sup>167</sup> Here, the X-ray depth distribution function is assumed to follow straight lines connecting the surface  $(0, \varphi_0)$  with the maximum  $(\rho z_{\max}, \varphi_{\max})$  and falling to zero at maximum depth  $(\rho z_r, 0)$ . A concise overview over the different absorption correction models is found in the literature.<sup>168</sup>

### 3.3.3 *The $\varphi(\rho z)$ Technique*

An alternative formulation of the atomic number correction is implemented by applying the X-ray depth distribution function as given in *eq. 2.47* :

$$Y_{ij}^1 = \frac{\Omega}{4\pi} \varepsilon(E_{ij}) \cdot c_i \omega_{ij} p_{ij} \frac{I_p}{e} \cdot \int_0^{\infty} \varphi(\rho z) d(\rho z) \quad (3.22)$$

The ZAF correction procedure relies on *eq. 3.18* for atomic number (Z) correction and separately accounts for absorption (A) and fluorescence (F) effects. In contrast, the  $\varphi(\rho z)$  correction scheme starts from *eq. 3.22* and implements a unified atomic number and absorption correction factor. By introducing the result of the absorption correction (*eq. 3.21*) the above expression directly yields the primary fluorescent intensity according to :

$$I_{ij}^1 = \frac{\Omega}{4\pi} \varepsilon(E_{ij}) \cdot c_i \omega_{ij} p_{ij} \frac{I_p}{e} \cdot \int_0^{\infty} \varphi(\rho z) e^{-\chi(E_{ij})\rho z} d(\rho z) \quad (3.23)$$

The backscatter correction is not necessary in this approach as the loss of X-ray intensity by backscattering is inherently considered in the X-ray depth distribution functions.

The  $\varphi(\rho z)$  method is more sensitive towards simplifications of the X-ray depth distribution than the ZAF approach. Therefore, sophisticated analytical fits are necessary as the total generated intensity has to be predicted precisely. Especially in light element analysis where absorption is the most prominent matrix effect, the surface ionisation has to be modelled accurately.

POUCHOU and PICOIR have selected two parabolic branches joined smoothly and falling to zero with zero slope at a certain depth related to the electron range. Though numerical integration is avoided extensive calculations are necessary to obtain the parameters of the parabolae.<sup>58</sup> The narrowing of the maximum of the X-ray depth distributions at low overvoltages sets a practical limit to the parabolic model.

The approximate GAUSSIAN shape of  $\varphi(\rho z)$  curves has been noticed by WITTRY<sup>169</sup> and has given rise to offset GAUSSIAN fitting functions centred at  $\rho z_{\max}$ .<sup>170,171</sup> An alternative description by PACKWOOD and BROWN employing a centred GAUSSIAN curve modified by a transient function in the near-surface region has received great attention.<sup>108</sup> Analytical integration of this model function has been performed and optimised sets of parameters have been reported to enable analysis at low overvoltages and of light elements.<sup>109,172,173</sup>

### 3.3.4 Fluorescence (F-) Correction

The knowledge of the primary intensity of both X-ray lines enhanced by fluorescence as well as of all X-ray lines contributing to fluorescence effects is a necessary prerequisite for fluorescence correction. The assessment of fluorescence correction starts from the relation :

$$I_{gen,ij}^1 \sim (u_{ij} - 1)^n = \left( \frac{E_0 - E_{crit,ij}}{E_{crit,ij}} \right)^n \quad (3.24)$$

which empirically describes the total generated characteristic X-ray intensity. A commonly adopted value for the exponent is  $n = 1.67$  though different values have been reported.<sup>163,164</sup> Subsequently, re-absorption of characteristic X-rays and their conversion to secondary X-rays has to be considered. The probability of absorption is not only ruled by the photoelectric cross-section of the sample but also by the depth distribution of X-rays evoking secondary fluorescence. In the commonly employed formulation, the fluorescence enhancement factor  $H_{ij}$  is given by<sup>19,174,175</sup> :

$$H_{ij} = \frac{I_{gen,ij}^1 + \sum_{lm} I_{ijlm}}{I_{gen,ij}^1} \quad (3.25)$$

$$= \sum_{lm} c_l \cdot \left[ \frac{u_{lm} - 1}{u_{ij} - 1} \right]^{1.67} \cdot \left[ \frac{\mu_i(E_{lm})}{\mu(E_{lm})} \right] \cdot \left[ \frac{\ln(1 + \bar{u})}{\bar{u}} + \frac{\ln(1 + \bar{v})}{\bar{v}} \right] \cdot \left[ \frac{1}{2} \frac{S_{ij} - 1}{S_{ij}} \omega_{lm} \frac{A_i}{A_l} \cdot p_{jm} \right]$$

$$\text{with } \bar{u} = \frac{1}{\sin \psi} \cdot \frac{\mu(E_{ij})}{\mu(E_{lm})} \text{ and } \bar{v} = \frac{\sigma_{ij}}{\mu(E_{lm})} \quad (3.26)$$

where the photoelectric cross-sections are approximated by mass attenuation coefficients. Generally, efficient interelement fluorescence is possible only if the overvoltage ratio of line  $j$  experiencing enhancement exceeds that of the exciting line  $m$ . Additionally, absorption of line  $m$  by the element  $i$  emitting fluorescent X-rays has to contribute significantly to the total absorption of the sample. These conditions are only met if the lines involved are of comparable energies, as this is the case between elements which are only separated by a few

atomic numbers in the periodic table. Fluorescence effects between lines which are more than 5 keV apart are usually disregarded.

To obtain a comprehensive expression, this approach uses the X-ray depth distribution estimated by CASTAING (*eq. 2.46*). Several empirical calibrations have been reported for LENARD's constant  $\sigma$  [ $\text{cm}^2\text{g}^{-1}$ ] with energies given in [keV] in connection with different absorption correction models<sup>174</sup> :

$$\sigma_{ij} = \frac{\text{const.}}{E_0^n - E_{crit,ij}^n} \begin{cases} \text{const.} = 2.39 \cdot 10^5, & n = 1.5 \\ \text{const.} = 3.3 \cdot 10^5, & n = 1.65 \\ \text{const.} = 6.8 \cdot 10^5, & n = 1.86 \end{cases} \quad (3.27)$$

Fluorescent interactions take place with different efficiencies, depending on whether K or L lines are involved as excited or exciting lines. The factor  $p_{jm}$  entering the conversion probability term in *eq. 3.25* accounts for this phenomenon<sup>175</sup> :

$$p_{jm} = \begin{cases} 1 & j = m \\ 0.24 & j = K, m = L \\ 4.76 & j = L, m = K \end{cases} \quad (3.28)$$

*Eq. 3.25* corrects for fluorescence effects arising from absorption of characteristic X-rays. Bremsstrahlung of sufficiently high energy can also generate characteristic X-rays causing 'continuum fluorescence'. The mathematical treatment of this phenomenon is similar to that of characteristic fluorescence.<sup>58</sup> It is usually neglected but has to be taken into account for samples exhibiting severe self-absorption effects, for example heavy elements in a light matrix such as in oxides. The derivation of a continuum fluorescence correction, which takes the depth distribution of Bremsstrahlung into account explicitly has been put forward.<sup>176</sup>

### 3.4 Modelling the Detection Process

The natural width of an X-ray emission line is smaller than 0.5 eV and therefore beyond the resolution of both energy and wavelength dispersive detection systems. The multi-channel analyser of an energy dispersive detector renders the spectrum as an array of integer numbers.

When a photon of energy  $E_X$  hits the detector, the number of counts in channel  $i$  corresponding to :

$$E_X = E_{offset} + i \cdot \Delta E_{gain} \quad (3.29)$$

is increased by one. The energy gain  $\Delta E_{gain}$  of a semiconductor device is usually 10 eV/channel. X-ray quanta with energies of 20 or 25 keV are therefore recorded with a total number  $n_{ch}$  of channels of 2000 and 2500, respectively.

### 3.4.1 Detector Resolution and Efficiency

When processed by an energy dispersive X-ray detector, a monochromatic X-ray line exhibits a GAUSSIAN shape with a full width at half maximum ('fwhm') that defines resolution. The effect of the noise amplitude of the preamplifier  $\Delta E_{noise}$  and the statistics of electron-hole production  $\Delta E_{st}$  are superimposed independently to result in the total energy resolution  $\Delta E_{fwhm}$  of :

$$\Delta E_{fwhm} = \sqrt{\Delta E_{noise}^2 + \Delta E_{st}^2} \quad (3.30)$$

The resolution due to electronic noise contributes a constant value of typically 80 to 120 eV to  $\Delta E$ . For generation of an electron-hole pair in silicon, a mean energy  $E_{intr}$  of 3.86 eV is necessary.<sup>177</sup> Therefore, an X-ray quantum with energy  $E_x$  will give rise to a mean number of

$$N = \frac{E_x}{E_{intr}} \quad (3.31)$$

when absorbed in the intrinsic zone of a Si(Li) detector. This quantity is subject to a statistical variation of :

$$\Delta N = \sqrt{\text{var}(N)} = \sqrt{NF} = \sqrt{\frac{E_x}{E_{intr}} F} \quad (3.32)$$

and therefore causes a peak broadening, which depends on the energy of the impinging X-ray quanta :

$$\Delta E_{st} = \sqrt{8 \ln 2} \cdot E_{intr} \Delta N = \sqrt{8 \ln 2 \cdot E_x E_{intr} F} \approx 2.35 \cdot \sqrt{E_x E_{intr} F} \quad (3.33)$$

Consequently, the resolution of an energy dispersive X-ray detector slightly decreases at high energies. The constant factor converts the width of the GAUSSIAN distribution into its full width at half maximum. The FANO factor F takes into account that the processes of electron-hole generation are not statistically independent. It is much less than unity and values commonly observed for Si(Li) detectors are between  $F = 0.09-0.125$ .

X-ray quanta striking the detector have to pass the detector entrance window, the gold contacts, and an inactive silicon 'dead layer' Si\* with a thickness of about 100 nm. In the low energy range, the detection efficiency is therefore limited by absorption effects, whereas on the high energy side X-ray quanta fail to generate a signal due to transmission through the intrinsic layer with an effective thickness  $t_{Si}^*$ . The detection efficiency (also referred to as 'spectrometer function' or 'detector response function') is defined as probability of detection  $\varepsilon(E_x)$  and depends on the X-ray energy. For an energy dispersive Si(Li) detector it is readily computed by :

$$\varepsilon(E_x) = \prod_{\substack{i=window, \\ Au, Si^*}} e^{-\mu_i(E_x) \rho_i t_i} \cdot \left( 1 - e^{-\mu_{Si} \rho_{Si} t_{Si}^*} \right) \quad (3.34)$$

With modern detectors equipped with ultrathin windows,  $\varepsilon(E_x)$  does not significantly deviate from unity in the energy range of about 1 to 20 keV. The detection efficiency of energy dispersive solid-state detectors has received considerable interest<sup>160,178-181</sup> as it is involved in the theoretical determination of intensities in standardless X-ray fluorescence and electron microprobe analysis. However, in principle no experiments are necessary to access the efficiency of an energy dispersive detector. In contrast, resolution and efficiency of wavelength dispersive systems are influenced by several parameters, such as the geometric arrangement of the spectrometer system and the reflectivity and size of the crystal. The detection efficiency of a wavelength dispersive system varies over up to two orders of magnitude in the energy range supported by a crystal. A concise description of the

performance of wavelength dispersive X-ray spectrometers concerning efficiency, resolution, and temperature dependence of lattice distances of commonly used crystals has been provided by REED.<sup>58</sup>

### 3.4.2 *Detector Artifacts*

When absorbed photoelectrically within an energy dispersive detector, photons with an energy exceeding the K edge energy of the detector material, 1.840 keV in the case of silicon, cause ionisation events and the emission of either AUGER electron or characteristic K X-rays. Due to their low range in matter, AUGER electrons lose their entire energy in inelastic scattering processes inside the detector. Characteristic K X-rays, however, are able to leave the detector. As the energy of the emitted X-ray photon is no longer available for the detection process, an escape peak will be observed at an energy of :

$$E_{K\alpha,esc} = E_X - E_{SiK\alpha} \quad (3.35)$$

with a silicon detector. Occurrence of escape peaks does not only influence characteristic intensities, but can also overlap or obscure lines of low intensity as especially encountered in the detection of traces by X-ray fluorescence analysis.

Assuming that monochromatic radiation impinges onto the centre of a planar solid-state X-ray detector manufactured of material *i* (*i* = Si, Ge, NaI), the fraction of  $K_\alpha$  X-rays escaping through its anterior surface is given according to<sup>182-184</sup> :

$$p_{esc}(E) = \frac{1}{2} \omega_{iK\alpha} p_{iK\alpha} f_{iK\alpha} \left\{ 1 - \frac{\mu_i(iK_\alpha)}{\mu_i(E)} \cos \vartheta \cdot \ln \left[ 1 + \frac{\mu_i(E)}{\mu_i(iK_\alpha) \cos \vartheta} \right] \right\} \quad (3.36)$$

Here,  $\theta$  denotes the angle enclosed by the incident radiation and the crystal axis,  $\omega_{iK}$  the fluorescence yield,  $p_{iK\alpha}$  the transition probability, and  $f_{iK\alpha}$  the absorption edge jump factor with respect to the K edge according to *eq. 2.10*. As primary absorption occurs at deeper layers at normal incidence of X-rays, the escape probability is lowest for 'good' geometry ( $\cos\theta = 1$ ) and also decreases with energy. The intensity of an escape peak relative to its parent line is obtained by :

$$R_{esc}(E) = \frac{p_{esc}(E)}{1 - p_{esc}(E)} \quad (3.37)$$

Generally, escape peak intensities decrease with X-ray energy, and in the case of silicon do not exceed a relative intensity of approximately 1.5 %. Correction terms to allow for emerging of photons through the back or the side of the detector are available<sup>183</sup> but are not included in the present discussion due to the low escape probability at high energies. Owing to its significantly higher fluorescence yield and reduced self-absorbing properties, escape lines become more predominant for germanium detectors. Also, escape peaks related to the Ge K<sub>β</sub> line are observed, necessitating to modify *eq. 3.36* by substituting  $f_{ij}$  by  $(1-f_{ij})$  in this case.

### 3.5 Matrix Correction Procedures in Practice

As shown in the previous sections, the net intensity of characteristic X-ray peaks emitted from a sample can be calculated theoretically when applying suitable matrix correction factors. In X-ray fluorescence analysis, the intensity emitted by an element of the sample in the general case of polychromatic excitation is given by introducing *eq. 3.16* to *eq. 3.17* :

$$I_{ij}^{poly}(\underline{c}) = m_i \cdot Y_{ij}^{1,poly}(\underline{c}) \cdot A_{ij}^{poly}(\underline{c}) \cdot H_{ij}^{poly}(\underline{c}) \quad (3.38)$$

Summarising the corresponding expressions for electron probe microanalysis, *eq. 3.20* to *3.25* provides :

$$I_{ij}(\underline{c}) = \begin{cases} R_{B,ij}(\underline{c}) \cdot Y_{ij}^1(\underline{c}) \cdot A_{ij}(\underline{c}) \cdot H_{ij}(\underline{c}) & \text{ZAF formalism} \\ \frac{\Omega}{4\pi} \varepsilon(E_{ij}) \cdot c_i \omega_{ij} p_{ij} \frac{I_p}{e} \cdot \left[ \int_0^\infty \varphi(\rho z) e^{-\chi(E_{ij})\rho z} d(\rho z) \right] \cdot H_{ij}(\underline{c}) & \varphi(\rho z) \text{ procedure} \end{cases} \quad (3.39)$$

The task of matrix correction procedures consists in finding a set  $\underline{c}$  of concentrations for which the calculated intensities from *eq. 3.38* or *eq. 3.39* match the experimentally determined ones. This can only be achieved iteratively as the correction factors themselves

depend on the initially unknown composition of the sample. When analysis is performed standardless, relative intensities are defined by normalisation to the total intensity of the characteristic spectrum according to :

$$R_i = \frac{I_{ij}}{\sum_{i=1}^n I_{ij}} \quad (3.40)$$

Setting the concentrations equal to the measured relative intensities corresponds to a complete neglect of matrix effects in a zero-order approximation and provides an initial guess of the sample composition :

$$c_i^0 = R_{meas,i} = \frac{I_{meas,ij}}{\sum_{i=1}^n I_{meas,ij}} \quad (3.41)$$

An improved estimate of  $\underline{c}^{n+1}$  is obtained from the currently assumed composition  $\underline{c}^n$  by comparing the calculated relative intensities  $R_i^n$  to the experimental values according to

$$c_i^{n+1} = \frac{R_{meas,i}}{R_i^n} c_i^n \quad (3.42)$$

Independent of the iteration algorithm employed, the new set  $\underline{c}^{n+1}$  of concentrations has to be re-normalised as given in *eq. 3.2*. The 'method of successive approximation' defined by this iteration (*eq. 3.42*) is the most straightforward matrix correction procedure. It is equivalent to a linear interpolation between the points (0,0) and ( $c_i, R_i$ ) on the calibration curve  $R_i(c_i)$ . In the case of strong matrix effects, this algorithm tends to overestimate the correction of the current concentration values  $\underline{c}^n$  giving rise to oscillations thus preventing convergence. The problem of non-convergence is virtually eliminated when a three point interpolation scheme between the points (0,0), ( $c_i, R_i$ ), and (1,1) is used. Taking the empirical shape of calibration curves into account, a hyperbola is chosen to connect these points. This results in the iteration equation proposed by *CRISS and BIRKS*<sup>131</sup> :

$$c_i^{n+1} = \frac{R_{meas,i} \cdot c_i^n \cdot (1 - R_i^n)}{R_{meas,i} \cdot (c_i^n - R_i^n) + R_i^n \cdot (1 - c_i^n)} \quad (3.43)$$

Typically, convergence is achieved within four to twelve iteration steps when the matrix composition is not too complex. Subsequent concentration values are estimated more precisely when the slope of the calibration curve is incorporated into the iteration process. Approximating the derivative of  $R_i(c_i)$  as difference ratio results in the WEGSTEIN formula<sup>185</sup> :

$$c_i^{n+1} = c_i^n + \frac{(c_i^n - c_i^{n-1}) \cdot (R_i^n - c_i^n)}{(c_i^n - c_i^{n-1}) - (R_i^n - R_i^{n-1})} \quad (3.44)$$

which is a realisation of NEWTON's regula falsi and significantly accelerates and ensures convergence in extreme cases also. Here, a new estimate is calculated from two previous sets of concentrations and therefore one 'successive approximation' step is always necessary before entering the WEGSTEIN iteration.

The iteration cycle is stopped when the concentration of each sample component in subsequent refinement steps fulfils the convergence criterion :

$$\varepsilon \leq |c_i^{n+1} - c_i^n| \quad (3.45)$$

The convergence limit  $\varepsilon$  is usually set to  $10^{-5}$  corresponding to three significant digits in the mass percentage.

### 3.6 Analytical Sensitivity and Detection Limits

In electron probe microanalysis the primary beam only probes a very small volume of typically  $1-10 \mu\text{m}^3$ . Assuming a mean sample density of  $5-10 \text{ g/cm}^3$  this corresponds to a detected mass in the range of  $5-100 \text{ pg}$ . In contrast, sample areas of about  $1000 \mu\text{m}^2$  are illuminated in micro X-ray fluorescence analysis under favourable conditions. A depth of  $100-1000 \mu\text{m}$  is probed owing to the weaker interaction of X-rays with matter and therefore the detected mass is in the order of  $0.5-10 \mu\text{g}$ . This value significantly increases in

conventional X-ray fluorescence analysis where no elaborate beam focussing is available. In electron microprobe analysis, minimal detected masses are more than five orders of magnitude smaller than in X-ray fluorescence analysis.

The detection limit provides an estimate of the minimal detectable concentration  $c_{md}$  of an element in the probed mass of a multielement sample. The presence of an element in a sample is confirmed with a 99.7% level of confidence when the number of net counts  $N_{ij}$  collected in the corresponding characteristic X-ray emission line exceeds three times the standard deviation  $\sigma_{Bkg,ij}$  of the background under the peak. The net number  $N_{ij}$  of X-ray quanta recorded depends on the dead time corrected counting time  $\tau$  :

$$N_{ij} = I_{ij}\tau \quad (3.46)$$

The probability of detecting  $N_{ij}$  counts follows a GAUSSIAN distribution. With the actual concentration  $c_i$  and the number of counts  $N_{Bkg,ij}$  belonging to the background under the emission line of interest, the minimal detectable concentration  $c_{md}$  becomes :

$$\frac{c_{md}}{c_i} = \frac{N_{ij,min}}{N_{ij}} = \frac{3\sigma_{Bkg,ij}}{N_{ij}} = 3 \frac{\sqrt{N_{Bkg,ij}}}{N_{ij}} = 3 \frac{\sqrt{I_{Bkg,ij}}}{\sqrt{\tau} \cdot I_{ij}} = \frac{3}{\sqrt{I_{ij} \cdot \tau \cdot (S/B)_{ij}}} \quad (3.47)$$

where the signal-to-background ratio  $(S/B)_{ij}$  is defined according to :

$$(S/B)_{ij} = \frac{I_{ij}}{I_{Bkg,ij}} \quad (3.48)$$

An increase of measuring time is the only possibility to reduce the detection limit. This is useful only if long-term drift effects in the experimental set-up are negligible. Additionally, sample contamination sets a practical limit to the counting time in electron microprobe analysis. The number  $N_{ij}$  of detected net counts can be optimised by choosing an appropriate energy window  $\Delta E_{w,ij}$  for integration of the corresponding emission line. A small energy window results in a large statistical uncertainty, whereas the number of measured counts saturates for too wide integration boundaries and the background is overestimated. The optimal energy width has been shown to be<sup>19</sup> :

$$\Delta E_{w,ij} = 1.2 \cdot \Delta E_{fwhm} \quad (3.49)$$

Apart from the higher X-ray generation probability of light elements in the case of electron excitation, the amount of Bremsstrahlung generated increases with atomic number according to eq. 2.23. Therefore, detection limits are lower for light elements in electron microprobe analysis. In contrast, continuous contributions to the emission spectrum are almost entirely missing in X-ray fluorescence analysis resulting in significantly increased signal-to-background ratios and lower detection limits. Detection limits are decreasing with increasing atomic number in X-ray fluorescence analysis due to a higher probability of X-ray generation as is to be estimated from fluorescence yield and photoelectric cross-sections in Figure 2-2 and Figure 2-13.

The detection limit has to be distinguished from the analytical sensitivity defined as the minimal detectable difference of concentration  $\Delta c$ . As two recorded intensities are subject to the same distribution, the law of error propagation predicts that they are different on a 99.7% level if :

$$\begin{aligned} \frac{\Delta c}{c} &= \frac{(N_{2,ij} - N_{1,ij})_{\min}}{N} = \frac{\Delta N_{\min}}{N} = 3 \frac{\sqrt{\sigma_{1,ij}^2 + \sigma_{2,ij}^2}}{N} = 3 \frac{\sqrt{N_{1,ij} + N_{2,ij}}}{N} \\ &\approx \frac{3\sqrt{2}}{\sqrt{N}} = \frac{3\sqrt{2}}{\sqrt{I_{ij}\tau}} \end{aligned} \quad (3.50)$$

Here it is assumed that a similar number of counts  $N_{1,ij} \approx N_{2,ij} \approx N$  results from different measurements.



---

#### 4 Monte Carlo Simulation of X-Ray Emission Spectra

In the previous section, the basic principles of fundamental parameter approaches in X-ray fluorescence and electron microprobe analysis have been outlined. Theoretical X-ray intensities can be calculated with various degrees of sophistication depending on the models applied.

The correction of interelement effects in multicomponent samples remains a complex task. In X-ray fluorescence analysis, the geometry of the system and the spectral distribution of the impinging radiation have to be considered. In laboratory systems operated with X-ray tubes or radioisotope sources, the sample is usually not illuminated by a parallel beam but by a divergent bundle of rays. Incidence and take-off angles therefore cover a certain range and are usually substituted by mean values. Special care has to be taken in this fixed-angle approximation as a wrong choice of angles deteriorates the quality of analysis.<sup>132,186</sup>

Additionally, the excitation spectrum can only be represented by an effective wavelength or energy under appropriate operating conditions. Normally, the spectral output of the X-ray source has to be taken into account explicitly. In terms of the fundamental parameter approach, this necessitates summation over the whole range of excitation wavelengths or energies, respectively. Especially the correction of third order fluorescence effects with polychromatic excitation involves the numerical solution of tedious improper integrals, and no correction formulae are available for fluorescence effects higher than third order.

The geometry is less complex in electron microprobe analysis as a scanning or transmission electron microscope provides a virtually monochromatic and parallel electron beam with negligible lateral extension. X-rays originate from the electron diffusion area within the sample, which is small compared to the sample-detector distance. Therefore, the take-off angle of X-rays emerging towards the detector is constant in a very good approximation.

Standardless quantitative electron microprobe analysis can be performed either employing the ZAF or the  $\varphi(\rho z)$  correction scheme. Detailed knowledge of a number of phenomenological quantities for a sufficiently large set of experimental conditions likely to be encountered is a prerequisite for the application of both methods. For example, the backscatter coefficient and the spectral distribution of backscattered electrons enter the atomic number correction in the ZAF scheme. The  $\varphi(\rho z)$  correction method instead employs the depth distribution function of characteristic X-rays of any line occurring in the spectrum.

---

In this section, a probabilistic Monte Carlo model based on first principles will be proposed. This involves X-ray and electron single scattering and subsequent processes occurring with sample atoms as outlined in section 2.2. Algorithms are devised which produce the entire spectral response of multielement samples under X-ray and electron irradiation and with arbitrary system geometry.

#### 4.1 The Fundamental Computational Procedure

The probabilistic Monte Carlo method successively simulates individual physical processes, which are subject to statistical fluctuations. Single events are modelled by sampling randomly from an appropriate probability distribution function, thereby accurately representing the relative probability of every possible event. These functions are chosen from realistic physical models for the parameters under investigation.

The probability of an event  $X$  of a physical process characterised by a normalised probability density function  $f(u)$  defined in the interval  $[x_{\min}, x_{\max}]$  is determined by the cumulative probability distribution  $F(X)$  :

$$F(X) = \int_{x_{\min}}^X f(u)du \in [0,1] \text{ with } \int_{x_{\min}}^{x_{\max}} f(u)du = 1 \quad (4.1)$$

A probability  $F(X)$  is chosen by setting *eq. 4.1* equal to a random variable  $R \in ]0,1]$ , which is subject to another density function  $g(v)$  according to

$$F(X) = \int_{x_{\min}}^X f(u)du = \int_0^R g(v)dv = R \text{ with } \int_0^1 g(v)dv = 1 \quad (4.2)$$

Here, the integral over  $g(v)$  equals  $R$  when the random variable is sampled from a rectangular distribution :

$$g(R) = \begin{cases} 1 & \text{if } 0 < R \leq 1 \\ 0 & \text{else} \end{cases} \quad (4.3)$$

---

as implemented in the random number generator of computers. Consequently, the randomly sampled event  $X$  is obtained by :

$$X = F^{-1}(R) \quad (4.4)$$

The basic formalism of Monte Carlo simulations is outlined by *eqs. 4.2 and 4.4*. It consists of sampling an event  $X$  by evaluating the inverse cumulative probability distribution function  $F^{-1}$  at a randomly chosen position  $R$ .<sup>186</sup> Since Monte Carlo methods are statistical techniques, a single event or a sequence of statistically dependent events simulated will not be observed in practice. Statistically meaningful results are obtained only by successive application of the Monte Carlo algorithm. A sufficiently large number of typically  $10^3$  to  $10^6$  simulation runs has to be collected depending on the desired accuracy. Average values extracted from the ensemble of Monte Carlo runs are used to model observable quantities of the phenomenon under investigation. The necessity of a large number of repetitions makes Monte Carlo calculations notoriously time-consuming techniques. However, computational simplicity is obtained at the expense of computation time. As any quantity involved in the calculation can be easily traced, information is gained simultaneously on different phenomena of interest during one simulation. The efficiency of Monte Carlo techniques is significantly increased when applying variance reduction techniques resulting in higher accuracy with the same number of simulation runs. Variance reduction is performed by forcing an event to occur within boundaries which are favourable for a successful completion of the process. The restriction to a limited set of possible events for a given process is compensated by weighting this process with the corresponding probability for the event falling into the given interval. In other words, a weight factor of  $n^{-1} \in [0,1]$  is associated with a process rather than completing  $n$  unsuccessful simulation runs until finally the desired event occurs.<sup>187</sup> Thus, variance reduction is equivalent to defining 'fractional events' though there may be no physical meaning for justifying this procedure. In a sequence of statistically dependent processes, the corresponding weight takes the form of a sequential probability as all following events use the probability of the preceding one.

In contrast to fundamental parameter approaches, which are based on the evaluation of analytical expressions describing the X-ray intensity emitted from a sample, Monte Carlo methods focus on the accurate modelling of individual sample-photon interactions. For this

---

purpose, the propagation of individual photons in X-ray fluorescence analysis as well as of photons and electrons in electron microprobe analysis is simulated. Irrespective of the probe, the basic computational sequence is the same for both techniques. After a free-flight distance  $\Delta s_i$  along the direction  $(\Theta_i, \Phi_i)$  defined by the polar angle  $\Theta_i$  and the azimuthal angle  $\Phi_i$ , a change of direction occurs due to an interaction with an atom at a position  $\underline{r}_i = (x_i, y_i, z_i)^T$  in the sample. At the interaction point, the type of atom with which the interaction takes place as well as the type of interaction have to be selected randomly. As a result the direction of the probe relative to its present direction changes. This is described by an appropriate set of polar and azimuthal scattering angles  $(\theta_i, \varphi_i)$ . The new direction in the laboratory system is given by<sup>188,19</sup> :

$$\begin{pmatrix} \sin \Theta_{i+1} \cos \Phi_{i+1} \\ \sin \Theta_{i+1} \sin \Phi_{i+1} \\ \cos \Theta_{i+1} \end{pmatrix} = \begin{pmatrix} \cos \mathcal{G}_i \cos \varphi_i & -\sin \varphi_i & \sin \mathcal{G}_i \cos \varphi_i \\ \cos \mathcal{G}_i \sin \varphi_i & \cos \varphi_i & \sin \mathcal{G}_i \sin \varphi_i \\ -\sin \mathcal{G}_i & 0 & \cos \mathcal{G}_i \end{pmatrix} \cdot \begin{pmatrix} \sin \Theta_i \cos \Phi_i \\ \sin \Theta_i \sin \Phi_i \\ \cos \Theta_i \end{pmatrix} \quad (4.5)$$

Subsequently, the free-flight distance  $\Delta s_{i+1}$  is selected and the particle is guided to the new interaction point  $\underline{r}_{i+1} = (x_{i+1}, y_{i+1}, z_{i+1})^T$ , which is determined according to :

$$\underline{r}_{i+1} = \underline{r}_i + \Delta s_i \cdot \begin{pmatrix} \sin \Theta_{i+1} \cos \Phi_{i+1} \\ \sin \Theta_{i+1} \sin \Phi_{i+1} \\ \cos \Theta_{i+1} \end{pmatrix} \quad (4.6)$$

The geometry of scattering described by the above formulae is summarised in Figure 4-1.

#### 4.2 The Spectral Response of X-Ray Excited Samples

In a typical laboratory X-ray fluorescer system, a point source, for example the point of electron impact on the anode of an X-ray tube, is situated above the sample. It provides a cone illumination with a spectral distribution  $I_0(E)$  of unpolarised radiation. Without loss of generality, the X-ray source is placed in the xz-plane of the set-up, which is described with the centre of the illuminated sample area chosen as the origin in the laboratory coordinate system.

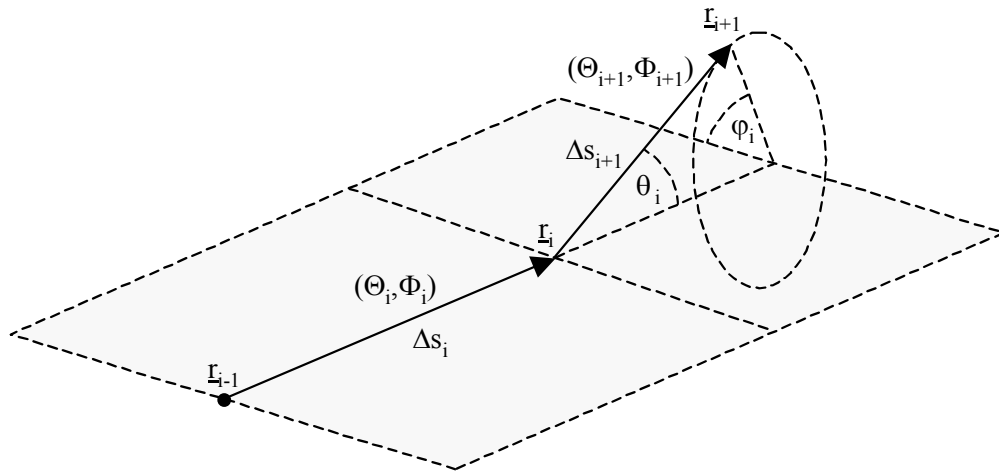


**Figure 4-1.** The basic computational element of a Monte Carlo simulation of photon and electron transport in matter. The probe is scattered at a position  $\mathbf{r}_i$  after a step  $\Delta s_i$ . After selection of the polar and azimuthal scattering angles  $\theta_i$  and  $\varphi_i$ , its new direction  $(\Theta_{i+1}, \Phi_{i+1})$  is calculated and with a step  $\Delta s_{i+1}$  the probe is guided to its new interaction point.

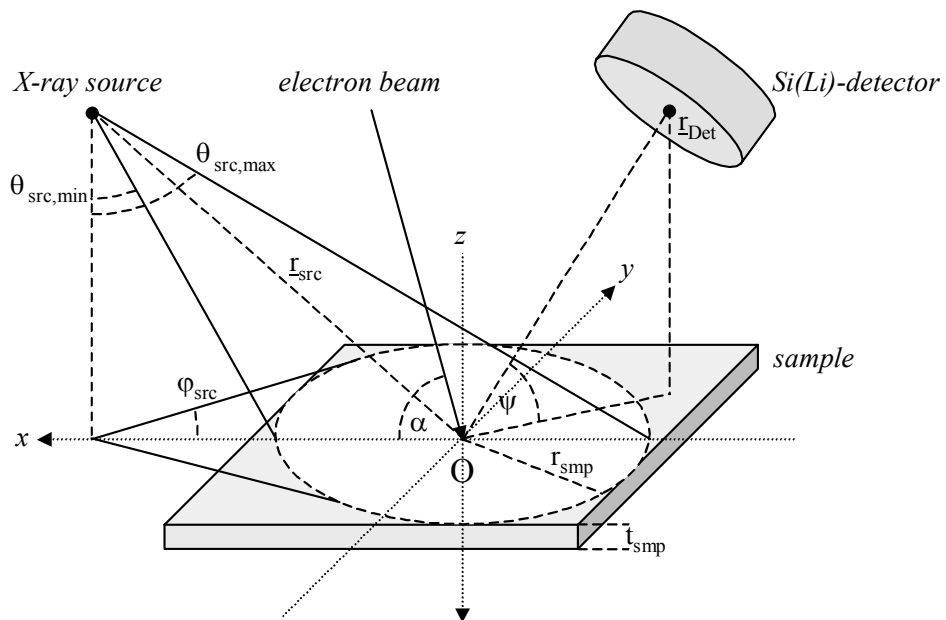


**Figure 4-2.** The basic geometry of an X-ray fluorescence and an electron microprobe set-up with a circular Si(Li) detector in the laboratory system. The origin is placed in the centre of the illuminated sample area and at the point of electron impact, respectively. Without loss of generality, the X-ray and electron sources are situated in the xz-plane of the system.

The sample is considered to be homogeneous with respect to composition  $\underline{c}$ , thickness  $t$ , and density  $\rho$ . X-rays emitted from the sample are guided to the detection unit characterised by the sample-detector centerline distance and the corresponding polar angles, as given by detector elevation and azimuth. Figure 4-2 depicts the geometric situation described and assumes the detection unit to be represented by a planar, circular detector. As Monte Carlo models yield the spectral response of the sample rather than the spectrum itself, other types of detection units can also be implemented.

This section outlines the Monte Carlo model employed to predict the entire spectral response of multicomponent samples under polychromatic X-ray irradiation. The present method partly adapts earlier approaches for radioisotope and synchrotron sources proposed by GARDNER et al.<sup>186,189-196</sup> and JANSSENS et al.<sup>187,188</sup>, respectively.

#### 4.2.1 X-Ray Source Emission

Under appropriate operating conditions, the contribution of the Bremsstrahlung background to the spectral output of an X-ray tube is negligible or eliminated by the use of filters and the excitation spectrum approximately consists of one or a few single discrete energies. In the latter case, an average excitation energy can be used by intensity averaging the contributions of each line. When this is not desirable, the need of a sampling algorithm to select the energy of X-ray photons incident on the sample arises. A line  $k$  out of a set of  $n_{exc}$  available excitation lines is selected when a random number is found to fulfil the condition :

$$\frac{\sum_{j=0}^k I_0(E_{ij})}{\sum_{j=0}^{n_{exc}} I_0(E_{ij})} < R \leq \frac{\sum_{j=0}^{k+1} I_0(E_{ij})}{\sum_{j=0}^{n_{exc}} I_0(E_{ij})} \text{ with } k + 1 \leq n_{exc} \quad (4.7)$$

where  $I_0(E_{ij})$  is the intensity of the excitation spectrum at the energy of characteristic line  $j$  emitted by the anode material  $i$  of an X-ray tube and  $R$  a rectangularly distributed random number. Usually only  $K$  lines are obtained from X-ray tubes as lines of lower energies are eliminated by self-absorption in the anode material. Rewriting *eq. 4.7* with a mean energy for the  $K\alpha$  line doublet results in the condition :

$$\text{if } \begin{cases} 0 < R \leq \frac{I_0(E_{iK_\alpha})}{I_0(E_{iK_\alpha}) + I_0(E_{iK_\beta})} & \Rightarrow E_0 \equiv E_{iK_\alpha} \\ \frac{I_0(E_{iK_\alpha})}{I_0(E_{iK_\alpha}) + I_0(E_{iK_\beta})} < R \leq 1 & \Rightarrow E_0 \equiv E_{iK_\beta} \end{cases} \quad (4.8)$$

which can be implemented in a single 'if'-condition.

Under conditions of polychromatic irradiation the incident photon energy is sampled from a known excitation spectrum  $I_0(E)$  extending over an energy range  $[E_{\min}, E_{\max}]$ . In this interval it exhibits some maximal intensity at point  $I_{0,pivot}(E_{pivot})$ . As an explicit value of the randomly distributed energy cannot be obtained in terms of a rectangularly distributed random variable, a rejection technique has to be used.<sup>190</sup> In a first step, an energy is chosen randomly from the range by setting :

$$E = E_{\min} + R \cdot (E_{\max} - E_{\min}) \quad (4.9)$$

In a second step, another random variable is generated and the selected value of the energy  $E$  is either accepted or rejected according to :

$$\text{if } I_0(E) \begin{cases} < R \cdot I_{0,pivot} : E_0 \equiv E \\ \geq R \cdot I_{0,pivot} : E \text{ rejected} \end{cases} \quad (4.10)$$

These two steps are performed repeatedly until a value of  $E_0$  is successfully chosen. Due to *eq. 4.10* the distribution of accepted values approximates the excitation spectrum  $I_0(E)$  after a large number of sampling processes. As the number of selected energies always exceeds that of accepted values, the efficiency of this procedure depends on the shape of the excitation spectrum.

Instead of randomly choosing a certain energy  $E$  out of the region of interest, a spectrum given as an array of intensity values  $I_{0,k}(E_k)$  in a number of discrete channels can be scanned in a stepwise manner. After selection of the energy  $E_k$  corresponding to channel  $k$  a statistical weight of :

$$P_{exc} = \frac{I_k(E_k)}{\sum_{k=1}^{channels} I_k(E_k)} \quad (4.11)$$

is attached to the photon and all its subsequent processes. The simulation is then continued with sampling from channel  $k+1$ . Though this may be advantageous in terms of variance reduction and sampling efficiency, the number of photons to be simulated is restricted to an integer multiple of the number of channels in the excitation spectrum.

The direction of the initial photon emitted from the X-ray source into a uniform cone is forced to occur with a directional angle  $\theta_{src} \in [\theta_{src,min}, \theta_{src,max}]$  and a rotational angle  $\varphi_{src}$ , which define the entrance point of an X-ray photon within the sample circle. The limitational directions are defined by :

$$\begin{aligned} \vartheta_{src,min} &= \arctan \frac{x_{src} - r_{src}}{z_{src}} \\ \vartheta_{src,max} &= \arctan \frac{x_{src} + r_{src}}{z_{src}} \end{aligned} \quad (4.12)$$

When the source is situated above the sample, as this is the case when  $x_{src} < r_{smp}$ , the minimal directional angle  $|\theta_{src,min}|$  falls into the range of interest  $[0, \theta_{src,max}]$ . Otherwise, angles below  $\theta_{src,min}$  are not desired and therefore the interval  $[\theta_{src,min}, \theta_{src,max}]$  has to be sampled as indicated in Figure 4-2. Within these boundaries,  $\theta_{src}$  is chosen by applying *eq. 4.2* and taking the necessity of normalisation into account :

$$\left. \begin{aligned} \frac{\int_0^{\vartheta_{src}} \sin \vartheta d\vartheta}{\int_0^{\vartheta_{src,max}} \sin \vartheta d\vartheta} = R \Leftrightarrow \cos \vartheta_{src} &= R \cdot (\cos \vartheta_{src,max} - 1) + 1, & \vartheta_{src,min} < 0 \\ \frac{\int_{\vartheta_{src,min}}^{\vartheta_{src}} \sin \vartheta d\vartheta}{\int_{\vartheta_{src,min}}^{\vartheta_{src,max}} \sin \vartheta d\vartheta} = R \Leftrightarrow \cos \vartheta_{src} &= R \cdot (\cos \vartheta_{src,min} - \cos \vartheta_{src,max}) + \cos \vartheta_{src,min}, & \vartheta_{src,min} \geq 0 \end{aligned} \right\} (4.13)$$

In terms of variance reduction, the associated statistical weight  $P_{src,\theta}$  for the random choice of the direction cosine  $\cos\theta_{src}$  is obtained by evaluating the probability of the emission falling into the desired interval :

$$P_{src,\vartheta} = \begin{cases} \frac{\int_0^{\vartheta_{src,max}} \sin \vartheta d\vartheta}{\int_0^{\pi} \sin \vartheta d\vartheta} = \frac{1}{2}(1 - \cos \vartheta_{src,max}), & \vartheta_{src,min} < 0 \\ \frac{\int_{\vartheta_{src,min}}^{\vartheta_{src,max}} \sin \vartheta d\vartheta}{\int_0^{\pi} \sin \vartheta d\vartheta} = \frac{1}{2}(\cos \vartheta_{src,min} - \cos \vartheta_{src,max}), & \vartheta_{src,min} \geq 0 \end{cases} \quad (4.14)$$

The rotational angle  $\varphi_{src}$  has to be selected in a way that the entrance point of the X-ray photon into the sample lies within a circle, which ends at the sample boundary defined by  $r_{smp}$ . This is the case if the rotational angle does not exceed :

$$\varphi_{max} = \begin{cases} \pi & \vartheta_{src} < \vartheta_{src,min}, x_{src} < r_{smp} \\ \arccos \frac{x_{src}^2 + z_{src}^2 \tan^2 \vartheta_{src} - r_{src}^2}{2x_{src}z_{src} \tan \vartheta_{src}} & \vartheta_{src,min} < \vartheta_{src} \leq \vartheta_{src,max} \end{cases} \quad (4.15)$$

The selection of  $\varphi_{src}$  from the interval  $[0, \varphi_{max}]$  is straightforwardly accomplished by setting :

$$\varphi_{src} = R \cdot \varphi_{max} \quad (4.16)$$

and attaching the statistical weight :

$$P_{src,\varphi} = \frac{\varphi_{max}}{\pi} \quad (4.17)$$

to the rotational angle in order to fulfil the requirements of variance reduction.<sup>189</sup>

### 4.2.2 Photon-Matter Interactions

A photon emitted from the X-ray source as outlined in the previous section is characterised by its direction and energy. The geometry of source emission determines the point of impact of the primary photon on the surface from where it is guided through the sample. Prior to an interaction, the photon travels along a straight path  $\Delta s$  as indicated in Figure 4-1. The length of this way is derived by integrating the LAMBERT-BEER law (eq. 2.5) to result in the probability distribution function according to eq. 4.2 :

$$\frac{\int_0^{\Delta s} e^{-\frac{s}{\lambda}} ds}{\int_0^{\infty} e^{-\frac{s}{\lambda}} ds} = 1 - e^{-\frac{\Delta s}{\lambda}} = R' \quad (4.18)$$

Considering that the mean free path length  $\lambda$  of a photon is connected to the mass absorption coefficient of the sample due to eq. 2.6 and therefore depends on its energy, eq. 4.18 is easily inverted to yield the desired path length :

$$\Delta s = -\lambda \ln(1 - R') = -\lambda \ln R = -\frac{\ln R}{\mu(E)\rho} \quad (4.19)$$

in terms of a variable  $R$ , which is distributed randomly as  $R'$ . At its new position given by eq. 4.6 the photon experiences an interaction with an atom. An appropriate criterion of finding an atom of type  $k$  is provided by the mass absorption coefficient the corresponding element contributes to the total mass absorption coefficient of the sample at the current photon energy. According to eq. 2.6, X-ray cross-sections are superposed in an additive manner. The selection of an element  $k+1$  with which the interaction takes place out of the set of  $n_i$  elements present in the sample is accomplished by finding a random number  $R$  for which

$$\sum_{i=0}^k \frac{c_i \mu_i(E)}{\mu(E)} < R \leq \sum_{i=0}^{k+1} \frac{c_i \mu_i(E)}{\mu(E)} \quad \text{with } k+1 \leq n_i \quad (4.20)$$

Photon-atom interactions either consist in the photoelectric effect, RAYLEIGH or COMPTON scattering, respectively. The relative probability of each of these three processes is given by the corresponding total cross-sections  $\tau$ ,  $\sigma_{\text{Ray}}$  and  $\sigma_{\text{Com}}$  of the element selected as introduced in eq. 2.7. It provides a criterion for random selection of the interaction type of an X-ray photon with energy  $E$  with an atom of element  $i$  selected before :

$$\left. \begin{aligned}
 0 < R \leq \frac{\tau_i(E)}{\mu_i(E)} & \quad \text{Photoelectric effect} \\
 \frac{\tau_i(E)}{\mu_i(E)} < R \leq \frac{\tau_i(E) + \sigma_{i,\text{Ray}}(E)}{\mu_i(E)} & \quad \text{Rayleigh scattering} \\
 \frac{\tau_i(E) + \sigma_{i,\text{Ray}}(E)}{\mu_i(E)} < R \leq \frac{\tau_i(E) + \sigma_{i,\text{Ray}}(E) + \sigma_{i,\text{Com}}(E)}{\mu_i(E)} = 1 & \quad \text{Compton scattering}
 \end{aligned} \right\} \quad (4.21)$$

In the energy range of interest, the photoelectric effect is the predominant interaction mechanism as demonstrated in Figure 2-4. Fundamental parameter methods therefore set  $\tau_i(E) \approx \mu_i(E)$  without introducing a significant numerical error. Monte Carlo simulations can also be carried out using this approximation to calculate the emitted X-ray intensity.<sup>189</sup> However, the prediction of the entire spectral response of a sample includes RAYLEIGH and COMPTON scattering, which constitute a significant contribution to X-ray fluorescence spectra of light elements. The correct modelling of multiple scattering and photoelectric interaction sequences of arbitrary complexity is one of the main advantages of Monte Carlo approaches over fundamental parameter methods.

#### 4.2.3 Modelling the Photoelectric Effect

In the photoelectric effect, the original X-ray photon is annihilated by transferring its energy and momentum to the atom of type  $i$  as selected due to eq. 4.20. The ejection of a fluorescent photon with energy  $E_{ij}$  of a certain line  $k$  is stimulated when a random number  $R$  is found, which falls into the interval limited by the emission probabilities of the various available characteristic lines  $n_j$  of the atom :

$$\sum_{j=0}^k \omega_{ij} \frac{\tau_{ij}(E)}{\mu_{ij}(E)} p_{ij} < R \leq \sum_{j=0}^{k+1} \omega_{ij} \frac{\tau_{ij}(E)}{\mu_{ij}(E)} p_{ij} \leq 1 \text{ with } k+1 \leq n_j \quad (4.22)$$

A new photon is generated at the interaction point and traced through the sample. In contrast to the selection procedures described above, the cumulative probabilities represented by the sums of eq. 4.22 do not sum up to unity for  $j = n_j$ . Therefore, a random number can be chosen which fails to select a characteristic line. This is attributed to a non-radiative relaxation of the atom and in this case a new photon trajectory has to be started from the source. Fluorescent X-rays are emitted isotropically from a core-shell ionised atom, which means that any initial direction  $(\Theta_0, \Phi_0)$  for the new photon can be chosen with equal probability :

$$\frac{\int_0^{\Theta} \sin \vartheta \, d\vartheta}{\int_0^{\pi} \sin \vartheta \, d\vartheta} = \frac{1 - \cos \Theta}{2} = R \Leftrightarrow \cos \Theta = 1 - 2R \quad (4.23)$$

$$\frac{\int_0^{\Phi} \frac{d\varphi}{2\pi}}{\int_0^{2\pi} \frac{d\varphi}{2\pi}} = R \Leftrightarrow \Phi = 2\pi R \quad (4.24)$$

The fluorescent photon originating from the interaction point is subsequently traced through the sample in the same manner as the primary radiation.

#### 4.2.4 *Modelling Photon Scattering*

In a scatter-type interaction, a photon is deflected relative towards its previous direction of movement through a polar and azimuthal scattering angle  $\theta$  and  $\varphi$ . An appropriate probability distribution function for the set  $(\theta, \varphi)$  of scattering angles is obtained by normalising the double differential cross-sections for RAYLEIGH and COMPTON scattering occurring with an atom  $i$  according to :

$$f_i(E, \vartheta, \varphi) \sin \vartheta \, d\vartheta \, d\varphi = \frac{\frac{\partial^2 \sigma_i(E, \vartheta, \varphi)}{\partial \vartheta \partial \varphi} \sin \vartheta \, d\vartheta \, d\varphi}{\int_0^\pi \int_0^{2\pi} \frac{\partial^2 \sigma_i(E, \vartheta, \varphi)}{\partial \vartheta \partial \varphi} \sin \vartheta \, d\vartheta \, d\varphi} = \frac{1}{\sigma_i(E)} \frac{\partial^2 \sigma_i(E, \vartheta, \varphi)}{d\vartheta \partial \varphi} \sin \vartheta \, d\vartheta \, d\varphi \quad (4.25)$$

in the most common case. Deflection of X-rays is caused by the electron shell of an atom, which is effectively of rotational symmetry. Therefore the double differential cross-sections are independent of the azimuthal angle  $\varphi$  for unpolarised radiation. The angle  $\varphi$  can be chosen at random in analogy to *eq. 4.26* for RAYLEIGH and COMPTON scattering alike :

$$\varphi = 2\pi R \quad (4.26)$$

Consequently, integration can be carried out to eliminate the azimuthal angle from *eq. 4.25* resulting in :

$$\begin{aligned} f_i(E, \vartheta) \sin \vartheta \, d\vartheta &= \frac{1}{\sigma_i(E)} \int_0^{2\pi} \left( \frac{\partial^2 \sigma_i(E, \vartheta, \varphi)}{\partial \vartheta \partial \varphi} \sin \vartheta \, d\vartheta \right) d\varphi \\ &= \frac{2\pi}{\sigma_i(E)} \frac{d\sigma_i(E, \vartheta)}{d\vartheta} \sin \vartheta \, d\vartheta \end{aligned} \quad (4.27)$$

which involves the differential RAYLEIGH cross-sections (*eq. 2.12*) in case of elastic and the differential COMPTON cross-sections (*eq. 2.13*) for inelastic scattering interactions. The shape of the surface defined by the probability distribution function  $f_i(E, \theta)$  is depicted exemplarily in Figure 4-3 for RAYLEIGH scattering of X-rays at a copper atom. The required cumulative probability distribution function  $F_i(E, \theta)$  is given by :

$$F_i(E, \vartheta) = \int_0^\vartheta f_i(E, \vartheta') \sin \vartheta' \, d\vartheta' = \frac{2\pi}{\sigma_i(E)} \int_0^\vartheta \frac{d\sigma_i(E, \vartheta')}{d\vartheta'} \sin \vartheta' \, d\vartheta' \quad (4.28)$$

As outlined in *eq. 4.4*, the inverse of  $F_i(E, \theta)$  has to be used to explicitly select a scattering angle on the basis of the differential cross-sections :

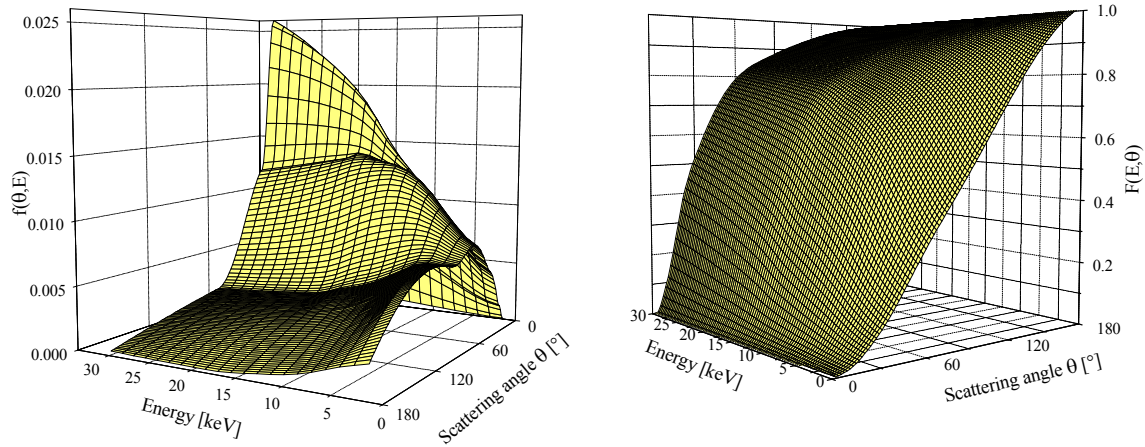


**Figure 4-3.** Probability distribution function  $f_{\text{Ray,Cu}}(E, \theta)$  for RAYLEIGH scattering of an X-ray photon by a copper atom.

**Figure 4-4.** Cumulative probability distribution function  $F_{\text{Ray,Cu}}(E, \theta)$  for RAYLEIGH scattering of an X-ray photon by a copper atom.

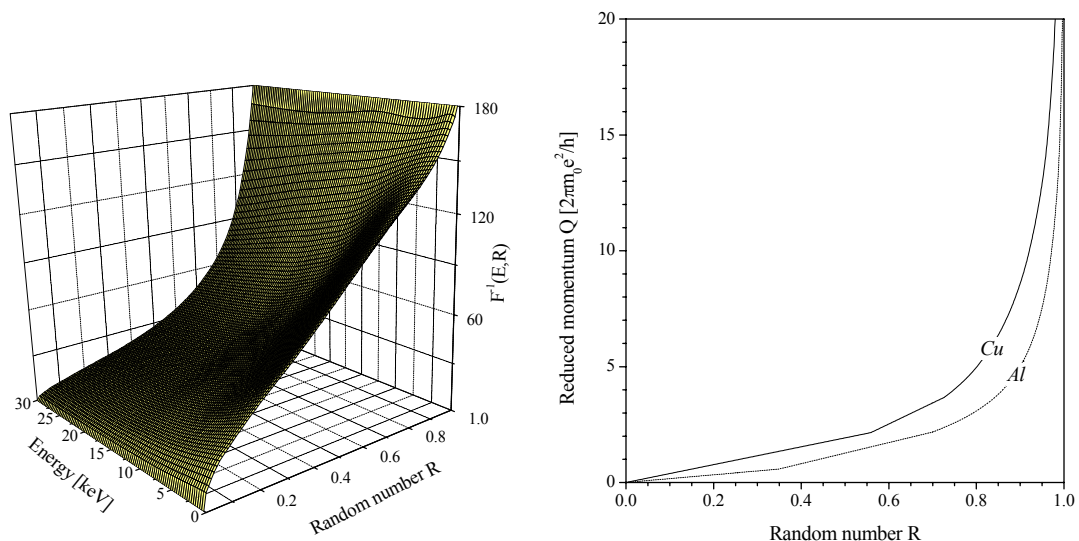


**Figure 4-5.** Inverse cumulative probability distribution function  $F^{-1}_{\text{Ray,Cu}}(E, R)$  for RAYLEIGH scattering of an X-ray photon by a copper atom. Polar scattering angles are sampled from this surface. Analogous datasets exist to describe COMPTON scattering in the same manner.

**Figure 4-6.** Inverse cumulative probability distribution  $Q(R)$  of the momentum of bound electrons ('COMPTON profile', see also Figure 2-7) in aluminium and copper. Momentum values are sampled from these functions to describe the DOPPLER broadening of COMPTON scatter lines in X-ray fluorescence spectra.

$$F_i(E, \mathcal{G}) = R \Leftrightarrow \mathcal{G} = F_i^{-1}(E, R) \quad (4.29)$$

Inversion of *eq. 4.29* is not straightforward since in the computational practice the dependence of  $F_i(E, \theta)$  on both scattering angle and photon energy is established numerically. Fits to the cumulative probability distribution function and its inverse are available from the literature as bicubic spline representations based on measurements of the differential X-ray cross-sections.<sup>197</sup> The functions  $F_i(E, \theta)$  and  $F_i^{-1}(E, R)$  as derived from the normalised differential cross-sections shown in Figure 4-3 are displayed in Figure 4-4 and Figure 4-5, respectively.

A scattering event is modelled by selecting the azimuthal and polar angles  $\varphi$  and  $\theta$ , respectively, from *eq. 4.26* and *4.29*. The energy of the photon is preserved and the trajectory is continued by finding a new step length  $\Delta s$  and its new position according to *eq. 4.6* and *4.19*, when RAYLEIGH scattering takes place. In contrast, COMPTON scattering is accompanied by an energy change of the photon, which has to be taken into account prior to continuing its trajectory. The energy change depends on the polar angle and the momentum transfer  $p_z$  between photon and bound electron as outlined in *eq. 2.15*. In order to correctly model the DOPPLER broadening of inelastically scattered photons, values of the reduced momentum  $Q$  are sampled from the COMPTON profile  $J_i(Q)$ . The functions  $J_i(Q)$  are not known analytically. Therefore, numerical inversion of the tabulated<sup>57</sup> values following normalisation and integration results in :

$$F_i(Q) = \frac{\int_0^Q J_i(Q') dQ'}{\int_0^\infty J_i(Q') dQ'} = R \Leftrightarrow Q = F_i^{-1}(R) \quad (4.30)$$

In this way, the reduced momentum  $Q$  is drawn randomly from the COMPTON profile  $J_i(Q)$  to calculate the new energy of a photon scattered inelastically through an angle  $\theta$  by a bound electron of atom  $i$  according to *eq. 4.30*. The use of rejection techniques for direct sampling of  $Q$  from the corresponding distribution function  $J_i(Q)$  is abandoned due to its inefficiency. The result of the conversion of  $J_i(Q)$  of aluminium and copper as displayed in Figure 2-7 into the related inverse cumulative probability distribution function is shown in Figure 4-6.

#### 4.2.5 *Probabilistic Interpretation of X-Ray Emission*

In X-ray fluorescence and electron microprobe analysis, only a very small fraction of the radiation emerging from the sample hits the detector. For example, a 10 mm<sup>2</sup> X-ray detector located at a distance of 50 mm from the sample surface subtends a solid angle of  $\Omega_{\text{det}} \approx 0.0003$ . According to the geometric collection efficiency, only approximately 0.03 % of isotropically emitted characteristic photons are directed to finally impinge onto the detector. As Monte Carlo methods are designed to simulate the movement of X-rays through matter, they are subject to the same statistical considerations. A simulation routine that rigorously processes photon trajectories irrespective of whether they finally end on the detector surface or not is therefore extremely ineffective. It is therefore more convenient not to count successfully detected photons but to record the detection probability of every photon interacting with the sample.

In practice, the energy distribution of the photon count rates constitutes the X-ray emission spectrum, which is stored as an array of integer numbers in a multichannel analyser memory. Unlike in the experiment, the Monte Carlo simulated X-ray response of a sample is understood as energy distribution of photon detection probabilities, which can be thought of as 'fractional photons'.<sup>187,198</sup> The spectrum is therefore represented by an array of real numbers simulating the multichannel analyser memory.

During a Monte Carlo simulation run, the probability of a photon arriving at the detector is calculated at each interaction point without terminating its trajectory. The photon impinges onto the detector surface with a probability which is composed of the sequential probability of the photon being scattered into the solid angle of detection and the escape probability of the photon reaching the detector without further interaction in the sample :

$$P_{\text{det}}(E) = P_{\text{dir}}(E, \mathcal{G}) \cdot P_{\text{esc}}(E, r_{\text{esc}}) \quad (4.31)$$

This resulting weight factor is sorted into the appropriate channel of the virtual multichannel analyser memory according to *eq. 3.29*.  $P_{\text{det}}(E)$  describes the contribution of a photon to the inherently unmeasurable spectral response of the sample impinging onto the detector. Signal processing is considered separately and will be described later.

Irrespective of the interaction type experienced, the escape probability of the photon is determined by the path length  $r_{\text{esc}}$  it travels through matter before leaving the sample towards

the detector. This distance is calculated trigonometrically by randomly choosing a point of incidence on the detector surface. Recalling the LAMBERT-BEER law (eq. 2.5) gives :

$$P_{esc}(E, r_{esc}) = e^{-\mu(E)\rho r_{esc}} \quad (4.32)$$

When a photon is emitted isotropically in the photoelectric effect, its directional probability of travelling towards the detector depends on the area of the detector  $A_{det}$  and its distance from the sample  $r_{det}$  according to :

$$P_{dir}^{photo} = \frac{\Omega_{det}}{4\pi} = \frac{A_{det}}{4\pi r_{det}^2} \quad (4.33)$$

which equals the geometric detection efficiency. After a scattering event, the double differential cross-sections describe the probability of the photon turning into the correct direction to hit the detector. For unpolarised radiation, the cross-sections are independent of the azimuthal angle, which is therefore only limited by the solid angle of detection. Thus the directional probability becomes :

$$P_{dir}^{scatter}(E, \vartheta) = \frac{\Omega}{\sigma_i(E)} \cdot \int_0^{2\pi} \frac{\partial^2 \sigma_i(E, \vartheta, \varphi)}{\partial \vartheta \partial \varphi} d\varphi = \Omega \frac{2\pi}{\sigma_i(E)} \cdot \frac{d\sigma_i(E, \vartheta)}{d\vartheta} \quad (4.34)$$

The detector subtends a solid angle which also allows the photon to hit it within a range of polar angles  $[\vartheta_{min}, \vartheta_{max}]$ . Employing the definition of the cumulative probability distribution yields the directional probability in the case of a scattering event<sup>193</sup> :

$$\begin{aligned} P_{dir}^{scatter}(E, \vartheta_{min}, \vartheta_{max}) &= \Omega \frac{2\pi}{\sigma_i(E)} \int_{\vartheta_{min}}^{\vartheta_{max}} \frac{d\sigma_i(E, \vartheta)}{d\vartheta} d\vartheta \\ &= \Omega \frac{2\pi}{\sigma_i(E)} \cdot \left[ \int_0^{\vartheta_{max}} \frac{d\sigma_i(E, \vartheta)}{d\vartheta} d\vartheta - \int_0^{\vartheta_{min}} \frac{d\sigma_i(E, \vartheta)}{d\vartheta} d\vartheta \right] \\ &= \Omega \cdot [F_i(\vartheta_{max}) - F_i(\vartheta_{min})] \end{aligned} \quad (4.35)$$

A detailed discussion on refined algorithms for the computation of particle scattering probabilities into finite detectors is provided in the literature.<sup>199,200</sup> A schematic overview of the Monte Carlo algorithm proposed in this section is presented in the flow diagram Figure 9-1 in section 9.1.

#### 4.3 The Spectral Response of Electron Excited Samples

Correct modelling of electron-matter interactions is a prerequisite to the theoretical prediction of the X-ray response of a sample under the conditions of electron microprobe analysis. The propagation of electrons through matter can be understood as a diffusion process. An extensive discussion on the use of transport equations to describe this process has been provided by THÜMMEL.<sup>94</sup> However, analytical solutions are only obtained by introducing simplifications, which limit the accuracy of results from transport theory. On the other hand, Monte Carlo methods have received considerable interest in modelling diffusion phenomena ever since electronic computation facilities are available. In the simulation of electron diffusion, the main advantage of Monte Carlo techniques over transport theory is their high accuracy and their capability of providing a huge amount of information simultaneously during one simulation run. Energy and angular distribution of secondary, backscattered and transmitted electrons as well as depth distribution of energy deposition and X-ray generation have been investigated. In this context, Monte Carlo calculations have also been designed to obtain databases for the ZAF and the  $\phi(\rho z)$  matrix correction procedure in quantitative electron microprobe analysis.

Electrons gradually lose their energy on their way through matter. Therefore, the number of scattering acts experienced by an electron until it has lost its entire kinetic energy is typically 1000 to 4000. With a number of typically  $10^5$  electron trajectories to be simulated to gain statistical significance, this corresponds to simulating and keeping track of  $1 \cdot 10^8$  to  $4 \cdot 10^8$  individual scattering acts depending on composition and primary beam energy. This requires a large computation time which also differs from sample to sample. An approach to the Monte Carlo simulation of successive electron-photon showers has only been reported in the recent years.<sup>76,201-204</sup> Solution of the inverse problem, retrieval of the concentrations from the X-ray intensities, was not reported.

---

In this section, a different procedure to simulate the entire spectral response of electron excited samples is proposed. For this purpose, the principles of X-ray fluorescence as described in the previous section are readily incorporated in a Monte Carlo algorithm for electron diffusion. The use of variance reduction is beneficial to keep the computational effort as low as possible.

#### 4.3.1 Electron Diffusion

In electron probe microanalysis, an electron beam with a primary energy  $E_0$  is impinging onto a sample under a certain angle of incidence as illustrated in Figure 4-2. Assuming a point-like probe is justified as the extension of the electron diffusion volume by far exceeds the probe size. The beam aperture can also be neglected under the conditions commonly encountered in microanalysis. However, this does not mean a loss of generality as a probe of finite size can be easily implemented by modelling a GAUSSIAN or any other beam shape when desired.

Inelastic scattering does virtually not change the electron direction. Therefore, the mean free path length  $\lambda$  an electron travels between two scattering acts is determined by the total elastic cross-section of the sample in analogy to *eq. 4.19*<sup>61,65</sup> :

$$\Delta s = -\lambda \ln R = -\frac{\ln R}{\rho \sigma_{el}(E)} \quad (4.36)$$

where  $\sigma_{el}(E)$  is obtained from *eq. 2.32* and either represents total RUTHERFORD or MOTT cross-sections. After travelling the distance  $\Delta s$ , the electron is found at a new position  $\underline{r}_{i+1}$  given by *eq. 4.6*. According to BETHE's continuous loss approximation (*eq. 2.36*), the mean energy loss along its path  $\Delta s$  is given by :

$$\Delta E_{mean} = \left( \frac{dE_{mean}}{ds} \right) \cdot \rho \Delta s \quad (4.37)$$

which is justified since the mean free path length  $\lambda$  is in the order of a few nanometres and the electron probes a large number of atoms along  $\Delta s$ . Through the mean ionisation potential of the sample as defined in *eq. 2.37*, every possible inelastic interaction of the electron

contributes to this value. Consequently, the electron arrives at its next interaction point  $\underline{r}_{i+1}$  with an energy of :

$$E(r_{i+1}) = E(r_i) + \Delta E_{mean}(\Delta s) \quad (4.38)$$

Here, an atom of type  $k+1$  is selected out of the number  $n_i$  of sample elements using the total electron cross-section by finding a random number  $R$  such that :

$$\sum_{i=0}^k \frac{c_i \sigma_{tot,i}(E)}{\sigma_{tot}(E)} < R \leq \sum_{i=0}^{k+1} \frac{c_i \sigma_{tot,i}(E)}{\sigma_{tot}(E)} \text{ with } k+1 \leq n_i \quad (4.39)$$

which is analogous to the corresponding selection procedure for X-ray fluorescence analysis (eq. 4.20). In interacting with the sample atom the electron is deflected from its original direction by scattering. The azimuthal scattering can be chosen at random by eq. 4.26. In contrast, the normalised cumulative probability distribution function for the polar angle of collision employs the differential elastic electron cross-sections :

$$F_i(E, \vartheta) = \frac{\int_0^{\vartheta} \frac{d\sigma_{el,i}(E, \vartheta')}{d\vartheta'} d\vartheta'}{\int_0^{\pi} \frac{d\sigma_{el,i}(E, \vartheta')}{d\vartheta'} d\vartheta'} = \frac{\int_0^{\vartheta} \frac{d\sigma_{el,i}(E, \vartheta')}{d\vartheta'} d\vartheta'}{\sigma_{el,i}(E)} = R \quad (4.40)$$

Using the differential RUTHERFORD cross-section as given in eq. 2.17, this expression is evaluated and inverted analytically resulting in<sup>205</sup> :

$$F_i^{-1}(E, R) = \cos \vartheta = \frac{2\alpha R}{1 + \alpha - R} \quad (4.41)$$

with the screening parameter  $\alpha$  as described in eq. 2.18. When the cross-sections are taken from the MOTT theory, eq. 4.40 has to be solved numerically as no analytical solution exists in this case. However, JOY et al. have demonstrated that eq. 4.41 remains valid for the use with MOTT cross-sections with an appropriate numerical adjustment of  $R$  and  $\alpha$ , which also includes a correction to account for inelastic scattering events.<sup>205</sup>

After being scattered, the electron is guided to its next interaction site by means of *eq. 4.6* and continues to interact with the sample according to the principles outlined above. A trajectory is finished when the electron energy falls below a critical cut-off value or the electron exits the sample. The energy threshold for termination of the trajectory depends on the range of validity of the database but is typically in the order of 20-50 eV. Electrons leaving the sample are considered backscattered or transmitted, depending on whether they emerge into the upper or lower half-sphere. By sorting backscattered and transmitted electrons according to their energy, backscatter spectra and electron energy loss spectra are obtained in the simulation. The procedure of simulating electron diffusion is summarised in the flow diagram Figure 9-2 presented in section 9.1.

#### 4.3.2 Implementation of X-Ray Emission

Electrons are guided through the sample in a stepwise manner by a typical Monte Carlo algorithm. At the end of each path segment, an atom *i* is situated which acts as scatterer for an electron arriving with energy  $E(\underline{r})$ . The incorporation of X-ray emission in this algorithm requires the probability for the generation of either a characteristic or a Bremsstrahlung photon connected for each interaction along the electron trajectory to be known.

Characteristic X-ray photons are generated by relaxation of atoms ionised in an inner shell by electron impact. The ionisation probability  $P_{ion,ij}$  of shell *j* of an atom *i* is obtained by combining the probability of an inelastic interaction,  $P_{inel}$ , and of the inelastic event consisting in an inner-shell ionisation  $P_{ij}$  in a sequential manner :

$$P_{ion,ij}(E) = P_{inel}(E) \cdot P_{ij}(E) = \frac{\sigma_{inel}(E)}{\sigma_{tot}(E)} \cdot \frac{\sigma_{ij}(E)}{\sigma_{inel}(E)} = \frac{\sigma_{ij}(E)}{\sigma_{tot}(E)} \quad (4.42)$$

Inner-shell ionisation cross-sections  $\sigma_{ij}(E)$  are readily available with good accuracy from the semi-empirical treatment of GRZYNSKI given in *eq. 2.33*. Total electron cross-sections are assessed numerically via *eq. 2.31* and *2.32* either using elastic RUTHERFORD or MOTT cross-sections of *eq. 2.19* and *2.22*, respectively. Due to their energy dependence, the ionisation probability is implicitly coupled to the electron path. As pointed out in connection with Figure

2-13, the ionisation of an inner shell is a very unlikely event with a probability of  $P_{ion,ij}$  in the order of typically  $10^{-5}$  to  $10^{-6}$ , depending on the sample composition.

Emission of a Bremsstrahlung photon occurs with an even lower probability. KRAMERS's description *eq. 2.23* predicts that the cross-section for generation of continuous X-rays depends on the energy  $E_X$  of the emitted Bremsstrahlung photon. Therefore, the energy  $E_X$  has to be selected randomly prior to calculating the corresponding emission probability. A normalised cumulative probability distribution function for the emission of a Bremsstrahlung photon with energy  $E_X$  from an atom with nuclear charge  $Z$  caused by an electron of energy  $E$  is obtained from the interval  $[E_{min}, E_0]$  by means of *eq. 4.2* :

$$\frac{\int_{E_{min}}^{E_X} \frac{a_K}{E'_X} \cdot \frac{Z^2 m_e c^2}{2E} dE'_X}{\int_{E_{min}}^{E_0} \frac{a_K}{E'_X} \cdot \frac{Z^2 m_e c^2}{2E} dE'_X} = \frac{\int_{E_{min}}^{E_X} \frac{dE'_X}{E'_X} \ln \frac{E_X}{E_{min}}}{\int_{E_{min}}^{E_0} \frac{dE'_X}{E'_X} \ln \frac{E_0}{E_{min}}} = R \quad (4.43)$$

This expression is easily inverted to result in the desired randomly chosen Bremsstrahlung energy  $E_X$  :

$$E_X = E_0^R \cdot E_{min}^{(1-R)} \quad (4.44)$$

A Bremsstrahlung photon with energy  $E_X$  is consequently ejected in the interaction between electron and sample atom with the probability

$$P_{brake}(E) = \frac{\int_{E_{min}}^{E_X} \frac{a_K}{E'_X} \cdot \frac{Z^2 m_e c^2}{2E} dE'_X}{\sigma_{tot}(E)} = \frac{a_K}{\sigma_{tot}(E)} \frac{Z^2 m_e c^2}{2E} \ln \frac{E_X}{E_{min}} \quad (4.45)$$

which depends on the nuclear charge of the atom involved but is typically three orders of magnitude lower than the probability of characteristic emissions.

An atom of type  $i$  is selected to interact with an electron, which is guided to a new interaction site  $\underline{i}_{i+1}$ . Implementation of X-ray emission is accomplished by forcing an photon of each characteristic line of interest with energy  $E_{ij}$  and a Bremsstrahlung photon to occur. Before

proceeding to the next electron path segment, the trajectory of each of these photons is traced using the procedure outlined in the previous section. In contrast to the simulation of X-ray induced spectra, modelling the emission of an external source can be omitted here as the origin of X-rays is now solely located within the sample.

Characteristic and Bremsstrahlung photons are simulated to be emitted isotropically by application of *eqs. 4.23 and 4.24*. Though not exactly true in the case of Bremsstrahlung as discussed in section 2.2.1, this is a good approximation as the randomisation of the directions of electron movement has a strong averaging effect on the anisotropy of Bremsstrahlung emission. In this respect further inaccuracies are introduced by the KRAMERS constant  $a_K$ , which is not strictly constant but varies slowly and continuously with both energy and atomic number. Deviations from the constant value of  $a_K$  are more pronounced for light elements at low X-ray energies.

In order to comply with the principle of variance reduction, a statistical weight of :

$$P_{char}^{photon}(E) = \omega_{ij} P_{ion,ij}(E) \quad (4.46)$$

is attached to each characteristic photon trajectory started at the present electron position to account for both, the probability of ionisation and subsequent emission of an X-ray photon rather than an AUGER electron. Since no alternative process exists in the case of Bremsstrahlung the emission probability is adequately represented by :

$$P_{brake}^{photon}(E) = P_{brake}(E) \quad (4.47)$$

In the common model adopted here to simulate electron diffusion, all possible energy loss mechanisms are already included in the continuous loss approximation via the mean ionisation potential of the sample. Therefore, the calculation of electron energy loss by excitation of emission of characteristic and Bremsstrahlung photons is not required at this point. The procedure of simulating photon trajectories in the case of electron excitation of the emission spectrum is summarised in the flow diagram Figure 9-3 depicted in section 9.1.

#### 4.4 Processing of Simulation Data

The simulation algorithms proposed in the previous section predict the spectral distribution of fluorescent X-rays from electron and X-ray excited samples before its processing by the detector. Simulated spectra are obtained by imposing the detection characteristics as given by detection efficiency and resolution upon the calculated spectral response. Subsequently, theoretical and measured spectra are scaled to each other for the purpose of direct comparison, as for example in standardless quantitative analysis.

##### 4.4.1 Conversion of Simulation Data into Spectra

Due to the detection process, a monochromatic X-ray line becomes GAUSSIAN in shape irrespective of the type of device involved. In the absence of artifacts, for example shelf effects, the contribution of an X-ray line at energy  $E'$  to the intensity at another energy  $E$  in the spectrum is described by a normalised GAUSSIAN spreading function  $G(E'-E, \Delta E')$ . It has to be taken into account that the X-ray photon only generates a signal with a probability given by the detection efficiency  $\varepsilon(E)$  :

$$\varepsilon(E)G(E' - E, \Delta E') = \frac{\varepsilon(E)}{\sqrt{2\pi}\Delta E'(E')} e^{-\frac{(E'-E)^2}{2\Delta E'(E')^2}} \quad (4.48)$$

The full width at half maximum of an X-ray line, which has been introduced as a measure of detector resolution in *eq. 3.30*, is related to the standard deviation of the GAUSSIAN spreading function according to :

$$\Delta E'(E') = \frac{\Delta E'_{fwhm}(E')}{\sqrt{8 \ln 2}} \quad (4.49)$$

In the spectral distribution  $I(E')$  of X-rays, each energy  $E'$  is the centre of a GAUSSIAN distribution and adds a weight to the signal at any energy  $E$  which is given by *eq. 4.48*. Therefore, the spectrum  $S(E)$  is obtained by integration over the energy range covered by the detector :

$$\begin{aligned}
S(E) &= \varepsilon(E) \cdot \int_0^{E_{\max}} I(E') G(E' - E, \Delta E') dE' = \frac{\varepsilon(E)}{\sqrt{2\pi}} \cdot \int_0^{E_{\max}} \frac{I(E')}{\Delta E'(E')} e^{-\frac{(E'-E)^2}{2\Delta E'(E')^2}} dE' \quad (4.50) \\
&= \varepsilon(E) \cdot I(E') * G(E', \Delta E')
\end{aligned}$$

which is just the convolution of the intensity distribution  $I(E')$  with the GAUSSIAN spreading function, multiplied by the detection efficiency. In practice, the spectral X-ray distribution is not a continuous function but obtained as an array of count rate versus channel number. Therefore, the spreading function is expressed in terms of channel numbers :

$$\varepsilon(i) \cdot G(k - i, \Delta k) = \frac{\varepsilon(i)}{\sqrt{2\pi} \Delta k(k)} e^{-\frac{(k-i)^2}{2\Delta k(k)^2}} \quad (4.51)$$

for a GAUSSIAN peak centred at channel  $k$ . The energy gain of the detector is used to obtain the peak width in units of channels :

$$\Delta k(k) = \frac{\Delta E_{fwhm}(E)}{\Delta E_{gain} \cdot \sqrt{8 \ln 2}} \quad (4.52)$$

For practical purposes, the intensity distribution is convoluted with the spreading function on a discrete dataset by replacing integration by summation over all channels  $n_{ch}$

$$\begin{aligned}
S(i) &= \varepsilon(i) \cdot \sum_{k=1}^{n_{ch}} I(k) G(k - i, \Delta k) = \frac{\varepsilon(i)}{\sqrt{2\pi}} \sum_{k=1}^{n_{ch}} \frac{I(k)}{\Delta k(k)} e^{-\frac{(k-i)^2}{2\Delta k(k)^2}} \quad (4.53) \\
&= \varepsilon(i) \cdot I(k) * G(k)
\end{aligned}$$

and results in the discrete representation of the spectrum  $S(i)$ .

#### 4.4.2 *Comparison of Experimental and Simulated Data*

Due to the application of variance reduction, it is hardly ever possible nor necessary to simulate spectra until the total theoretical intensity matches that of an experimental spectrum. Therefore, simulations  $S_{calc}(E)$  have to be scaled to experimentally determined data  $S_{meas}(E)$  for direct comparison. The best fit of simulated to measured spectra is obtained by adjusting the total intensities by multiplying  $S_{calc}(i)$  with a scale factor in the energy range of interest (ROI) in a way that :

$$\frac{\int_{ROI} S_{meas}(E)dE}{\int_{ROI} S_{calc}(E)dE} = f_{scale} = \frac{\sum_{ROI} S_{meas}(i)}{\sum_{ROI} S_{calc}(i)} \quad (4.54)$$

without changing the relative intensities. An appropriate figure of merit describing the quality of the resulting fit is obtained by calculating  $\chi^2$  according to<sup>186,193,206</sup> :

$$\chi^2 = \frac{1}{n_{ROI}} \sum_{ROI} \frac{[S_{meas}(i) - S_{calc}(i)]^2}{S_{calc}(i)} \quad (4.55)$$

where  $n_{ROI}$  is the number of channels comprising the region of interest. In the case of a solid-state semiconductor device, for example a Si(Li) detector, a linear relation between energy and channel number exists as outlined in *eq. 3.29*. Also, the detection efficiency and the energy dependence of resolution are well defined quantities, which are readily available applying *eq. 3.33* and *3.34*. Modified GAUSSIAN functions to describe the peak form of energy dispersive X-ray detectors in order to model artifacts are discussed in the literature.<sup>181,207</sup>

Spectrometer calibration is more complex for wavelength dispersive systems. For example, the reflectivity of the crystal has to be known exactly, and its size has a strong effect on the resolution of the system, which can vary by over one order of magnitude in the range of BRAGG angles of interest. Generally, calibration data of wavelength dispersive systems depend on the spectrometer geometry and cannot be used universally by adjusting only a few parameters as in the case of an energy dispersive system. A general discussion on the properties of wavelength dispersive systems is provided by REED<sup>58</sup>, and data on detection efficiencies and resolution of specific set-ups are reported exemplarily in the literature.<sup>175</sup>

#### 4.5 Conclusions

A Monte Carlo algorithm to simulate the entire spectral response of X-ray and electron excited homogeneous multielement samples is devised. Apart from instrumental parameters, the procedures are based on atomic properties, such as cross-sections of X-ray and electron-matter interactions. In contrast to fundamental parameter methods the use of integral quantities, for example backscatter coefficients, is not required. X-ray scattering as encountered in X-ray fluorescence analysis and Bremsstrahlung continuum occurring in electron microprobe analysis are included in the simulation routine.

---



---

## 5 X-Ray Fluorescence Analysis in the Scanning Electron Microscope

Due to the different probe-matter interactions as discussed in the previous section, X-ray fluorescence and electron microprobe analysis are complementary techniques. As outlined in section 1.1, very low absolute masses are detected in electron microprobe analysis. Here, minimum detectable concentrations are confined to the upper ppm range as signal-to-background ratios are inevitably limited by the Bremsstrahlung background, which extends over the whole energy range. Characteristic X-rays are produced more efficiently from light elements due to larger core-shell ionisation cross-section for electrons as displayed in Figure 2-13. Apart from the particular detector characteristics, electron probe microanalysis is therefore more sensitive towards light elements. X-ray fluorescence analysis will favour heavier elements, as fluorescence yields increase with atomic number (see Figure 2-2). The background is mainly determined by inelastic scattering of source radiation. It is therefore restricted to the high-energy part of the spectrum, which results in increased signal-to-background ratios leading to detection limits in the low ppm regime.

### 5.1 Lowering the Detection Limits in the Scanning Electron Microscope

Together with the possibility of investigating non-conductive samples, these properties make X-ray fluorescence analysis an interesting supplementary technique to enhance the analytical capabilities of an electron microscope at the expense of lateral resolution. It has already been noticed earlier that the focussed beam of a scanning electron microscope can be employed to generate X-rays for X-ray fluorescence analysis instead of directly exciting a sample. In the past, a number of experimental set-ups have been proposed making use of this principle. GOULD and HEALEY demonstrated that a simple X-ray source is obtained by focussing the electron beam into a depression at the base of a massive metal rod serving as 'anode' taking the form of a truncated cylinder.<sup>208</sup> The sample, which is mounted on the same specimen stage and positioned to face the point of electron impact, is thus illuminated by X-rays. However, spectra recorded with this arrangement still exhibit Bremsstrahlung background, which means that the sample is also excited by backscattered electrons from the X-ray source. Therefore, signal-to-background ratios are only moderately increased.

A closed massive anode set-up was presented by ECKERT, who provided a housing for the anode, into which the electron beam enters through a narrow hole.<sup>209</sup> X-rays are emitted

---

towards the sample through a side window closed by thin metal or metallised polymer filter foils serving as an absorber for backscattered and stray electrons as well as low energy Bremsstrahlung. This configuration basically transfers the operation principle of a conventional side-window X-ray tube to the scanning electron microscope. Optimisation of the filter thickness by measuring the current across the foil in order to completely eliminate electron excitation is also reported for several anode/filter combinations and various primary beam energies. With a molybdenum anode, a 50  $\mu\text{m}$  molybdenum filter foil and probe currents as high as 20  $\mu\text{A}$  at a primary beam energy of 35 keV, detection limits of about 4 ppm arsenic in silicon were obtained within an acquisition time of 20 min irradiating a sample area of approximately 1  $\text{cm}^2$ .

A transmission type end-window X-ray tube is simulated when thin metal sheets are used as sources to excite the sample. The target thickness has to be chosen adequately to ensure both complete absorption of electrons and high X-ray transparency. X-ray generation and filtering are therefore always coupled to some degree in transmission type sources. Though this was originally claimed to be a major disadvantage, transmission type X-ray fluorescence attachments are especially attractive as they are more flexibly implemented to specimen chambers with different spectrometer geometries and limited available space. Analytical results comparable to massive anode set-ups have generally been obtained with lower probe currents. A transmission target assembly which is directly attached to an energy dispersive X-ray detector was presented by MIDDLEMAN and GELLER.<sup>210</sup> This arrangement is especially advantageous with retractable detectors as the X-ray source can be taken out of the electron beam without breaking the vacuum when acquisition of electron excited spectra is desired. The target foil rests in a cylindrical cavity with walls consisting of a layered tungsten-aluminium material. It shields the detector from source radiation and prevents spectral contaminations by fluorescence of the specimen chamber. Source X-rays are allowed to reach the sample through a hole 1 mm in diameter below the foil. Input counting rates of  $10^4 \text{ sec}^{-1}$  arise with a 2.5  $\mu\text{m}$  molybdenum target excited by a 10 nA electron beam at 30 keV. The efficiency of this construction has to be attributed to the inherently low source-sample and sample-detector distances as well as to a large illuminated sample area of up to 25  $\text{mm}^2$ . An improvement in signal-to-background ratios by a factor of up to fifty compared to electron excitation of the spectrum was demonstrated. Detection limits between 2 and 9 ppm for

---

---

elements with K lines in the range between 5 to 15 keV were observed with a standardised glass sample (NIST SRM 612) with counting times of 1200 sec.

POZSGAI stated detection limits extrapolated to a counting time of 1000 sec between 0.5 and 3 ppm for the same standardised glass sample with a very similar system.<sup>211</sup> This was, however, operated with significantly thicker targets such as a 100  $\mu\text{m}$  molybdenum and a 70  $\mu\text{m}$  germanium foil. To maintain comparable count rates, a 25  $\mu\text{A}$  electron beam with an energy of 39 keV was necessary. Here a distance of only 0.7 mm between source and sample and 20 mm between sample and detector is given, respectively. It is to be seen from these examples that the onset of the low energy tail of the scattered source radiation shifts to higher energies as the target thickness increases, which is the basic reason for the further gain in analytical sensitivity. By choosing narrower bore diameters beneath the target foil, lateral resolution can also be obtained to some extent with this system. A full width half maximum of 300  $\mu\text{m}$  was obtained from the intensity distribution obtained by moving a 30  $\mu\text{m}$  nickel wire across the X-ray beam.<sup>212</sup> The intensity loss introduced by collimation has to be compensated by lowering the target thickness, in this case by using a 10  $\mu\text{m}$  molybdenum foil. Under the same excitation conditions as mentioned above, a loss of analytical sensitivity by a factor of two to three has to be taken into account. Also, spectral contaminations by Pb L radiation from the layered lead and aluminium walls of the housing were observed.

In an alternative approach, WARREN and KRANER placed copper and molybdenum target foils in the aperture tray of the objective lens and utilised the final pole-piece to hold a molybdenum collimator. Owing to scattering of source radiation by the specimen stage, spectra exhibited a large background level, which severely limited the analytical sensitivity of this construction.<sup>213</sup> A transmission X-ray source to be placed below the final aperture was described by VALDRÈ. It consists of a bronze joint, a multi-target rod and a lead collimator and is plugged in the objective lens pole-piece.<sup>214</sup> The targets were pierced to enable positioning, electron excitation of the sample and imaging without the necessity of breaking the vacuum. The system is reported to convey a lateral resolution of 300  $\mu\text{m}$  according to the nickel wire method. A 5  $\mu\text{m}$  copper target excited by a 4  $\mu\text{A}$  electron beam with an energy of 30 keV produced detection limits of 50-100 ppm for elements between titanium and nickel in a NIST SRM 611 glass standard within an acquisition time of 700 sec. Higher signal-to-background ratios were observed for sodium and oxygen with a 10  $\mu\text{m}$  aluminium target operated at 10 keV than with electron excitation. Despite lower net intensities in these peaks,

---

detection limits of lower than 1 % and 600 ppm are given for oxygen and sodium, respectively, with counting times of 1000 sec. These are compared to values of approximately 1 % for both elements excited by 10 keV electrons for 70 sec.

A commercially available X-ray fluorescence attachment based on the work of ECKERT appeared as the so called 'Röntgenbox'.<sup>215,216</sup> Here, the sample is situated in a housing containing a specimen support, which is closed by the target at its top, and the fluorescent radiation emerges towards the detector through a side window. The Röntgenbox is not attached to any part of the microscope and can therefore be removed like a specimen holder. When operated with a 25  $\mu\text{m}$  copper anode at 20 keV for 1000 sec, the system delivers detection limits of approximately 2000 ppm for silicon and 4 to 40 ppm for elements between titanium and nickel in a glass matrix. Probe currents of 1  $\mu\text{A}$  or more are recommended and count rates are reported to approach values of 2000  $\text{sec}^{-1}$ . Geometric parameters of the Röntgenbox are not provided in the literature.

X-ray transparent samples can be investigated in transmission mode by directly attaching them to the metal target foil as suggested by CAZAUX.<sup>217</sup> The small distance between source and sample provides high X-ray intensities at the sample and, additionally, a good lateral resolution. In a specialised solution, X-ray fluorescence analysis was also implemented in a transmission electron microscope by LINNEMANN and REIMER.<sup>218</sup> After deflection by a 90° magnetic prism, the electron beam is directed onto a thin metal foil anode in the photo plate chamber of the instrument. Direct measurements of the excitation spectra emitted by 3.5  $\mu\text{m}$  copper and 10  $\mu\text{m}$  molybdenum targets were carried out and the dependence of the available source intensity on the target thickness and primary beam energy is given quantitatively. In spectra of pure elements ranging from chromium to arsenic and tantalum to bismuth, the signal-to-background ratio was found to increase by a factor of two to 17.5. This was achieved by a one to nine fold increase in counting time and an applied charge 230 to 3900 times higher compared to electron excitation. X-ray fluorescence was carried out with probe currents of 3 to 15  $\mu\text{A}$ .

Reviews on methods of X-ray fluorescence analysis including laboratory and synchrotron sources are provided by POZSGAI<sup>217</sup> and ECKERT.<sup>215</sup>

---

## 5.2 Sample Holder Design

X-ray fluorescence analysis in the scanning electron microscope proves to be a useful method for qualitative elemental analysis with significantly improved sensitivity compared to electron excitation. Each approach in this field is adapted to a special specimen chamber geometry. For example, the Röntgenbox developed by ECKERT<sup>215</sup> as well as the massive anode constructions are only applicable with horizontally mounted detectors due to their side window. Plug-in attachments to the objective lens are more flexible in this context, but exhibit the weakest performance with respect to analytical sensitivity. Most probably due to the lack of quantitative information, the proof of validity of former X-ray fluorescence set-ups was mainly restricted to a few standardised samples. Additionally, spectral contamination by spurious radiation excited from the parts of the fluorescer system or the specimen chamber of the microscope is a shortcoming encountered with a considerable number of constructions cited above.

This section describes the development of a new X-ray fluorescence specimen holder for application in a scanning electron microscope, its characterisation, and application to different industrial alloy samples.

### 5.2.1 Instrumental Parameters and Geometric Preconditions

The present work was carried out in an XL30 scanning electron microscope by PHILIPS equipped with a SCHOTTKY emitter. With an appropriate choice of condenser excitation and final aperture, the probe current can be maximised to approximately 470 nA at a primary beam energy of 25 keV without manipulating the hardware of the instrument. At the highest possible beam energy of 30 keV, probe currents of up to 400 nA are available. The chamber is provided with a tray-type x-y specimen stage with rotation around the z-axis and tilt in the x-z plane as further degrees of freedom.

An energy dispersive X-ray detection unit by EDAX is attached to the specimen chamber. It is based on a liquid nitrogen cooled circular Si(Li) detector with an active area of 10 mm<sup>2</sup> and a silicon dead layer thickness of 170 nm. A reverse bias of 750 V across the crystal is applied through 27 nm gold contacts. Separation from the chamber atmosphere is accomplished by an ultrathin 300 nm window consisting of alternating layers of aluminium and polymer foils supported by a silica grid with 70 % transmission. Data on the mass absorption coefficient of

the detector window are not provided. However, its transmission is given to be 25 % for K X-rays of boron (0.183 keV), 85 % for carbon (0.277 keV), 42 % for nitrogen (0.392 keV), 60 % for oxygen (0.525 keV), and 70 % for fluorine (0.677 keV).<sup>219</sup>

With an energy gain of 10 eV per channel and an amplifier time constant of 40  $\mu$ sec the detector resolution is  $\Delta E_{\text{fwhm}} = 150.4$  eV for Mn  $K_{\alpha}$  radiation (5.985 keV). Spectra are acquired up to an energy of 25 keV corresponding to a multichannel analyser memory of 2500 channels. Signals generated by X-ray quanta with higher energies are suppressed. Information on the detector crystal thickness is not available.

In the present system, the energy dispersive X-ray detector occupies the back left upper port of the specimen chamber resulting in an azimuthal angle of  $45^{\circ}$  towards the x-z-plane and an elevation angle of  $35^{\circ}$  towards the x-y-plane. The spectrometer geometry necessitates a working distance of 10 mm. In this particular case the detector axis intersects the sample surface at the point of electron impact and defines the sample-detector distance. This amounts to 50 mm and yields a geometric collection efficiency of  $3.183 \cdot 10^{-4} \approx 0.032$  % as entering *eq.* 3.5.

### 5.2.2 Implementation

According to *eq.* 3.24, the X-ray intensity generated from a given material by electron bombardment strongly depends on the overvoltage ratio. As efficient sample excitation is only possible with a sufficiently bright source, the range of useful primary X-ray energies is limited by the highest possible electron beam energy supported by the instrument in use. In the present case, where this energy is limited to 30 keV, molybdenum ( $E_{\text{crit}} = 20.003$  keV) is the highest reasonable choice among the materials most commonly used as targets. Available excitation energies therefore range up to the principal Mo K lines located at 17.476 keV ( $K_{\alpha 1}$ ), 17.371 keV ( $K_{\alpha 2}$ ), and 19.605 keV ( $K_{\beta}$ ). This is not a severe limitation as all elements exhibit characteristic lines in the energy range up to Mo  $K_{\alpha 1}$ .

In order to avoid contamination of the emission spectrum to be acquired, the X-ray fluorescence set-up must neither be excited by sample or source radiation nor scatter it into the detector. Materials of sufficiently high atomic number comply with both preconditions as they relate strongly absorbing and weakly scattering properties as to be seen from Figure 2-4. To prevent spectral interference with the source emission, a material with a K edge energy equal to or above the Mo  $K_{\beta}$  line has to be chosen. Therefore, molybdenum is a reasonable

---

---

choice with respect to processability and costs among elements with an atomic number  $Z \geq 42$ , especially as it is also available with high purity. Due to the large self absorption coefficient for L X-rays of  $\mu_{\text{Mo}}(\text{Mo } L_{\alpha 1}) \approx 770 \text{ cm}^2/\text{g}$  spectral contamination resulting from excitation of the Mo L line series by sample X-rays is excluded. This situation is less favourable in the case of lead, for which more energetic L lines above 10 keV are encountered. The much lower self-absorption coefficient of  $\mu_{\text{Pb}}(\text{Pb } L_{\alpha 1}) \approx 120 \text{ cm}^2/\text{g}$  explains the occurrence of spurious X-rays obtained with X-ray fluorescence set-ups based on lead.<sup>212</sup> In general, some basic design rules for an X-ray fluorescence set-up can be formulated based on the preceding discussion:

- i. Contamination of the sample spectrum has to be avoided. Apart from a correct choice of material as mentioned above, this also implies complete screening of the sample from the primary beam or backscattered electrons. In addition, the sample must not excite the specimen chamber of the microscope, which is usually made of steel.
- ii. The possibility of filtering the excitation spectrum emerging from the target should be included. This strongly influences the analytical sensitivity. Introduction of a beam limiting aperture behind the filter can be useful.
- iii. To solve very different analytical problems, fast exchange of sample, target, and filter foil is necessary.
- iv. A reliable measurement of the probe current is desirable in order to gain information on the X-ray production efficiency.
- v. The whole set-up should be easy to install, to adjust, and to be removed from the specimen chamber.
- vi. If possible, the necessity of manipulating the microscope hardware is to be avoided.

With the present system geometry, the X-ray detector always views the point of electron impact. For this reason, only a transmission type arrangement is feasible. The higher efficiency of thin targets is beneficial because the highest available probe current is lower than those applied in previous works by more than one order of magnitude. As a further requirement, X-ray generation, filtering, and beam shaping has to fit within the working distance of 10 mm required for a well defined spectrometer geometry. A sample holder to allow X-ray fluorescence analysis, and which complies the above needs, was developed and is depicted in Figure 5-1 to Figure 5-3 and in the construction drawings of section 9.2 in a more detailed manner.

---

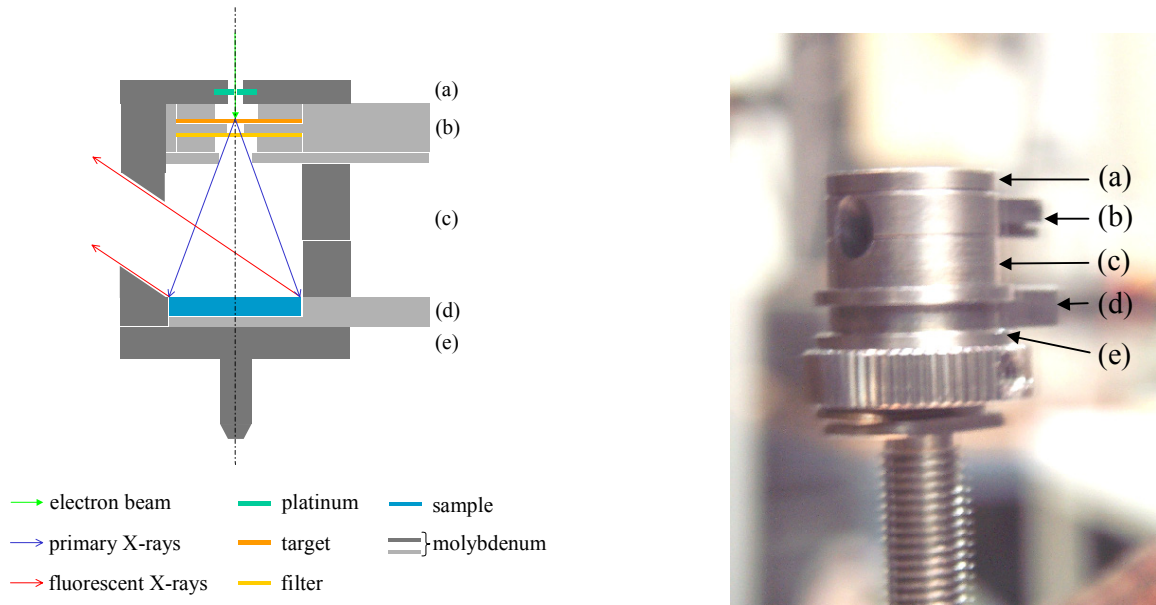


**Figure 5-1.** Schematic drawing of the developed X-ray fluorescence sample holder showing its operation principle. The molybdenum top plate (a), housing (c), and base plate (e) are depicted dark grey. In contrast, the movable molybdenum parts carrying target, filter, and aperture (b) and the sample (d), respectively, are coloured light grey for clarity. Brass screws ensuring a proper alignment of the system have been omitted from the schematic drawing given above.

**Figure 5-2.** The X-ray fluorescence sample holder mounted to the specimen stage of an XL30 scanning electron microscope by PHILIPS.

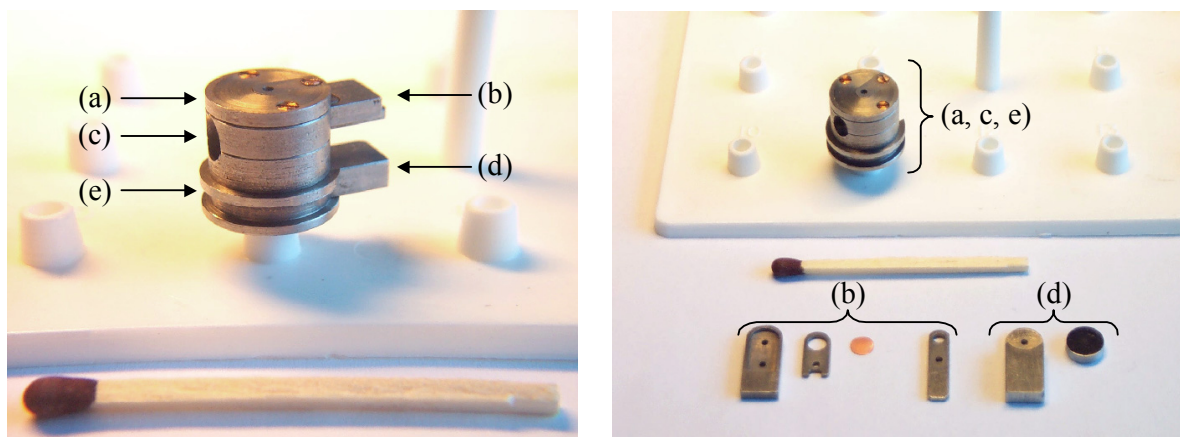


**Figure 5-3.** Photographs showing the assembled (left) and disassembled (right) X-ray fluorescence sample holder. The function of the main building blocks is to be seen from the schematic overview given above. A copper target and a typical sample are also depicted in the disassembled state. Details of the construction are found in section 9.2. A match (approximately 4.4 cm long) is shown for comparison of the size.

---

In this assembly, the electron beam enters the holder through a commercial 100  $\mu\text{m}$  platinum aperture and impinges onto the target foil acting as anode. Before striking the sample, the X-ray beam passes a filter foil clinged to the target holder, and the beam limiting aperture. Both target holder and aperture are constructed as side-entry tray-type inserts to the housing. The housing itself is designed to screen the specimen chamber of the microscope from sample X-rays. Therefore, the holder is only open towards the detector through a bore with a diameter of 3.60 mm forming an angle of  $35.0^\circ$  with the sample surface. The housing is mounted to the specimen support, which also contains a sample tray capable of holding samples 6.30 mm in diameter and 2.00 mm thick. As to be seen from Figure 5-1, the centre points of all elements are found on an axis intersecting the sample surface at an angle of  $90^\circ$ . A distance of 5.65 mm between target and sample surface is obtained, and the total height of the assembly measured from the sample surface is 8.90 mm. All parts were manufactured of pure molybdenum (> 99.9 %). The space between target foil and the platinum aperture closing the set-up towards the objective lens forms a FARADAY cup. Therefore, online monitoring of the electron probe current is possible. Despite the high backscatter coefficient and secondary electron yield of molybdenum, comparative measurements with a usual graphitised FARADAY cup do not show significant deviations.

### 5.3 Characterisation of X-Ray Sources

Detailed knowledge of the source characteristics is of central interest in X-ray fluorescence analysis. Information in this field is, however, not always to be obtained directly. This section describes theoretical considerations and experimental approaches to characterise the spectral and angular distribution of source emission in the X-ray fluorescence sample holder presented in the previous section.

#### 5.3.1 Spectral Distribution of X-Ray Source Emission

X-ray fluorescence spectra are acquired in a reflection type spectrometer geometry. The excitation spectrum, which is represented by the spectral distribution of X-rays transmitted through target and filter foil, is therefore not accessible directly. However, a conventional electron induced X-ray emission spectrum of the target foil (referred to by subscript 't') reflects the generated intensity according to :

---

$$I_{t,meas}(E) = I_{t,gen}(E) \cdot e^{-\frac{\mu_t(E)\rho_t t_{mean}}{\sin\psi}} \quad (5.1)$$

when the radiation is thought to originate from a mean depth  $t_{mean}$ . As outlined in section 4.2.3, X-rays are produced isotropically, and the fraction of radiation transmitted through a target foil with the total mass thickness of  $\rho_t t_t$  becomes :

$$I_{t,trans}(E) = I_{t,gen}(E) \cdot e^{-\mu_t(E)\rho_t(t_t - t_{mean})} \quad (5.2)$$

Introducing a filter (referenced by subscript 'f') of mass thickness  $\rho_f t_f$  and applying *eq. 5.1*, an expression for the excitation spectrum is formed, which is based on the measured target spectrum and the mass thicknesses of target and filter, respectively :

$$I_0(E) \cong I_{t,trans}(E) \cdot e^{-\mu_f(E)\rho_f t_f} = I_{t,meas}(E) \cdot e^{-\left\{ \mu_t(E)\rho_t \left[ t_t - t_{mean} \left( 1 + \frac{1}{\sin\psi} \right) \right] + \mu_f(E)\rho_f t_f \right\}} \quad (5.3)$$

As the mean depth of X-ray generation also depends on the energy, only an estimate of the excitation spectrum will be provided by *eq. 5.3*. Inaccuracies will be low, however, as the target thickness has to be chosen larger than the electron range and will therefore exceed the mean depth of X-ray generation. Mean depths for the generation of  $K_\alpha$  radiation in different target materials are summarised in Table 5-1 for a primary beam energy of 30 keV.

	$^{13}\text{Al}$	$^{22}\text{Ti}$	$^{29}\text{Cu}$	$^{42}\text{Mo}$	$^{47}\text{Ag}$
$t_{mean}$ [ $\mu\text{m}$ ]	2.60	1.37	0.61	0.34	0.18
electron range [ $\mu\text{m}$ ]	8.86	6.40	5.45	3.65	3.70
$E_{K\alpha}$ [keV]	1.487	4.509	8.041	17.445	22.104

**Table 5-1.** Calculated mean depth of X-ray generation for  $K_\alpha$  radiation and range of 30 keV electrons in several materials at normal incidence.<sup>175</sup>

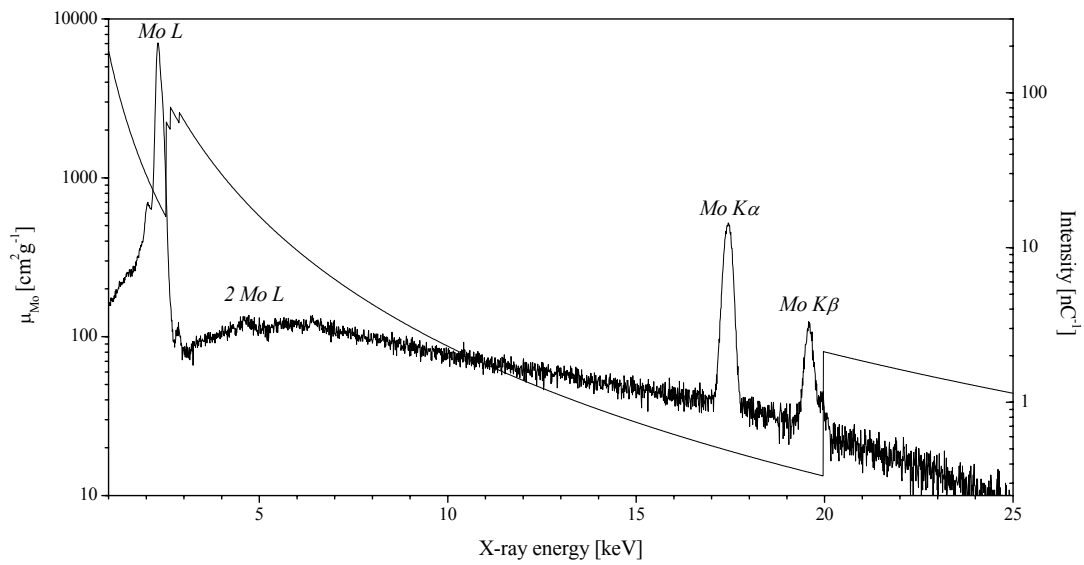


**Figure 5-4.** Electron excited X-ray emission spectrum of molybdenum acquired at 30 keV primary beam energy together with the mass absorption coefficient of molybdenum. Continuous background at low energies and just above the absorption edge will be efficiently filtered.

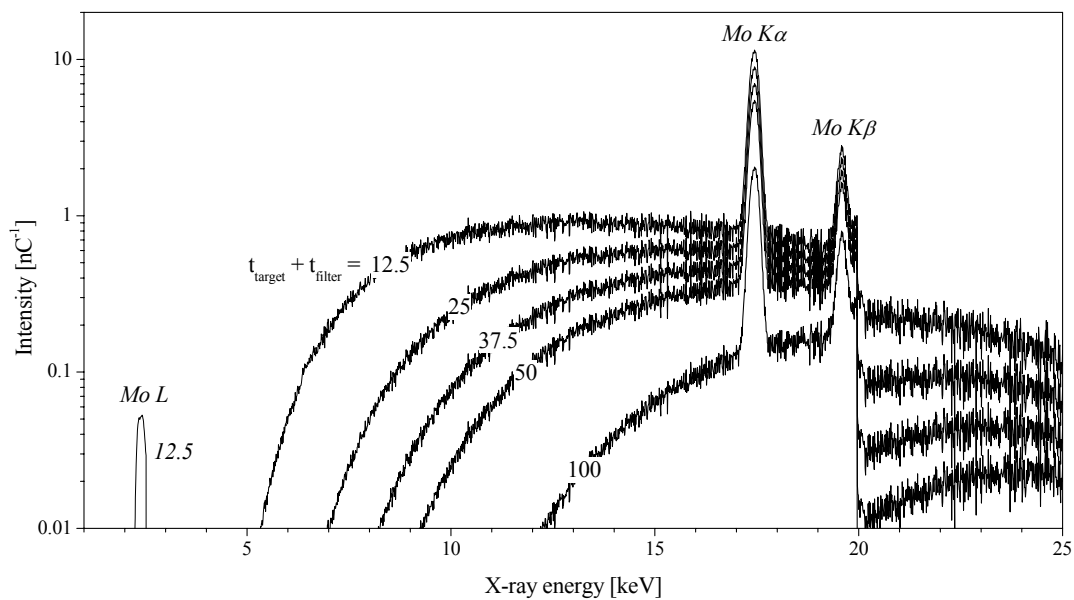


**Figure 5-5.** Excitation spectra emitted by a self-filtered molybdenum target calculated according to eq. 5.3. Numbers given with the curves indicate the total layer thickness  $t_{\text{target}}+t_{\text{filter}}$  in units of  $\mu\text{m}$ . The onset of spectral background due to Bremsstrahlung, which is less strongly suppressed at intermediate energies, is shifted to higher energies with increasing filter thickness. L lines occur only in the case of the lowest source layer thickness of  $12.5 \mu\text{m}$ .

It is further assumed in the above equations that the source rays are directed normally to the surface of target and filter and no extra paths due to tilted incidence occur. Figure 5-4 displays an electron excited spectrum of molybdenum together with the mass absorption coefficient of the same material. Owing to the low self-absorption of the K line series, a high source intensity of characteristic X-rays is achieved when target and filter consist of the same material. This situation is illustrated in Figure 5-5 where a series of excitation spectra calculated from *eq. 5.3* with increasing total layer thickness of target and filter  $t_t+t_f$  between 12.5 and 100  $\mu\text{m}$  molybdenum foil is shown exemplarily. Throughout this work, spectra are normalised to the total charge applied during their acquisition and consequently given in units of  $[\text{nC}^{-1}]$ . This ensures comparability of data originating from measurements under different excitation conditions.

Generally, the continuous background is efficiently filtered at low energies and just above the K edge. In the intermediate region below the  $K_\alpha$  line and at energies well above the

Target/filter	$t_{\text{target}} [\mu\text{m}]$	$t_{\text{filter}} [\mu\text{m}]$	background onset [keV]	$I(\text{target } K_\alpha) / I(\text{target } K_\beta)$
$_{29}\text{Cu} / _{29}\text{Cu}$	10.0	0.0	2.2	88.1 : 11.9
		10.0	2.9	84.9 : 15.1
		30.0	3.9	84.4 : 15.6
$_{42}\text{Mo} / _{42}\text{Mo}$	12.5	0.0	5.3	84.4 : 15.6
		12.5	7.0	83.5 : 16.5
		25.0	8.2	82.6 : 17.4
		37.5	9.3	81.5 : 18.5
		87.5	12.2	79.1 : 20.9

**Table 5-2.** Characteristic features of X-ray source spectra derived by applying *eq. 5.3* to electron excited target spectra as demonstrated in Figure 5-5. With increasing filter thickness, intensity ratios tend to deviate more strongly from the transition probabilities due to absorption effects, but the region of negligible background then extends to higher energies.

absorption edge, Bremsstrahlung is less strongly suppressed as the mass absorption coefficient strongly decreases in these regions. With increasing filter thickness, the background onset shifts to higher energies, and L lines are entirely removed from the excitation spectra.  $K_\alpha/K_\beta$  intensity ratios are predicted to slightly decrease and deviate more strongly from the transition probabilities of  $p_{\text{Mo}K\alpha} = 83.51\%$  and  $p_{\text{Cu}K\alpha} = 87.69\%$  due to the stronger absorption effect of the filter on the  $K_\alpha$  line. Despite the approximate nature of *eq. 5.3*, the shape of spectra shown in Figure 5-5 agrees very well with the emission spectra measured from thin metal foils<sup>218</sup> and also with theoretical X-ray tube spectra.<sup>149</sup> The characteristic features of excitation spectra are summarised in Table 5-2. Total photoelectric cross-sections and fluorescence yields are very low for light elements, and X-ray scattering plays a more important role compared to high atomic number matrices. For example, a carbon sample can be used to scatter the spectral distribution of source radiation into the detector. This is demonstrated in Figure 5-6, which presents X-ray spectra of the same high purity carbon sample excited by molybdenum and copper sources of varying thickness. Spectra were acquired with a probe current of approximately 360 nA at 30 keV primary beam energy for 1200 seconds. Due to the very low X-ray yield of light elements and strong self-absorption the C  $K_\alpha$  (0.277 keV) line is absent.

As the most predominant feature in the molybdenum excited spectra the Mo K line series appears, which is partly the result of RAYLEIGH scattering of the source emission. COMPTON scattering leads to the appearance of strongly DOPPLER broadened inelastic scatter lines at the low energy side of each elastic peak. The relative fraction of inelastically scattered radiation is not found to be constant but increases to some extent with filter thickness as reported in Table 5-3. It has to be noted that with an absorption coefficient of  $\mu_{\text{C}}(\text{Mo } K_\alpha) \approx 0.7 \text{ cm}^2/\text{g}$  about 73 % of the incident Mo  $K_\alpha$  radiation are transmitted through a carbon sample of 2.0 mm thickness that is even more transparent at higher energies. Bremsstrahlung with energies just above the Mo K edge penetrating the sample will be readily absorbed by the holder and excite Mo K X-rays with a high fluorescence yield of  $\omega_{\text{Mo}K} = 0.78467$ . Under a take-off angle of  $35^\circ$ , a fraction of nearly 58 % of fluorescent Mo  $K_\alpha$  radiation will emerge towards the detector through the sample. For this reason, the Mo K line series in the spectra displayed in Figure 5-6 are composed of both RAYLEIGH scattered source radiation and fluorescent radiation from the sample holder to various degrees. As less high energy background becomes available with increasing filter thickness, the ratio of inelastic to elastic peak intensity approaches the genuine value to be obtained with this arrangement.

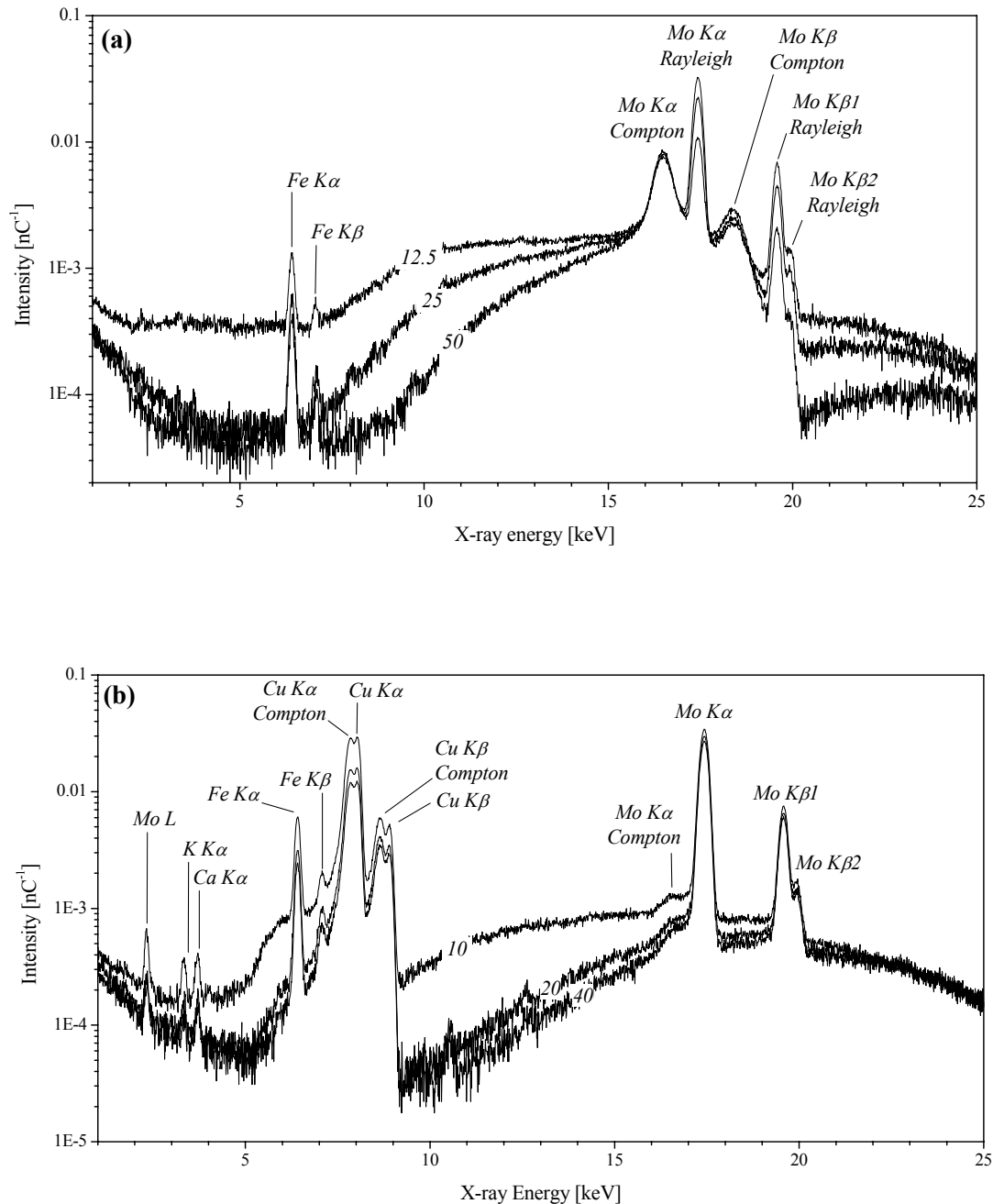


**Figure 5-6.** X-ray spectra obtained from a high purity carbon sample with a Mo (a) and a Cu (b) source operated with beam currents of approximately 370 nA at 30 keV primary beam energy for 1200 seconds. Fe lines stem from the collimator of the EDX detector, Ca and K lines due to impurities in the carbon sample are only effectively excited by Cu radiation. Numbers given with the curves indicate the total thickness of target and filter in units of  $\mu\text{m}$ . The varying intensity of the COMPTON peaks is discussed in the text.

target/filter	$t_{\text{target}} [\mu\text{m}]$	$t_{\text{filter}} [\mu\text{m}]$	sample	$I_{\text{COMPTON}} / I_{\text{RAYLEIGH}}$			
				Cu $K_{\alpha}$	Cu $K_{\beta}$	Mo $K_{\alpha}$	Mo $K_{\beta 1}$
$^{29}\text{Cu} / ^{29}\text{Cu}$	10.0	0.0	C	4.722	6.917	0.077	0.200
		10.0	C	4.709	7.381	0.048	0.165
		30.0	C	4.733	7.138	0.041	0.141
$^{29}\text{Cu} / ^{29}\text{Cu}$	10.0	10.0	none	0.275	0.369	0.033	0.138
$^{42}\text{Mo} / ^{42}\text{Mo}$	12.5	0.0	C	---	---	0.596	1.123
		12.5	C	---	---	0.919	2.068
		25.0	C	---	---	1.384	3.470
		37.5	C	---	---	2.000	5.739
$^{42}\text{Mo} / ^{42}\text{Mo}$	12.5	12.5	none	---	---	0.067	0.217

**Table 5-3.** Ratios of inelastic to elastic scatter intensities in spectra excited by different copper and molybdenum source arrangements. A detailed discussion on the origin of the Mo K peaks is provided in the text.

Finally, the low ratio extracted from a 'blank' spectrum without sample demonstrates that the amount of scattered radiation from the sample holder is negligible.

Very weak Fe  $K_{\alpha}$  and Fe  $K_{\beta}$  signals are observed, which originate from the collimator of the energy dispersive detector. This effect has been noticed earlier<sup>212</sup> and is too weak to affect trace analysis. Bremsstrahlung is also scattered into the detector and generates the continuous background expected for intermediate energies. As predicted by *eq. 5.3*, the region of negligible background extends to higher energies with increasing filter thickness. For practical purposes, a compromise between source intensity and filtering has to be found as with a total layer thickness of  $t_t+t_f$  larger than 50  $\mu\text{m}$  of molybdenum, the spectral intensity drops to inacceptably low values.

Spectra excited by a copper source with filter foils of different thickness as shown in Figure 5-6 are dominated by the COMPTON peaks of Cu  $K_\alpha$  and Cu  $K_\beta$  as the larger fraction of characteristic source radiation interacts with the sample. Under the present conditions, mass absorption coefficients of  $\mu_C(\text{Cu } K_\alpha) \approx 6.0 \text{ cm}^2/\text{g}$  and  $\mu_C(\text{Cu } K_\beta) \approx 4.6 \text{ cm}^2/\text{g}$  correspond to transmittances of only 6.7 % and 12.6 %, respectively. As expected in the absence of artifacts, the inelastic to elastic scatter peak ratio is virtually constant for Cu  $K_\alpha$  and  $K_\beta$  lines.

At energies well above its K absorption edge (8.980 keV), copper is a less efficient filter and Bremsstrahlung plays a more important role compared to spectra excited by a molybdenum source. Intense Mo  $K_\alpha$  and  $K_\beta$  lines accompanied by very weak COMPTON scatter peaks are superimposed to this background. The low fraction of inelastically scattered radiation proves that the Mo K peaks result from fluorescent excitation of the sample holder rather than from an impure source emission. Due to a more effective excitation by copper than by molybdenum radiation, a comparatively stronger signal from the collimator is observed. Also, impurities in the carbon sample give rise to weak emission lines of calcium and potassium that are not excited strongly enough by the molybdenum source.

Though it is concluded that the excitation spectra of copper sources contain only a negligible fraction of Mo K radiation, a slight decrease of the relative COMPTON scatter intensity is observed. This circumstance raises the question if excitation of the molybdenum housing by backscattered electrons from the target foil contaminates the source spectrum. Spurious X-rays can be produced by backscattered electrons with energies ranging from the Mo K edge to the primary beam energy. The fraction of electrons available in this energy interval is given by :

$$\eta_B(E_{crit,MoK}, E_0) = \eta_B(E_0) \cdot \int_{E_{crit,MoK}}^{E_0} \left( \frac{d\eta_B}{dE_B} \right) dE_B \quad (5.4)$$

In order to describe the energy spectrum of backscattered electrons, a POISSONIAN distribution function in which the most probable energy  $E_p$  is empirically related to the atomic number of the scattering material was proposed by RIVEROS et al.<sup>161,162</sup> The total intensity of spurious Mo  $K_\alpha$  X-rays generated by backscattered electrons is obtained by integrating the contributions of all electrons with sufficiently high energy. By relating this quantity to the

intensity of characteristic  $K_{\alpha}$  source radiation, the contamination of the excitation spectrum is estimated in terms of the ratio  $R_{src}$  according to :

$$R_{src} = \frac{I_{gen,MoK\alpha}}{I_{gen,tK\alpha}} = \frac{\eta(E_0) \int_{E_{crit,MoK}}^{E_0} \left( \frac{d\eta_B}{dE_B} \right) I_{gen,MoK}(E_B) dE_B}{I_{gen,t}(E_0)} \quad (5.5)$$

The characteristic X-ray intensity  $I_{gen}$  generated by electrons of energy  $E_B$  in the target and the housing, respectively, can be readily computed with fundamental parameter methods. An average number of X-ray quanta per incident electron is derived by the formalism of WERNISCH<sup>175</sup>, which was applied to *eq. 5.5*.

Target	<sup>13</sup> Al	<sup>22</sup> Ti	<sup>29</sup> Cu	<sup>47</sup> Ag
$E_p$ [keV]	22.812	24.558	25.308	26.391
$\eta(E_0)$	0.1110	0.2280	0.2899	0.3989
$\eta(E_{crit,MoK}, E_0) / \eta(E_0)$	0.4049	0.5480	0.6281	0.7637
$\eta(E_{crit,MoK}, E_0)$	0.0449	0.1249	0.1821	0.3046
$I_{gen, MoK\alpha}$	$1.19 \cdot 10^{-10}$	$3.65 \cdot 10^{-10}$	$5.23 \cdot 10^{-10}$	$9.34 \cdot 10^{-10}$
$I_{gen, tK\alpha}$	$1.98 \cdot 10^{-7}$	$9.24 \cdot 10^{-8}$	$4.16 \cdot 10^{-8}$	$3.59 \cdot 10^{-10}$
$R_{src}$	$6.02 \cdot 10^{-4}$	$3.95 \cdot 10^{-3}$	$1.26 \cdot 10^{-2}$	2.60

**Table 5-4.** Characteristic X-ray intensities generated in different targets in comparison with the intensity of Mo  $K_{\alpha}$  radiation from the housing excited by backscattered electrons with a most probable energy of  $E_p$ . A primary beam energy of 30 keV is assumed. Intensity is expressed in terms of X-ray quanta per incident electron.

Absorption in target and filter changes the intensity ratio  $R_{src}$  incident on the sample due to different transmissions  $T$  and is taken into account by :

$$R_{sample} = R_{src} \cdot \frac{T_{MoK\alpha}}{T_{tK\alpha}} = R_{src} \cdot \frac{e^{-\mu_t(MoK\alpha)\rho_t t_t - \mu_f(MoK\alpha)\rho_f t_f}}{e^{-\mu_t(E_{iK\alpha,t})\rho_t(t_t - t_{mean}) - \mu_f(E_{iK\alpha})\rho_f t_f}} \quad (5.6)$$

thereby referencing target and filter properties as in the preceding equations. Table 5-4 lists the characteristic figures as given by *eq. 5.5* for different targets.

In general, the spectral distribution of backscattered electrons shifts to higher energies with increasing atomic number. This effect is accompanied by an increase in the total amount of backscattering. The resulting larger fraction of backscattered electrons with energies above the Mo K shell ionisation threshold generates larger intensities of spurious radiation when proceeding from aluminium to silver targets. Together with the poor X-ray yield of heavy elements as pointed out in section 3.6, the best ratios of generated intensities  $R_{src}$  are obtained with light elements. For a copper target, an acceptable fraction of about 1.3 % Mo  $K_\alpha$  radiation is expected, whereas the amount of spurious X-rays exceeds the characteristic source intensity with a silver target.

This situation changes, however, when absorption is taken into account. Self-absorption deteriorates the better performance of light element targets, and especially for increasingly thick target-filter combinations the absorption term of *eq. 5.6* takes very large values. In the case of copper, the self-absorption and absorption of Mo $K_\alpha$  almost balance each other, and consequently the intensity ratios remain virtually unchanged as reported in Table 5-5. For heavier elements such as silver, the situation is reversed and absorption effects cause the intensity ratio  $R_{sample}$  to decrease with increasing source thickness, though satisfactory values are not achieved.

It has to be noted, however, that the above considerations on the spectral contamination of different sources are a worst-case scenario. In the fundamental parameter formalism adopted to derive the intensities to enter *eq. 5.5*, electrons are assumed to impinge onto the material perpendicularly. This is the case for beam electrons hitting the target but not for backscattered electrons exciting the housing of the sample holder. As the generated X-ray intensity at normal incidence is considerably larger than with an inclined beam, the spectral purity of the excitation spectrum is considered to be better than indicated by the figures of Table 5-5 in any case.

$t_t+t_f$ [ $\mu\text{m}$ ]	$T_{\text{MoK}\alpha} / T_{\text{tK}\alpha}$				$R_{\text{sample}}$			
	$^{13}\text{Al}$	$^{22}\text{Ti}$	$^{29}\text{Cu}$	$^{47}\text{Ag}$	$^{13}\text{Al}$	$^{22}\text{Ti}$	$^{29}\text{Cu}$	$^{47}\text{Ag}$
10	2.31	1.36	0.97	0.90	$1.38 \cdot 10^{-3}$	$5.37 \cdot 10^{-3}$	$1.22 \cdot 10^{-2}$	2.34
20	7.17	1.96	0.98	0.81	$4.32 \cdot 10^{-3}$	$7.74 \cdot 10^{-3}$	$1.23 \cdot 10^{-2}$	2.11
30	22.30	2.84	0.98	0.73	$1.34 \cdot 10^{-2}$	$1.12 \cdot 10^{-2}$	$1.23 \cdot 10^{-2}$	2.11
40	69.34	4.12	0.99	0.66	$4.17 \cdot 10^{-2}$	$1.63 \cdot 10^{-2}$	$1.25 \cdot 10^{-2}$	1.72
50	215.62	5.96	0.99	0.60	$1.30 \cdot 10^{-1}$	$2.35 \cdot 10^{-2}$	$1.25 \cdot 10^{-2}$	1.56

**Table 5-5.** Intensity ratios  $R_{\text{sample}}$  of spurious Mo  $K_{\alpha}$  X-rays and  $K_{\alpha}$  source lines for various targets according to eq. 5.6 along with the corresponding relative transmissions. The better performance of light element targets as indicated by  $R_{\text{src}}$  is deteriorated by strong self-absorption effects.

At normal beam incidence, the angular distribution of backscattered electrons is maximal in backward direction. From a practical point of view, electrons backscattered from the target are directed onto the platinum aperture closing the sample holder towards the objective pole-piece of the microscope. Though excitation of Pt L X-rays is possible in principle under these conditions, these lines are subject to strong self-absorption and are also efficiently attenuated by any target material of practical use. Contamination of spectra by Pt L radiation was not detectable.

### 5.3.2 *Angular Distribution of X-Ray Source Emission*

The range of primary beam electrons in different target materials amounts only to a few micrometres as to be seen from Table 5-1. With respect to the spectrometer dimensions, the electron interaction volume in the target constitutes an isotropic point source of characteristic X-rays in a very good approximation. Disregarding the target foil thickness, the source is located 5.65 mm above the centre of the sample. The opening angle of the resulting illumination cone can be adjusted by the aperture located below the filter foil. According to

the instrumental preconditions, the present device was designed to maximise intensity rather than to achieve a good lateral resolution and therefore collimation of the source was abandoned. An aperture of 3.60 mm diameter was used allowing the whole sample with a diameter of 6.30 mm to be completely irradiated by a divergent X-ray bundle exhibiting a half apex angle of  $29.1^\circ$ . These illumination conditions can be readily visualised using the Monte Carlo simulation techniques proposed in section 4.2.1. To obtain meaningful results, the stronger absorption of source rays emerging with an inclination towards the cone axis has to be taken into account. For example, the path length through target and filter foil increases by 14.4 % for radiation emitted with the maximum angle of  $29.1^\circ$  compared to X-rays directed towards the sample perpendicularly. Figure 5-7 shows the Monte Carlo simulated intensity distribution of  $10^8$  source rays impinging onto a circular sample under the circumstances described above. An intensity profile is obtained by taking a linescan including the centre point of the sample, which is depicted in Figure 5-8.

In order to achieve empirical information on the lateral distribution of source rays, characteristic X-ray intensities of circular nickel samples with concentric copper cores of different diameters were acquired from X-ray fluorescence spectra excited with a 25  $\mu\text{m}$  molybdenum source at 30 keV primary beam energy. Due to the neighbouring positions of copper and nickel in the periodic table, X-ray production efficiencies will be very similar, and especially fluorescence effects at the phase boundary affecting the relative intensities are negligible. Sigmoidal intensity profiles observed for the  $K_\alpha$  line intensity of both elements are presented in Figure 5-9. A measure of the 'lateral resolution' is provided by the full width at half maximum of the simulated as well as the experimentally determined intensity distributions. The agreement of simulated and experimental data is demonstrated in Table 5-6.

	simulation	exp. (Cu $K_\alpha$ )	exp. (Ni $K_\alpha$ )
$\Delta d_{\text{fwhm}}$ [mm]	$3.56 \pm 0.02$	$3.53 \pm 0.35$	$3.67 \pm 0.38$

**Table 5-6.** Simulated and experimentally determined full width at half maximum  $\Delta d_{\text{fwhm}}$  of the lateral distribution of source X-rays ('lateral resolution'). The geometric situation underlying these data is discussed in the text.

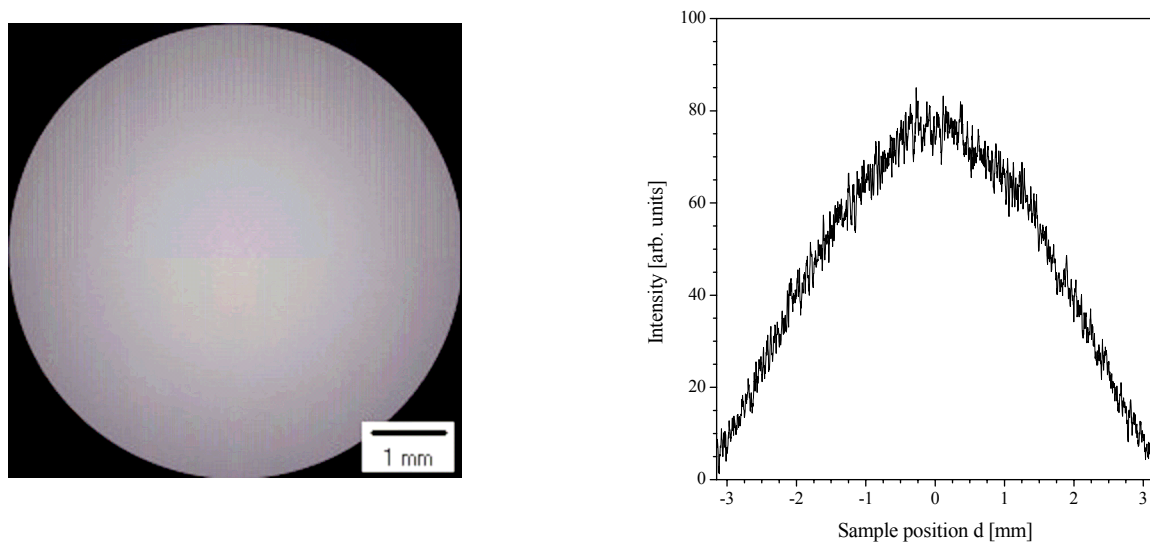


**Figure 5-7.** Monte Carlo simulated intensity distribution of  $10^8$  source rays emitted from a point source situated 5.65 mm above the centre of a sample 6.30 mm in diameter. This situation is encountered in the present X-ray fluorescence device.

**Figure 5-8.** Intensity profile of source X-rays as linescan across the simulated two dimensional intensity distribution as presented in Figure 5-7. The lateral resolution is usually identified with the full width at half maximum.

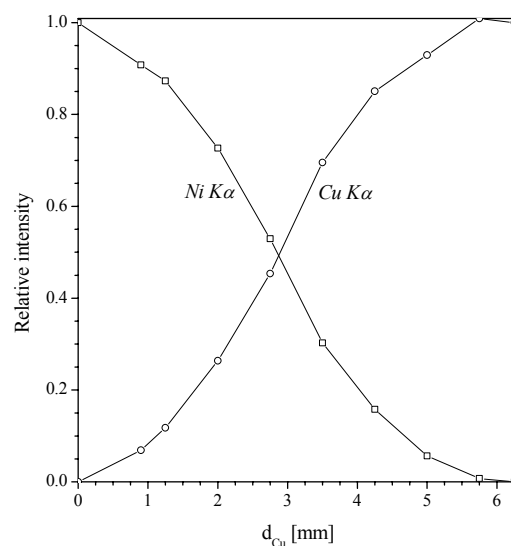


**Figure 5-9.**  $K_{\alpha}$  line intensities of circular nickel samples with concentric copper cores of different diameters  $d_{Cu}$ . Intensities are normalised to values obtained with pure copper and nickel samples, respectively. The full width at half maximum of the sigmoidal profile is consistent with simulated data.

#### 5.4 Performance of X-Ray Fluorescence Analysis

The analytical capabilities of X-ray fluorescence analysis are strongly dependent on the experimental conditions. In this section, the influence of experimental parameters on the appearance of X-ray fluorescence spectra is investigated to evaluate the performance of the present approach.

##### 5.4.1 Adjustment and Efficiency of Excitation

X-ray fluorescence spectra of a industrial aluminium alloy (Al97.5/Si1.0/Mg0.8/Mn0.7) sample excited by molybdenum sources of different thickness are displayed in Figure 5-10. Though not specified, iron, nickel, copper, zinc, gallium, and lead are clearly detectable. The characteristic peaks exhibit a purely GAUSSIAN shape proving that scattering of sample X-rays at the housing of the sample holder is absent and does not affect the spectra. Excitation of the sample holder is negligible as only a minor fraction of continuous source radiation penetrates a 2.0 mm aluminium sample, and consequently the intensity ratio of COMPTON and RAYLEIGH scattered X-rays is found to remain constant.

Continuous background contributes to the spectra though its effect is less pronounced than in Figure 5-6 due to the predominant role of the photoelectric interaction compared to scattering in higher atomic number matrices. Nevertheless, the rising background obscures characteristic peaks and thus negatively affects the analytical sensitivity. This circumstance is in accordance with the findings reported in the previous section. On a quantitative scale, the signal-to-background ratios of the characteristic peaks summarised in Table 5-7 provide a measure of the increasing background level.

The  $K_{\alpha}$  lines of manganese and iron are located in a region of low background, which is reflected in a moderate improvement of signal-to-background ratios when proceeding from a 12.5  $\mu\text{m}$  to a 50  $\mu\text{m}$  molybdenum source. A more pronounced effect is observed at higher energies, where a three to four times increase in signal-to-background ratios is obtained. As a detector artifact, the background level at low energies is not influenced by the measuring conditions. Therefore, signal-to-background ratios for the Al  $K_{\alpha}$  line deteriorate as a consequence of the lower spectral intensities.

---

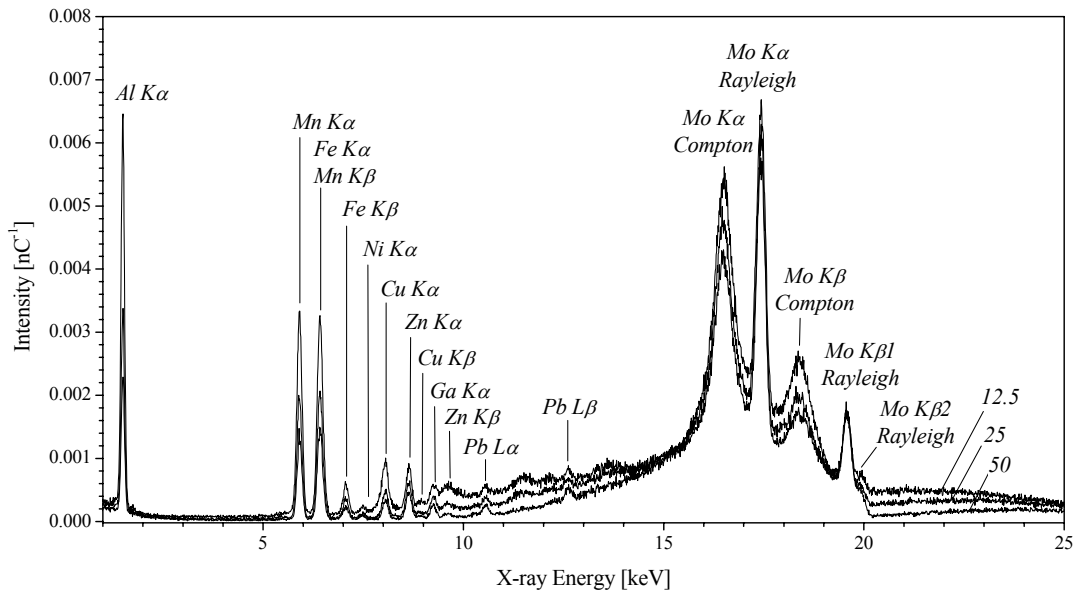


**Figure 5-10.** X-ray fluorescence spectra of Al97.5/Si1.0/Mg0.8/Mn0.7 acquired with different molybdenum sources operated at 30 keV primary beam energy and a probe current of approximately 375 nA for a live time of 1200 sec. Numbers indicate the total thickness of target and filter in units of  $\mu\text{m}$ . Background suppression by filtering is accompanied by better signal-to-background ratios but diminishes intensities.

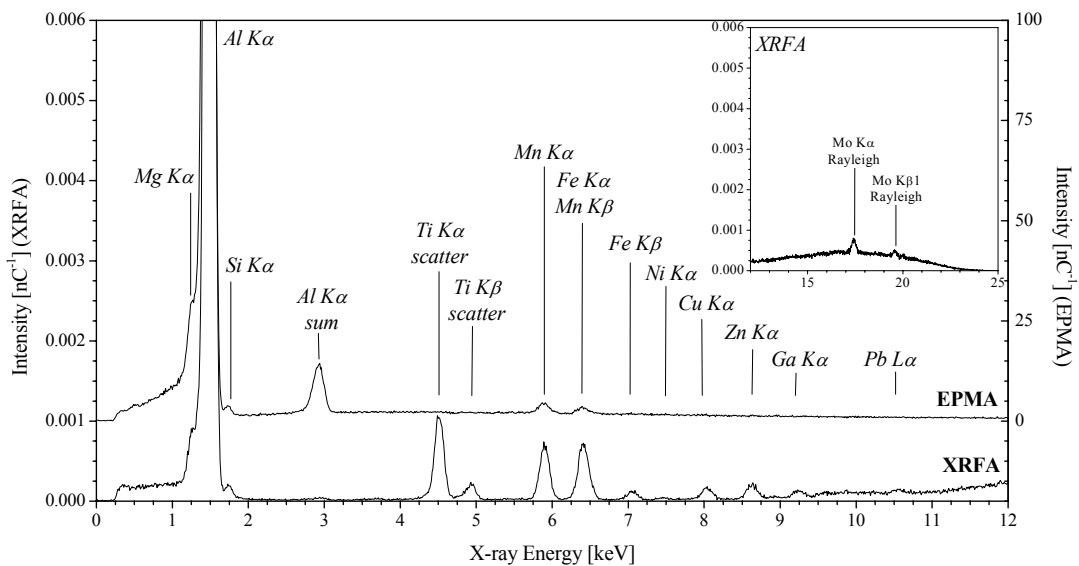


**Figure 5-11.** Electron excited spectrum of Al97.5/Si1.0/Mg0.8/Mn0.7 (30 keV, 0.115 nA, 900 live sec) and X-ray fluorescence spectrum excited by a 50  $\mu\text{m}$  Ti target (30 keV, 472 nA, 1200 live sec). The sensitivity of X-ray fluorescence analysis for light elements can be significantly enhanced by suitable choice of excitation conditions. Excitation of manganese and heavier elements is caused by continuous background and Mo K radiation.

According to *eq. 3.47*, detection limits are determined by the product of signal-to-background ratio and net intensity of the corresponding characteristic line. Therefore, a 25  $\mu\text{m}$  molybdenum source is expected to be an appropriate compromise between background level and intensity and to provide the best detection limits. Table 5-7 also demonstrates the high sensitivity of X-ray fluorescence analysis towards heavy elements that are beyond the limit of detection for electron probe microanalysis. For light elements the reverse situation is encountered as magnesium and silicon are detectable by electron excitation but not by X-ray fluorescence analysis.

Line	energy [keV]	S/B					
		<sup>42</sup> Mo 12.5 $\mu\text{m}$	<sup>42</sup> Mo 25.0 $\mu\text{m}$	<sup>42</sup> Mo 37.5 $\mu\text{m}$	<sup>42</sup> Mo 50 $\mu\text{m}$	<sup>22</sup> Ti 50 $\mu\text{m}$	electrons 30 keV
<sup>12</sup> Mg K $_{\alpha}$	1.254	0.00	0.00	0.00	0.00	2.69	3.11
<sup>13</sup> Al K $_{\alpha}$	1.487	22.15	13.38	12.25	12.27	243.26	187.34
<sup>14</sup> Si K $_{\alpha}$	1.740	0.00	0.00	0.00	0.00	14.45	15.34
<sup>24</sup> Cr K $_{\alpha}$	5.412	0.47	0.74	0.81	1.04	0.70	0.00
<sup>25</sup> Mn K $_{\alpha}$	5.985	17.51	22.29	23.32	26.47	22.90	1.04
<sup>26</sup> Fe K $_{\alpha}$	6.399	14.34	18.94	20.55	20.96	23.07	0.68
<sup>28</sup> Ni K $_{\alpha}$	7.472	0.52	1.24	1.60	1.60	1.33	0.00
<sup>29</sup> Cu K $_{\alpha}$	8.041	3.19	4.72	6.31	6.67	5.47	0.00
<sup>30</sup> Zn K $_{\alpha}$	8.631	1.94	3.87	5.66	6.41	4.33	0.00
<sup>31</sup> Ga K $_{\alpha}$	9.243	0.65	1.28	2.11	2.54	1.31	0.00
<sup>82</sup> Pb L $_{\alpha}$	10.551	0.31	0.54	0.87	1.33	0.48	0.00

**Table 5-7.** Signal-to-background ratios S/B for the principal emission lines of Al97.5/Si1.0/Mg0.8/Mn0.7 excited by different X-ray sources and electrons. Data are based on spectra displayed in Figure 5-10 and Figure 5-11.

It has been pointed out that the energy of the source radiation should be as close as possible above the absorption edge of the analyte to achieve the most efficient excitation conditions.<sup>209</sup> In this case, the mass absorption coefficient of the analyte relative to that of the whole sample is as large as possible and an analyte-source ray interaction becomes most probable (*eq. 4.20*). For practical purposes, the excitation energy should be chosen high enough to avoid overlap between COMPTON scattered source radiation and the characteristic line in question. X-ray fluorescence excited by a Bremsstrahlung continuum containing a range of energies suitable to excite elements of different atomic number with comparable efficiency would therefore be desirable.<sup>209</sup> Tungsten sources are rather advantageous in this context, but high electron energies are required to compensate for the low X-ray yield of heavy elements and to obtain acceptable count rates. With the primary beam energy limited to 30 keV the implementation of a tungsten based continuous X-ray source is not feasible in the system described.

In the present system, the sensitivity of X-ray fluorescence analysis towards light elements can be significantly improved by lowering the excitation energy. To illustrate this effect, an X-ray fluorescence spectrum of Al<sub>197.5</sub>/Si<sub>1.0</sub>/Mg<sub>0.8</sub>/Mn<sub>0.7</sub> obtained with a 50  $\mu\text{m}$  Ti source is depicted in Figure 5-11, and an electron excited spectrum is also shown for comparison. Scattered Ti K source lines occur in the X-ray fluorescence spectrum, which exhibit a slight tail towards lower energies due to unresolved COMPTON peaks. The Mg  $K_{\alpha}$  line (1.254 keV) appears in the spectrum but cannot be separated from the Al  $K_{\alpha}$  peak (1.487 keV). With an energy of 1.740 keV, the Si  $K_{\alpha}$  line is situated just above the Al K edge (1.560 keV) and therefore subject to strong absorption effects of the matrix. Despite this unfavourable condition, silicon is clearly detected in the spectrum. The signal-to-background ratios for magnesium, aluminium, and silicon are now well comparable to those achieved in electron probe microanalysis. Additionally, heavier trace elements are also detected as a consequence of impure source emission. As to be seen from the inlay of Figure 5-11, elastically scattered Mo  $K_{\alpha}$  and  $K_{\beta}$  lines give evidence of the contaminated excitation spectrum as to be expected with thick Ti targets according to Table 5-5. The characteristic shape of the spectral background at higher energies also indicates the presence of Bremsstrahlung from the source. Despite the lower total intensity, the use of a thicker target proves to be advantageous in this analytical context for several reasons. The target efficiently suppresses the continuous part of the source emission in the region of interest, this means up to an energy of approximately 11 keV in this case. Moreover, due to the self-attenuation of Ti K lines the relative fraction of Mo K radiation and continuum becomes sufficiently high to detect heavier trace elements.

As to be seen from Table 5-7, the signal-to background ratios of manganese and iron are equal to or even larger for a 50  $\mu\text{m}$  Ti source than those obtained with a 50  $\mu\text{m}$  Mo foil. For the remaining trace elements with high atomic numbers, signal-to-background ratios are slightly better than values measured with a 25  $\mu\text{m}$  Mo source and take an intermediate position except for lead, which is affected by the increasing background at higher X-ray energies.

In X-ray fluorescence analysis, the conversion of primary beam energy into fluorescent radiation is a two-step process. Apart from the X-ray production efficiency of different materials, a considerable amount of electron energy is lost during the generation of source radiation in the target due to the isotropy of emission. The spectral yield of various samples measured in terms of detected quanta per incident charge is compared in Table 5-8 for X-ray fluorescence and electron microprobe analysis under different excitation conditions. Generally, the spectral yield of X-ray excited samples is seen to be lower by three to four orders of magnitude compared to electron excitation. With primary beam energies between 15-30 keV, probe currents of approximately 0.1-0.5 nA are applied in electron microprobe analysis. The low yield of X-ray excited samples can be compensated by using higher probe currents of 300-400 nA. Count rates and acquisition times comparable to those of electron excited samples are therefore achievable except for light element matrices for which lower but nevertheless reasonable count rates have to be taken into account.

The lower X-ray production efficiency of heavy elements in electron probe microanalysis is not evident from the figures reported in Table 5-8. It has to be emphasised, however, that the discussion on elemental yields  $Y_{ij}$  according to *eq. 3.24* refers to the X-ray intensity generated within the sample, whereas Table 5-8 refers to emitted intensities, which are influenced by different absorption effects encountered with each particular sample composition. In contrast, X-ray yields strongly increase with the atomic number of the sample in X-ray fluorescence analysis. Here, absorption is outweighed by the effect of the significantly increased photoelectric cross-sections and fluorescence yields. Setting the excitation energy closer to the absorption edge of the analyte leads to an improvement of the spectral X-ray yield as to be seen from values reported for Ti90/Al6/V4 and Co49/Fe49/V2. This emphasises the necessity of a proper adjustment of excitation conditions. Due to the presence of spurious Mo K radiation in the spectrum of Al97.5/Si1.0/Mg0.8/Mn0.7 as discussed above, this effect is not observable in this case.

---

Sample	X-ray yield [nC <sup>-1</sup> ]	XRFA			EPMA	
		Mo 25 μm	Cu 44 μm	Ti 50 μm	15keV	30 keV
Al97.5/Si1.0/ Mg0.8/Mn0.7	char.	0.6 (35 %)	0.9 (82 %)	0.7 (64 %)	---	15729 (89 %)
	bkg.	1.1 (65 %)	0.2 (18 %)	0.4 (36 %)	---	1976 (11 %)
	<b>total</b>	<b>1.7</b>	<b>1.1</b>	<b>1.1</b>	---	<b>17705</b>
Ti90/Al6/V4	char.	1.4 (82 %)	3.5 (95 %)	---	1965 (65 %)	6122 (69 %)
	bkg.	0.3 (18 %)	0.2 (5 %)	---	1041 (35 %)	2712 (31 %)
	<b>total</b>	<b>1.7</b>	<b>3.7</b>	---	<b>3006</b>	<b>8834</b>
Co49/Fe49/V2	char.	4.2 (95 %)	7.7 (96 %)	---	1510 (47 %)	8311 (66 %)
	bkg.	0.2 (5 %)	0.3 (4 %)	---	1673 (53 %)	3642 (34 %)
	<b>total</b>	<b>4.4</b>	<b>8.0</b>	---	<b>3183</b>	<b>12675</b>
Cu	char.	6.5 (96 %)	---	---	1551 (46 %)	4648 (60 %)
	bkg.	0.3 (4 %)	---	---	1846 (54 %)	3059 (40 %)
	<b>total</b>	<b>6.8</b>	---	---	<b>3397</b>	<b>7707</b>

**Table 5-8.** X-ray yield of various samples under different excitation conditions in X-ray fluorescence and electron microprobe analysis, measured in terms of counts per incident charge in the characteristic spectrum, background, and the entire spectrum, respectively. The geometric collection efficiency is the same for all measurements (see section 5.2.1 for details).

The influence of the continuous background on X-ray fluorescence spectra is reduced with increasing atomic number as the scattering properties of the sample diminish. Concerning energy and atomic number dependence, background levels of electron excited spectra reported in Table 5-8 exhibit the opposite behaviour in accordance with the KRAMERS cross-section *eq. 2.23*. The circumstance that a significantly lower amount of incident radiation is wasted for generation of background in X-ray fluorescence analysis partially compensates for the low spectral yield for medium and high atomic number elements.

#### 5.4.2 X-Ray Scatter Peaks

Dedicated X-ray fluorescence spectrometers are most commonly designed to detect fluorescent radiation under an angle of  $90^\circ$  towards the incident X-ray beam. Under these conditions, the energy shift of inelastically scattered radiation vanishes according to *eq. 2.14*. This geometry is particularly advantageous as the resulting coincidence of RAYLEIGH and COMPTON peaks minimises the influence of scattered X-rays on the spectra. The geometric constraints encountered with the specimen chamber of the scanning electron microscope prevents implementation of an optimised spectrometer geometry, and the occurrence of scatter lines is inevitable.

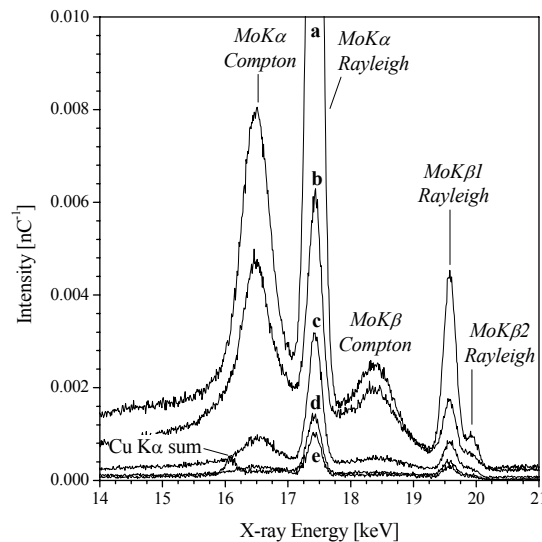


**Figure 5-12.** Scatter region in X-ray fluorescence spectra of (a) graphite, (b) Al97.5/Si1.0/Mg0.8/Mn0.7, (c) Ti90/Al6/V4, (d) Co49/Fe49/V2, and (e) Cu excited with a 25  $\mu\text{m}$  molybdenum source. Scattering reduces as the mean atomic number of the samples increases from (a) to (e). The position of COMPTON peaks is independent of the sample.

Intensity and width of these peaks, however, also convey analytical information, for example on mass thickness, density or mean atomic number of a sample.<sup>17,187,191</sup> This is illustrated in Figure 5-12, which shows the scatter region of X-ray fluorescence spectra of different samples excited with a 25  $\mu\text{m}$  Mo source. As discussed in the previous section, the RAYLEIGH lines are composed of fluorescent and scatter contributions in the case of X-ray transparent samples such as graphite and Al97.5/Si1.0/Mg0.8/Mn0.7, and do not reflect the genuine elastic scatter intensity. This does, however, not affect the COMPTON lines and therefore, the decrease of inelastically scattered Mo  $K_\alpha$  and  $K_\beta$  line intensity correctly reflects the increase in the mean atomic number of the sample.

As a consequence of the momentum distribution of bound electrons in the sample, COMPTON peaks appear broadened. Their position only depends on the energy of the incident radiation and can be used to extract information about the scattering angle, which in turn is connected with the spectrometer geometry. The divergent source emission forces a range of different scattering angles to be covered in the present system leading to an additional broadening of the COMPTON peaks.

Sample	excitation conditions	COMPTON shift of $K_\alpha$ source line [eV]	Scattering angle $\theta$ [°]
Graphite	Mo 50 $\mu\text{m}$	945	$132.9 \pm 4.2$
Al97.5/Si1.0/ Mg0.8/Mn0.7	Mo 50 $\mu\text{m}$	908	$127.8 \pm 3.9$
Ti90/Al6/V4	Mo 25 $\mu\text{m}$	902	$126.8 \pm 3.8$
Co49/Fe49/V2	Mo 25 $\mu\text{m}$	886	$124.9 \pm 3.7$
Graphite	Cu 44 $\mu\text{m}$	193	$123.7 \pm 16.8$

**Table 5-9.** Scattering angles deduced from the COMPTON shift of the  $K_\alpha$  source line in X-ray fluorescence spectra of different samples by means of *eq. 2.14*. An absolute uncertainty of 0.03 keV was assumed in the determination of the line position to take into account inaccuracies of spectrometer calibration and to calculate the statistical errors.

Owing to the symmetry of the illumination cone, however, the distribution of scattering angles is expected to be centred around the geometrical average of  $125^\circ$  in the present system under the condition of proper alignment. According to the law of error propagation, the determination of scattering angles is associated with an error of about 3.2 % for Mo  $K_\alpha$  radiation assuming an absolute uncertainty of line positions of 0.03 keV. Table 5-9 summarises the results of measurements with various samples and validates the geometry of the X-ray fluorescer system within the limits of error. Continuous background is an especially dominant feature of graphite spectra excited by molybdenum sources, and therefore the systematic deviation encountered in this case is introduced by background correction. At lower energies, the inaccuracies in peak location lead to inacceptably high error limits. Also, measurements are not performed reasonably with samples of higher mean atomic numbers than Co49/Fe49/V2 due to the very low intensity of scattered radiation.

### 5.5 Conclusions

A new design of a sample holder to facilitate X-ray fluorescence analysis in the scanning electron microscope is presented. Theoretical considerations and experimental results prove that a flexible X-ray fluorescer system with well defined geometry providing clean excitation spectra is obtained. A significant increase in signal-to-background ratios compared to electron microprobe analysis is achieved.

---





---

## 6 Application of Monte Carlo Methods in X-Ray Emission Spectroscopy

Monte Carlo algorithms to predict the emission spectra of X-ray and electron excited samples along with other observable quantities were described in section 4. The aim of this section is to prove the validity of simulated data and to apply Monte Carlo techniques for standardless quantitative X-ray emission spectroscopy including X-ray fluorescence and electron microprobe analysis performed in the scanning electron microscope as discussed in section 5.

### 6.1 Assessment of Fundamental Parameters in Electron Microprobe Analysis

Monte Carlo modelling of X-ray emission spectra is based on a set of atomic properties such as electron and X-ray interaction cross-sections, fluorescence yields, and transition probabilities. Quantities characterising the behaviour of a large ensemble of impinging electrons, for example the spectral distribution of backscattered electrons and the X-ray depth distribution profiles  $\phi(\rho z)$ , are obtained as a by-product in the Monte Carlo simulation of emission spectra. A number of parameters, which are a necessary input of fundamental parameter methods in electron microprobe analysis, is therefore additionally accessible. In this context, the correct assessment of these quantities ensures an adequate description of electron diffusion and is a necessary prerequisite for quantitative Monte Carlo based electron microprobe analysis. In X-ray fluorescence analysis, simulated spectra are more directly related to atomic properties and validation is possible by comparison of theoretical and experimentally determined emission spectra.

#### 6.1.1 Backscatter Coefficient and Energy Spectra of Backscattered Electrons

The backscatter coefficient plays an important role in the ZAF approach. It is usually not only employed to calculate the backscatter correction factor (*eq. 3.19*), but also serves as the central parameter to compute the mean depth of X-ray generation. In this way, it governs the atomic number and absorption correction factor.<sup>91,92,167,220</sup> Though no such factors exist in the Monte Carlo simulation of X-ray emission spectra, the amount of backscattering also defines the fraction of primary beam energy lost for the generation of characteristic radiation and is therefore directly connected to the emission spectra. Moreover, modelling of backscatter coefficient and energy spectra of backscattered electrons is an interesting task as these

---

quantities are comparably easy to measure and convey additional analytical information about the sample under investigation.<sup>221-225</sup>

In terms of Monte Carlo calculations, the backscatter coefficient  $\eta_B$  is most easily determined by keeping track of the number of backscattered electrons  $n_{BSE}$  relative to the total number  $n$  of simulated trajectories :

$$\eta_B(E_0, \alpha, t) = \frac{n_{BSE}}{n} \quad (6.1)$$

which corresponds to the elimination of charge and time in *eq. 2.42*. Backscattering is a statistical process with two complementary events as an impinging electron is either backscattered or comes to rest within an infinitely thick sample. Therefore, the determination of  $\eta_B$  is associated with an uncertainty  $\Delta\eta_B$ , which is readily computed from the deviation of a binomial distribution according to :

$$\Delta\eta_B(E_0, \alpha, t) = \frac{\Delta n_{BSE}}{n} = \frac{\sqrt{\eta_B(1-\eta_B) \cdot n}}{n} = \sqrt{\frac{\eta_B(1-\eta_B)}{n}} \quad (6.2)$$

Consequently, an expression for the relative error is established by :

$$\frac{\Delta\eta_B}{\eta_B} = \sqrt{\frac{1-\eta_B}{n \cdot \eta_B}} \quad (6.3)$$

*Eqs. 6.2* and *6.3* show that both absolute and relative error of  $\eta_B$  decrease with the total number of simulated electron trajectories like  $n^{-0.5}$ . A survey of numerical values for statistical errors encountered under different conditions is presented in Table 6-1. It is evident that the simulation of  $10^6$  trajectories is necessary to keep the relative error well below 1% over the whole range of interest.

As outlined in section 2.2.1, electrons are more likely deflected through large angles by heavy atoms<sup>205</sup>, and consequently the fraction of backscattered electrons continuously increases with atomic number.

n	$\Delta\eta_B$ [%] at $\eta_B$ [%]				$\Delta\eta_B/\eta_B$ [%] at $\eta_B$ [%]			
	5.000	10.000	25.000	50.000	5.000	10.000	25.000	50.000
$10^3$	0.689	0.949	1.369	1.581	13.784	9.487	5.477	3.162
$10^4$	0.218	0.300	0.433	0.500	4.359	3.000	1.732	1.000
$10^5$	0.069	0.095	0.137	0.158	1.378	0.949	0.548	0.316
$10^6$	0.022	0.030	0.043	0.050	0.436	0.300	0.173	0.100

**Table 6-1.** Absolute and relative error in the determination of backscatter coefficients  $\eta_B$  with different numbers  $n$  of simulated electron trajectories. With  $10^6$  simulated trajectories, the relative error stays well below 1% over the whole range of interest.

The physical principles underlying electron backscattering are surveyed by NIEDRIG<sup>97</sup>, and a broad numerical database concerning the backscatter coefficient based on experimental data<sup>91,223,224,226-230</sup>, scattering models<sup>94,231-235</sup>, and Monte Carlo<sup>236</sup> simulations<sup>237</sup> is available. In general, different compilations agree well for light elements but tend to deviate from each other with increasing atomic number. Backscatter coefficients of elements from  ${}_5\text{B}$  to  ${}_{92}\text{U}$ , at primary beam energy of 10, 20, and 30 keV at normal incidence, calculated by Monte Carlo methods simulating  $10^6$  electrons are rendered in Figure 6-1.

Under these conditions most likely encountered in electron microprobe analysis performed in the scanning electron microscope, the backscatter coefficient is virtually independent of the primary beam energy except for very high atomic number elements. This behaviour is correctly reproduced by Monte Carlo simulations, which are also found to excellently fit values reported for light elements up to  ${}_{16}\text{S}$ . Slight overestimation at medium atomic numbers from  ${}_{22}\text{Ti}$  to  ${}_{51}\text{Sb}$  is a well known phenomenon with Monte Carlo simulations based on MOTT cross-sections, whereas the values for high atomic numbers are found to fall well between the literature data.<sup>236</sup> No serious discrepancies from reference data are observed for any element. Simulations of the backscatter coefficient of multicomponent samples are also in accordance with the linear mass weighed superposition of the single element contributions as expressed in *eq. 2.43*.

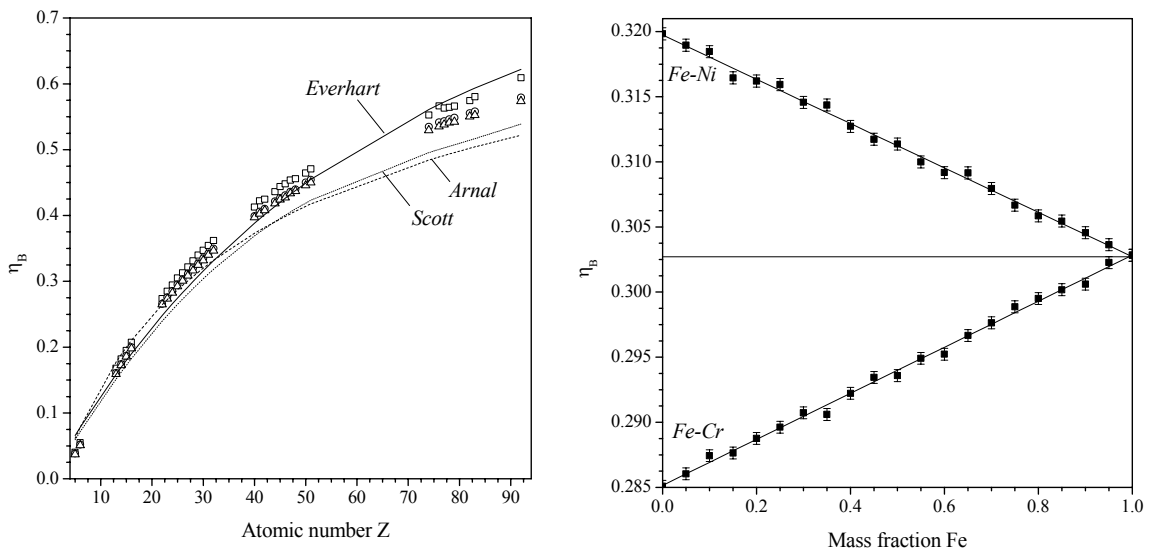


**Figure 6-1.** Monte Carlo simulated backscatter coefficients for elements ranging from  ${}_5\text{B}$  to  ${}_{92}\text{U}$  at 10 ( $\square$ ), 20 ( $\circ$ ), and 30 keV ( $\triangle$ ) primary beam energy and normal incidence. Values reported by EVERHART<sup>231</sup> (solid line), SCOTT et al.<sup>91</sup> (dotted line) and ARNAL<sup>234,235</sup> (dashed line) are depicted for comparison.

**Figure 6-2.** Monte Carlo simulation of the backscatter coefficient in the binary systems Fe-Cr and Fe-Ni at 20 keV primary beam energy at normal beam incidence. The linear superposition of the pure element backscatter coefficients (eq. 2.43, indicated by solid lines) is reproduced by the simulations.

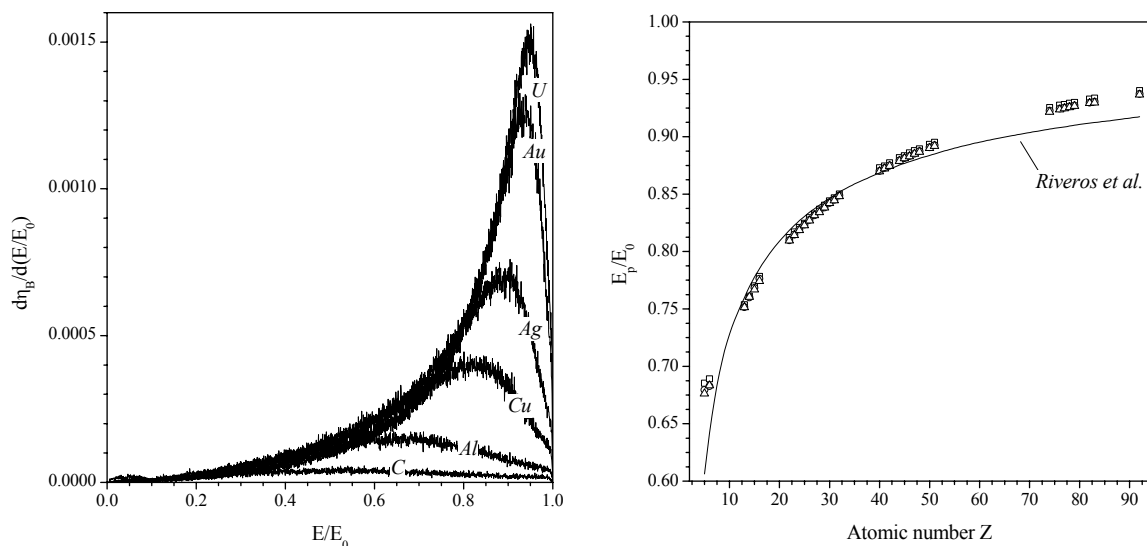


**Figure 6-3.** Spectral distribution of backscattered electrons from different pure element samples at 20 keV primary beam energy at normal incidence, simulated with Monte Carlo methods.

**Figure 6-4.** Reduced most probable relative energy  $E_p/E_0$  of backscattered electrons at 10 ( $\square$ ), 20 ( $\circ$ ), and 30 keV ( $\triangle$ ) primary beam energy compared obtained by Monte Carlo simulation and compared to values reported by RIVEROS et al.<sup>161,162</sup> All Monte Carlo simulation results presented in this and the previous figures are based on  $10^6$  electron trajectories.

This is demonstrated in Figure 6-2 displaying the backscatter coefficient of the binary model systems Fe-Cr and Fe-Ni at a primary beam energy of 20 keV and normal incidence over the whole concentration range. Only negligible deviations from the expected straight line behaviour are found, which are attributed to uncertainties in the assessment of the sample density given in the literature<sup>238</sup> and slightly influencing the simulation results.

Mean ionisation potentials increase with atomic number according to *eq. 2.24*, and consequently energy losses per path length resulting from the BETHE formula (*eq. 2.36*) decrease. For this reason, the most probable energy of backscattered electrons shifts to lower values for elements with decreasing atomic number, which is confirmed by Monte Carlo simulations. Figure 6-3 shows the backscatter spectra of different pure elements at 20 keV and normal incidence originating from the simulation of  $10^6$  electrons. Spectra are sharply peaked at energies close to the primary beam energy for heavy elements. The profiles, however, flatten with decreasing atomic number and the shift of the maximum towards lower energies is accompanied by a loss of spectral intensity due to the diminishing backscatter coefficient.

RIVEROS et al.<sup>161,162</sup> pointed out that the shape of backscatter spectra can be described by a POISSONIAN distribution function in very good accuracy according to :

$$\frac{d\eta_B(p)}{dp} = \eta_B \frac{p}{\lambda^2} e^{-\frac{p}{\lambda}} \quad (6.4)$$

in which the backscatter coefficient  $\eta_B$  serves as scaling factor. In this expression, the independent variable  $p$  is related to the electron energy  $E$  by :

$$p = 1 - \frac{E}{E_0} \quad (6.5)$$

The variable  $\lambda$  describes both the width of the distribution and its maximum. It is parametrised with the atomic number of the scattering element but does not depend on the primary beam energy.<sup>161,162</sup> Carlo simulated backscatter spectra of numerous elements irradiated at primary electron energies between 10 to 30 keV were fitted to the POISSONIAN distribution of *eq. 6.4*.

When  $p$  equals  $\lambda$ , the maximum of the distribution function is reached and renders the reduced most probable energy of backscattered electrons  $E_p/E_0$ , which is predicted to be independent of the primary beam energy  $E_0$  by *eq. 6.4*. As depicted in Figure 6-4, the resulting relationship between the most probable energy of backscattered electrons  $E_p/E_0$  and the atomic number  $Z$  matches the reference data.<sup>161,162</sup> Though deviations occur for light elements like  ${}_5\text{B}$  and  ${}_6\text{C}$ , and data for very high atomic numbers are slightly overestimated, an excellent agreement is observed for most elements. Finally, the expected independence of  $E_p/E_0$  on the primary beam energy is also reproduced by Monte Carlo simulations and renders the modelling of backscattering basically correct.

### *6.1.2 Intensity of Characteristic Radiation*

In the case of pure elements, the computation of characteristic X-ray intensities excited below the sample surface is reduced to the evaluation of the backscatter factor and the stopping power integral as defined in *eq. 3.20*. A survey of  $K_\alpha$  X-ray intensities as a function of atomic number and at different primary beam energies is given in Figure 6-5. As discussed in section 3.3.1, the number of photons generated by an electron beam reduces with increasing atomic number and decreasing primary beam energy. In contrast to fundamental parameter methods, the proposed Monte Carlo algorithm is not designed to start quantification by calculating X-ray intensities generated within the sample, but rather collects the spectral intensity in a virtual multichannel analyser memory. By keeping track of the number of quanta released at each interaction point of an electron in the sample, however, information on the total X-ray yield and the depth distribution profiles is gained. Except for a slight underestimation of intensities at low atomic numbers, the results of Monte Carlo simulations plotted in Figure 6-5 are in close agreement with the ZAF model<sup>46,175</sup> up to a primary beam energy of 20 keV. At higher energies, Monte Carlo simulated intensities are slightly higher than those predicted by the ZAF approach for elements of medium atomic number.

For reasons of computational simplicity, the dependence of characteristic X-ray intensity on primary beam energy is usually expressed by a power law with constant exponent as discussed in connection with *eq. 3.24*. Detailed investigations, however, reveal that for a more precise description the exponent varies for different elements and is found to be close to one for light elements but increases to a value of 1.72 for  ${}_{47}\text{Ag}$ .<sup>164</sup>

---

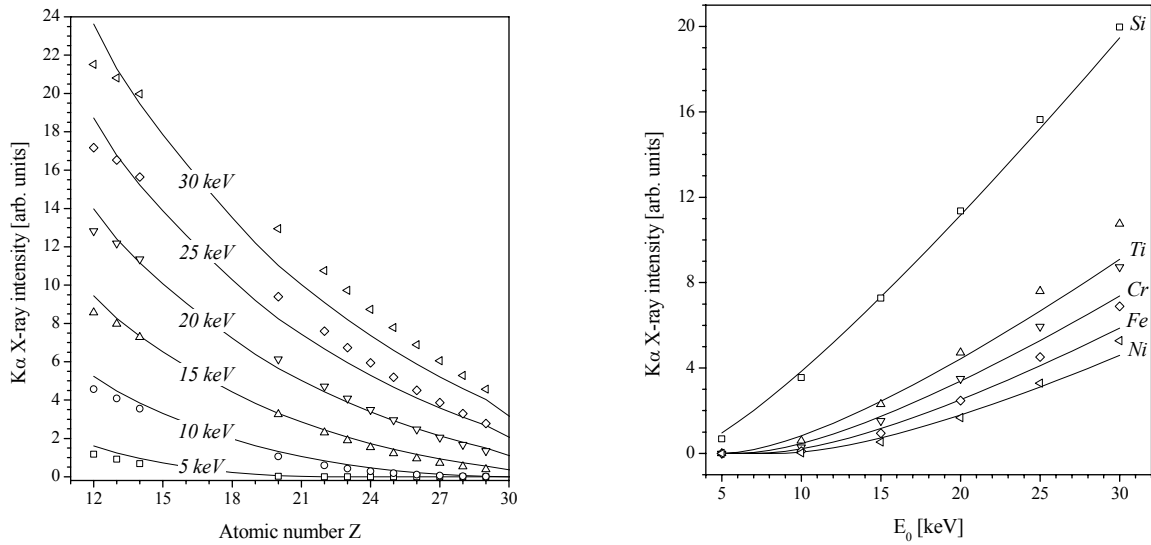


**Figure 6-5.** Atomic number dependence of K $\alpha$  X-ray intensity predicted by the ZAF model of WERNISCH et al.<sup>46,175</sup> for different primary beam energies (solid lines). Data originating from Monte Carlo simulations (symbols) are also plotted.

**Figure 6-6.** Total intensity of K $\alpha$  X-rays produced by various elements as a function of primary beam energy. Monte Carlo simulations (symbols) are compared to empirically determined data (solid lines) due to eq. 3.24 with numerical values provided by COSSLETT.<sup>164</sup>

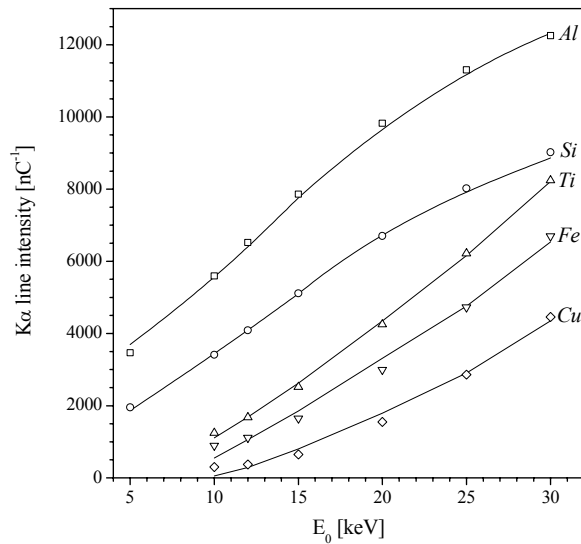


**Figure 6-7.** Intensity of K $\alpha$  X-rays emitted from several pure element samples under a take-off-angle of 35°. Measurements (solid line) were performed with a Si(Li) detector (see section 5.2.1 for details) and cover overvoltage ratios ranging from 1.1 for copper to 19.2 for aluminium. Monte Carlo simulations (symbols) are shown to be in accordance with the empirical data (solid lines).

Intensities obtained by Monte Carlo simulations agree more closely with those calculated by the empirically adjusted power law (*eq. 3.24*) as to be seen from Figure 6-6. This circumstance indicates that the discrepancies observed in Figure 6-5 originate from approximations inherent to the ZAF procedure.

The increase of the characteristic intensity with primary electron energy is partially compensated by self-absorption as X-ray generation shifts to larger depths. This effect is almost negligible for medium atomic numbers but especially pronounced for light elements. Measurements of  $K_{\alpha}$  intensities emitted from several pure element samples performed in the microanalyser system described in section 5.2.1 with different primary beam energies are presented in Figure 6-7. Comparison with the generated intensities in Figure 6-6 shows that attenuation has little effect on the X-ray intensity emitted from  ${}_{29}\text{Cu}$ . In contrast, the almost linear increase in the case of  ${}_{13}\text{Al}$  and  ${}_{14}\text{Si}$  is considerably reduced at primary beam energies above 20 keV. Monte Carlo simulations are in accordance with the experimental data indicating that the gain in the depth of X-ray generation with primary beam energy is correctly modelled.

More detailed information is provided by the depth distribution function  $\varphi(\rho z)$  of X-ray generation, which is also independent of the correctness of mass absorption coefficients. Monte Carlo simulated  $K_{\alpha}$  depth distribution profiles of aluminium and copper at various primary beam energies are exemplarily depicted in Figure 6-8. As expected, the maximum of X-ray generation shifts to higher mass depths with increasing primary beam energy. In the same direction, the enlarged area below the profiles reflects the gain of intensity generated below the sample surface according to *eq. 3.24*. Compared to the functions given by the modified GAUSSIAN model<sup>109,173,239-241</sup>, Monte Carlo simulated profiles reach their maximum at higher mass depths but are also more strongly attenuated towards deeper sample layers. The maximum depth of X-ray generation  $\rho z_{\text{max}}$  as a function of primary beam energy is plotted in Figure 6-9 for different models. The results of Monte Carlo simulations are close to the values predicted by the quadrilateral model and tend to shift towards those provided by the modified GAUSSIAN approach with increasing atomic number. In general, the maximum depths of X-ray generation rendered by the present Monte Carlo approach are well within the range of data produced by different fundamental parameter methods and prove the shape differences of the depth distribution profiles observed above to be of minor importance.

---

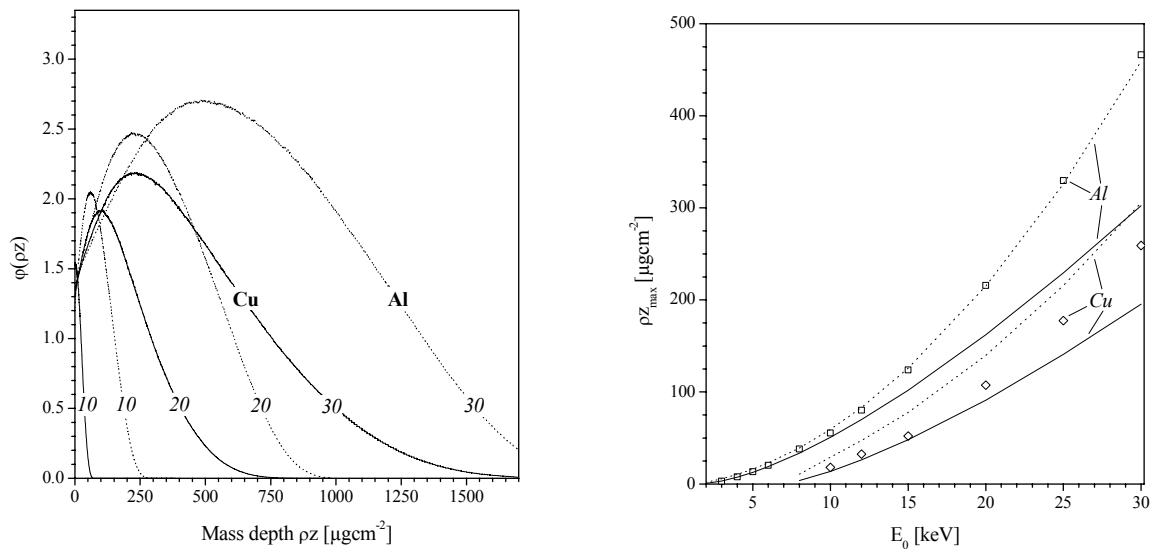


**Figure 6-8.**  $K_{\alpha}$  depth distribution profile  $\phi(\rho z)$  in pure aluminium (dotted line) and copper (solid line) at different primary beam energies and normal incidence resulting from Monte Carlo simulations. Numbers indicate the primary beam energy in units of keV.

**Figure 6-9.** Mass depth  $\rho z_{\max}$  of maximal  $K_{\alpha}$  X-ray production in pure aluminium and copper at different primary beam energies at normal incidence. Data obtained from the quadrilateral<sup>167</sup> (dotted line) and modified GAUSSian<sup>109,173,239-241</sup> (solid line) model are displayed with results of Monte Carlo simulations (symbols). All Monte Carlo simulation results presented in this and the previous figures are based on  $10^6$  electron trajectories.

## 6.2 Simulation of X-Ray Emission Spectra

Depending on the primary beam energy and sample composition, an electron experiences  $1 \cdot 10^3$  to  $4 \cdot 10^3$  scattering events until it has lost its entire kinetic energy. Neglecting backscattering, an ensemble of  $10^4$  electrons thus requires the simulation of about  $1 \cdot 10^7$  to  $4 \cdot 10^7$  interactions with atoms. Photons are very likely annihilated in the photoelectric process. Secondary and higher order fluorescence effects and scattering events increase the number of interaction sites, but these are comparably rare events. Therefore, the number of interaction sites to be simulated is only slightly larger than the ensemble size of primary photons in X-ray fluorescence analysis. The statistical significance achieved in a Monte Carlo calculation, however, is proportional to the number of simulated probe-matter interactions. Therefore, larger ensembles of primary projectiles are required in X-ray fluorescence than in electron microprobe analysis to gain the same level of significance. The effect on this circumstance on the necessary computation time is discussed in section 6.4.

In order to maintain the highest possible computational speed, it is advisable to keep all necessary quantities available in the computer memory. Analytical formulae to compute electron-matter interaction cross-sections exist and are readily inverted to facilitate the random choice of scattering angles.<sup>205</sup> As discussed in section 4.2.4, X-ray scattering is described in terms of the cumulative probability distribution functions  $F_i(E, \theta)$  and their inverse  $F_i^{-1}(E, R)$  for which only numerical expressions are found. A discrete representation of these surfaces is obtained by evaluating the corresponding bicubic splines. As depicted exemplarily in Figure 4-4 and Figure 4-5, the cumulative probability distribution functions  $F_i(E, \theta)$  and their inverses  $F_i^{-1}(E, R)$  are smoothly curved as a function of energy, but exhibit a stronger dependence on the scattering angle  $\theta$  and the random number  $R$ , respectively. Therefore, a grid containing twenty knots in the energy range of interest and 200 knots in dimensions of scattering angle and random number was found to be adequate for discretisation. Random sampling is performed on matrices providing the working space for this operation. Data located between the grid points are extracted by bilinear interpolation in a computationally very efficient way without introducing significant errors.<sup>187</sup> In a similar manner, the total cross-sections for the photoelectric effect, RAYLEIGH and COMPTON scattering are computed at 2000 grid points within the energy range of interest and stored in arrays to ensure fast access. Linear interpolation is straightforwardly applied to calculate cross-sections at arbitrary energies. In total, the description of X-ray scattering and absorption requires the storage of 22000 real numbers corresponding to a data size of about 172 kB per element. The memory size necessary to store all other parameters, for example absorption edge energies, transition probabilities, and fluorescence yields, is negligible. Even under the most unfavourable analytical conditions, current memory sizes by far exceed these requirements. Calculating the  $F_i(E, \theta)$  and  $F_i^{-1}(E, R)$  surfaces and the total cross-sections only once from the database<sup>53,197</sup> prior to each simulation, however, significantly enhances the computational speed.

In the course of a Monte Carlo simulation of X-ray emission, the spectral response of the sample as defined in section 4.4.1 is collected in an array representing a virtual multichannel analyser memory. As the resolution of any spectrometer system by far exceeds the natural width of an X-ray emission line, the energy gain of the virtual multichannel analyser can be freely chosen to suit the requirements of the particular detection unit to be modelled. The spectral response of a pure copper sample excited with a 15 keV electron beam at normal incidence obtained by Monte Carlo simulation of  $10^4$  trajectories is depicted in Figure 6-10.

---

---

With a value of 10 eV/channel, the energy gain of the virtual detection unit was chosen to equal that of the energy dispersive Si(Li) detector used to acquire experimental data. Throughout all simulations electrons were traced down to an energy of 20 eV.

The characteristic X-ray emission lines of copper appear as sharp peaks superimposed to the Bremsstrahlung background. The more detailed view of the peak region shows the discontinuity expected due to the Cu K edge at 8.980 keV. It is also clearly visible that data produced by Monte Carlo techniques are subject to white noise. The spectral response denotes the energy distribution of X-rays emitted from the sample into the direction of the detector, which is inherently unmeasurable as interference with the detector itself is not yet regarded at this stage. Peak shaping is described as discrete convolution with an appropriate GAUSSIAN profile according to *eq. 4.53*, and the effect of the Si(Li) detector specified in section 5.2.1 on the spectral response of a pure copper sample is also depicted in Figure 6-10. White noise observed in the spectral response is strongly smoothed when converted into a spectrum because the content of every channel is distributed over several of its neighbours. Signal-to-background ratios, however, deteriorate due to the limited resolution. The averaging effect of the convolution leaves the background level as a weakly varying feature almost unaffected, but strongly reduces the amplitude of characteristic peaks.

Scaling of the simulated spectrum presented in Figure 6-10 to experimental data was performed by application of *eq. 4.54* with the region of interest set to the Cu  $K_{\alpha}$  peak and within an energy window defined by *eq. 3.49*. Figure 6-11 depicts the result of this operation and indicates that the scaling factor derived for the Cu  $K_{\alpha}$  line correctly applies to the entire spectrum. Good agreement between theory and experiment is demonstrated quantitatively by the low differences between simulated and measured data. A weak upward drift of the difference spectrum towards higher energies is observed and points to the fact that the continuous background is underestimated at low energies, whereas slight overestimation is encountered in the high energy region of the spectrum. Errors are introduced due to the variation of KRAMERS 'constant' with energy and atomic number, but these are rather low. In addition, the difference spectrum is curved towards positive and negative values in the peak regions. As contributions from either side of the peak centre balance each other, this phenomenon results from a minute shift of the measured emission lines from their expected position as a consequence of slightly incorrect spectrometer calibration.

---

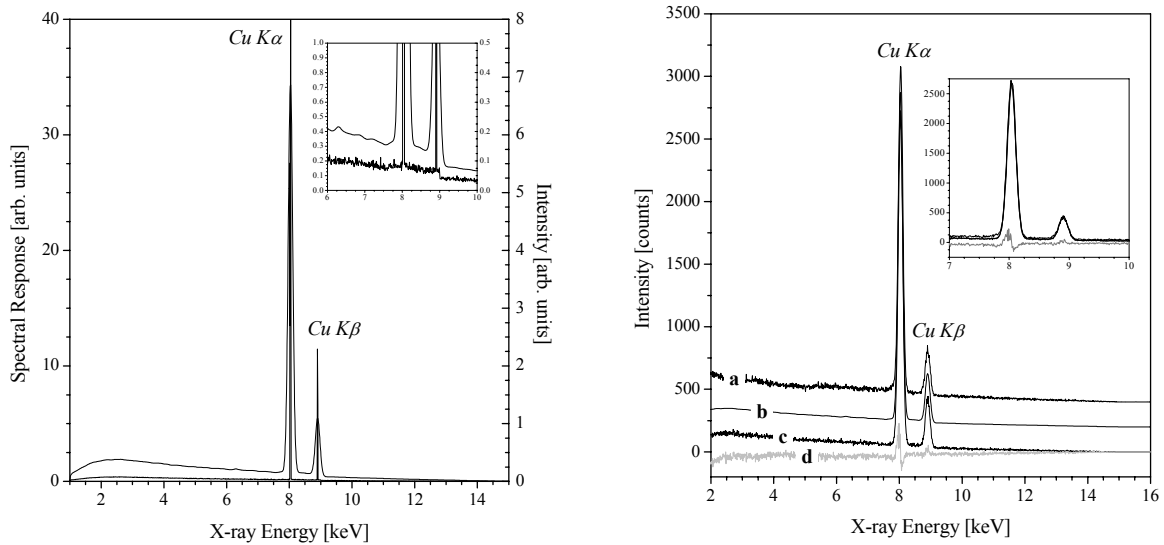


**Figure 6-10.** Monte Carlo simulated spectral response emitted from a pure copper sample under a take-off angle of  $35^\circ$  when excited with electrons at an energy of 15 keV. The spectrum depicted was obtained by convolution with the resolution of a Si(Li) detector as described in eq. 4.53.

**Figure 6-11.** Electron excited X-ray emission spectra of a pure copper sample, recorded with a Si(Li) detector. (a) Measured spectrum (probe current 190 pA at 15 keV primary beam energy at normal incidence, 300 sec live time), (b) Monte Carlo simulation of  $10^4$  electron trajectories scaled to experimental data, (c) Monte Carlo simulation with POISSONIAN noise, (d) difference of simulation data (b) and experiment. Spectra in the inlay are shown without offset.

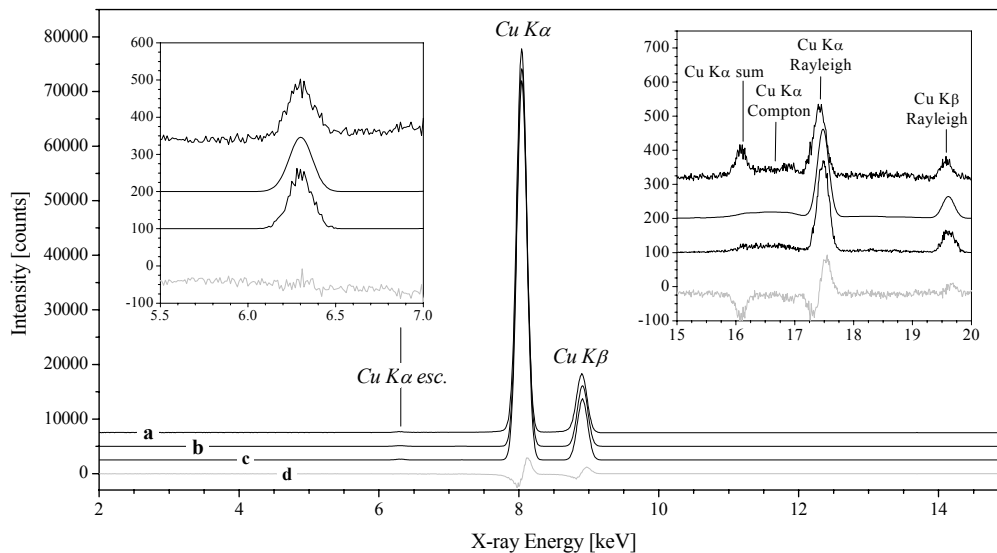


**Figure 6-12.** X-ray fluorescence spectra of pure copper obtained in the scanning electron microscope as described in section 5 in detail. (a) Experiment (12.5  $\mu\text{m}$  Mo target and filter operated with a probe current of 378 nA at 30 keV primary beam energy, 600 sec live time), (b) Monte Carlo simulation of  $10^6$  photons sampled from a dichromatic source scaled to measured data, (c) Monte Carlo simulation with POISSONIAN noise added, (d) difference of simulation data (b) and experiment. The spectra are offset for clarity.

An enlarged view of the peak region given in Figure 6-11 shows that theoretical and experimental data are hardly to be distinguished from each other, especially when white POISSONIAN noise is added to the simulated spectrum to account for the counting statistics.

An X-ray fluorescence spectrum of a pure copper sample obtained in the scanning electron microscope is presented in Figure 6-12. The sample was excited by primary X-rays emerging from a 12.5  $\mu\text{m}$  molybdenum anode operated at a primary beam energy of 30 keV and combined with a molybdenum filter of the same thickness. The lack of Bremsstrahlung background is reflected in a signal-to-background ratio as high as 399.2 for the Cu  $K_{\alpha}$  line, which by far exceeds the value of 25.6 as achieved in the electron excited copper spectrum discussed above. Again, comparison with a Monte Carlo simulation based on  $10^6$  photons assumed to originate from a dichromatic source of Mo  $K_{\alpha}$  and Mo  $K_{\beta}$  radiation shows excellent agreement with the experimental data in the characteristic peak region. Though only scaled to the Cu  $K_{\alpha}$  line, the simulation is also found to model the scatter region of the spectrum correctly. COMPTON scattering of the Cu  $K_{\alpha}$  line gives rise to a very broad feature in the energy range between 16 and 17 keV. On its low energy side, it is overlaid by the Cu  $K_{\alpha}$  sum peak at 16.082 keV, which is not included in the simulation. The Mo  $K_{\alpha}$  RAYLEIGH scatter line is broader than predicted by the Monte Carlo simulation, and a slight shift in its position is noted again.

With electron excitation, the Cu  $K_{\alpha}$  escape peak located at 6.301 keV is obscured by Bremsstrahlung, which is not the case in X-ray fluorescence analysis owing to the low background level. Escape peaks are straightforwardly modelled by applying *eq. 3.36* to every channel of the Monte Carlo simulated spectral response of the sample. This is accomplished in a single-pass routine prior to convolution with the peak profile function. As to be seen from Figure 6-12, this procedure is capable of accurately modelling the escape peak intensity.

### 6.3 Quantitative X-Ray Emission Spectroscopy

Spectra obtained by Monte Carlo simulations are in close agreement with experimental data and thus prove the probabilistic interpretation of X-ray and electron-matter interactions as outlined in section 4 to be basically correct. Monte Carlo simulation of X-ray emission spectra is therefore a promising tool for standardless quantitative X-ray fluorescence and electron microprobe analysis. The best fit between experimental and simulated spectra of multielement samples is achieved by iteratively adjusting the composition according to the

---

principles discussed in section 3.5. In the case of X-ray fluorescence analysis, characteristic line intensities can vary very strongly with concentration. This effect is particularly marked for heavy elements embedded in a light matrix and has been demonstrated in connection with the X-ray fluorescence spectrum of Al97.5/Si1.0/Mg0.8/Mn0.7 where traces of manganese, iron, and copper give rise to signals, which are in sum stronger than the emission line of the aluminium matrix. For this reason, the application of the WEGSTEIN iteration formula (*eq. 3.44*) is especially advantageous to ensure convergence. Though relative line intensities are generally closer to the concentrations of the corresponding elements in electron microprobe analysis, nonlinear iteration accelerates convergence and thus enhances computation speed.

Monte Carlo simulation is designed to produce spectra which are directly comparable to experimental data. Therefore, GAUSSIAN fitting in order to integrate characteristic emission lines and peak overlap correction are not required. Due to excellent signal-to-background ratios in X-ray fluorescence analysis, it is also not necessary to perform background subtraction. Thus, X-ray excited spectra are quantitatively evaluated by Monte Carlo methods without the need of preprocessing. Iterations were based on  $K_{\alpha}$  line intensities extracted from experimental and simulated data by simply adding the content of the corresponding channels within an energy window defined by *eq. 3.49*. After each iteration step, simulations are scaled to experimental data by means of *eq. 4.54*. The region of interest for this process is composed of all channels belonging to  $K_{\alpha}$  lines. X-ray fluorescence spectra were simulated using  $10^6$  photons emerging from a dichromatic source according to *eq. 4.8*. Convergence was assumed to be achieved when the change of all concentrations in successive iteration steps was found to be below  $10^{-5}$ , corresponding to three significant digits in the composition when expressed as percentage. Thus an accuracy well below the statistical errors encountered in common applications is provided.

Examples of iteratively refined Monte Carlo spectrum simulations are provided in Figure 6-13 in connection with the quantitative analysis of Co49/Fe49/V2 (PERMENDUR 49) excited by different X-ray sources in the scanning electron microscope. No serious discrepancies between simulated and experimental spectra are detectable. Difference spectra reveal moderate peak shifts, which are, however, too low to affect quantification results. Simulated scatter intensities are basically correct although the width of the elastic Mo  $K_{\alpha}$  scatter line is underestimated. These discrepancies are, however, not introduced by the simulation algorithm itself as they are totally absent in spectra excited by Cu K radiation.

---

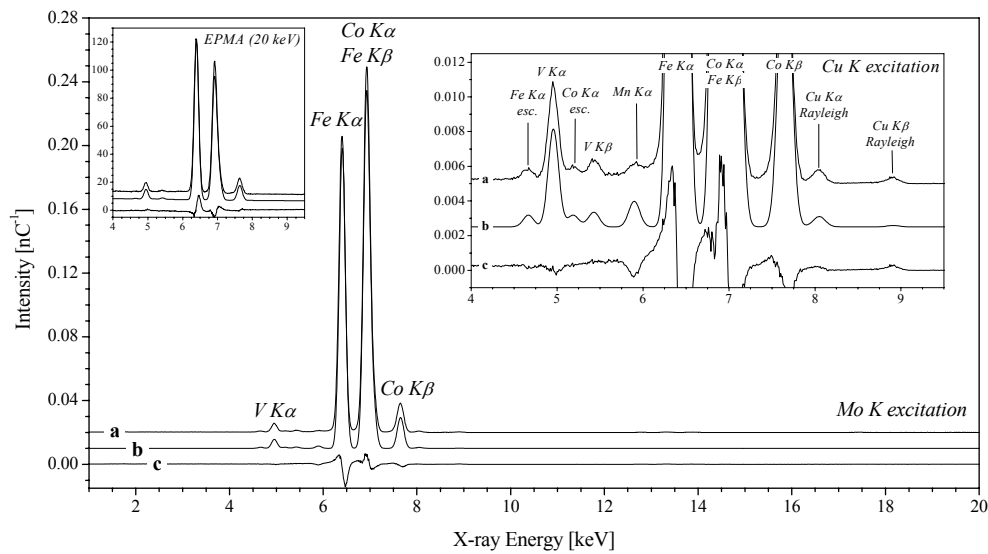


**Figure 6-13.** Quantitative X-ray fluorescence analysis of Co49/Fe49/V2 (PERMENDUR 49) in the scanning electron microscope under different excitation conditions. Measured spectra (a) were excited by Mo K radiation (12.5  $\mu\text{m}$  Mo anode and filter, 378 nA at 30 keV, 1200 live sec) and Cu K radiation (10  $\mu\text{m}$  Cu anode combined with a 34  $\mu\text{m}$  Cu filter, 253 nA at 30 keV, 1200 live sec), respectively. Iteratively refined Monte Carlo simulations (b) result from  $10^6$  photons incident from a dichromatic X-ray source. The difference spectrum between simulation and experiment (c) demonstrates good agreement between theory and experiment. The result of Monte Carlo based quantitative electron microprobe analysis is also depicted for comparison. All spectra are offset for clarity.

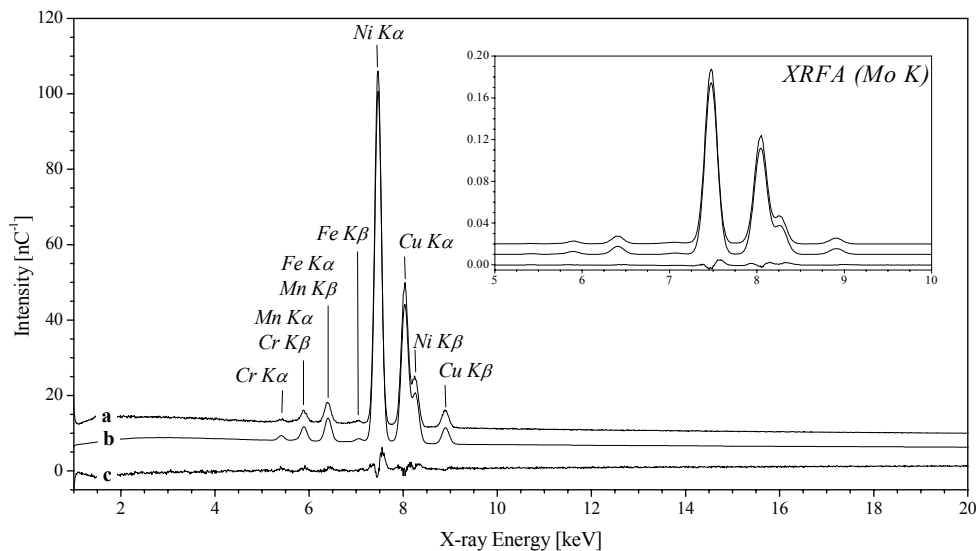


**Figure 6-14.** Quantitative electron microprobe analysis of Ni65/Cu33/Fe2 (MONEL alloy 400). (a) Measured spectrum (194 pA at 20 keV, 900 live sec), (b) iteratively refined Monte Carlo simulation ( $10^4$  electrons), and (c) difference between simulated and measured spectrum. Analysis is performed without background subtraction, overlap correction, or peak fitting. Monte Carlo based X-ray fluorescence analysis of the same sample using Mo K radiation is depicted in the inlay for comparison.

The Monte Carlo simulation correctly reproduces scattering of the Cu  $K_{\alpha}$  and  $K_{\beta}$  source lines from the sample. In both cases, escape peaks originating from the Fe  $K_{\alpha}$  and Co  $K_{\alpha}$  emissions located on either side of the V  $K_{\alpha}$  line are also correctly modelled by *eq. 3.36*. Quantitative results of X-ray fluorescence analyses of Co49/Fe49/V2 (PERMENDUR 49) and Ni65/Cu33/Fe2 (MONEL alloy 400) under different excitation conditions are summarised in Table 6-2.

	Co/49Fe49/V2 (PERMENDUR 49)				Ni65/Cu33/Fe2 (MONEL alloy 400)			
method	MC [%]		FP [%]		MC [%]		FP [%]	
excitation	Cu $K_{\alpha/\beta}$	Mo $K_{\alpha/\beta}$	Cu $K_{\alpha/\beta}$	Mo $K_{\alpha/\beta}$	Mo $K_{\alpha/\beta}$	Ag $K_{\alpha/\beta}$	Mo $K_{\alpha/\beta}$	Ag $K_{\alpha/\beta}$
$^{23}\text{V}$	3.07 <sub>8</sub>	3.1 <sub>1</sub>	2.99 <sub>8</sub>	3.3 <sub>1</sub>	---	---	---	---
$^{24}\text{Cr}$	---	---	---	---	0.49 <sub>4</sub>	0.50 <sub>5</sub>	0.36 <sub>3</sub>	0.38 <sub>5</sub>
$^{25}\text{Mn}$	0.47 <sub>2</sub>	0.49 <sub>3</sub>	0.15 <sub>1</sub>	0.15 <sub>2</sub>	1.86 <sub>6</sub>	1.92 <sub>8</sub>	2.02 <sub>6</sub>	1.60 <sub>8</sub>
$^{26}\text{Fe}$	49.9 <sub>2</sub>	49.7 <sub>2</sub>	49.1 <sub>2</sub>	49.9 <sub>3</sub>	3.66 <sub>7</sub>	3.71 <sub>9</sub>	4.18 <sub>7</sub>	4.1 <sub>1</sub>
$^{27}\text{Co}$	46.6 <sub>2</sub>	46.7 <sub>2</sub>	47.7 <sub>2</sub>	46.7 <sub>2</sub>	---	---	---	---
$^{28}\text{Ni}$	---	---	---	---	63.0 <sub>2</sub>	63.8 <sub>3</sub>	64.1 <sub>2</sub>	64.0 <sub>3</sub>
$^{29}\text{Cu}$	---	---	---	---	31.0 <sub>1</sub>	30.1 <sub>2</sub>	29.4 <sub>1</sub>	29.9 <sub>2</sub>

**Table 6-2.** Exemplarical quantitative X-ray fluorescence analyses of alloys composed of first transition row elements. Spectra acquired in the scanning electron microscope under different excitation conditions were quantified by Monte Carlo simulation (MC) and conventional fundamental parameter methods (FP) for comparison. A graphical survey of experimental and simulated spectra is found in Figure 6-13 and Figure 6-14.

These are compared to concentrations determined from the same spectra using the fundamental parameter approach outlined in section 3.2.2.<sup>132,153-159</sup> For this purpose, background was removed by nonlinear iterative peak clipping as proposed by VOLKOV<sup>114</sup> prior to determination of characteristic peak intensities by GAUSSIAN fitting.<sup>206</sup> Intensity values were subsequently corrected for line overlap according to the procedure described by

---

REED<sup>58</sup> before entering the WEGSTEIN<sup>185</sup> iteration procedure *eq. 3.44*. Third-order fluorescence effects were incorporated into the fundamental parameter algorithm based on formulae reported in the literature.<sup>132,153-159</sup> Evaluation of improper integrals required by these formulae was performed using numerical standard techniques.<sup>206</sup> For both Monte Carlo and fundamental parameter quantification the statistical errors in concentrations are calculated by *eq. 3.50*.

Monte Carlo quantification is also successfully applied to electron microprobe analysis. An experimental emission spectrum of Ni65/Cu33/Fe2 at 20 keV is depicted together with an iteratively refined simulation of  $10^4$  electrons in Figure 6-14. Though the spectrum is rather complex due to the Cr  $K_{\beta}$ -Mn  $K_{\alpha}$ , Mn  $K_{\beta}$ -Fe $K_{\alpha}$ , and Cu  $K_{\alpha}$ -Ni  $K_{\beta}$  line overlaps, no preprocessing was performed prior to analysis. Nevertheless, the simulation is entirely consistent with the experiment except for negligible differences in the shape of the continuous background already discussed. Quantitative electron microprobe analyses of Co49/Fe49/V2 and Ni65/Cu33/Fe2 excited at energies ranging from 15 to 30 keV are given in Table 6-3.

Concentrations were also determined using the ZAF approach as outlined in section 3.3 in the numerical formulation of WERNISCH<sup>46,175</sup> and are listed for comparison. Background subtraction, peak fitting, and overlap correction were applied to the spectra using the algorithms mentioned above prior to performing the ZAF correction procedure.

These examples show that the proposed Monte Carlo technique correctly predicts X-ray emission spectra of multielement samples. It is therefore well suited to be employed for both standardless quantitative X-ray fluorescence analysis as well as electron probe microanalysis. From the analytical results exemplarily presented in Table 6-2 and Table 6-3, it is evident that concentrations are determined precisely from spectra acquired under different measuring conditions. Nevertheless, systematic trends in concentrations with varying primary beam energy are a commonly observed phenomenon in electron microprobe analysis. For example, the cobalt content of Co49/Fe49/V2 tends to decrease with increasing excitation energy when determined with the Monte Carlo method and develops in the opposite manner in the fundamental parameter approach. However, the figures indicate that this behaviour is more pronounced in fundamental parameter quantification. Monte Carlo analyses are in good agreement with results produced by fundamental parameter approaches. Usually, large relative deviations are observed with trace elements when comparing different analytical approaches. The determinations of manganese in Co49/Fe49/V2 and chromium in Ni65/Cu33/Fe2 by X-ray fluorescence analysis are therefore found to be least accurate. These

---

do, however, hardly affect the quantification of major components as absolute errors remain low.

method	Co49/Fe49/V2 (PERMENDUR 49)						Ni65/Cu33/Fe2 (MONEL alloy 400)			
	MC [%]			ZAF [%]			MC [%]		ZAF [%]	
$E_0$ [keV]	15	20	25	15	20	25	20	30	20	30
$^{23}\text{V}$	1.55 <sub>5</sub>	1.73 <sub>6</sub>	1.94 <sub>5</sub>	1.45 <sub>4</sub>	1.53 <sub>3</sub>	1.63 <sub>4</sub>	---	---	---	---
$^{24}\text{Cr}$	---	---	---	---	---	---	0.37 <sub>1</sub>	0.47 <sub>2</sub>	0.22 <sub>2</sub>	0.22 <sub>1</sub>
$^{25}\text{Mn}$	0.11 <sub>1</sub>	0.14 <sub>2</sub>	0.11 <sub>1</sub>	0.15 <sub>2</sub>	0.17 <sub>2</sub>	0.15 <sub>2</sub>	1.19 <sub>4</sub>	1.34 <sub>3</sub>	1.26 <sub>5</sub>	1.28 <sub>4</sub>
$^{26}\text{Fe}$	50.7 <sub>4</sub>	50.8 <sub>4</sub>	51.0 <sub>3</sub>	49.9 <sub>3</sub>	48.7 <sub>4</sub>	48.1 <sub>3</sub>	2.10 <sub>6</sub>	2.21 <sub>4</sub>	2.46 <sub>8</sub>	2.47 <sub>6</sub>
$^{27}\text{Co}$	47.6 <sub>4</sub>	47.4 <sub>4</sub>	47.0 <sub>2</sub>	48.5 <sub>4</sub>	49.5 <sub>4</sub>	50.2 <sub>3</sub>	---	---	---	---
$^{28}\text{Ni}$	---	---	---	---	---	---	63.9 <sub>5</sub>	62.9 <sub>3</sub>	63.1 <sub>5</sub>	60.5 <sub>3</sub>
$^{29}\text{Cu}$	---	---	---	---	---	---	32.5 <sub>4</sub>	33.1 <sub>3</sub>	32.9 <sub>4</sub>	35.5 <sub>3</sub>

**Table 6-3.** Quantitative electron microprobe analysis performed by Monte Carlo simulation and by applying a ZAF<sup>175</sup> correction procedure to spectra recorded at different primary beam energies. The data show a less pronounced energy dependent drift of concentrations in the case of Monte Carlo quantification. Details on the iterative refinement of simulated spectra are found in the text. Some of the spectra underlying the quantification results are plotted in Figure 6-13 and Figure 6-14.

In order to estimate the performance of Monte Carlo techniques, numerous commercial alloys containing elements between  $^{13}\text{Al}$  and  $^{29}\text{Cu}$  (listed in section 9.5) were subjected to X-ray fluorescence and electron microprobe analysis under various conditions. Theoretically, subsequent analyses of the same sample should render the same concentrations, which is hardly ever found in practice. Hence, precision is defined as deviation of a single determination from the mean concentration  $c_{\text{mean}}$  resulting from measurements under various excitation conditions. It describes the repeatability of analysis, which is either possible in terms of absolute concentration differences  $c - c_{\text{mean}}$  or by forming relative deviations  $c/c_{\text{mean}}$ . Absolute and relative precision were evaluated for both X-ray fluorescence and electron

microprobe analyses. They result in error distribution functions shown in Figure 6-15 and Figure 6-16 a and b, respectively. Information on the accuracy of the analytical procedure is gained by monitoring the determined concentration  $c$  relative to values  $c^*$  obtained by evaluation of the same data with a different matrix correction procedure regarded as standard. For this purpose, reference data were gained using conventional fundamental parameter approaches for X-ray fluorescence and electron microprobe analysis in connection with suitable preprocessing algorithms. Electron excited spectra were additionally quantified using the ZAF approach implemented in the commercially available software by EDAX.<sup>242</sup> Error distribution functions describing absolute accuracy  $c-c^*$  and relative accuracy  $c/c^*$  of Monte Carlo based X-ray fluorescence and electron microprobe analyses compared to fundamental parameter approaches are presented in Figure 6-15 and Figure 6-16 c and d.

The width of the absolute error distribution function reflects accuracy and precision in the determination of main components. In contrast, relative error distribution functions react rather sensitive towards deviations in trace analysis as significant relative errors are mainly encountered at low concentrations. Therefore, both absolute and relative precision and accuracy are considered to characterise the quality of Monte Carlo quantification. Though the distribution functions are rather noisy, it is clearly seen that they are properly centred around zero and one, respectively, thus showing that systematic deviations are not encountered. The cumulative representations also depicted in Figure 6-15 and Figure 6-16 appear smoother, and due to their sigmoidal shape it is justified to assume that errors are distributed in a GAUSSIAN manner. In this case, accuracy and precision are readily estimated by the standard deviation of the corresponding error distribution function. The features of different quantification algorithms including the proposed Monte Carlo approach are listed in Table 6-4 and Table 6-5.

Concerning electron microprobe analysis, absolute and relative precision achieved with the matrix correction procedure adapted from the literature are found to be virtually equal to the values obtained with a commercially available ZAF algorithm by EDAX.<sup>242</sup> This circumstance provides clear evidence that the combination of nonlinear peak clipping<sup>114</sup>, overlap correction<sup>58</sup>, and GAUSSIAN fitting<sup>206</sup> in connection with the ZAF procedure by WERNISCH<sup>175</sup> result in a valid quantification algorithm.

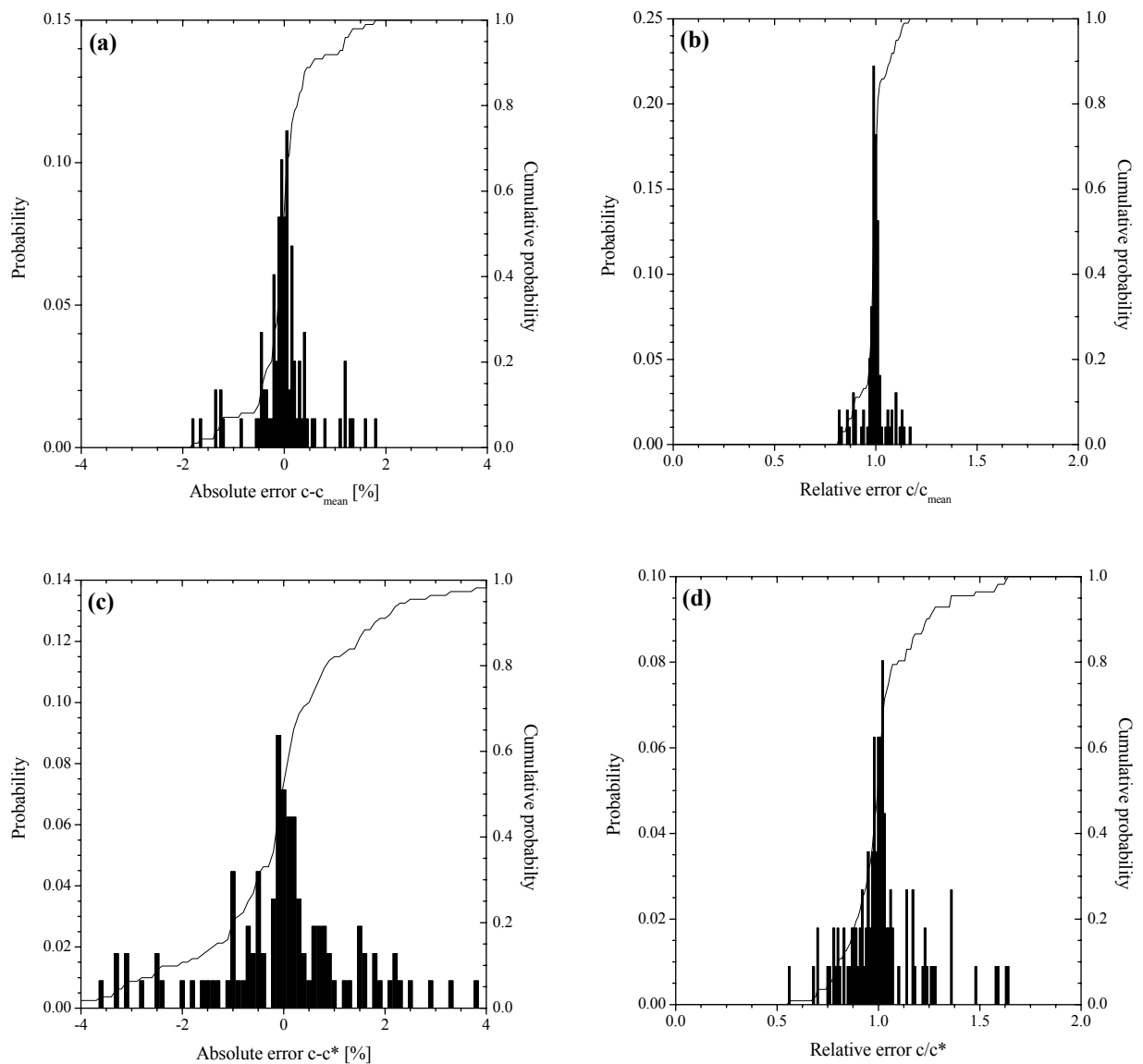


**Figure 6-15.** Error histograms characterising the performance of Monte Carlo techniques for standardless quantitative X-ray fluorescence analysis performed in the scanning electron microscope. 112 determinations of elements between  $_{13}\text{Al}$  and  $_{29}\text{Cu}$  excited with various X-ray sources and covering the entire range of concentrations are evaluated. Precision is described as **(a)** absolute and **(b)** relative deviation from the average concentration  $c_{\text{mean}}$  measured under different conditions. Accuracy is given by the **(c)** absolute and **(d)** relative deviation from concentrations  $c^*$  determined by a conventional fundamental parameter approach involving preprocessing of spectra. Cumulative probability distributions are also displayed.

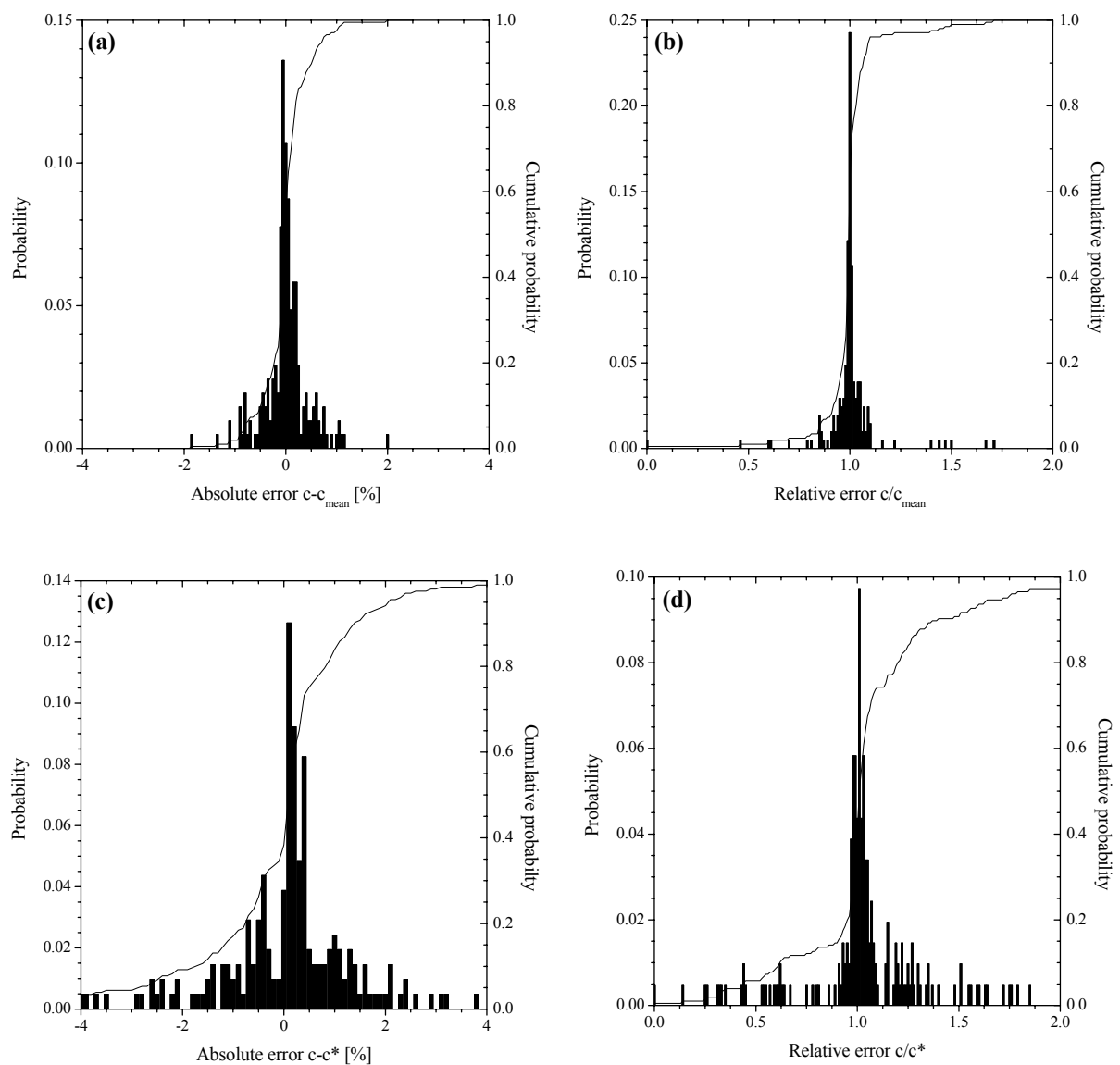


**Figure 6-16.** Statistical features of Monte Carlo techniques applied to standardless quantitative electron probe microanalysis. The error histograms summarise 206 determinations between  $^{13}\text{Al}$  and  $^{29}\text{Cu}$  with primary beam energies from 10-30 keV at normal beam incidence over the entire concentration range. In order to characterise precision, the (a) absolute and (b) relative deviation from the concentration average  $c_{\text{mean}}$  is given. Reference data  $c^*$  to determine (c) absolute and (d) relative accuracy are provided by a conventional ZAF correction procedure. Preprocessing of spectra prior to analysis was abandoned for Monte Carlo quantification but is necessary for the ZAF approach. Solid curves represent the cumulative probability distribution.

		XRFA		EPMA		
quantification		FP	MC	ZAF <sup>175</sup>	ZAF <sup>242</sup>	MC
precision	abs. [%]	0.050 <sub>5</sub>	0.11 <sub>2</sub>	0.065 <sub>8</sub>	0.061 <sub>5</sub>	0.11 <sub>1</sub>
	rel. [%]	1.6 <sub>2</sub>	1.3 <sub>2</sub>	0.73 <sub>5</sub>	0.74 <sub>3</sub>	0.83 <sub>5</sub>

**Table 6-4.** Comparison of the absolute and relative precision expressed as standard deviations of the corresponding error distributions achieved with different matrix correction procedures in X-ray fluorescence and electron microprobe analysis.

The relative precision achieved by fundamental parameter quantification of X-ray fluorescence spectra is lower compared to electron microprobe analysis, but values nevertheless indicate that the application of the above preprocessing routines is also established successfully in X-ray fluorescence analysis. In general, the precision of Monte Carlo quantification fits into the data obtained for fundamental parameter approaches. Their somewhat lower absolute precision appears well acceptable, especially as X-ray emission spectra are not preprocessed. In terms of relative precision, however, Monte Carlo quantification is comparable to fundamental parameter approaches in electron microprobe analysis, and is even found to exceed them in the case of X-ray fluorescence analysis.

		XRFA		EPMA	
reference		FP	ZAF <sup>175</sup>	ZAF <sup>242</sup>	
accuracy	abs. [%]	0.21 <sub>3</sub>	0.51 <sub>6</sub>	0.40 <sub>3</sub>	
	rel. [%]	2.7 <sub>4</sub>	3.4 <sub>2</sub>	3.0 <sub>1</sub>	

**Table 6-5.** Absolute and relative accuracy of Monte Carlo techniques in standardless quantitative X-ray emission spectroscopy. Reference concentrations are gained by evaluation of the same data by different fundamental parameter approaches. Figures represent standard deviations of the corresponding error distribution functions.

---

As summarised in Table 6-5, referencing of Monte Carlo quantification against fundamental parameter approaches indicates a relative accuracy of approximately 3 % in both X-ray fluorescence and electron microprobe analysis. These features reveal that the proposed Monte Carlo technique reaches a considerably higher level of accuracy than achieved by the fundamental parameter approaches reported in the literature.<sup>91,168,175,243</sup>

#### 6.4 Computation Speed

By condensing the large physical dataset summarised in Table 3-1 with a considerable amount of sophistication, fundamental parameter approaches fit theoretical characteristic X-ray line intensities into approximative analytical expressions. As they are straightforwardly implemented and most rapidly evaluated numerically, quantitative analysis with fundamental parameter methods is accomplished almost instantaneously. The correction of tertiary fluorescence effects in X-ray fluorescence analysis necessitates evaluation of an improper integral<sup>157</sup>, which rather decelerates analysis. However, computation times exceeding a couple of seconds to reach the convergence limit are hardly ever encountered for monochromatic or dichromatic excitation conditions.

Despite optimised variance reduction, Monte Carlo techniques are more time-demanding. The computational effort does not only increase with the number of elements per sample due to sampling from a longer list of elements (*eq. 4.20*), but also depends on the excitation conditions. The trajectories of primary X-ray photons are most probably terminated at their first interaction point by photoelectric absorption, and the number of subsequent secondary and higher order fluorescent events is usually rather limited. Electrons, however, experience a large number of scattering events within the sample until their path ends when the predefined cut-off energy of 20 eV is reached. Higher primary beam energies will result in longer computation times, as a larger number of interaction points has to be simulated due to the increased electron path. In addition, samples with a higher backscatter coefficient will be less time-consuming at a given primary beam energy. For these reasons, quantification of electron excited spectra by Monte Carlo methods is considerably more time-consuming than X-ray fluorescence analysis.

---

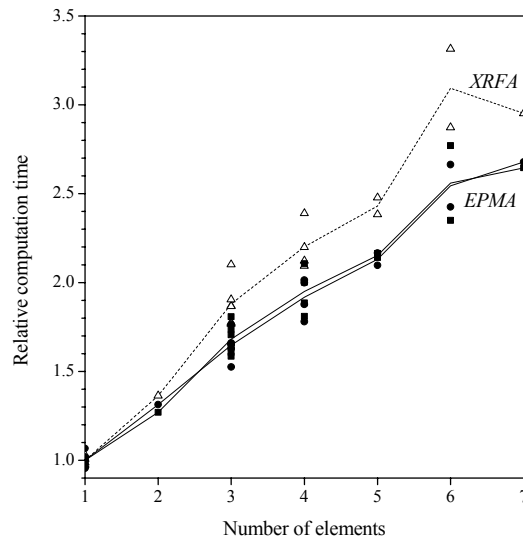


**Figure 6-17.** Dependence of the relative computation time on the number of elements present in the sample. Datapoints represent the computation time for samples listed in section 9.5 and pure aluminium, titanium, nickel, and copper, respectively. Excitation was due to Mo K ( $\Delta$ ) radiation and electrons with at an energy of 20 ( $\bullet$ ) and 30 keV ( $\blacksquare$ ). Solid lines represent the average computation time. All data were normalised to the average computation time for a pure element sample to eliminate the speed of the machine used. Simulations are based on  $10^6$  photons and  $10^4$  electrons per spectrum.

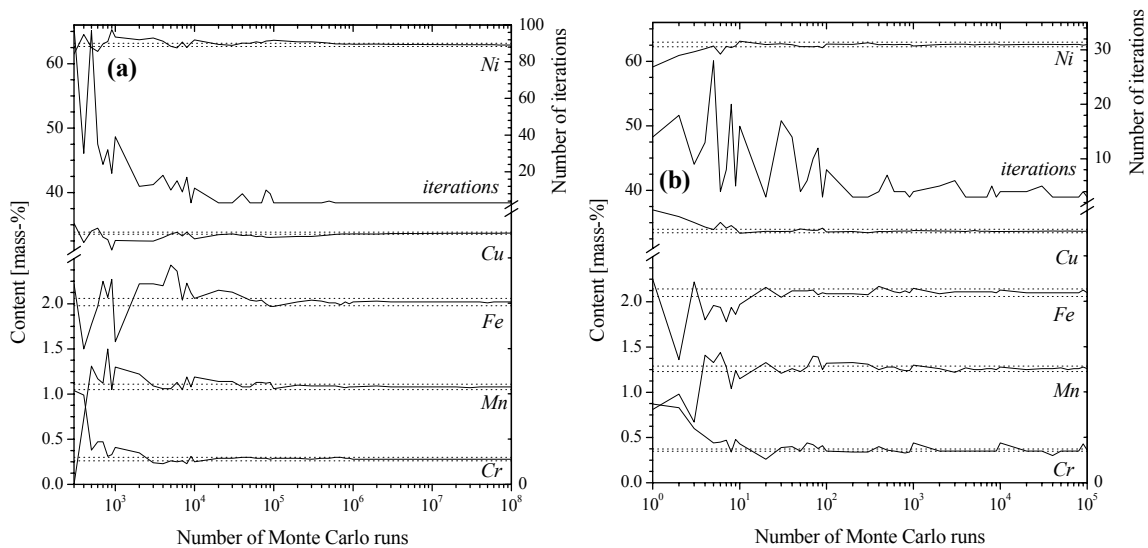


**Figure 6-18.** Quantification results for Ni65/Cu33/Fe2 (MONEL alloy 400) as function of the number of simulated primary (a) Mo K photons and (b) electrons at a primary beam energy of 30 keV. Dotted lines represent the statistical limits of sensitivity according to eq. 3.50 as calculated from the analysis with the maximum number of simulation runs. The number of iterations necessary to achieve the convergence limit of  $10^{-5}$  is also plotted.

The dependence of relative computation time on the number of elements per sample is plotted in Figure 6-17. Datapoints render the time necessary to simulate spectra of multicomponent samples listed in section 9.5 and of pure aluminium, titanium, nickel, and copper under conditions of X-ray fluorescence and electron microprobe analysis. In order to obtain a representation which reflects the performance of the Monte Carlo algorithm rather than the speed of the machine used, the data were normalised to the average of the computation time encountered for pure element samples. For a given number of elements, the computational effort is not uniform but scatters over a certain range. This effect is significantly more pronounced in the case of X-ray fluorescence analysis and is therefore attributed to the differing length of fluorescent pathways within the sample. As the numerical treatment is the same for every element, the differences observed with electron excited spectra are related to the varying amount of backscattering. The increase of average relative computation times is also depicted in Figure 6-17 and indicates a linear relationship with the number of elements present in the sample. It is evident that the relative computation time increases by approximately 35 % per element in the case of X-ray fluorescence and by only 28.5 % in electron microprobe analysis at 20 and 30 keV. This rather advantageous behaviour results from the circumstance that the various random decision processes in Monte Carlo simulation according to *eq. 4.20-4.22* are treated as a search in an ordered list, which is accomplished very efficiently.<sup>206</sup> In both experiment and Monte Carlo simulation, X-ray emission is a statistical process and governs the sensitivity of analysis. An increase in measuring time or number of simulated primary projectiles in Monte Carlo simulation, respectively, basically act in the same way and enhance analytical sensitivity via improvement of counting statistics. This is illustrated in Figure 6-18, which depicts the dependence of the quantification result on the number of trajectories simulated per spectrum. Concentrations are found to converge and fluctuate within the interval determined by the counting statistics of the experimental data according to *eq. 3.50* with simulation of  $10^6$  photons and  $10^4$  electrons in X-ray fluorescence and electron microprobe analysis, respectively. In the present example, the determination of chromium traces by electron microprobe analysis keeps fluctuating to values slightly above and below the statistical limits. This effect does not occur with X-ray fluorescence analysis and therefore originates from the slightly incorrect estimation of the background level as described in section 6.2.

The convergence of concentrations is accompanied by a drastic reduction in the number of iterations required. When the number of simulated trajectories is chosen too low, fluctuations

due to poor counting statistics lead to an overestimation of concentration correction in successive iteration cycles. Concentrations tend to oscillate in this case and convergence only occurs after a large number of iterations. For this reason, lowering the number of simulation runs does not necessarily decrease the computation time due to an increase in the number of iteration cycles, and, in addition, concentrations may converge towards inaccurate values.

With a convergence limit of  $10^{-5}$  corresponding to three significant digits in mass percentage, the refinement of simulated spectra is usually terminated after no more than four WEGSTEIN iteration cycles. According to *eq. 3.44*, two preceding steps of successive iteration have to be added, and therefore quantitative analysis is completed after simulation of six spectra. Under the conditions discussed above, this requires a total of  $6 \cdot 10^6$  primary photons and  $6 \cdot 10^4$  electrons to be simulated for X-ray fluorescence and electron microprobe analysis, respectively. The present simulation code implements the principles outlined in section 4 and is embedded in an interactive MICROSOFT WINDOWS multi-thread software, which was developed using DELPHI 5.0 by BORLAND. In a pure element sample, a single primary X-ray photon and subsequent processes are traced within an average time of 28.5  $\mu$ sec on an AMD ATHLON XP 1600+ personal computer. In contrast, average times of 1.3 and 2.0 msec are required to simulate one trajectory of electrons with energies of 20 and 30 keV, respectively, including all subsequent processes caused by X-rays. Considering the relationship between computation time and the number of elements, a typical X-ray fluorescence analysis of five elements takes 366 seconds. An average of 167 seconds is required for electron microprobe analysis at 20 keV and increases to 257 seconds at a primary beam energy of 30 keV. Though the time demand of Monte Carlo quantification exceeds that of fundamental parameter methods by far, it is still lower than common spectrum acquisition times unless a very fast energy dispersive X-ray detector is used. Therefore, Monte Carlo simulations are not restricted to offline use in standardless quantitative X-ray emission spectroscopy.

---

### 6.5 Detection Limits

The detection limit achieved for a particular analyte is governed by the signal-to-background ratio and the net X-ray intensity of its emission line, and therefore depends on the composition of the matrix into which it is embedded. For Ni65/Cu33/Fe2 (MONEL alloy 400), which comprises of elements with rather narrow range of atomic numbers, detection limits were determined under different excitation conditions by means of *eq. 3.47* and are depicted in Figure 6-19.

The reduction of Bremsstrahlung background with increasing primary beam energy in electron microprobe analysis improves signal-to-background ratios and the detection limits, which show an optimum for  ${}_{26}\text{Fe}$ . In contrast, detection limits tend to decrease with increasing atomic number in X-ray fluorescence analysis and are virtually equal for excitation by Mo K and Ag K radiation, respectively. Absence of Bremsstrahlung provides an improvement by a factor of about two to seven in the case of Ni65/Cu33/Fe2.

X-ray fluorescence analysis is, however, particularly well suited to resolve traces of heavy elements in a light matrix. Detection limits of elements present in Al97.5/Si1.0/Mg0.8/Mn0.7 are compared in Table 6-6 for various excitation conditions. A drastic decrease of the detection limits is observed with increasing atomic number of the analyte in X-ray fluorescence analysis.

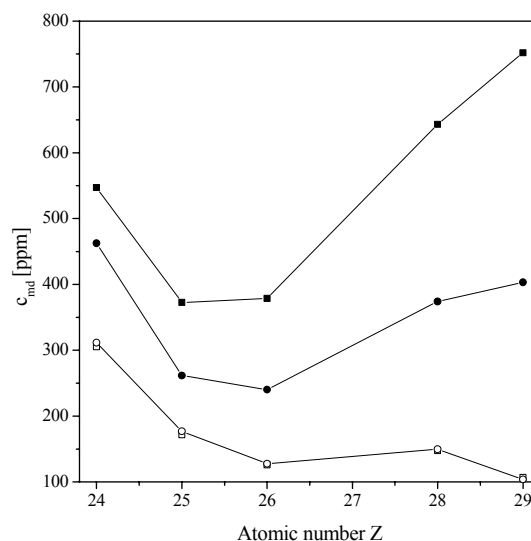


**Figure 6-19.** Detection limits  $c_{md}$  of elements present in Ni65/Cu33/Fe2 (MONEL alloy 400) investigated by electron microprobe analysis at 20 (■) and 30 (●) keV primary beam energy, and by X-ray fluorescence analysis in the scanning electron microscope using Mo K (□) and Ag K radiation (○). Figures refer to an acquisition time of 1200 sec.

The minimum value of 3.1 ppm Pb by mass corresponding to an atomic percentage of approximately 400 ppb is found with a 12.5  $\mu\text{m}$  Mo source, whereas the optimum for  $^{28}\text{Ni}$ ,  $^{29}\text{Cu}$  and  $^{30}\text{Zn}$  is obtained with a target foil thickness of 25  $\mu\text{m}$ . This indicates that in order to achieve the best detection limits not only the signal-to background ratio but rather the product of net intensity and signal-to-background ratio has to be maximised for the analyte in question according to *eq. 3.47*.

Line	Energy [keV]	$c_{\text{md}}$ [ppm] with excitation by						electrons 30 keV
		$^{42}\text{Mo}$ 12.5 $\mu\text{m}$	$^{42}\text{Mo}$ 25.0 $\mu\text{m}$	$^{42}\text{Mo}$ 37.5 $\mu\text{m}$	$^{42}\text{Mo}$ 50 $\mu\text{m}$	$^{22}\text{Ti}$ 50 $\mu\text{m}$		
$^{12}\text{Mg}$ $\text{K}_{\alpha}$	1.254	n.d.	n.d.	n.d.	n.d.	535.6	168.4	
$^{13}\text{Al}$ $\text{K}_{\alpha}$	1.487	3349.2	5904.3	7130.0	7707.9	253.6	128.6	
$^{14}\text{Si}$ $\text{K}_{\alpha}$	1.740	n.d.	n.d.	n.d.	n.d.	76.6	48.7	
$^{24}\text{Cr}$ $\text{K}_{\alpha}$	5.412	23.2	25.3	27.3	26.8	32.4	n.d.	
$^{25}\text{Mn}$ $\text{K}_{\alpha}$	5.985	17.7	19.1	21.8	21.8	26.2	115.4	
$^{26}\text{Fe}$ $\text{K}_{\alpha}$	6.399	12.0	12.9	15.1	15.4	16.9	125.8	
$^{28}\text{Ni}$ $\text{K}_{\alpha}$	7.472	6.4	6.0	6.6	6.7	7.6	n.d.	
$^{29}\text{Cu}$ $\text{K}_{\alpha}$	8.041	5.1	4.8	5.1	5.2	8.6	n.d.	
$^{30}\text{Zn}$ $\text{K}_{\alpha}$	8.631	4.9	4.8	5.0	5.1	5.7	n.d.	
$^{31}\text{Ga}$ $\text{K}_{\alpha}$	9.243	4.1	4.3	4.5	4.2	5.0	n.d.	
$^{82}\text{Pb}$ $\text{L}_{\alpha}$	10.551	3.1	3.6	3.8	3.5	3.7	n.d.	

**Table 6-6.** Detection limits  $c_{\text{md}}$  of elements in Al97.5/Si1.0/Mg0.8/Mn0.7 excited with various X-ray sources in the scanning electron microscope for 1200 sec. Elements higher than silicon are excited due to Bremsstrahlung contained in the excitation spectrum when working with a titanium X-ray source. The lowest detection limits to be obtained with electron microprobe analysis in the same instrument are also listed for comparison.

---

By lowering the excitation energy to Ti K radiation, traces of  $^{12}\text{Mg}$  and  $^{14}\text{Si}$  are resolved and the detection limit of  $^{13}\text{Al}$  is decreased from several thousand to about 250 ppm, which is only about two times larger than the best value achieved by electron microprobe analysis. As to be seen from Figure 6-19 and Table 6-6, the Bremsstrahlung continuum emitted from the  $^{22}\text{Ti}$  source also efficiently excites heavier elements as it contains a large range of suitable X-ray energies. Detection limits of elements from  $^{24}\text{Cr}$  to  $^{82}\text{Pb}$  are therefore only slightly higher compared to X-ray fluorescence analysis with Mo K radiation.

These examples show that X-ray fluorescence analysis in the scanning electron microscope enhances the detection limits of medium and high atomic number elements achievable with an energy-dispersive X-ray detector. With electron excitation, similar values are only achieved with wavelength-dispersive spectrometers providing better signal-to-background ratios due to their higher energy resolution. For heavy elements, however, the detection limits reported here are still slightly below those of wavelength-dispersive systems ranging down to typically 15-80 ppm under similar excitation conditions.<sup>21</sup>

## 6.6 Conclusions

X-ray and electron induced emission spectra simulated with Monte Carlo methods as outlined in section 4 are in good agreement with experimental data. Standardless quantitative X-ray fluorescence and electron microprobe analysis based on Monte Carlo techniques is possible with high accuracy and precision without the necessity of preprocessing spectra. X-ray fluorescence analysis in the scanning electron microscope significantly lowers the detection limits of medium and high atomic number elements achievable with an energy-dispersive X-ray detector. Additional analytical information on the sample under investigation is obtained simultaneously by using the novel unified Monte Carlo algorithm described.

---



## 7 Further Applications

The use of Monte Carlo techniques is very attractive in quantitative X-ray emission spectroscopy. Analyses are based on first principles, which are photon and electron scattering and diffusion, and therefore avoid the need to accept simplified assumptions. Monte Carlo simulations are computationally rather straightforward and versatile procedures, which allow easy implementation of special requirements concerning the experimental conditions. Insight into inherently unmeasurable details of analysis, for example the magnitude of interelement effects, is also provided by Monte Carlo methods.

### 7.1 Determination of k Ratios and Detection of Fluorescent Pathways

Along with the concentrations of each element, fundamental parameter approaches usually provide k ratios (denoted R in the case of X-ray fluorescence analysis). According to *eq. 3.3*, these are readily computed by relating the net intensity of characteristic X-ray lines obtained after the last iteration step to the calculated intensities of a sample with known composition. This is especially easy when the standard consists of a pure element. Determination of k ratios is the basic experiment in analytical procedures involving standard samples. Though they are not necessary in standardless analysis, k ratios reveal the influence of matrix effects on the recorded intensity by comparison with concentrations.

Determination of k ratios is also possible with Monte Carlo methods. After iteratively matching simulated to experimental spectra, emission spectra of a set of standard samples are calculated with the same number of X-ray and electron trajectories, respectively. Characteristic net intensities extracted from the sample and standard spectra using the methods summarised in section 6.3 are then directly comparable and straightforwardly yield a complete set of theoretical k ratios. This is demonstrated exemplarily for quantification of a stainless steel sample by X-ray fluorescence and electron microprobe analysis. Concentrations and k ratios determined with Monte Carlo and fundamental parameter methods are compared in Table 7-1 and show good agreement. As commonly found, k ratios more closely reflect the mass fractions in the case of electron microprobe analysis, whereas the determination of iron, nickel, and copper by X-ray fluorescence analysis is subject to particularly strong matrix effects. Ternary Cr-Fe-Ni alloys are known to exhibit pronounced interelement fluorescence effects.<sup>131,132,158</sup> In this system, the  $K_{\alpha}$  lines of iron and nickel are

located only slightly above the absorption edges of chromium and iron, respectively, and high mass absorption coefficients of  $\mu_{\text{Cr}}(\text{FeK}\alpha) \approx 474 \text{ cm}^2/\text{g}$  and  $\mu_{\text{Fe}}(\text{Ni K}\alpha) \approx 380 \text{ cm}^2/\text{g}$  are encountered. For this reason, strong photoelectric absorption of characteristic X-rays enables secondary and tertiary fluorescent interactions within the sample. The magnitude of fluorescence effects also depends on the concentrations. Copper will be omitted from the discussion as it is only present in traces.

		${}_{24}\text{Cr}$	${}_{26}\text{Fe}$	${}_{28}\text{Ni}$	${}_{29}\text{Cu}$		
XRFA	c [%]	MC	$16.52 \pm 0.19$	$74.64 \pm 0.43$	$8.54 \pm 0.18$	$0.29 \pm 0.02$	
		FP	$19.77 \pm 0.21$	$72.86 \pm 0.38$	$7.03 \pm 0.13$	$0.33 \pm 0.03$	
	$R_{i,K\alpha}$	MC	0.1537	0.4338	0.0204	0.0007	
		FP	0.1587	0.3999	0.0191	0.0010	
	EPMA	c [%]	MC	$16.30 \pm 0.17$	$74.26 \pm 0.45$	$8.59 \pm 0.25$	$0.87 \pm 0.04$
			ZAF	$15.95 \pm 0.16$	$75.23 \pm 0.42$	$8.31 \pm 0.18$	$0.52 \pm 0.05$
ZAF			16.72	74.50	8.25	0.53	
$k_{i,K\alpha}$		MC	0.1814	0.6548	0.0598	0.0052	
		ZAF	0.1751	0.6757	0.0580	0.0037	
		ZAF	0.1964	0.7078	0.0657	0.0042	

**Table 7-1.** Determination of ratios R and k, respectively, by different matrix correction procedures in the quantitative analysis of stainless steel 1.4301 by X-ray fluorescence and electron microprobe analysis.

Monte Carlo methods are well suited to study the influence of fluorescence effects on the characteristic X-ray emission line intensities. Fluorescence is simply 'switched off' by terminating the trajectory of a primary characteristic X-ray photon after its generation and release towards the detector. In this way, the characteristic X-ray line intensities originating from secondary and higher order interelement effects can be easily distinguished from the primary X-ray spectrum. With the analytical data from Monte Carlo quantification provided in Table 7-1, emission spectra of stainless steel were simulated with and without fluorescence effects. The relative spectral intensities  $R_{i,K\alpha}$  of  $K\alpha$  lines are summarised in Table 7-2. In

X-ray fluorescence analysis, interelement effects have virtually no influence on the Ni  $K_{\alpha}$  intensity, whereas the Cr  $K_{\alpha}$  line is enhanced due to secondary fluorescence by Fe  $K_{\alpha}$  radiation. This is also seen to be the main pathway in electron microprobe analysis of stainless steel. However, the Ni  $K_{\alpha}$  line also loses intensity and therefore contributes to interelement effects.

			$^{24}\text{Cr}$	$^{26}\text{Fe}$	$^{28}\text{Ni}$	$^{29}\text{Cu}$
XRFA	$R_{i,K_{\alpha}}$	fl.	0.1784	0.7607	0.0571	0.0038
		no fl.	0.1592	0.7813	0.0571	0.0024
	c [%]	fl.	$16.52 \pm 0.19$	$74.64 \pm 0.43$	$8.54 \pm 0.18$	$0.29 \pm 0.02$
		no fl.	$17.84 \pm 0.21$	$73.67 \pm 0.42$	$8.21 \pm 0.17$	$0.28 \pm 0.02$
EPMA	$k_{i,K_{\alpha}}$	fl.	0.2279	0.7161	0.0513	0.0046
		no fl.	0.1947	0.7416	0.0586	0.0050
	c [%]	fl.	$16.30 \pm 0.17$	$74.26 \pm 0.45$	$8.59 \pm 0.45$	$0.87 \pm 0.04$
		no fl.	$19.14 \pm 0.20$	$72.69 \pm 0.44$	$7.48 \pm 0.16$	$0.69 \pm 0.03$

**Table 7-2.** Relative net intensities  $R_{i,K_{\alpha}}$  and  $k_{i,K_{\alpha}}$  as defined by eq. 3.3 for  $K_{\alpha}$  lines in Monte Carlo simulated emission spectra computed with and without fluorescence effects (marked 'fl.' and 'no fl.', respectively) using the concentrations summarised in Table 7-1. Vice versa, the effect of 'switching off' interelement fluorescence on the result of standardless quantitative Monte Carlo analysis is also shown.

The fraction of Cr  $K_{\alpha}$  intensity originating from secondary and higher order effects amounts to about 11 % in X-ray fluorescence and 15 % in electron microprobe analysis. Consequently, the neglect of interelement fluorescence greatly influences quantification results and leads to an overestimation of the chromium concentration by about 7 % in X-ray fluorescence analysis. Absorption correction partly balances the effect of a lacking fluorescence correction, as this is less than the 11 % change of relative intensities obtained with fixed concentrations. This effect is less pronounced in electron microprobe analysis, and the chromium concentration is subject to an error of 15 % when determined without fluorescence effects. The quantitative detection of fluorescent pathways within a sample can be performed in a

more detailed manner by selectively excluding interactions between particular elements, which is, however, not within the scope of the present study.

In a similar manner, the total suppression of X-ray generation by source radiation in Monte Carlo simulations yields information on the amount of fluorescence induced by scatter radiation. Figure 7-1 shows that the good agreement between experimental and simulated spectra also applies to the scatter region. Underestimation of the Cr  $K_{\beta}$  intensity by the Monte Carlo simulation in this particular example is negligible as only  $K_{\alpha}$  lines are employed for quantification. Steel exhibits rather weak scattering properties, and only about 3.5 % of the total spectral intensity consist of scattered source radiation. Nevertheless, an X-ray fluorescence spectrum simulated without direct excitation of characteristic emissions exhibits weak characteristic peaks. Table 7-3 indicates that characteristic X-rays excited by scattered source radiation and subsequent interelement fluorescence effects amount to 0.5 % of the intensity in the case of chromium. The relative intensity of chromium and iron escape peaks obtained from *eq. 3.36* is in the same range. Therefore, disregarding fluorescence by scattered radiation is not advisable.

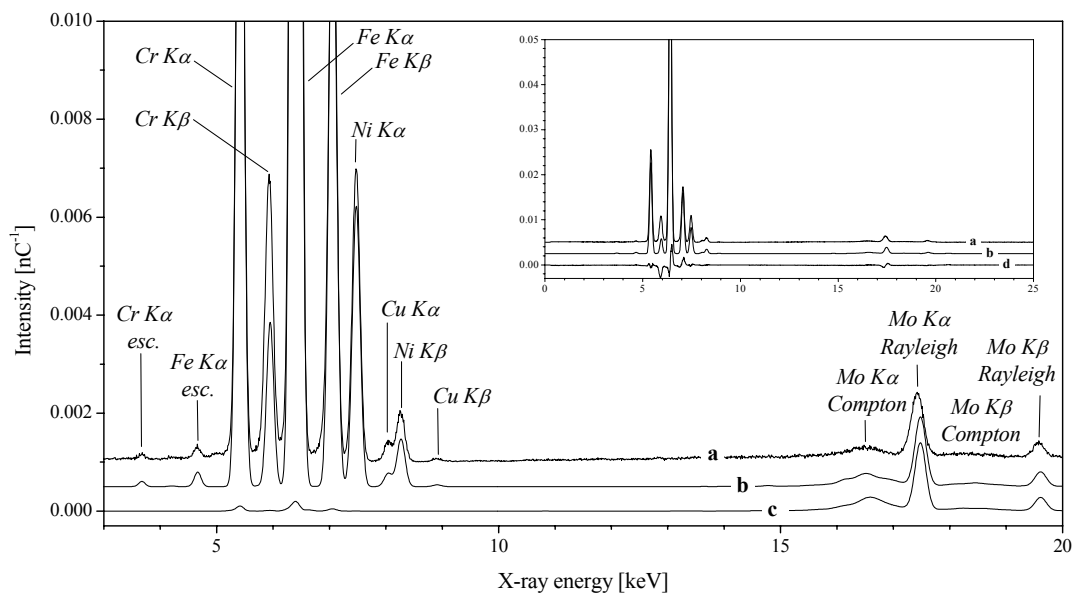


**Figure 7-1.** Quantitative X-ray fluorescence analysis of stainless steel 1.4301 in the scanning electron microscope. The experimental (a), simulated (b), and difference spectra (d) are shown. Fluorescent excitation of characteristic X-rays by scattered source radiation is separated by 'switching off' excitation by source radiation in the Monte Carlo simulation (c). Spectra are offset for clarity.

Relative Intensity [%] of	$^{24}\text{Cr K}_\alpha$	$^{26}\text{Fe K}_\alpha$	$^{28}\text{Ni K}_\alpha$	$^{29}\text{Cu K}_\alpha$
fluorescence by scatter radiation	0.52	0.25	0.02	0.02
escape peaks	0.93	0.65	0.45	0.38

**Table 7-3.** Contribution of characteristic X-rays excited by RAYLEIGH and COMPTON scattered Mo K source radiation to the net characteristic line intensity in the X-ray fluorescence analysis of stainless steel 1.4301. The relative intensity of escape peaks is given for comparison.

Neglecting the generation of characteristic X-rays by electrons allows to discriminate the continuous from the characteristic spectrum and in this way to detect continuum fluorescence. As elements of high atomic number produce a huge amount of continuous radiation, excitation of characteristic X-rays by Bremsstrahlung occurs to a significant degree only in matrices comprising very light and very heavy elements at the same time, for example carbides and oxides of late transition row metals. Due to exceptionally high absorption effects, these are, however, rather unfavourable cases in X-ray emission spectroscopy and are not within the scope of the present discussion.

## 7.2 Thin Samples

The preceding discussion on unified quantification of X-ray emission spectroscopy by Monte Carlo methods refers to the analysis of homogeneous samples with a sufficiently flat surface. Additionally, they are assumed to be of infinite thickness, which means that they are intransparent for either source X-rays or electrons, respectively. These conditions apply to a large fraction of samples occurring in practice and the criterion of flatness is less restrictive especially in the case of X-ray fluorescence analysis due to the large penetration range of X-rays. However, the need to analyse samples of less regular shape cannot be neglected. Fundamental parameter methods are commonly restricted to a specific sample geometry, for example flat, thick, and homogeneous samples. They can be adapted to a special analytical situations, but for this purpose the entire procedure has to be rewritten. In contrast, Monte Carlo procedures are capable of dealing with any given sample geometry. This is

implemented into the simulation routine by adding a simple 'if'-condition checking whether the incident primary photon or electron is still within the sample boundaries or not.

Thin samples are the simplest, but probably also most widespread example of a special analytical situation. As pointed out in section 5.4.2, the intensity of scattered source radiation in an X-ray fluorescence spectrum conveys information about the mass thickness of the sample. Due to the smaller cross-sections, the mean free path length of X-rays is much larger for scattering than for the photoelectric effect. Therefore, the scatter intensities react much more sensitive to changes of the mass thickness of the sample than the fluorescent X-ray intensities. Apart from measuring the X-ray transmittance, this effect can also be exploited to determine the thickness of samples with constant composition or to gain information on the mass thickness of an unknown sample.

Figure 7-2 depicts the intensity of coherently and incoherently scattered Mo K source radiation extracted from Monte Carlo simulated X-ray fluorescence spectra of pure aluminium samples with different thickness, assuming a spectrometer set-up as described in section 5.2.1. For thin layers, the scatter intensity exhibits a strong dependence on sample thickness and runs into saturation as it increases.

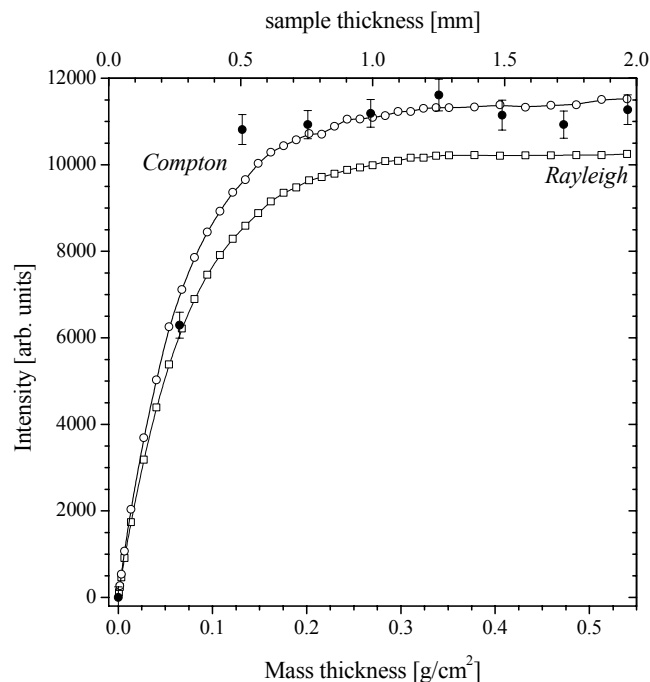


**Figure 7-2.** Intensity of Mo  $K_{\alpha}$  scatter lines in X-ray fluorescence spectra of aluminium as a function of sample thickness. Experimental COMPTON scatter intensities (●) are extracted from spectra of thin aluminium samples placed on a molybdenum backing and excited by a 25  $\mu\text{m}$  Mo source operated at 30 keV. Simulated RAYLEIGH (□) and COMPTON (○) scatter intensities are shown for comparison.

---

This behaviour is in accordance with previous findings reported in the literature.<sup>187</sup> With the present set-up, acquisition of X-ray fluorescence spectra emitted from unsupported thin samples in the scanning electron microscope is not possible. As described in section 5.3.1, highly energetic Bremsstrahlung emitted from the source and transmitted through the sample excites the molybdenum backing. For this reason, determination of the genuine elastic scatter intensity is not possible. Due to the weakly scattering properties of molybdenum, however, the inelastic part remains unaffected by artifacts and thus contains only COMPTON scattered source radiation generated by interaction with the aluminium sample.

X-ray fluorescence spectra of pure aluminium samples with different thicknesses up to 2.00 mm were acquired using a 25  $\mu\text{m}$  Mo target. They are taken from the same batch of material and therefore exhibit the same composition. The relative spectral intensities are only affected by the varying sample thickness, and the presence of trace elements such as iron and copper can be disregarded for this reason. Inelastic scatter intensities were extracted from the X-ray fluorescence spectra by GAUSSIAN fitting of the inelastic scatter peak after background removal and subsequently normalised to the charge applied to the target during the measurement. The experimental data are also plotted in Figure 7-2. Except for a single measurement at a sample thickness of 0.50 mm, these are in quantitative agreement with the data predicted by Monte Carlo simulations within the limits of error that are defined by the counting statistics according to *eq. 3.50*.

The use of Monte Carlo simulations can be further extended by considering electron excited thin samples as encountered in transmission electron microscopy or in the transmission mode of a scanning electron microscope. In this case, thickness dependent backscattering and transmission of electrons have to be regarded. As an example, Figure 7-3 displays the Monte Carlo simulated spectral distributions of electrons transmitted through thin samples of copper at various primary beam energies. In accordance with experimental<sup>95,244,245</sup> and theoretical<sup>89</sup> findings, the energy distributions broaden and their onset shifts to lower energies with increasing sample thickness. The intensity loss of the spectra reflects the decrease of total transmission through the sample.

---

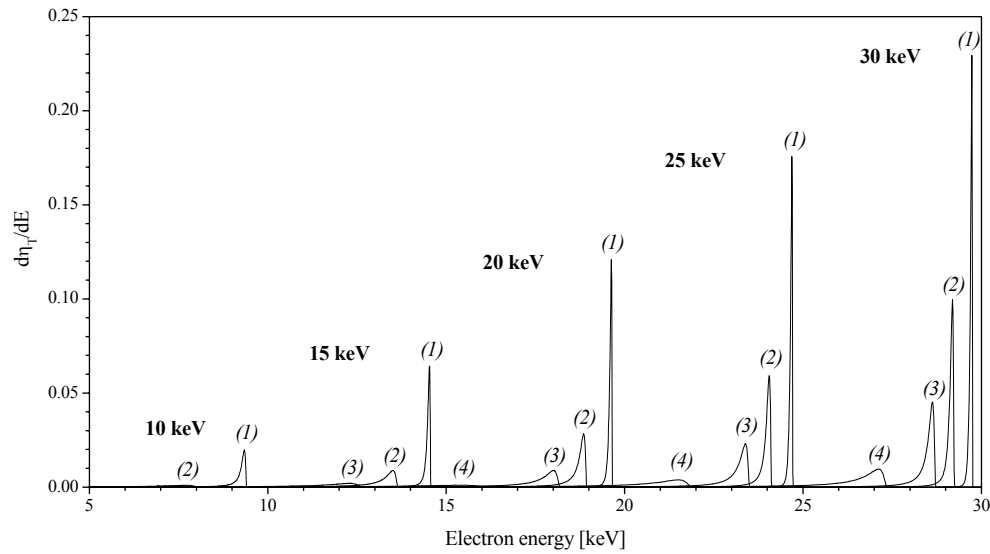


**Figure 7-3.** Spectral distribution of 10-30 keV electrons transmitted through copper layers of 50 nm (1), 150 nm (2), 250 nm (3), and 500 nm (4) thickness, resulting from Monte Carlo simulation of  $10^6$  electrons. With increasing layer thickness, energy distributions broaden and their onset is shifted to lower energies. The intensity loss is related to the decrease of the transmission coefficient with decreasing primary beam energy.

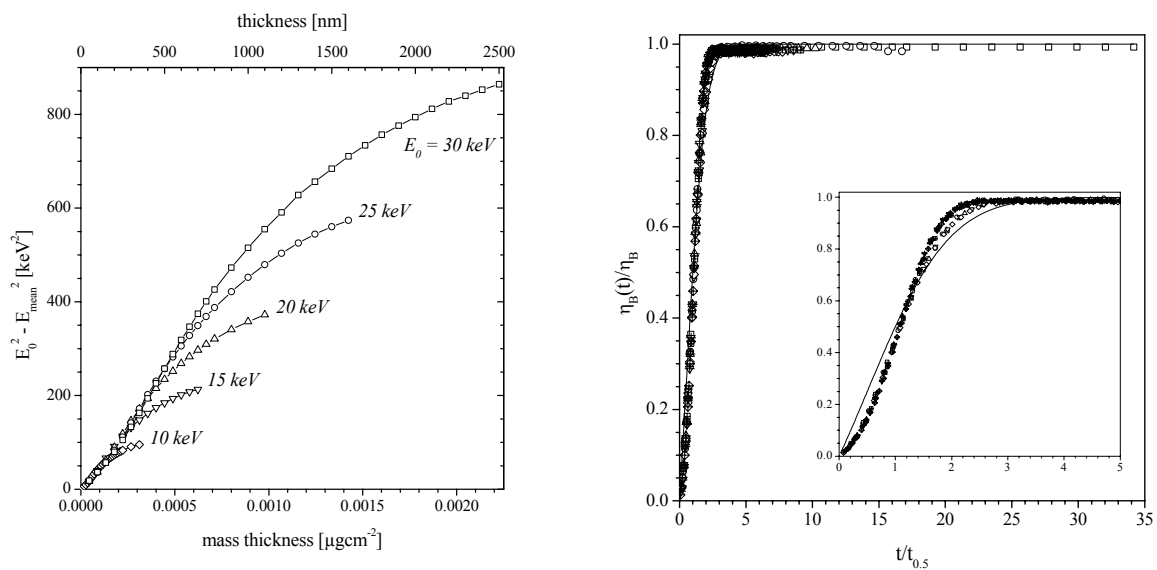


**Figure 7-4.** THOMSON-WHIDDINGTON plot of the mean energy  $E_{\text{mean}}$  of 10-30 keV electrons transmitted through thin copper layers. The mean energies are extracted by applying eq. 2.47 to energy loss spectra obtained by Monte Carlo simulation of  $10^6$  primary beam electrons. The linear branch extending to higher mass thicknesses with increasing primary beam energy is used to derive theoretical values of TERRILL's constant.

**Figure 7-5.** Backscatter coefficient of aluminium and copper as a function of sample thickness. Symbols represent results of Monte Carlo simulations at 10 ( $\square$ ), 15 ( $\circ$ ), 20 ( $\triangle$ ), 25 ( $\nabla$ ), and 30 keV ( $\diamond$ ) and are in accordance with the universal empirical fit proposed by SOGARD<sup>246</sup> (line). Hollow symbols represent simulations for copper and crossed symbols for aluminium.

For a quantitative comparison with experimental data, the simulated mean energy  $E_{\text{mean}}$  of transmitted electrons is determined by using *eq. 2.44*. The THOMSON-WHIDDINGTON plot of  $E_{\text{mean}}$  versus the sample mass thickness is displayed in Figure 7-4. Its linear branch defines the range of validity of *eq. 2.38*, which extends to higher mass thicknesses as the primary beam energy increases. At larger depths, where electrons have lost a large fraction of their initial energy, the energy loss per path length increases significantly and the linear model of *eq. 2.38* becomes invalid. Evaluating the slope of the linear regions yields TERRILL's 'constant'  $c_T$  as a function of primary beam energy, and a survey of simulated numerical values is provided in Table 7-4. The generally accepted constant of 4.0-4.1  $\text{eV}^2\text{cm}^2\text{g}^{-1}$  is observed only for light elements and low primary beam energies, in the present case for aluminium at 10 keV. In all other cases, constants tend to decrease with atomic number and to increase with primary beam energy. This is in accordance with empirical findings<sup>95</sup> reporting the 'constants'  $c_T$  to vary between 4.0-5.2  $\text{eV}^2\text{cm}^2\text{g}^{-1}$  for aluminium and between 3.4-4.9  $\text{eV}^2\text{cm}^2\text{g}^{-1}$  for copper within the energy range of 9-18 keV.

$E_0$ [keV]	10	15	20	25	30	TERRILL
Al	4.0 <sub>1</sub>	4.4 <sub>1</sub>	4.88 <sub>9</sub>	5.30 <sub>7</sub>	5.37 <sub>7</sub>	4.0
Cu	4.3 <sub>1</sub>	4.5 <sub>2</sub>	4.9 <sub>2</sub>	5.0 <sub>2</sub>	5.2 <sub>1</sub>	

**Table 7-4.** TERRILL's 'constant'  $c_T$  for aluminium and copper as derived from the THOMSON-WHIDDINGTON plot Figure 7-4 in units of  $10^{11} \text{eV}^2\text{cm}^2\text{g}^{-1}$ . Its increase with primary beam energy and atomic number is in accordance with findings reported in the literature.

In contrast to the spectral distribution of transmitted electrons, determination of the backscatter coefficient of electron transparent samples is rather straightforwardly accomplished inside a conventional scanning electron microscope. Electron backscattering from thin films has received considerable interest<sup>233,246-250</sup>, especially as this phenomenon enables high accuracy thickness measurements by electron metrology.<sup>251,252</sup>

The elastic large-angle single-scattering approximation of EVERHART predicts a linear increase of the backscatter coefficient with thickness for very thin films.<sup>246</sup> At intermediate thicknesses, this model breaks down as plural scattering occurs during which electrons

experience significant energy losses. In this regime, the backscatter coefficient increases less strongly with sample thickness and saturates towards the bulk value of thick samples. This behaviour is basically the same for all elements, and therefore the shape of the resulting saturation curve can be represented by a single numerical expression of the form :

$$\frac{\eta_B(t)}{\eta_{B,0}} = \tanh \left[ A \cdot \left( \frac{t}{t_{0.5}} \right) + B \cdot \left( \frac{t}{t_{0.5}} \right)^2 \right] \quad (7.1)$$

This equation was proposed by SOGARD<sup>246</sup>, who found it to fit a broad experimental database best by setting the constants  $A = 0.473$  and  $B = 0.0782$ . Herein,  $t_{0.5}$  denotes the sample thickness at which the backscatter coefficient  $\eta_B(t)$  reaches 50 % of its bulk value  $\eta_{B,0}$ . The dependence of the backscatter coefficient on the primary beam energy is introduced into *eq. 7.1* via the parameter  $t_{0.5}$ , which is basically taken from EVERHART's theory and modified according to :

$$t_{0.5} = \frac{\rho Z^2}{\eta_{B,0} A E_0^2} [a(Z)E_0 + b(Z)] \quad (7.2)$$

with the energy  $E_0$  given in units of keV. The terms in brackets account for the energy and atomic number dependence and are given by :

$$\begin{aligned} a(Z) &= (0.040 \cdot Z + 4.34) \cdot 10^{-5} \\ b(Z) &= (-0.0417 \cdot Z + 5.74) \cdot 10^{-3} \end{aligned} \quad (7.3)$$

Results of Monte Carlo simulations of the backscatter coefficient of thin aluminium and copper samples together with the predictions of the model defined by *eq. 7.1* to *eq. 7.3* are summarised in Figure 7-5. Monte Carlo simulated backscatter coefficients are lower than those predicted by the analytical model below a value of  $\eta_B/\eta_{B,0} = 0.5$ , whereas the situation is reversed above. Additionally, the shape of the Monte Carlo simulated function is rather sigmoidal and does not reproduce the linear increase of the backscatter coefficient up to values of  $t/t_{0.5} = 1.0$  or even larger as given by the analytical fit of *eq. 7.1* to *7.3*.

As shown in Table 7-5, the deviations between both models do not exceed 4 % for aluminium

and 15 % for copper in terms of  $t_{0.5}$ . These discrepancies do, however, not originate from shortcomings of the Monte Carlo model, but arise from the analytical fit, which averages the thickness dependence of the backscatter coefficient over a large range of atomic numbers. An initial linear increase with thickness is observed for heavy elements such as gold, for which the closest approach of experiments and the analytical formulation of SOGARD<sup>246</sup> is observed.

E [keV]	$t_{0.5}$ [nm] for Al		$t_{0.5}$ [nm] for Cu	
	analytical	Monte Carlo	analytical	Monte Carlo
10	165.2	$172.8 \pm 7.2$	51.5	$47.3 \pm 1.1$
15	356.5	$363.3 \pm 13.2$	109.8	$96.0 \pm 2.8$
20	608.8	$596.2 \pm 22.3$	185.7	$158.4 \pm 5.2$
25	915.2	$885.4 \pm 25.9$	276.6	$236.3 \pm 7.6$
30	1269.7	$1233.0 \pm 30.0$	332.3	$330.5 \pm 10.0$

**Table 7-5.** Sample thickness  $t_{0.5}$  at which the backscatter coefficient reaches half of its bulk value, according to the analytical model of SOGARD<sup>246</sup> and determined by Monte Carlo simulations, for aluminium and copper at various primary beam energies. The discrepancies are mainly caused by the averaging nature of the analytical model.

In contrast, empirical data of light elements clearly exhibit the sigmoidal shape of the  $\eta_B(t)$  curve obtained with simulations. This example illustrates that Monte Carlo techniques are able to reproduce empirical data with higher reliability than an averaged analytical fit, for which an error level of 10-20 % is assumed.<sup>246</sup>

By summing up all electrons collected in the energy loss spectra as exemplarily shown in Figure 7-3, the transmission coefficient  $\eta_T$  of a thin sample is straightforwardly obtained. Figure 7-6 illustrates the transmission of electrons through copper as a function of sample thickness at primary beam energies of 20 and 30 keV. The function describing this relationship is of convex shape at low sample thickness. An exponential fit to this profile is represented as dashed curve. A nearly exponential decay of transmission as assumed by LENARD's law is only observed at large thickness and down to 20 keV. At lower energies, no

reasonable exponential fit to the Monte Carlo simulated data is possible. The 'mass absorption coefficients' for electrons thus obtained between 20 and 30 keV are summarised in Table 7-6 and show a good agreement with empirical data reported in the literature.<sup>95,244</sup>

$E_0$ [keV]		20	25	30
$\sigma$ [ $\mu\text{gcm}^{-2}$ ]	COSSLETT	4949.8	3541.8	2694.3
	Monte Carlo	$4770.3 \pm 264.0$	$3605.8 \pm 192.3$	$2596.1 \pm 129.3$

**Table 7-6.** 'Mass absorption coefficient'  $\sigma$  for electrons at different primary beam energies assuming an exponential decay of transmission according to LENARD's law *eq. 2.41*. Below 20 keV, no reasonable exponential relationship can be fitted to the Monte Carlo simulated data.

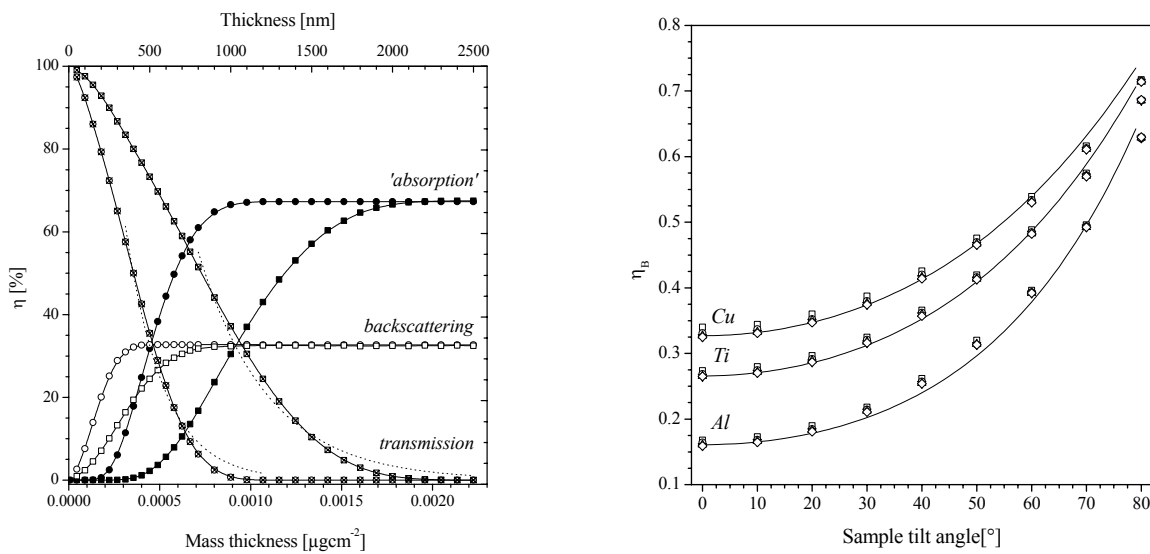


**Figure 7-6.** Monte Carlo simulated backscatter (hollow symbols), transmission (crossed symbols), and 'absorption' (solid symbols) coefficients of copper with varying thickness at primary beam energies of 20 (circles) and 30 keV (squares) at normal beam incidence. Dashed lines represent an exponential fit to the transmission curve according to LENARD's law.

**Figure 7-7.** Empirical<sup>224</sup> (line) and Monte Carlo simulated (symbols) backscatter coefficient of different pure elements as a function of the beam incidence angle. Monte Carlo data are based on the simulation of  $10^6$  electron trajectories and refer to primary beam energies of 10 ( $\square$ ), 15 ( $\circ$ ), 20 ( $\triangle$ ), 25 ( $\nabla$ ), and 30 keV ( $\diamond$ ).

With known transmission and backscatter coefficient, the fraction of electrons remaining in the sample can be deduced by applying the law of charge conservation (*eq. 2.45*). This is also depicted in Figure 7-6 as 'absorption'. Due to the relatively slow decrease of transmission, the fraction of electrons absorbed in the sample reaches its bulk value at considerably larger thicknesses than the backscatter coefficient. In terms of backscattering, a 1.0  $\mu\text{m}$  sample can be considered thick, whereas a thickness of approximately 2.0  $\mu\text{m}$  is needed in terms of absorption and transmission at 20 to 30 keV. This behaviour is in accordance with the characteristics reported in the literature.<sup>94,233</sup>

### 7.3 Tilted Samples

Though a less favourable condition for microanalysis, non-normal incidence of the electron beam may be encountered in scanning and transmission electron microscopy due to sample tilt. When the beam enters the specimen under an oblique angle, the diffusion volume remains closer to the surface, and as a consequence its intersection area with the surface is larger than at normal incidence. Therefore, a larger fraction of electrons is enabled to leave the sample and the backscatter coefficient continuously increases with sample tilt.<sup>224,228-230,237</sup> For a given beam energy and sample composition, a very reasonable description of the backscatter coefficient  $\eta_B$  as a function of the tilt angle  $\alpha$  of the electron beam is given by the formula :

$$\eta_B(\alpha) = B \cdot \left[ \frac{\eta_B(0^\circ)}{B} \right]^{\cos \alpha} \quad (7.4)$$

with the constant B set to 0.89.<sup>224</sup> Monte Carlo simulations of the backscatter coefficient for different elements and energies as a function of the incidence angle shown in Figure 7-7 agree excellently with the empirical data represented by the functional relationship of *eq. 7.4*.

Together with the electron interaction volume, the generation of X-rays is also concentrated in regions closer to the surface, and therefore absorption effects are less severe for tilted samples. This is, however, strongly overcompensated by the loss of energy, which is withdrawn from the sample by the increasing fraction of backscattered electrons compared to normal beam incidence. Therefore, tilting a sample considerably lowers the X-ray yield. Electron diffusion and X-ray generation under the condition of oblique beam incidence are

also accessible by Monte Carlo techniques, but are beyond the scope of the present discussion.

#### 7.4 Conclusions

Monte Carlo simulations are successfully employed to gain information on inherently inaccessible features of X-ray emission spectroscopy, such as to detect fluorescent pathways within a sample. They are also of practical use to solve special analytical problems and can be used to assist the determination of sample thickness by X-ray and electron metrology. It has been shown that Monte Carlo methods are easily adapted to special sample geometries. Correction models to enable the analysis of heterogeneous, porous or rough samples have already been described elsewhere.<sup>194,253,254</sup>

With respect to thin samples, Monte Carlo modelling of X-ray emission spectra should also be applicable to transmission electron microscopy, especially as the available total and differential electron and X-ray cross-sections of the database used range up to an energy of 120 keV. Unlike fundamental parameter methods, Monte Carlo simulations are easily modified to suit more complex analytical situations, for example layered structures, spherical, or even coated spherical particles, as long as the sample geometry is known.

---





---

## 8 Summary

The present work describes the development, application, and evaluation of a novel unified Monte Carlo simulation procedure for both standardless quantitative X-ray fluorescence and electron microprobe analysis. In this context it includes the design, characterisation, and test of an improved specimen stage facilitating X-ray fluorescence in a conventional scanning electron microscope with an energy dispersive X-ray detector.

As probabilistic techniques, Monte Carlo simulations are excellently suited to model statistical phenomena. An algorithm to predict the spectral response of homogeneous multielement samples in X-ray fluorescence analysis has been devised. It is capable of modelling polychromatic excitation conditions and arbitrary spectrometer geometries. Besides instrumental parameters, photoelectric, RAYLEIGH, and COMPTON cross-sections are used along with transition probabilities and fluorescence yields to simulate the path of individual photons and their interactions with the sample. In contrast to conventional fundamental parameter approaches, fluorescence effects beyond third order are not neglected as arbitrary multiple interactions of X-ray photons are accessible. This also involves the prediction of RAYLEIGH and COMPTON scatter peaks, which inevitably appear in X-ray fluorescence spectra and convey information about the mass thickness of the sample under investigation. Consequently, conventionally disregarded RAYLEIGH-photoelectric and COMPTON-photoelectric interaction sequences are taken into account.

Based on readily available MOTT cross-sections, Monte Carlo simulation is a versatile method to model electron diffusion. Due to the high accuracy offered by this technique, numerous approaches were developed in the past to establish a base of backscatter data and X-ray depth distribution functions to be used in fundamental parameter methods for quantitative electron microprobe analysis. Especially the possibility of assessing quantities, which are to be determined only with considerable experimental effort, high inaccuracy, or which are even inherently inaccessible makes Monte Carlo simulations very attractive. These advantages are achieved only at the expense of calculation time. For this reason, the simulation of electron diffusion with subsequent emission of X-rays from a sample under investigation has been out of reach so far.

A Monte Carlo routine simulating electron diffusion has been expanded by incorporation of the algorithm for tracing photons, thus introducing the principles of X-ray absorption and

---

scattering to electron excitation of the emission spectrum. In this way, virtually the same photon tracing procedure is utilised to simulate X-ray and electron excited spectra with the only difference that X-ray generation is located within the sample in the case of electron microprobe analysis. Owing to the incorporation of Bremsstrahlung production via the KRAMERS cross-section, the entire spectral response of the sample including the continuous background is now obtained. As fluorescence effects of arbitrary order are inherently modelled, no need exists to rely on formulae that are based on rather simplified assumptions or to neglect continuum fluorescence, which requires a tedious mathematical treatment and remains approximative in terms of fundamental parameter methods.

By directly coupling X-ray production and detection to electron diffusion on the basis of a Monte Carlo algorithm, information on X-ray emission and electron diffusion is obtained as a valuable by-product. Quantities which are input to fundamental parameter methods, for example X-ray depth distribution functions and backscatter electron spectra, are output quantities of a Monte Carlo based approach. Additionally, information on size and shape of the electron diffusion volume can be evaluated to estimate the lateral resolution and information depth in electron microprobe analysis.

In contrast to other approaches in this field, the present algorithm is not designed to model coupled electron-photon transport up to the GeV range. It rather traces electrons up to an energy of 120 keV and was operated in the energy range covered by an energy-dispersive Si(Li)-detector for the present study. Therefore, the proposed model is computationally straightforward, conveniently runs on a conventional personal computer and is thus well suited as a routine tool for material analysis.

Variance reduction techniques are employed to keep the computational effort as low as possible. In a statistical context, the spectral response of a sample is understood as energy-dependent probability of X-ray photons to impinge onto the detector. By convolution with the detector response function, the inherently unmeasurable X-ray response is converted into a simulated spectrum, which is subsequently scaled to experimental data.

By focussing the electron beam either onto a thin metal target instead of directly exciting the sample, X-ray fluorescence analysis can be performed inside the scanning electron microscope. In order to implement this principle, basic design rules are formulated according to which a sample holder facilitating X-ray fluorescence analysis is constructed. In this

---

---

optimised set-up, two easily exchangeable metal foils serve as target and filter, respectively. The target foil represents the primary source of X-rays, and its thickness of a few micrometres is sufficient to entirely screen the sample from beam electrons but ensures high X-ray transparency. The system imitates a transmission type end window X-ray tube. Above the target foil, the system is closed towards the pole-piece of the objective lens by a commercial platinum aperture with small diameter and thus forms a FARADAY cup, which advantageously enables online monitoring of the probe current during analysis. As a high intensity of emitted X-rays rather than lateral resolution was intended, the beam limiting aperture inserted below the filter foil was chosen to illuminate the entire sample area. All movable parts are constructed as side-entry tray-type inserts. Therefore, fast and simple exchange of target, filter, aperture, and sample is possible and allows a high throughput under different working conditions.

With probe currents of 300-400 nA at beam energies of up to 30 keV as to be obtained in most scanning electron microscopes, X-ray fluorescence spectra are recorded with count rates comparable to those achieved with electron excitation. Systematic investigations on the angular and spectral distribution of primary X-rays prove that the electron diffusion volume within the target establishes an isotropic point source resulting in a dichromatic illumination cone consisting of the corresponding  $K_{\alpha}/K_{\beta}$  line couple. Bremsstrahlung contributes to the excitation spectrum only to a minor extent and can be further reduced by filtering at the expense of source intensity. As the sample holder is open only towards the detector, spectral contamination by fluorescence of the specimen chamber or the pole-piece of the objective lens of the scanning electron microscope are absent. In addition, the constant shift of COMPTON scattered X-ray source lines observed in X-ray fluorescence spectra indicates that an excellent X-ray fluorescer system of well-defined and reproducible geometry is formed.

X-ray fluorescence analysis in the scanning electron microscope greatly improves the signal-to-background ratios of medium and high atomic number elements. Especially when embedded in a light element matrix, traces that are not found with electron excitation of the emission spectrum are clearly detected by X-ray fluorescence analysis. Owing to the absence of Bremsstrahlung, the background is generally considerably lower in X-ray excited spectra. Its shape rather differs from the continuous background encountered in electron microprobe analysis and exhibits a minimum at medium energies, which is shown to be expanded to higher energies by optimising the excitation conditions. Additionally, photoelectric absorption of source radiation preferentially occurs with heavy elements, which are therefore more

---

sensitively detected, whereas electron microprobe analysis remains advantageous for the analysis of light element matrices. However, the excitation conditions in X-ray fluorescence analysis can be tuned in a wide range and are thus adjustable to the analytical problem under investigation. An increased selectivity towards a particular analyte is achieved by setting the primary X-ray energy close to the corresponding absorption edge. This is accomplished by an appropriate choice of the target material. For example, magnesium, aluminium, and silicon are detectable with signal-to-background ratios similar to electron microprobe analysis when excited by Ti K radiation. In this case, the occurrence of continuous radiation with energies above the Ti K absorption edge transmitted through the target foil is rather advantageous. Its intensity suffices for efficient broadband excitation and facilitates detection of heavy element traces and light analytes at the same time.

These investigations prove that an X-ray fluorescer system with well-defined geometry capable of providing clean excitation spectra is formed and thus the basic requirements for quantitative X-ray fluorescence analysis inside the scanning electron microscope are well met. Monte Carlo simulations of emission spectra refer to the entire spectral response of the sample and show excellent agreement with experimental data. This includes RAYLEIGH and COMPTON scatter peaks in X-ray fluorescence spectra, thereby taking DOPPLER broadening of the COMPTON line into account. In the case of electron microprobe analysis, simulation of the Bremsstrahlung background is implemented via the KRAMERS cross-section. As this quantity is not strictly constant but varies smoothly with X-ray energy, simulated continuous background intensities are slightly underestimated in the low energy regime and overestimated at high X-ray energies. However, this effect is too small to seriously affect quantification.

Monte Carlo simulations are exploited to perform standardless quantitative X-ray fluorescence and electron microprobe analysis in the scanning electron microscope. Iterative refinement of simulated spectra is accomplished using the WEGSTEIN procedure, which ensures accelerated convergence. It also prevents oscillations due to overcorrection of concentrations in subsequent iteration cycles, especially in cases where intensities react very sensitive upon slight changes in composition, a situation which is rather commonly encountered in X-ray fluorescence analysis of heavy elements in a light element matrix. As simulations are designed not to distinguish between the characteristic spectrum and continuous background, preprocessing of experimental data to obtain net intensities, such as

---

---

background subtraction, line overlap correction, and peak fitting, is dispensable. With a convergence criterion of  $10^{-5}$  corresponding to three significant digits in mass percentage, quantitative analyses are typically completed within four iteration steps. This requires simulation of an ensemble containing  $10^6$  primary X-ray photons and  $10^4$  electrons per spectrum in X-ray fluorescence and electron microprobe analysis, respectively. Monte Carlo simulations are more time-demanding than fundamental parameter approaches. The computational effort to be taken depends on the excitation conditions and the number of elements present in the sample. Variance reduction is essential in this respect, and the use of effective algorithms reduces the time increase per element to about 30 %. At this expense of computation time, however, the size and shape of the electron diffusion volume, the energy distribution of backscattered electrons, and X-ray depth distribution functions are obtained while retrieving the concentrations of the sample under investigation. Therefore, valuable additional analytical information, which is used as input in conventional fundamental parameter methods, is produced as by-product of Monte Carlo analysis.

Quantification results reveal that X-ray fluorescence analysis significantly improves the detection limits. With samples composed of elements from a rather narrow range of atomic numbers such as Ni-Cu-Fe alloys, detection limits in the range of 100-300 ppm are observed, which means an improvement by a factor of 1.5 to seven compared to electron microprobe analysis. X-ray fluorescence analysis is an especially powerful technique to quantitatively resolve traces of heavy elements in a light matrix. Detection limits are found to decrease from 23.2 ppm  $^{24}\text{Cr}$  to 4.8 ppm  $^{29}\text{Cu}$  in aluminium.  $^{82}\text{Pb}$  is found to be detectable even at a limit of 3.1 ppm corresponding to an atomic percentage of only 400 ppb with measuring times of 1200 sec.

Numerous standardless quantitative X-ray fluorescence and electron microprobe analyses of industrial alloy samples containing elements between  $^{13}\text{Al}$  and  $^{29}\text{Cu}$  have been performed using the Monte Carlo method. Reproducibility representing the precision of analysis is quantified by the deviation of a concentration determination performed under different excitation conditions from its corresponding mean value. Accuracy of X-ray fluorescence analyses is referenced against a common fundamental parameter approach, whereas electron microprobe analyses are evaluated by comparison with the results of two different conventional ZAF matrix correction procedures. In the case of X-ray fluorescence analysis this appears questionable at first glance as in the present set-up the sample is not excited by a parallel but by a divergent bundle of primary photons. However, the illumination cone is

---

rotationally symmetrical as the X-ray source is located above the centre of the sample, and it is therefore acceptable and common practice to perform fundamental parameter calculations with a mean angle of incidence corresponding to a rectangle in the present case. Narrow GAUSSIAN error distribution functions of both relative and absolute precision and accuracy prove the validity of the proposed Monte Carlo quantification procedures. Monte Carlo methods can be easily adapted to more complex analytical situations. Their use in the detection of fluorescent pathways within a sample, and their application to thin samples in X-ray and electron metrology has been demonstrated.

The present work demonstrates that Monte Carlo simulations are very powerful techniques for both conventional electron microprobe analysis as well as standardless quantitative X-ray fluorescence analysis down to the low ppm regime even in the scanning electron microscope. Apart from its numerous intrinsic advantages over conventional fundamental parameter approaches, Monte Carlo quantification has been shown to be a very versatile tool also for non-standard analytical situations.

---





## 9 Appendix

### 9.1 Flow Diagrams of Monte Carlo Algorithms

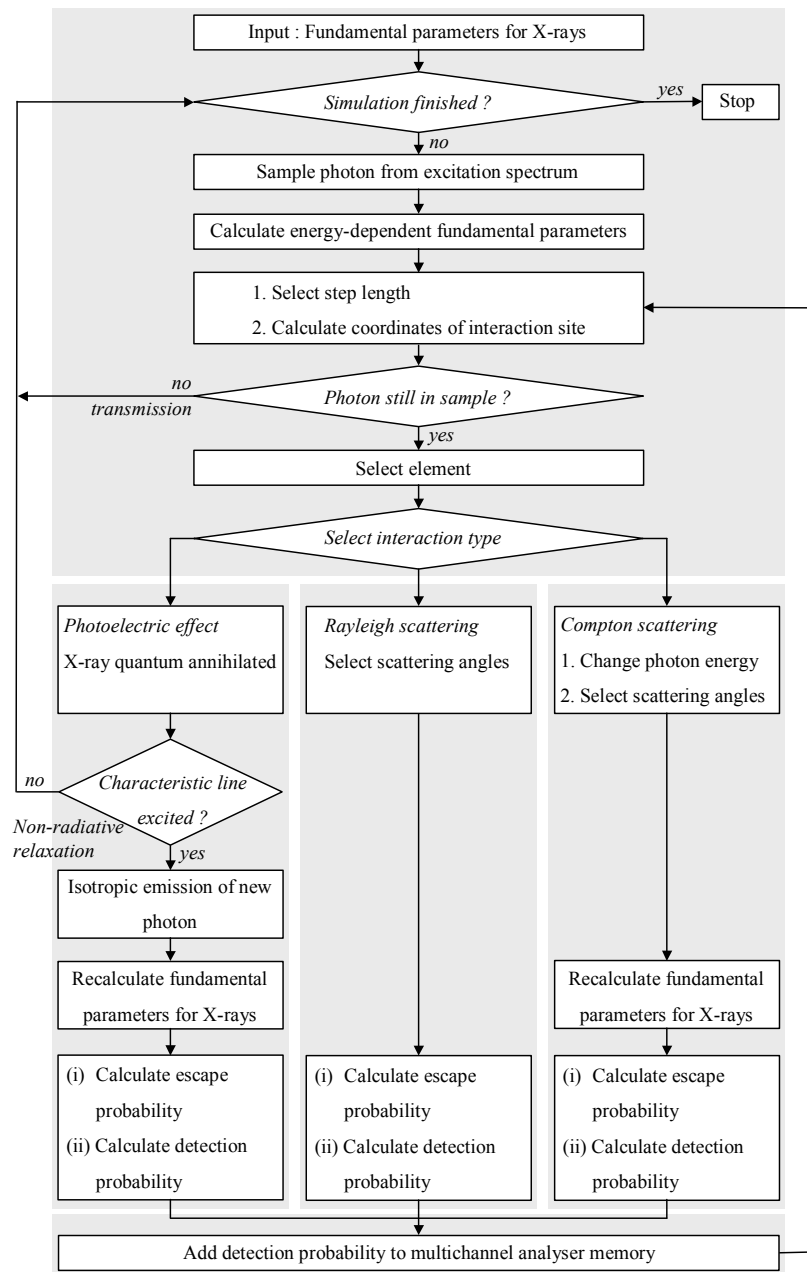


**Figure 9-1.** Flow diagram of the Monte Carlo algorithm to simulate the spectral response of multicomponent samples under polychromatic X-ray excitation in a spectrometer of arbitrary geometry. In order to achieve variance reduction, the probability of the photon striking the detector is calculated after each interaction. A trajectory is only terminated due to radiationless relaxation or when the photon is out of the sample boundaries. The detector characteristics are imposed to the X-ray signal after the simulation to yield the spectrum.

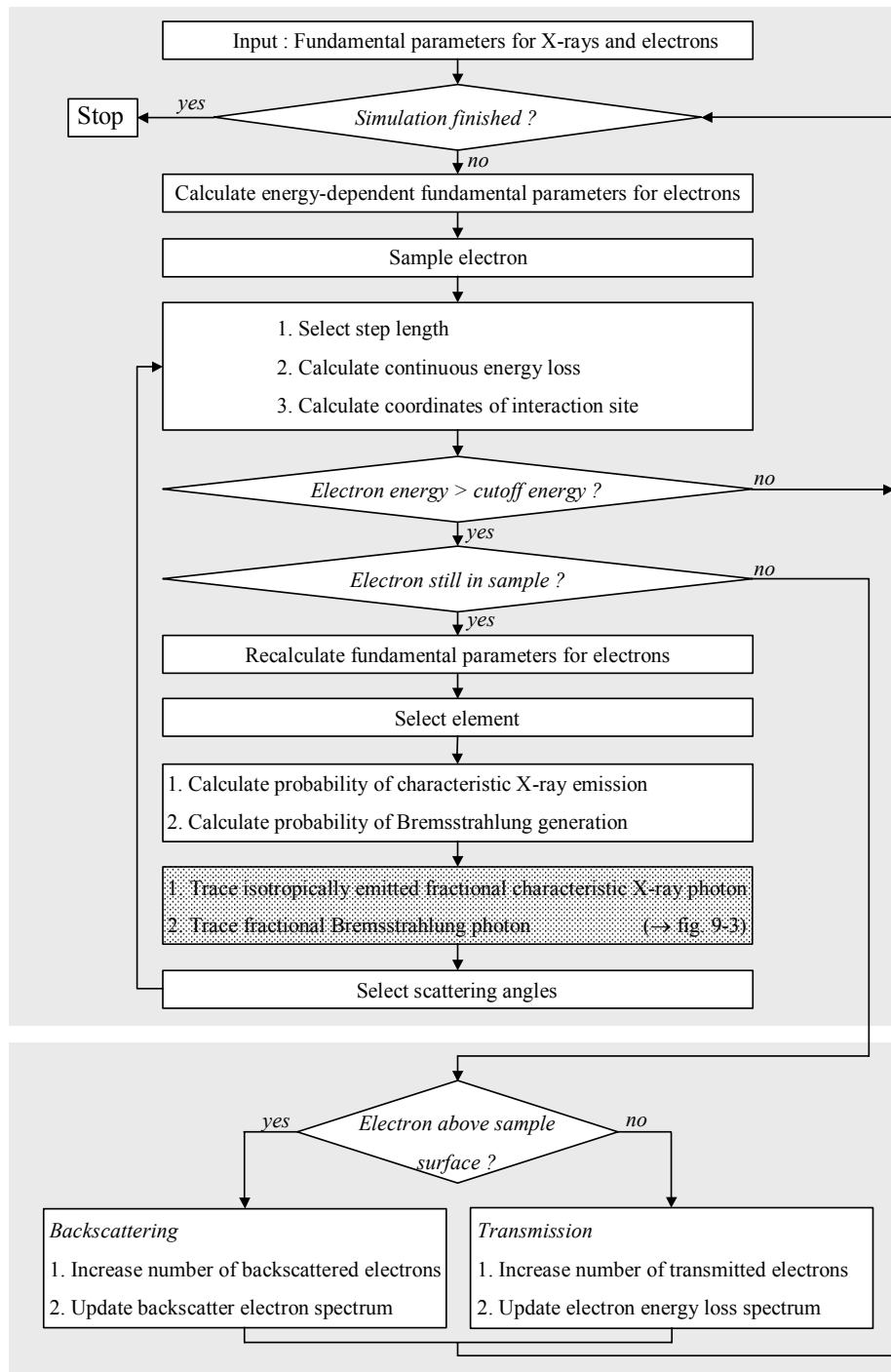


**Figure 9-2.** Flow diagram of a Monte Carlo algorithm to simulate diffusion of electrons through a multielement sample. RUTHERFORD or MOTT cross-sections can be used to select step length and scattering angle. Backscattered and transmitted electrons are recorded and can be sorted according to their energy to obtain the corresponding spectra. The simulation of electron diffusion is paused at the position marked dark grey to trace X-ray photons through the sample.

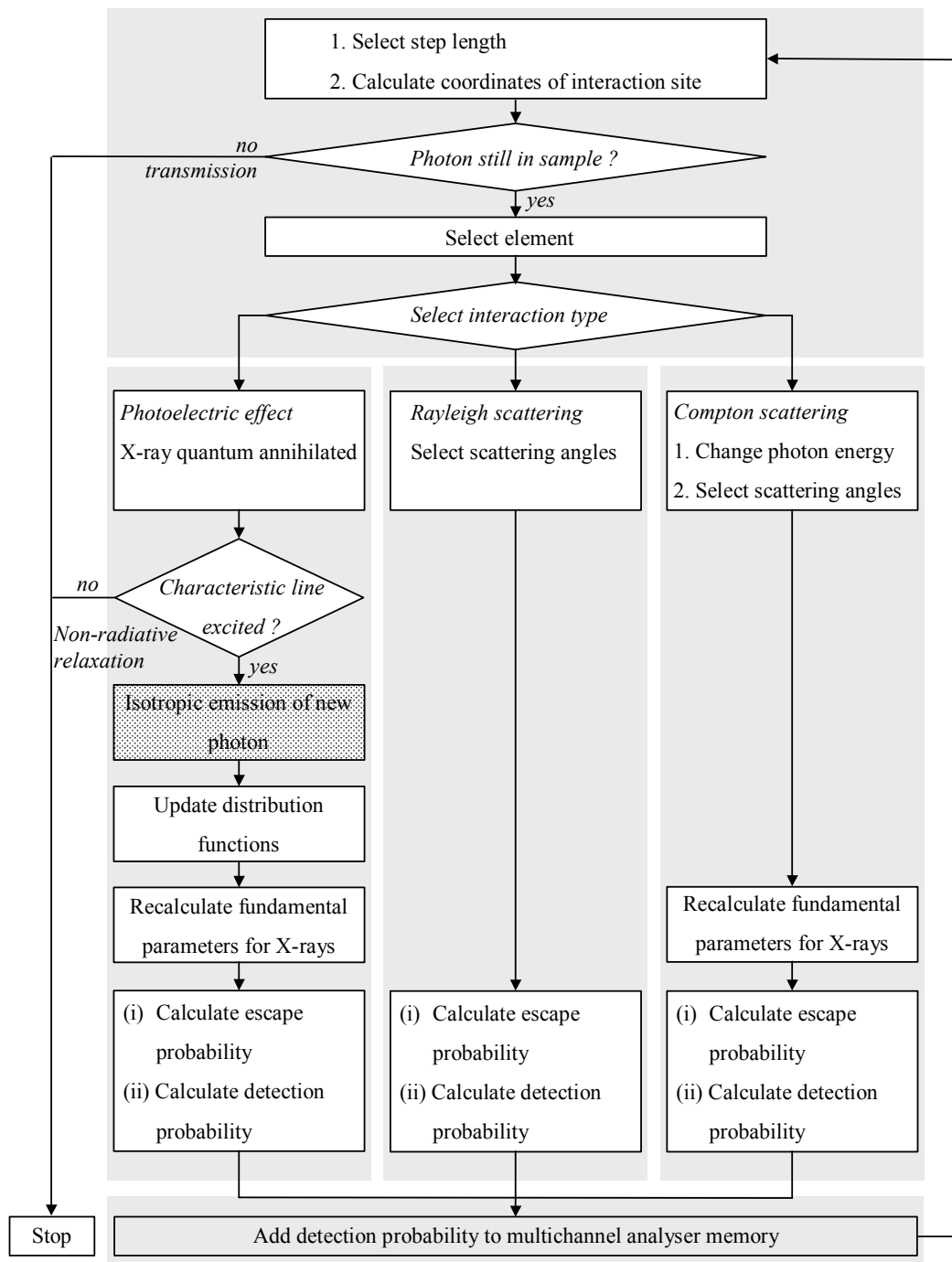


**Figure 9-3.** Simulation of X-ray emission from electron excited samples. The algorithm is started with the emission of a new photon (marked grey), which is either a characteristic or Bremsstrahlung photon, after pausing the simulation of electron diffusion. In terms of variance reduction, simultaneous emission of characteristic and continuous X-rays is accompanied by appropriate weight factors. Therefore, this routine is applied several times per electron-atom interaction.

## 9.2 Construction Drawings of the X-Ray Fluorescence Specimen Stage

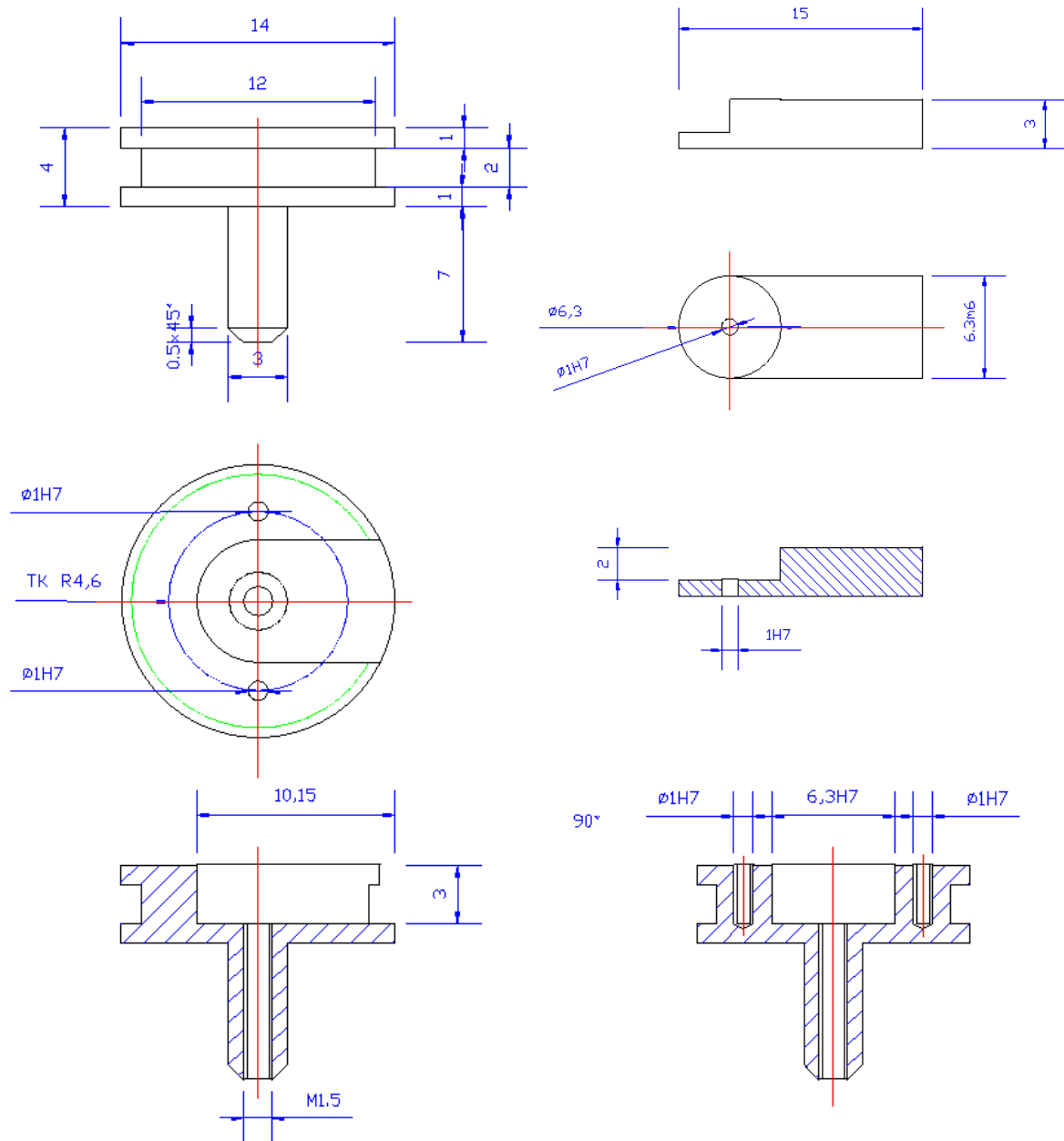


Figure 9-4. Base plate and sample tray.

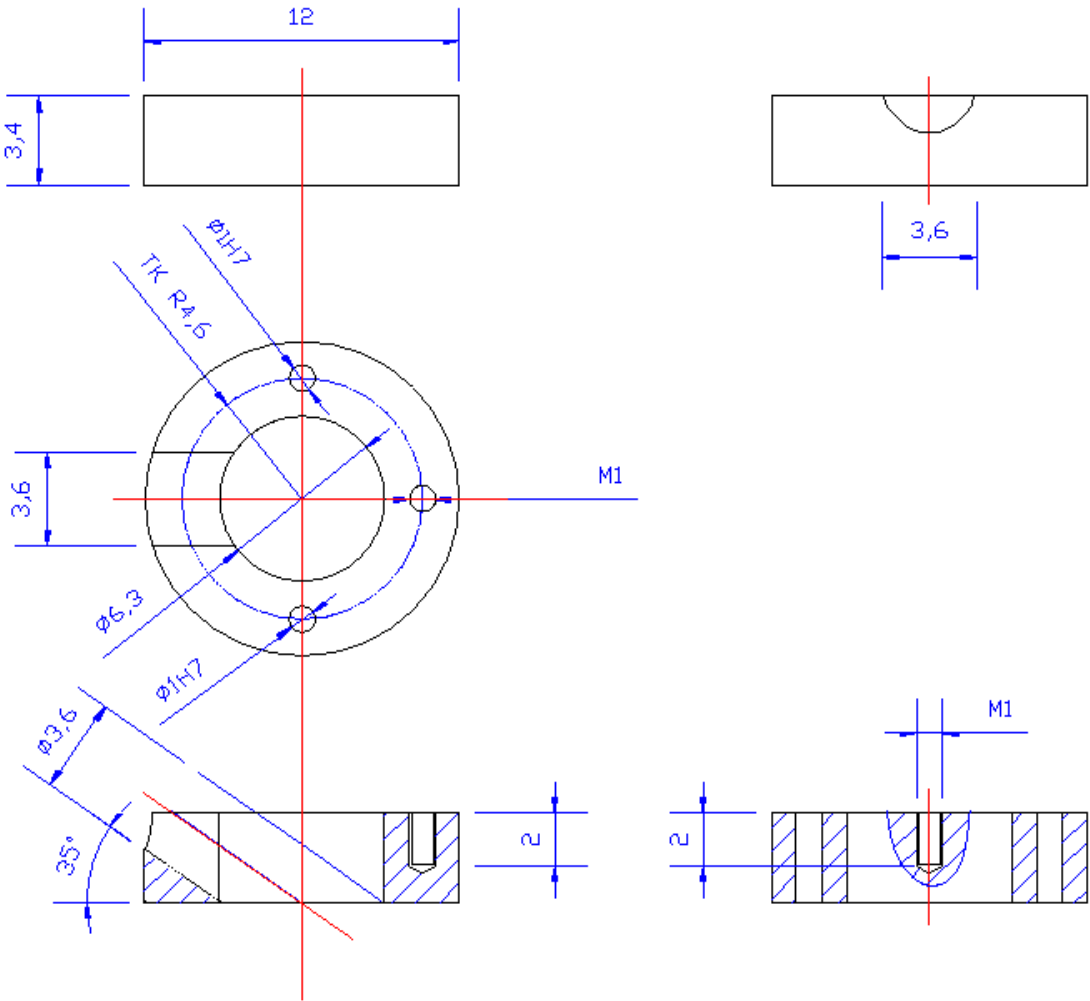


Figure 9-5. Specimen housing to be mounted to the base plate.

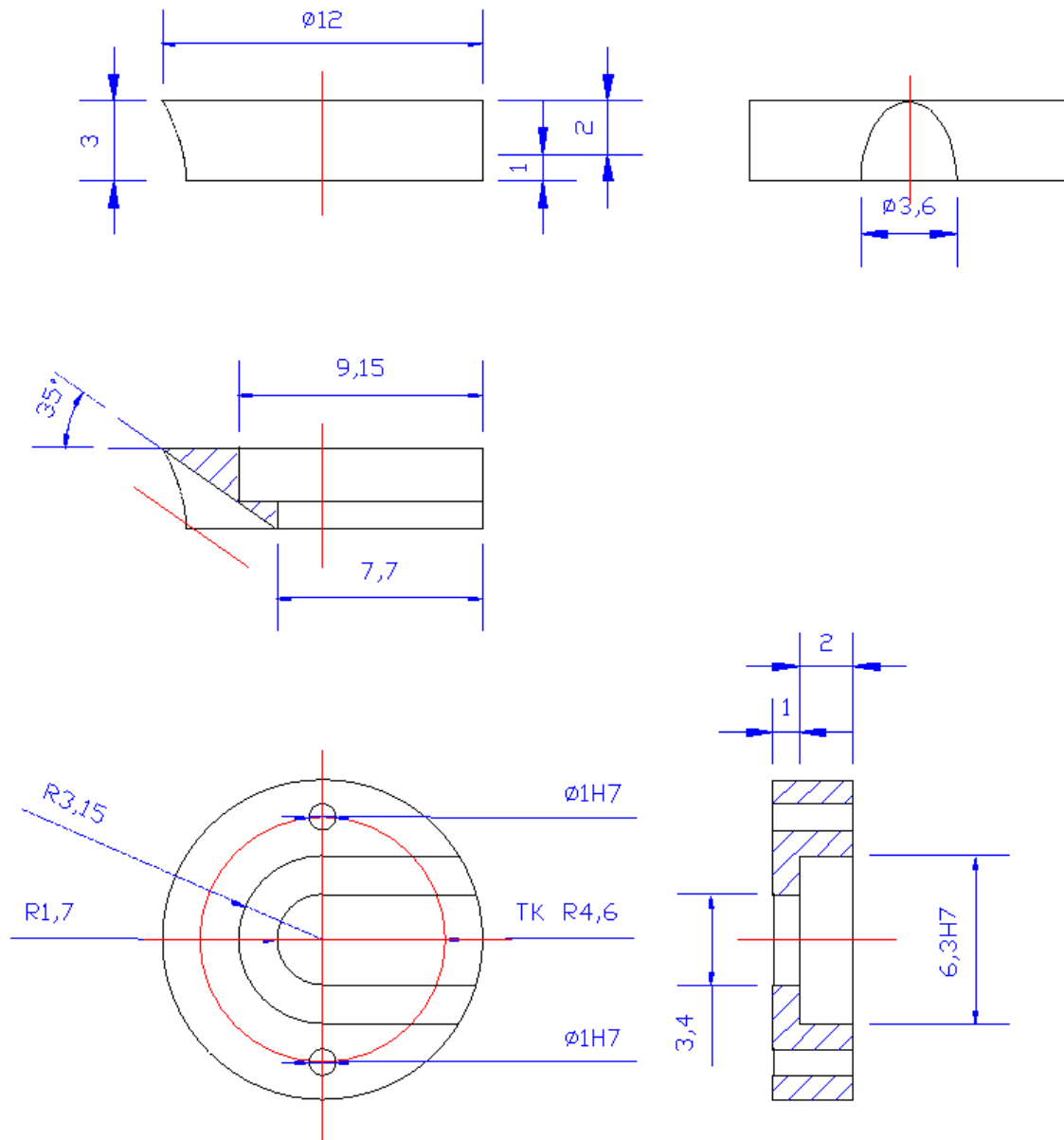


Figure 9-6. Target and filter tray holder.

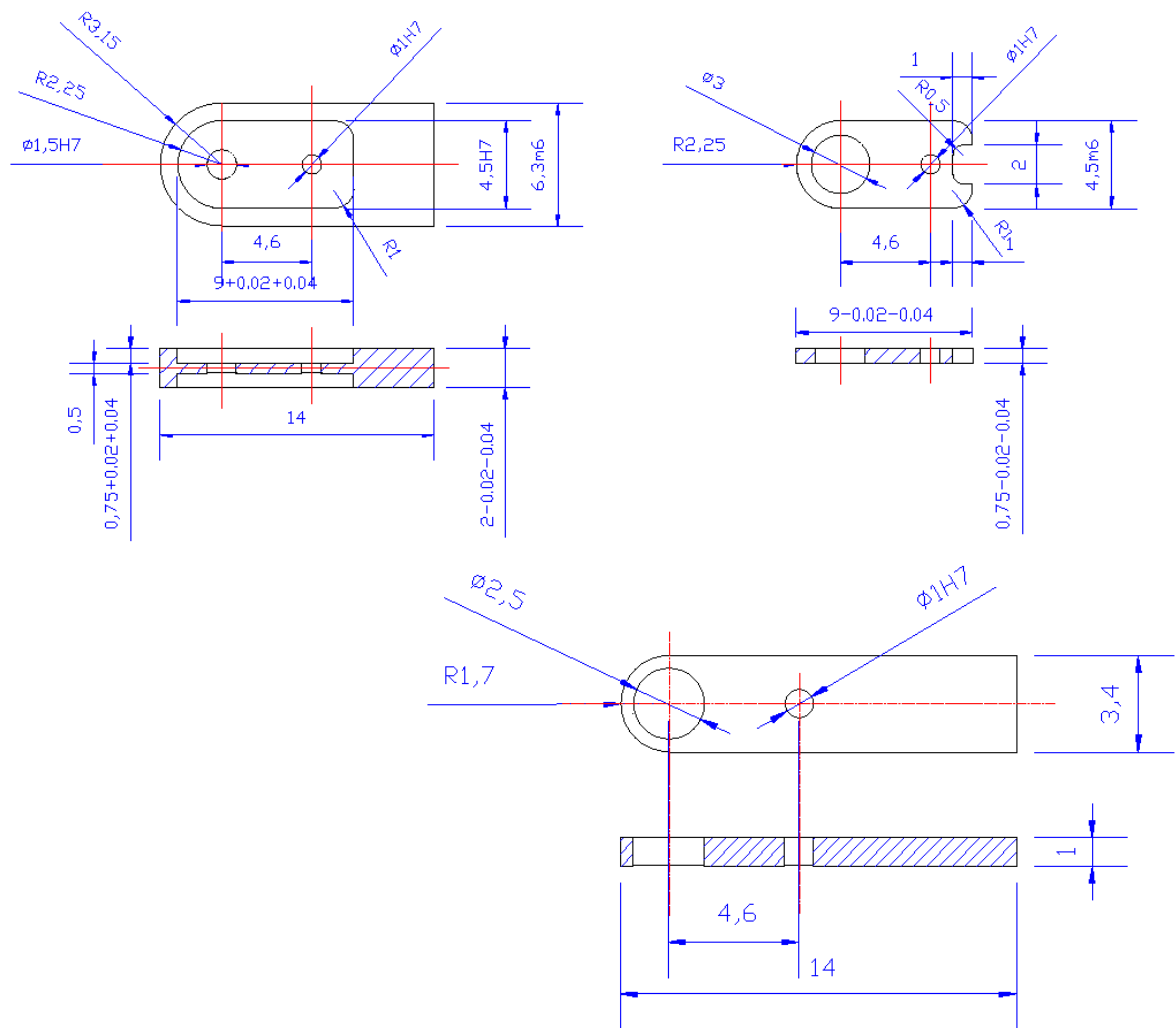
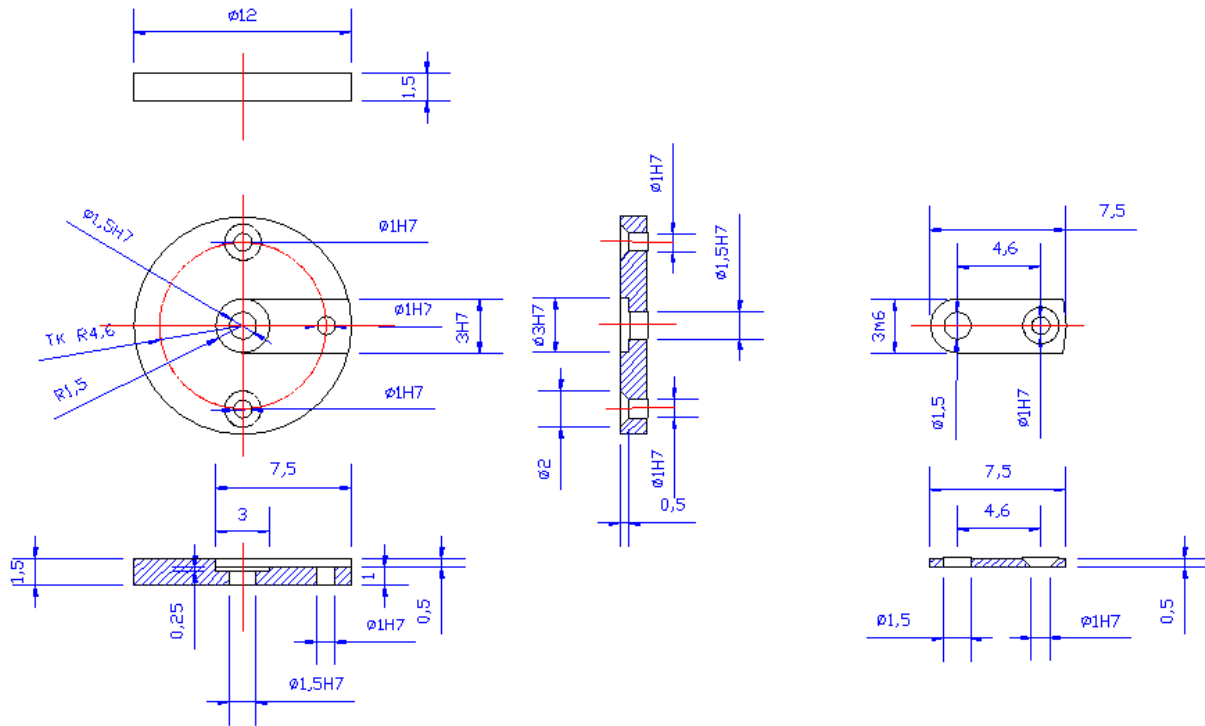
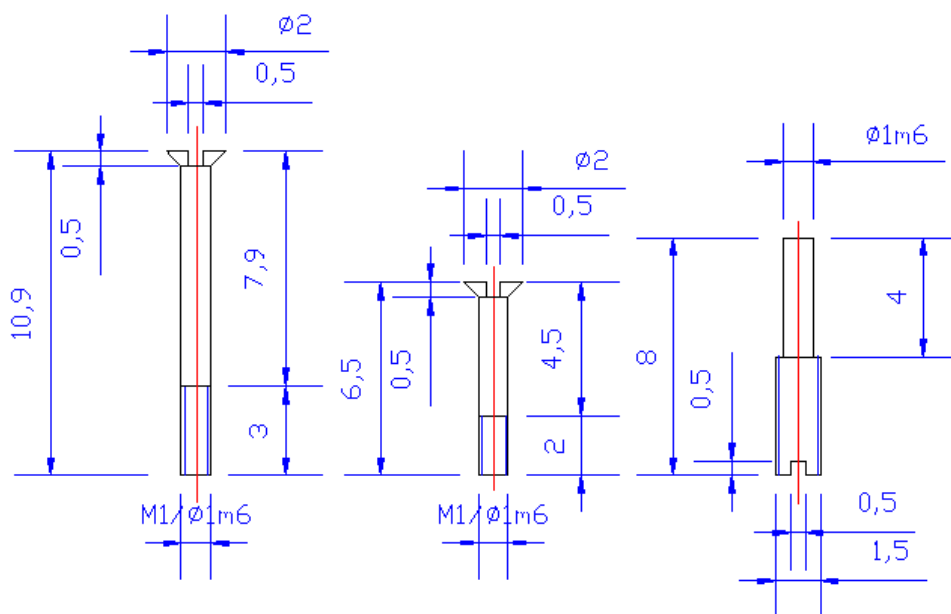


Figure 9-7. Target and filter tray, and beam limiting aperture.



**Figure 9-8.** Top plate closing the system towards the pole-piece of the objective lens of the scanning electron microscope. A commercial platinum aperture is placed in the central bevel.



**Figure 9-9.** Screws required to connect the specimen housing, target tray holder, and top plate to the base plate. An optional screw to allow height adjustment of the sample is also depicted.

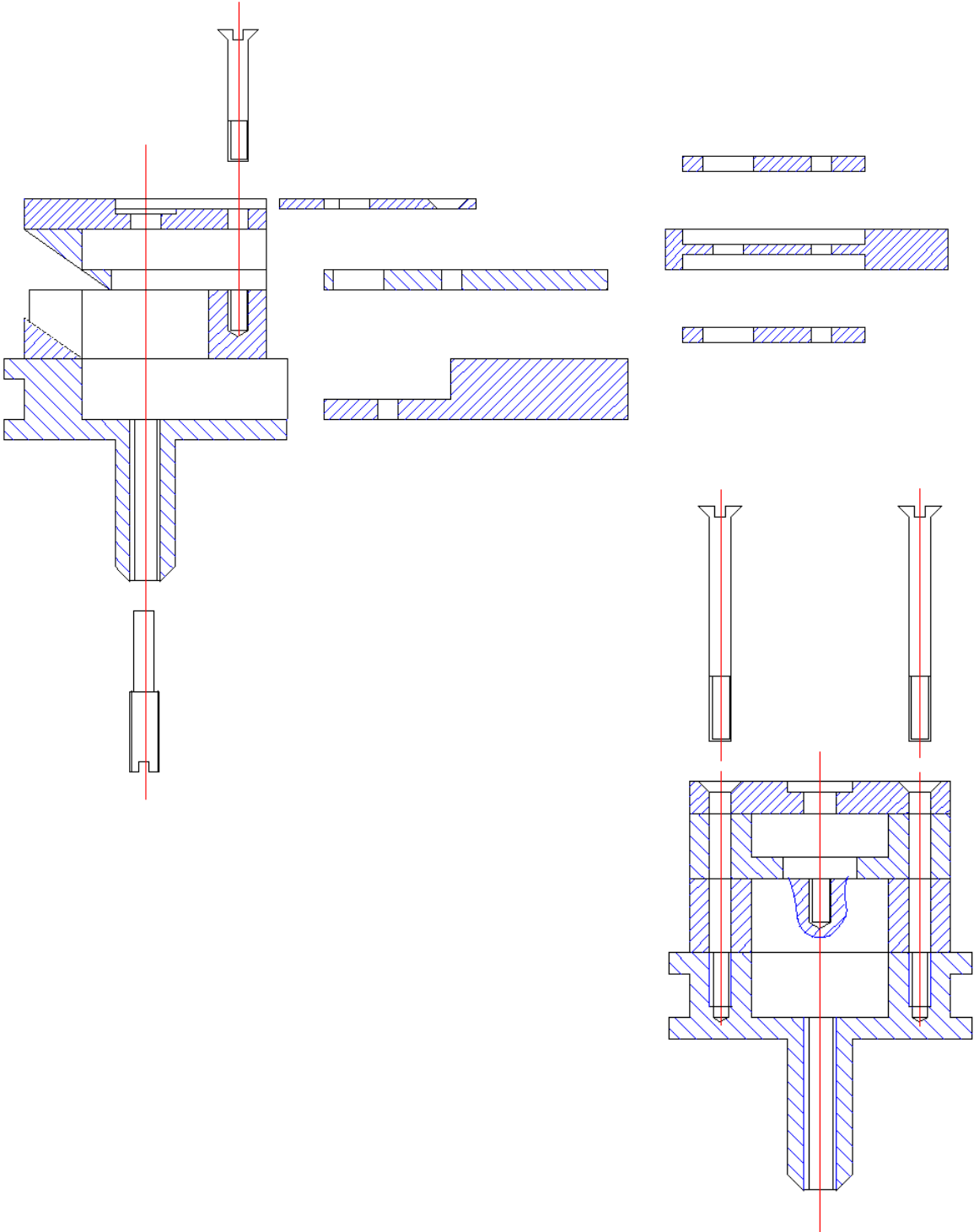
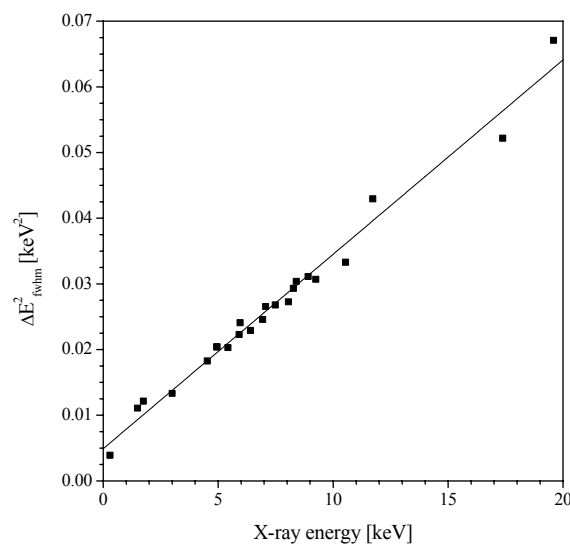


Figure 9-10. Cross-sectional view of the entire X-ray fluorescence specimen stage.

### 9.3 Resolution of the EDS Detection System

The resolution of the energy dispersive X-ray detection system described in section 3.4.1 was determined using *eq. 3.30*. For this purpose, the width of electron excited emission lines  $\Delta E_{\text{fwhm}}$  was recorded as a function of X-ray energy after proper background subtraction by nonlinear iterative peak clipping. Spectra were acquired under the same conditions as encountered in analysis, in this case with an amplifier time constant of 40  $\mu\text{sec}$ , an energy gain of 10 eV per channel and count rates of approximately  $2000 \text{ sec}^{-1}$  for 900 sec. The resulting data are plotted in Figure 9-11. Linear fitting of  $\Delta E_{\text{fwhm}}^2$  as a function of X-ray energy according to *eq. 3.30* renders a resolution due to electronic noise of  $\Delta E_{\text{noise}} = 70.1 \pm 10.9 \text{ eV}$  and a FANO factor of  $F = 0.140 \pm 0.004$ .



**Figure 9-11.** Square of the line width of emission lines as a function of X-ray energy to determine the instrumental parameters of the energy dispersive X-ray detector under the conditions listed in the text.

#### 9.4 List of Materials Utilised to Construct the X-Ray Fluorescence Facilities

Molybdenum (99.9+ %) for construction of the X-ray fluorescence specimen stage, copper (99.99+ %) and nickel (99.99 %) to characterise the angular distribution of X-ray source emission were purchased from CHEMPUR GmbH, Karlsruhe, Germany.

Molybdenum (50  $\mu\text{m}$ ) and titanium foils were supplied by MATECK GmbH, Jülich, Germany, copper, molybdenum (12.5  $\mu\text{m}$ ), and silver foils were purchased from GOODFELLOW GmbH, Bad Nauheim, Germany. Table 9-1 gives an overview of thickness and purity of metal foils employed as targets.

material	thickness [ $\mu\text{m}$ ]	purity [%]
Ti	50	99.6
Cu	10	99.9
Cu	35	99.95+
Mo	12.5	99.9
Mo	50	99.9+
Ag	12.5	99.95+
Ag	35	99.95+

**Table 9-1.** Thickness and purity of metal foils employed as X-ray source targets.

### 9.5 List of Samples and Experimental Conditions for Quantitative Analysis

Alloys were purchased from GOODFELLOW GmbH, Bad Nauheim, Germany, except for stainless steel 1.4301, which was donated by SGS GmbH, Frankenthal, Germany.

Measurements were performed on cylindrical samples 6.30 mm in diameter and 2.00 mm thick with highly polished surfaces. All electron excited spectra were acquired at normal beam incidence. Details on the geometry of the specimen chamber of the PHILIPS XL 30 FEG scanning electron microscope and the energy dispersive X-ray detector by EDAX have already been summarised in connection with design and test of the X-ray fluorescence specimen stage in section 5. Experimental conditions were chosen to yield count rates not above 2000 sec<sup>-1</sup> throughout all experiments in order to maintain reasonable detector resolution and to avoid the occurrence of sum peaks as far as possible.

The table also lists additional trace elements detected in X-ray fluorescence and electron microprobe analysis, respectively. Unless stated otherwise, X-ray fluorescence spectra were acquired for 1200 live seconds, whereas electron excited spectra were recorded for 900 live seconds. In order to obtain comparable figures, detection limits were extrapolated to a measuring time of 1200 sec in the case of electron probe microanalysis.

Sample		XRF		EPMA	
		traces	excitation	traces	E <sub>0</sub> [keV]
Al95/Cu4/Mg1	DURAL <sup>®</sup>	Mn, Fe	Mo	Si, Mn	15, 20, 25, 30
Al97.5/Si1.0/ Mg0.8/Mn0.7		Cr, Fe, Ni, Cu, Zn, Ga, Pb	Ti, Cu, Mo, Ag	Cr, Fe	20, 25, 30
Al98.5/Ni1.5			Mo		20, 25, 30

**Table 9-2.** List of samples and experimental conditions for X-ray fluorescence and electron microprobe analysis. Additional traces not specified in the nominal composition are also given.

Sample		XRF		EPMA	
		traces	excitation	traces	E <sub>0</sub> [keV]
Ti90/Al6/V4		Fe	Mo		10, 15, 20, 25, 30
Co49/Fe49/V2	PERMENDUR 49 <sup>®</sup>		Cu, Mo, Ag		15, 20, 25, 30
Fe54/Ni29/Co17	Glass Sealing Alloy	Mn	Mo, Ag	Mn	20, 25, 30
Fe55/Ni45		Mn	Mo, Ag	Mn	20, 25, 30
Fe64/Ni36	INVAR <sup>®</sup>	Mn	Mo, Ag	Mn	20, 25, 30
Fe72/Cr18/Ni10	stainless steel 1.4301	Cu	Mo, Ag	Cu	20, 25, 30
Ni53/Cr20/Co18/ Ti2.5/Al1.5/Fe1.5	NIMONIC <sup>®</sup> ALLOY 90		Mo, Ag		20, 25, 30
Ni65/Cu33/Fe2	MONEL <sup>®</sup> alloy 400	Mn, Cr	Mo, Ag		20, 25, 30
Ni72/Cr18/Fe8	INCONEL <sup>®</sup> alloy 600		Mo, Ag		20, 25, 30
Ni80/Fe20					20, 25, 30
Ni86/Mn12/Cu2	MANGANIN <sup>®</sup>		Mo, Ag		20, 25, 30
Ni90/Cr10	THERMOCOUPLE ALLOY T1	Fe	Mo, Ag	Fe	20, 25, 30
Ni95/(Al+Mn+Si)5	THERMOCOUPLE ALLOY T2	Co	Mo, Ag	Co	20, 25, 30
Cu55/Ni45	CONSTANTAN <sup>®</sup>	Mn	Mo, Ag	Mn	20, 25, 30
Cu70/Ni30		Mn, Fe	Mo, Ag	Mn, Fe	20, 25, 30

Table 9-2. (continued).



---

**10 References**

- [1] R. A. Morris, L. A. Schwalbe, J. R. London, *X-Ray Spectrometry* **1980**, 9 (2), 40.
  - [2] R. Castaing, *Adv. Electronics Electron Phys.* **1960**, 13, 317.
  - [3] L. S. Birks, R. E. Seebold, A. P. Batt, J. S. Grosso, *J. Appl. Phys.* **1964**, 35 (9), 2578.
  - [4] D. Mosher, S. J. Stephanakis, *Appl. Phys. Lett.* **1976**, 29 (2), 105.
  - [5] R. H. Pantell, P. S. Chung, *Applied Optics* **1979**, 18 (6), 897.
  - [6] A. Rindby, *Nucl. Inst. Meth. Phys. Res. A* **1986**, A249 (2-3), 536.
  - [7] A. Rindby, P. Engstroem, S. Larsson, B. Stocklassa, *X-Ray Spectrometry* **1989**, 18 (3), 109.
  - [8] P. Engstroem, S. Larsson, A. Rindby, B. Stocklassa, *Nucl. Inst. Meth. Phys. Res. B* **1989**, B36 (2), 222.
  - [9] D. A. Carpenter, *X-Ray Spectrometry* **1989**, 18 (6), 253.
  - [10] C. M. Dozier, D. A. Newman, J. V. Gilfrich, R. K. Freitag, J. P. Kirkland, *Adv. X-Ray Analysis* **1994**, 37, 499.
  - [11] N. Gao, I. Y. Ponomarev, Q. F. Xiao, W. M. Gibson, D. A. Carpenter, *Appl. Phys. Lett.* **1996**, 69 (11), 1529.
  - [12] N. Gao, I. Y. Ponomarev, Q. F. Xiao, W. M. Gibson, D. A. Carpenter, *Adv. X-Ray Analysis* **1997**, 39, 81.
  - [13] N. Gao, I. Y. Ponomarev, Q. F. Xiao, W. M. Gibson, D. A. Carpenter, *Appl. Phys. Lett.* **1997**, 71 (23), 3441.
  - [14] L. Vincze, K. Janssens, F. Adams, A. Rindby, *X-Ray Spectrometry* **1995**, 24 (1), 27.
  - [15] L. Brügemann, *MonoCap<sup>TM</sup> and PolyCap<sup>TM</sup> for DX and their applications*, Bruker AXS GmbH, Karlsruhe, presented on the 6th European Workshop on Modern Developments and Applications in Microbeam Analysis, Konstanz, **1999**.
  - [16] R. Klockenkämper, *Total reflection X-ray fluorescence analysis*, John Wiley, New York, **1997**.
  - [17] K. Janssens, F. Adams, A. Rindby, *Microscopic X-ray fluorescence analysis*, 1st ed., John Wiley, New York, **2000**.
  - [18] R. F. Egerton, *Electron energy-loss spectroscopy in the electron microscope*, 2nd ed., Plenum Press, New York, **1996**.
  - [19] L. Reimer, *Scanning electron microscopy*, 2nd ed., Springer Verlag, Berlin, Heidelberg, **1998**.
-

- 
- [20] L. Reimer, *Transmission electron microscopy*, 4th ed., Springer Verlag, Berlin, Heidelberg, **1997**.
- [21] J. Goldstein, D. Newbury, D. C. Joy, C. Lyman, P. Echlin, E. Lifshin, L. Sawyer, J. Michael, *Scanning electron microscopy and X-ray microanalysis*, 3rd ed., Kluwer Academic/Plenum Publishers, New York, **2003**.
- [22] S. A. E. Johansson, J. L. Campbell, K. G. Malmquist, *Particle-induced X-ray emission*, John Wiley, New York, **1995**.
- [23] J. W. Mayer, E. Rimini, *Ion Beam Handbook for Material Analysis*, Academic Press, New York, San Francisco, London, **2003**.
- [24] E. Clayton, P. Duerden, D. D. Cohen, *Nucl. Inst. Meth. Phys. Res. B* **1987**, B22 (1-3), 64.
- [25] C. G. Ryan, E. Clayton, W. L. Griffin, S. H. Sie, D. R. Cousens, *Nucl. Inst. Meth. Phys. Res. B* **1988**, B34 (3), 396.
- [26] E. Clayton, *Nucl. Inst. Meth. Phys. Res. B* **1988**, B30 (3), 303.
- [27] J. L. Campbell, J. A. Cookson, H. Paul, *Nucl. Inst. Meth.* **1983**, 212 (1-3), 427.
- [28] D. D. Cohen, E. Clayton, *Nucl. Inst. Meth. Phys. Res. B* **1987**, B22 (1-3), 59.
- [29] P. Lechner, S. Eckbauer, R. Hartmann, S. Krisch, D. Hauff, R. Richter, H. Soltau, L. Strueder, C. Fiorini, *Nucl. Inst. Meth. Phys. Res. A* **1996**, A377 (2-3), 346.
- [30] D. Newbury, D. Wollman, K. Irwin, G. Hilton, J. Martinis, *Ultramicroscopy* **1999**, 78 (1-4), 73.
- [31] D. A. Wollman, S. W. Nam, D. E. Newbury, G. C. Hilton, K. D. Irwin, N. F. Bergren, S. Deiker, D. A. Rudman, J. M. Martinis, *Nucl. Inst. Meth. Phys. Res. A* **2000**, A444 (1-2), 145.
- [32] C. Lyman, D. B. Williams, J. Goldstein, *Ultramicroscopy* **1989**, 28, 137.
- [33] J. A. Bearden, *Rev. Mod. Phys.* **1967**, 39 (1), 78.
- [34] W. Bambynek, B. Crasemann, R. W. Fink, H. U. Freund, H. Mark, C. D. Swift, R. E. Price, P. V. Rao, *Rev. Mod. Phys.* **1972**, 44 (4), 716.
- [35] H. U. Freund, *X-Ray Spectrometry* **1975**, 4, 90.
- [36] W. Hanke, J. Wernisch, C. Poehn, *X-Ray Spectrometry* **1985**, 14 (1), 43.
- [37] S. Singh, D. Mehta, R. R. Garg, S. Kumar, M. L. Garg, N. Singh, P. C. Mangal, J. H. Hubbell, P. N. Trehan, *Nucl. Inst. Meth. Phys. Res. B* **1990**, B51 (1), 5.
- [38] J. H. Scofield, *Phys. Rev.* **1969**, 179 (1), 9.
- [39] J. H. Scofield, *Phys. Rev. A* **1974**, 10 (5), 1507.
-

- 
- [40] J. H. Scofield, *At. Data Nucl. Data Tables* **1974**, 14 (2), 121.
- [41] J. H. Scofield, *Phys. Rev. A* **1974**, 9 (3), 1041.
- [42] D. G. W. Smith, S. J. B. Reed, N. G. Ware, *X-Ray Spectrometry* **1974**, 3 (4), 149.
- [43] S. I. Salem, S. L. Panossian, R. A. Krause, *At. Data Nucl. Data Tables* **1974**, 14 (2), 91.
- [44] T. P. Schreiber, A. M. Wims, *X-Ray Spectrometry* **1982**, 11 (2), 42.
- [45] J. Trincavelli, S. Montoro, P. Van Espen, R. Van Grieken, *X-Ray Spectrometry* **1993**, 22 (5), 372.
- [46] C. Poehn, J. Wernisch, W. Hanke, *X-Ray Spectrometry* **1985**, 14 (3), 120.
- [47] B. L. Henke, E. S. Ebsu, *Adv. X-Ray Analysis* **1974**, 17, 150.
- [48] J. H. Hubbell, W. H. McMaster, N. K. Del Grande, J. H. Mallett, *X-ray cross sections and attenuation coefficients*, in : J. A. Ibers, W. C. Hamilton, *International Tables for X-Ray Crystallography*, The Kynoch Press, Birmingham, **1974**.
- [49] E. B. Saloman, J. H. Hubbell, *Nucl. Inst. Meth. Phys. Res. A* **1987**, A255 (1-2), 38.
- [50] E. B. Saloman, J. H. Hubbell, J. H. Scofield, *At. Data Nucl. Data Tables* **1988**, 38 (1), 1.
- [51] H. L. Tran, M. Remy, C. Zeller, *J. Phys. D* **1977**, 10 (5), 717.
- [52] L. Gerward, *Nucl. Inst. Meth.* **1981**, 181 (1-3), 11.
- [53] A. M. Yacout, R. P. Gardner, K. Verghese, *Nucl. Inst. Meth. Phys. Res. A* **1984**, A220 (2-3), 461.
- [54] L. Gerward, *X-Ray Spectrometry* **1986**, 15 (1), 29.
- [55] L. Gerward, *Acta Cryst. A* **1983**, A39 (3), 322.
- [56] J. H. Hubbell, W. Veigele, E. A. Briggs, R. T. Brown, D. T. Cromer, R. J. Howerton, *J. Phys. Chem. Ref. Data* **1975**, 4 (3), 471.
- [57] F. Biggs, L. B. Mendelsohn, J. B. Mann, *At. Data Nucl. Data Tables* **1975**, 16 (3), 201.
- [58] S. J. B. Reed, *Electron microprobe analysis*, 2nd ed., Cambridge University Press, Cambridge, **1993**.
- [59] F. Lenz, *Z. Naturforsch.* **1954**, 9a, 185.
- [60] H. Wyrwich, F. Lenz, *Z. Naturforsch.* **1958**, 13a, 515.
- [61] R. Gauvin, D. Drouin, *Scanning* **1993**, 15 (3), 140.
- [62] M. E. Riley, C. J. MacCallum, F. Biggs, *At. Data Nucl. Data Tables* **1975**, 15 (5), 443.
-

- 
- [63] R. Browning, T. Z. Li, B. Chui, J. Ye, R. F. W. Pease, Z. Czyzewski, D. C. Joy, *J. Appl. Phys.* **1994**, 76 (4), 2016.
- [64] R. Browning, T. Z. Li, B. Chui, J. Ye, R. F. W. Pease, Z. Czyzewski, D. C. Joy, *Scanning* **1995**, 17 (4), 250.
- [65] R. Browning, T. Eimori, E. P. Traut, B. Chui, R. F. W. Pease, *J. Vac. Sci. Technol. B* **1991**, 9 (6), 3578.
- [66] R. Browning, *Appl. Phys. Lett.* **1991**, 58 (24), 2845.
- [67] L. Reimer, B. Loedding, *Scanning* **1984**, 6 (3), 128.
- [68] Z. Czyzewski, D. O. MacCallum, A. Romig, D. C. Joy, *J. Appl. Phys.* **1990**, 68 (7), 3066.
- [69] T. S. Rao-Sahib, D. B. Wittry, *J. Appl. Phys.* **1974**, 45 (11), 5060.
- [70] S. J. B. Reed, *X-Ray Spectrometry* **1975**, 4 (1), 14.
- [71] P. J. Statham, *X-Ray Spectrometry* **1976**, 5 (3), 154.
- [72] M. G. Brunetto, J. A. Riveros, *X-Ray Spectrometry* **1984**, 13 (2), 60.
- [73] L. Reimer, P. Bernsen, *Scanning Electron Microscopy* **1984**, 4, 1707.
- [74] P. Bernsen, L. Reimer, *J. Phys. Colloque* **1984**, C2, 297.
- [75] J. A. Small, S. D. Leigh, D. E. Newbury, R. L. Myklebust, *J. Appl. Phys.* **1987**, 61 (2), 459.
- [76] E. Acosta, X. Llovet, E. Coleoni, J. A. Riveros, F. Salvat, *J. Appl. Phys.* **1998**, 83 (11), 6038.
- [77] J. Riveros, G. Castellano, *X-Ray Spectrometry* **1993**, 22 (1), 3.
- [78] F. Bloch, *Z. Phys.* **1933**, 81, 363.
- [79] D. C. Joy, S. Luo, *Scanning* **1989**, 11, 176.
- [80] L. Reimer, M. Ross-Messemer, *J. Microscopy* **1990**, 159, 143.
- [81] R. F. Egerton, *Phys. Stat. Sol. A* **1976**, 37 (2), 663.
- [82] C. Möller, *Ann. Physik* **1932**, 14, 531.
- [83] M. Gryzinski, *Phys. Rev.* **1965**, 138 (2A), 336.
- [84] C. R. Worthington, S. G. Tomlin, *Proc. Phys. Soc.* **1956**, 69, 401.
- [85] N. F. Mott, H. S. W. Massey, *The Theory of Atomic Collisions*, 3rd ed., Oxford University Press, London, **1965**.
- [86] C. J. Powell, *Rev. Mod. Phys.* **1978**, 48, 33.
- [87] L. Reimer, *Ultramicroscopy* **1989**, 39 (1), 169.
- [88] L. Reimer, R. Senkel, *J. Phys. D* **1992**, 25 (9), 1371.
-

- 
- [89] R. Shimizu, Y. Kataoka, T. Ikuta, T. Koshikawa, H. Hashimoto, *J. Phys. D* **1976**, *9* (1), 101.
- [90] G. Love, M. G. C. Cox, V. D. Scott, *J. Phys. D* **1977**, *10* (1), 7.
- [91] G. Love, V. D. Scott, *J. Phys. D* **1978**, *11* (10), 1369.
- [92] G. Love, M. G. Cox, V. D. Scott, *J. Phys. D* **1978**, *11* (1), 7.
- [93] H. M. Terrill, *Phys. Rev.* **1923**, *22*, 101.
- [94] H. Thümmel, *Durchgang von Elektronen- und Betastrahlung durch Materieschichten*, Akademie-Verlag, Berlin, **1974**.
- [95] V. E. Cosslett, R. N. Thomas, *Brit. J. Appl. Phys.* **1964**, *15* (11), 1283.
- [96] P. Lenard, *Ann. Physik* **1895**, *56*, 229.
- [97] H. Niedrig, *Scanning* **1978**, *1*, 17.
- [98] A. Vignes, G. Dez, *Brit. J. Appl. Phys.* **1968**, *1* (10), 1309.
- [99] G. Duerr, W. O. Hofer, F. Schulz, K. Wittmaack, *Z. Phys.* **1971**, *246* (4), 312.
- [100] J. D. Brown, L. Parobek, *Adv. X-Ray Analysis* **1973**, *16*, 198.
- [101] L. Parobek, J. D. Brown, *Adv. X-Ray Analysis* **1974**, *17*, 479.
- [102] J. D. Brown, L. Parobek, *X-Ray Spectrometry* **1976**, *5* (1), 36.
- [103] D. A. Sewell, G. Love, V. D. Scott, *J. Phys. D* **1985**, *18* (7), 1233.
- [104] U. Werner, F. Koch, G. Oelgart, *J. Phys. D* **1988**, *21* (1), 116.
- [105] H. J. August, J. Wernisch, *X-Ray Spectrometry* **1991**, *20* (3), 141.
- [106] H. E. Bishop, *Proc. Phys. Soc.* **1965**, *85* (547), 855.
- [107] G. Oelgart, U. Werner, *Phys. Stat. Sol. A* **1984**, *85* (1), 205.
- [108] R. H. Packwood, J. D. Brown, *X-Ray Spectrometry* **1981**, *10* (3), 138.
- [109] G. F. Bastin, F. J. J. Van Loo, H. J. M. Heijligers, *X-Ray Spectrometry* **1984**, *13* (2), 91.
- [110] A. Savitzky, M. J. E. Golay, *Anal. Chem.* **1964**, *36* (8), 1627.
- [111] H. P. Yule, *Nucl. Inst. Meth.* **1967**, *54*, 61.
- [112] H. P. Yule, *Anal. Chem.* **1966**, *38* (1), 103.
- [113] M. A. Mariscotti, *Nucl. Inst. Meth.* **1967**, *50* (2), 309.
- [114] N. G. Volkov, *Nucl. Inst. Meth.* **1973**, *113* (4), 483.
- [115] J. T. Grant, T. W. Haas, J. E. Houston **1974**
- [116] R. Grote, C. R. Cothorn, *X-Ray Spectrometry* **1974**, *3* (4), 151.
- [117] P. J. Statham, *X-Ray Spectrometry* **1976**, *5* (1), 16.
- [118] K. K. Nielson, *X-Ray Spectrometry* **1978**, *7* (1), 15.
-

- 
- [119] B. Vekemans, K. Janssens, L. Vincze, F. Adams, P. Van Espen, *X-Ray Spectrometry* **1994**, 23 (6), 278.
- [120] P. Van Espen, F. Adams, *X-Ray Spectrometry* **1976**, 5 (3), 123.
- [121] B. Vekemans, K. Janssens, L. Vincze, F. Adams, P. Van Espen, *Spectrochim. Acta B* **1995**, 50B (2), 149.
- [122] R. P. Gardner, L. Wielopolski, *Nucl. Inst. Meth.* **1977**, 140 (2), 289.
- [123] L. Wielopolski, R. P. Gardner, *Nucl. Inst. Meth.* **1977**, 140 (2), 297.
- [124] F. Eggert, *X-Ray Spectrometry* **1990**, 19 (3), 97.
- [125] F. Eggert, W. Scholz, *Phys. Stat. Sol. A* **1985**, 88 (2), K123.
- [126] F. Eggert, W. Scholz, *Phys. Stat. Sol. A* **1986**, 97 (1), K9.
- [127] W. Zimmermann, *Rev. Sci. Instr.* **1961**, 32, 1063.
- [128] H. P. Yule, *Anal. Chem.* **1968**, 40 (10), 1480.
- [129] S. Ekelund, A. Thuren, T. Werlefors, *X-Ray Spectrometry* **1979**, 8 (1), 2.
- [130] G. Kennedy, *Nucl. Inst. Meth. Phys. Res. A* **1990**, A299 (1-3), 349.
- [131] J. W. Criss, L. S. Birks, *Anal. Chem.* **1968**, 40 (7), 1080.
- [132] A. R. Hawthorne, R. P. Gardner, *Anal. Chem.* **1976**, 48 (14), 2130.
- [133] J. W. Criss, *Adv. X-Ray Analysis* **1980**, 23, 93.
- [134] N. Broll, R. Tertian, *X-Ray Spectrometry* **1983**, 12 (1), 30.
- [135] R. Tertian, *X-Ray Spectrometry* **1986**, 15 (3), 177.
- [136] N. Broll, *X-Ray Spectrometry* **1986**, 15 (4), 271.
- [137] R. Tertian, *X-Ray Spectrometry* **1987**, 16 (6), 261.
- [138] N. Broll, *X-Ray Spectrometry* **1990**, 19 (4), 193.
- [139] G. R. Lachance, *Spectrochim. Acta B* **1993**, 48B (3), 343.
- [140] T. O. Ziebold, R. E. Ogilvie, *Anal. Chem.* **1964**, 36 (2), 322.
- [141] S. D. Rasberry, K. F. J. Heinrich, *Anal. Chem.* **1974**, 46 (1), 81.
- [142] B. Dziunikowski, *Energy dispersive X-ray fluorescence analysis*, Elsevier, Amsterdam, **1989**.
- [143] J. V. Gilfrich, L. S. Birks, *Anal. Chem.* **1968**, 40 (7), 1077.
- [144] J. V. Gilfrich, P. G. Burkhalter, R. R. Whitlock, E. S. Warden, L. S. Birks, *Anal. Chem.* **1971**, 43 (7), 934.
- [145] T. C. Loomis, H. D. Keith, *X-Ray Spectrometry* **1976**, 5 (2), 104.
- [146] H. R. Zulliger, J. E. Stewart, *Adv. X-Ray Analysis* **1975**, 18, 278.
- [147] R. Tertian, N. Broll, *X-Ray Spectrometry* **1984**, 13 (3), 134.
-

- 
- [148] P. A. Pella, L. Feng, J. A. Small, *X-Ray Spectrometry* **1985**, *14* (3), 125.
- [149] I. Pozsgai, *X-Ray Spectrometry* **1992**, *21* (5), 249.
- [150] D. B. Brown, J. V. Gilfrich, *J. Appl. Phys.* **1971**, *42* (10), 4044.
- [151] D. B. Brown, J. V. Gilfrich, M. C. Peckerar, *J. Appl. Phys.* **1975**, *46* (10), 4537.
- [152] M. Murata, H. Shibahara, *X-Ray Spectrometry* **1981**, *10* (1), 41.
- [153] E. Gillam, H. T. Heal, *Brit. J. Appl. Phys.* **1952**, *3*, 353.
- [154] J. Sherman, *Spectrochim. Acta* **1955**, *7*, 283.
- [155] J. Sherman, *Spectrochim. Acta* **1959**, *15*, 466.
- [156] R. P. Gardner, J. M. Doster, *Anal. Chem.* **1978**, *50* (12), 1703.
- [157] T. Shiraiwa, N. Fujino, *Jap. J. Appl. Phys.* **1966**, *5* (10), 886.
- [158] T. Shiraiwa, N. Fujino, *Bull. Chem. Soc. Jap.* **1967**, *40* (10), 2289.
- [159] T. Shiraiwa, N. Fujino, *X-Ray Spectrometry* **1974**, *3* (2), 64.
- [160] F. He, P. J. Van Espen, *Anal. Chem.* **1991**, *63* (20), 2237.
- [161] M. Del Giorgio, J. Trincavelli, J. A. Riveros, *X-Ray Spectrometry* **1989**, *18* (5), 229.
- [162] M. Del Giorgio, J. Trincavelli, J. A. Riveros, *X-Ray Spectrometry* **1990**, *19* (6), 261.
- [163] M. Green, V. E. Cosslett, *Proc. Phys. Soc.* **1961**, *78*, 1206.
- [164] M. Green, V. E. Cosslett, *Brit. J. Appl. Phys.* **1968**, *1* (4), 425.
- [165] G. Love, M. G. C. Cox, V. D. Scott, *J. Phys. D* **1975**, *8* (14), 1686.
- [166] H. E. Bishop, *J. Phys. D* **1974**, *7* (14), 2009.
- [167] D. A. Sewell, G. Love, V. D. Scott, *J. Phys. D* **1985**, *18* (7), 1245.
- [168] D. A. Sewell, G. Love, V. D. Scott, *J. Phys. D* **1985**, *18* (7), 1269.
- [169] D. B. Wittry, *J. Appl. Phys.* **1958**, *29*, 1543.
- [170] S. Tanuma, K. Nagashima, *Mikrochim. Acta* **1983**, *1* (3-4), 299.
- [171] S. Tanuma, K. Nagashima, *Mikrochim. Acta* **1984**, *3* (3-4), 265.
- [172] G. F. Bastin, H. J. M. Heijligers, F. J. J. Van Loo, *Scanning* **1984**, *6* (2), 58.
- [173] G. F. Bastin, H. J. M. Heijligers, F. J. J. Van Loo, *Scanning* **1986**, *8* (2), 45.
- [174] S. J. B. Reed, *Brit. J. Appl. Phys.* **1965**, *16* (7), 913.
- [175] J. Wernisch, *X-Ray Spectrometry* **1985**, *14* (3), 109.
- [176] A. Pfeiffer, C. Schiebl, J. Wernisch, *X-Ray Spectrometry* **1996**, *25* (3), 131.
- [177] T. J. White, D. R. Cousens, G. J. Auchterlonie, *J. Microscopy* **1991**, *162* (3), 379.
- [178] L. Wielopolski, R. P. Gardner, *Adv. X-Ray Analysis* **1979**, *22*, 317.
- [179] L. Wielopolski, R. P. Gardner, *Nucl. Inst. Meth.* **1979**, *165* (2), 297.
- [180] R. P. Gardner, J. M. Doster, *Nucl. Inst. Meth.* **1982**, *198* (2-3), 381.
-

- 
- [181] A. M. Yacout, R. P. Gardner, K. Verghese, *Nucl. Inst. Meth. Phys. Res. A* **1986**, *A243* (1), 121.
- [182] M. P. Fioratti, S. R. Piermattei, *Nucl. Inst. Meth.* **1971**, *96* (4), 605.
- [183] N. A. Dyson, *Nucl. Inst. Meth.* **1974**, *114* (1), 131.
- [184] L. H. Christensen, *X-Ray Spectrometry* **1979**, *8* (4), 146.
- [185] G. Springer, *X-Ray Spectrometry* **1976**, *5* (2), 88.
- [186] R. P. Gardner, J. M. Doster, *Adv. X-Ray Analysis* **1979**, *22*, 343.
- [187] L. Vincze, K. Janssens, F. Adams, *Spectrochim. Acta B* **1993**, *48B* (4), 553.
- [188] K. Janssens, L. Vincze, P. Van Espen, F. Adams, *X-Ray Spectrometry* **1993**, *22* (4), 234.
- [189] R. P. Gardner, A. R. Hawthorne, *X-Ray Spectrometry* **1975**, *4* (3), 138.
- [190] A. R. Hawthorne, R. P. Gardner, *Anal. Chem.* **1975**, *47* (13), 2220.
- [191] F. Arinc, R. P. Gardner, *J. Radioanal. Chem.* **1979**, *54* (1-2), 221.
- [192] J. M. Doster, R. P. Gardner, *Adv. X-Ray Analysis* **1980**, *23*, 117.
- [193] J. M. Doster, R. P. Gardner, *X-Ray Spectrometry* **1982**, *11* (4), 173.
- [194] A. M. Yacout, R. P. Gardner, K. Verghese, *Adv. X-Ray Analysis* **1987**, *30*, 121.
- [195] T. He, R. P. Gardner, K. Verghese, *Adv. X-Ray Analysis* **1992**, *35*, 727.
- [196] T. He, R. P. Gardner, K. Verghese, *Appl. Radiation Isotopes* **1993**, *44* (10-11), 1381.
- [197] A. M. Yacout, K. Verghese, R. P. Gardner, *X-Ray Spectrometry* **1986**, *15* (4), 259.
- [198] H. J. Sanchez, R. Sartori, *X-Ray Spectrometry* **1994**, *23* (3), 141.
- [199] R. P. Gardner, H. K. Choi, M. Mickael, A. M. Yacout, Y. Jin, K. Verghese, *Nucl. Sci. Eng.* **1987**, *95* (4), 245.
- [200] M. Mickael, R. P. Gardner, K. Verghese, *Nucl. Sci. Eng.* **1988**, *99* (3), 251.
- [201] J. Sempau, E. Acosta, J. Baro, J. M. Fernandez-Varea, F. Salvat, *Nucl. Inst. Meth. Phys. Res. B* **1997**, *B132* (3), 377.
- [202] E. Acosta, X. Llovet, E. Coleoni, F. Salvat, J. A. Riveros, *X-Ray Spectrometry* **1999**, *28* (2), 121.
- [203] A. F. Bielajew, F. Salvat, *Nucl. Inst. Meth. Phys. Res. B* **2001**, *B173* (3), 332.
- [204] E. Acosta, X. Llovet, F. Salvat, *Appl. Phys. Lett.* **2002**, *80* (17), 3228.
- [205] D. Drouin, R. Gauvin, D. C. Joy, *Scanning* **1994**, *16* (2), 67.
- [206] W. H. Press, B. P. Flannery, S. A. Teukolsky, W. T. Vetterling, *Numerical Recipes in Pascal*, Cambridge University Press, Cambridge, **1996**.
-

- 
- [207] T. He, R. P. Gardner, K. Verghese, *Nucl. Inst. Meth. Phys. Res. A* **1990**, A299 (1-3), 354.
- [208] R. W. Gould, J. T. Healey, *Rev. Sci. Instr.* **1975**, 46 (10), 1427.
- [209] R. Eckert, *Scanning Electron Microscopy* **1983**, 4, 1535.
- [210] L. M. Middleman, J. D. Geller, *Scanning Electron Microscopy* **1976**, 1, 171.
- [211] A. Barna, I. Pozsgai, C. E. Fiori, S. A. Wight, *X-Ray Spectrometry* **1994**, 23 (1), 32.
- [212] I. Pozsgai, *Scanning* **1987**, 9 (1), 36.
- [213] J. B. Warren, H. W. Kraner, *Scanning Electron Microscopy* **1982**, 4, 1373.
- [214] G. Valdre, *X-Ray Spectrometry* **1993**, 22 (1), 39.
- [215] R. Eckert, *Scanning* **1986**, 8 (5), 232.
- [216] R. Eckert, *Mikrochim. Acta* **1988**, 1 (1-6), 193.
- [217] I. Pozsgai, *X-Ray Spectrometry* **1991**, 20 (5), 215.
- [218] B. Linnemann, L. Reimer, *Scanning* **1978**, 1 (2), 109.
- [219] Detection Unit Users Manual, Revision 4.00, EDAX International, Mahwah, NJ, USA, **1992**.
- [220] V. D. Scott, G. Love, *X-Ray Spectrometry* **1992**, 21 (1), 27.
- [221] T. Matsukawa, R. Shimizu, H. Hashimoto, *J. Phys. D* **1974**, 7 (5), 695.
- [222] L. Reimer, H. Drescher, *J. Phys. D* **1977**, 10 (5), 805.
- [223] L. Reimer, C. Tollkamp, *Scanning* **1980**, 3, 35.
- [224] H. J. Fitting, R. Technow, *Phys. Stat. Sol. A* **1983**, 76 (2), K151.
- [225] R. Böngeler, U. Golla, M. Kässens, L. Reimer, B. Schindler, R. Senkel, M. Spranck, *Scanning* **1993**, 15, 1.
- [226] S. G. Tomlin, *Proc. Phys. Soc.* **1963**, 82 (465), 466.
- [227] E. Weinryb, J. Philibert, *Compt. Rend. Acad. Sc. Paris* **1964**, 258 (18), 4535.
- [228] H. Drescher, L. Reimer, H. Seidel, *Z. Angew. Phys* **1970**, 29 (6), 331.
- [229] E. H. Darlington, V. E. Cosslett, *J. Phys. D* **1972**, 5 (11), 1969.
- [230] E. H. Darlington, *J. Phys. D* **1975**, 8 (1), 85.
- [231] T. E. Everhart, *J. Appl. Phys.* **1960**, 31 (8), 1483.
- [232] G. D. Archard, *J. Appl. Phys.* **1961**, 32, 1505.
- [233] V. E. Cosslett, R. N. Thomas, *Brit. J. Appl. Phys.* **1965**, 16 (6), 779.
- [234] P. Verdier, F. Arnal, *Compt. Rend. Acad. Sc. Paris* **1968**, 267B (26), 1443.
- [235] P. Verdier, F. Arnal, *Compt. Rend. Acad. Sc. Paris* **1969**, 268B (16), 1101.
- [236] L. Reimer, D. Stelter, *Scanning* **1986**, 8, 265.
-

- 
- [237] H. J. Fitting, J. Reinhardt, *Phys. Stat. Sol. A* **1985**, 88 (1), 245.
- [238] K. Schäfer, G. Beggerow, *II. Band : Eigenschaften der Materie in ihren Aggregatzuständen, 1. Teil : Mechanisch-thermische Zustandsgrößen*, in : H. Borchers, H. Hausen, K.-H. Hellwege, K. Schäfer, E. Schmidt, *Landolt-Börnstein Zahlenwerte und Funktionen aus Physik, Chemie, Astronomie, Geophysik und Technik*, Springer Verlag, Berlin, **1971**.
- [239] J. D. Brown, R. H. Packwood, *X-Ray Spectrometry* **1982**, 11 (4), 187.
- [240] J. H. Tirira Saa, J. A. Riveros, *X-Ray Spectrometry* **1987**, 16 (1), 27.
- [241] J. H. Tirira Saa, M. A. Del Giorgio, J. A. Riveros, *X-Ray Spectrometry* **1987**, 16 (6), 243.
- [242] *DX-4 application software package*, version 2.11, EDAX International, Mahwah, NJ, USA, **1996**.
- [243] M. Gaber, *X-Ray Spectrometry* **1992**, 21 (5), 215.
- [244] V. E. Cosslett, R. N. Thomas, *Brit. J. Appl. Phys.* **1964**, 15 (8), 883.
- [245] L. Reimer, K. Brockmann, U. Rhein, *J. Phys. D* **1978**, 11 (15), 2151.
- [246] M. R. Sogard, *J. Appl. Phys.* **1980**, 51 (8), 4417.
- [247] H. Niedrig, P. Sieber, *Z. Angew. Phys* **1971**, 31 (1), 27.
- [248] F. J. Hohn, H. Niedrig, *Optik* **1972**, 35 (3), 290.
- [249] H. Niedrig, *Scanning Electron Microscopy* **1981**, 1, 29.
- [250] H. Niedrig, *J. Appl. Phys.* **1982**, 53 (4), R15.
- [251] T. Just, H. Niedrig, H. Yersin, *Z. Angew. Phys* **1968**, 25 (2), 89.
- [252] M. Baciocchi, E. Di Fabrizio, M. Gentili, L. Grella, R. Maggiora, L. Mastrogiamomo, D. Peschiaroli, *J. Vac. Sci. Technol. B* **1995**, 13 (6), 2676.
- [253] J. M. Doster, R. P. Gardner, *X-Ray Spectrometry* **1982**, 11 (4), 181.
- [254] C. Merlet, L. Sorbier, E. Rosenberg, F. Salvat, *Inst. Phys. Conf. Ser.* **2000**, 165 (Microbeam Analysis 2000), 277.
-

---

---

---

## Danksagungen

Meinen herzlichen Dank möchte ich allen aussprechen, die zum Gelingen dieser Arbeit beigetragen haben, vor allem

meinem Doktorvater, Herrn Prof. Dr. E. Plies, in dessen Arbeitsgruppe ich diese Arbeit anfertigen durfte.

Herrn Dipl.-Phys. Jan Bärtele für seine andauernde Hilfsbereitschaft bei allen Computerproblemen, seine kompetente Hilfe in allen Fragen der Programmierung sowie der Physik, für die exzellente Zusammenarbeit, die zahlreichen außeruniversitären Unternehmungen, die ich stets sehr genossen habe, und für seine Freundschaft.

Herrn Dipl.-Ing. B. Degel für die Instandhaltung des XL 30 Rasterelektronenmikroskops und seine schnelle und kompetente Hilfe bei technischen Problemen.

Frau D. Adam, die durch zahlreiche Routinemessungen oftmals dafür gesorgt hat, daß meine Arbeit nicht zu kurz kam.

Herrn Dipl.-Ing. M. Wener für die kritische Durchsicht und Korrektur der Konstruktionszeichnungen.

Herrn Prof. Dr. O. Eibl für wertvolle konstruktive Kritik an dieser Arbeit.

meinen Kolleginnen und Kollegen vom Graduiertenkolleg „Chemie in Interphasen“ für die intensive und ergiebige Zusammenarbeit im Rahmen zahlreicher Publikationen, sowie dem Graduiertenkolleg selbst für ein Stipendium.

meinen (ehemaligen) Kolleginnen und Kollegen Herrn Dipl.-Phys. A. Huber, Herrn. Dr. M. Kienle, Frau Dr. Y. Lutsch und Herrn Dipl.-Phys. M. Rauscher für die gute Zusammenarbeit und die stets angenehme und anregende Atmosphäre in der Arbeitsgruppe.

Angelika für ihre Unterstützung, die nicht in Worte zu fassen ist.

---